Seismic structures of the Acoculco and Los Humeros geothermal fields

D5.3

Seismic structures of the Acoculco and Los Humeros geothermal fields

Version 1.0

Philippe Jousset

and Kristjan Agustsson, Erika Barison, Gualtiero Böhm, Marco Caló, Ivan G. Chavarria, Blancamaria Farina, Emmanuel Gaucher, Katrin Loer, Joana Martins, Mathieu Perton, Flavio Poletto, Erik Saenger, Angel Figueroa Soto, Tania Toledo, Arie Verdel, Claudia Werner.

Work package 5 – Task 2

2019.04.30

Website: http://www.gemex-h2020.eu

The GEMex project is supported by the European Union's Horizon 2020 programme for Research and Innovation under grant agreement No 727550

Table of Contents[1]

[1] The content of this report reflects only the authors' view. The Innovation and Networks Executive Agency (INEA) is not responsible for any use that may be made of the information it contains.

List of figures

List of tables

Executive summary

Los Humeros and Acoculco geothermal fields are two different targets for geothermal sustainable energy resources in Mexico. In the framework of the GEMex project, we performed seismic and seismological data analysis to provide insight into structural features and velocity models.

This report summarises the first results obtained by various methods available in the seismic tool box, by both using previous seismic active data (provided by the CFE - Comisión Federal Electricitad, Mexico) and newly acquired passive seismic data using broadband and short-period seismic networks of several tens of stations deployed at both sites within this task.

The results are presented first on the Los Humeros geothermal field and second on the Acoculco geothermal field.

We provide first details on the methods used for the analysis and we show results from conventional and modern processing of both active and passive seismic data. Thus, we provide velocity models and local earthquake hypocentre locations from travel time tomography. We provide group and phase velocities obtained from ambient noise tomography. We also provide structural features from autocorrelation ambient noise techniques and other cutting edge seismic techniques.

In Acoculco, one major result is that no local seismic event has been detected, so far (stations are still recording at the time this report is written). Therefore, results can be based only on the ambient noise study.

In Los Humeros, results are numerous and mostly consistent to the first order. Results are rather consistent between the seismic methods and allow to locate velocity anomalies in the area that in a broad sense match with known structures from geological and tectonic studies. For example, the limit between the two main anomalies is underlined with the large structure that crosses the caldera from the NE to SW.

Those results provide a good basis for further investigations allowing more detailed studies and integration within other geophysical results of the work package 5 of the GEMex project.

1 Introduction

1.1 Objective of the task

In order to understand both the resource amount and the reservoir sustainability, it is mandatory to know as accurately as possible the structure of a geothermal field, the geographical boundaries of the reservoir, and its change with time. Task 5.2 of the GEMex project has been defined to obtain, as accurately as possible in the timeframe allowed, the structure of the geothermal fields Los Humeros and Acoculco, Mexico, from the acquisition, analysis, interpretation of seismic data.

We performed the task in close collaboration with our Mexican partners from Michoàcan University (Morelia) and UNAM (Mexico-city). In addition, the industrial partner CFE provided very valuable information for us to evaluate the validity of our results.

1.2 Limitations of the report

The time allocated to produce results presented here was very short, therefore, although great care has been put by all contributors, the results presented in this report have large uncertainty. Many results shown here have to be re-evaluated in light of further analysis. This report provides a first data input as accurate as possible for the further tasks of the GEMex project to be performed.

We show results at both geothermal sites, Los Humeros and Acoculco. However, the deployment on both sites were delayed due to the time shift between the European and the Mexican partner projects. Further delay in the deployment at Acoculco resulted from missing authorisations for the seismic network deployment to the site. Data is still being collected and only partial analysis can therefore be made for Acoculco.

Several important results have been achieved for Los Humeros, because a large number of earthquakes had occurred and the results represent a good overview of what seismological methods can bring for the study of geothermal structure as seen by seismic data. However, at Acoculco, no local seismic events have been detected so far. Therefore, results are concerning only ambient noise tomography for this site, and therefore add uncertainty to those results.

1.3 Structure of the report

This report is based on the description of work given by the proposal and project GEMex. In order to reach the objectives described in the main text of the proposal, we divided our task in four main sub-tasks concerning the methods.

- Seismic data acquisition (Los Humeros and Acoculco)
- Seismic data use to derive images of structure;

The report is separated in two main parts: Los Humeros and Acoculco.

1.3.1 Seismic data acquisition

This sub-task consists of

- Gather available data prior to any additional deployment
- Choose instruments and design a new acquisition network in order to acquire adequately new seismic data
- Retrieve, check, perform quality check and store new data in a coherent and accurate data base, in order to perform efficiently further analysis
- Distribute the data base to the different proponents of the task for them to start their own analysis

1.3.2 Seismic data analysis

Seismology has been shown to be one of the most relevant method for understanding both structure and processes of the crust, especially in geothermal reservoirs (e.g., Jousset et al., 2011). The description of work details the different methods that we employed to gather results.

1.3.2.1 Earthquakes analysis

The procedure we follow is the following:

- Detection of earthquakes. Initial frequency analysis in order to determine their potential origin
- Potential qualitative source process (strike-slip, long –period event fluid-related, etc.)
- Pick arrival times of P- and S- seismic waves
- Spatial localisation of the earthquakes
- Build a catalague with magnitudes
- Source mechanism of the clearest events

1.3.2.2 Earthquake based travel-time tomography

Several codes can be used for performing travel time tomography. The report indicate results from the different approaches

- VELEST to derive 1D velocity model
- SIMULPS for 3D velocity model
- CAT 3D which uses multi-wave arrival

We also tentativaly compare the results obtained by the different methods.

1.3.2.3 Ambient noise correlation methods

In recent years, it has been shown that ambient noise interferometry techniques were able to provide accurate images of the subsurface of the crust, even if there are no earthquakes. We performed several of those methods.

- **Noise interferometry** using existing and newly acquired data
- **Surface wave-tomography**
- **Body-wave interferometry**
- Tomography and interferometry using existing **active-source seismic data**

1.3.2.4 Attenuation methods

We could be perform attenuation tomography on the active seismic data from CFE. Additional work is needed to perform it on the passive data set.

1.3.2.5 Beamforming method

The method provides a complementary study for noise analysis. It provides evidence on the location of the source of noise used for the ambient noise tomography.

1.3.3 Fluids related processes

This section is incomplete in this report. The complement will be reported in the deliverable D5.4 – Time dependent processes.

- **Time dependent tomography**
  If the number of earthquake is sufficient, we can perform travel time tomography for a subset of data, at different times. The analysis of successive structural images can therefore be performed. It is also possible to perform the same approach with ambient noise cross-correlation techniques.
- **Time reversal modelling** to locate and characterize microseismic events
- **Identification of zones where seismic energy can accumulat**e and may cause fracture growth and/or fluid-related processes. This method uses a velocity model. However, the numerical setup is developed (Lupi et al. 2016, 2017, 2018), a theory is in progress (Barbosa & Lupi, 2019, personal communication), and the FD code Heidimod is optimized for providing the strain tensor at selected positions.
- **Time-lapse study of passive seismic attributes** caused by partially saturated rocks
- **Long-period seismicity.** If existent and recorded, test for full-wave form inversion to derive source moment tensor.

1.3.4 Modelling approaches

This section will be reported in the deliverable D5.5 – Modeling methods

- **Improve methods** for earthquake location, analysis of location errors, wave-form inversion, using computer facilities.
- **Comparison of wave-form modelling codes** by designing a benchmark. The parallel finite difference solving the elastodynamic wave equation using the rotated staggered grid technique (Saenger et al. 2000) code "Heidimod" can be used for several applications. For the TRI approach we use typically models with a size of 1100 by 1100 grid points and a depth of 350 grid points. With a grid spacing of 60 m this would correspond to a model size of 66 km by 66 km and a depth of 21 km. Using our in-house cluster computer, it takes about 10 seconds to compute the simulation of elastic wave propagation when using 3 compute nodes and 69 total tasks. This model was designed to be numerically stable for frequencies up to 3 Hz. Further tasks will be to decrease the grid spacing and the model size and thus be able to increase the frequency.
- **Full-waveform modelling in poro visco-elastic media** with temperature (including melting and BDT analysis), using temperature maps from WP6, and estimate initial stress, pressure conditions and Arrhenius parameters from geothermal info and (if available) laboratory data provided by other partners.

ACOCULCO geothermal field

2 Data acquisition (Acoculco)

2.1 Gathering and evaluation of existing and available data

Acoculco geothermal field was never studied with detail exploration. A preliminary study was performed with a deployment of 6 seismic stations and record for one month. Those records did not find any seismic event in the area of Acoculco.

2.2 Design of new acquisition networks

A passive seismological network of about 15 broadband seismological stations has been deployed in the area of Acoculco around the exploratory well. The network is still being recording, therefore only partial analysis can be reported here.

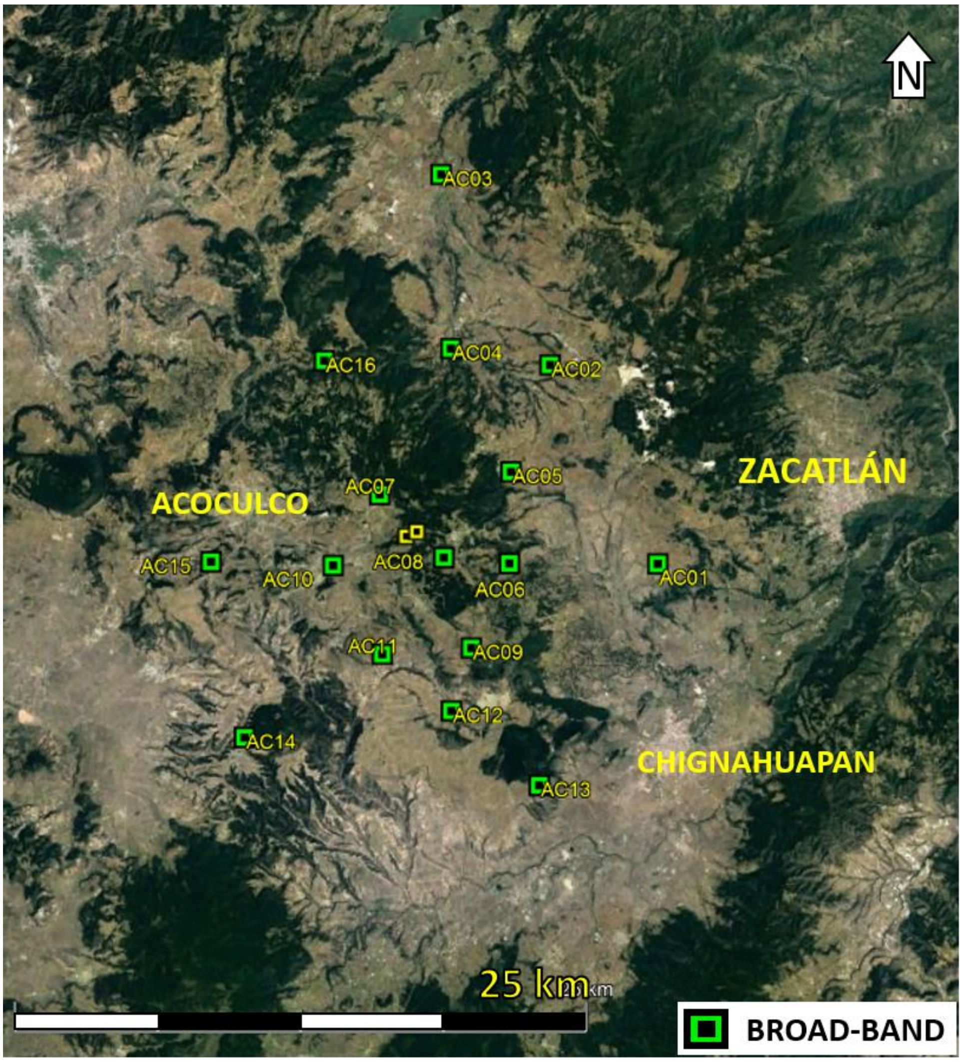

Figure 1 : Network deployment of the seismic broadband stations – Courtesy Marco Calo (UNAM)

3 Preliminary seismic structure (tomography methods) of Acoculco geothermal field

The first 10 stations were installed in the beginning of May 2018 and 16 stations were recording in the beginning of June 2018. The network is still in operation.

The data from start to the end of November 2018 has been analysed with the result that there are no local earthquakes detected yet, neither by using automatic detection algorithms nor with manual inspection. Both the detection using the methods described in the Los Humeros part and the methods used for routine locations in Icelandic geothermal areas were tested. However, the network is functional as regional and teleseismic events are observed (Figure 2).

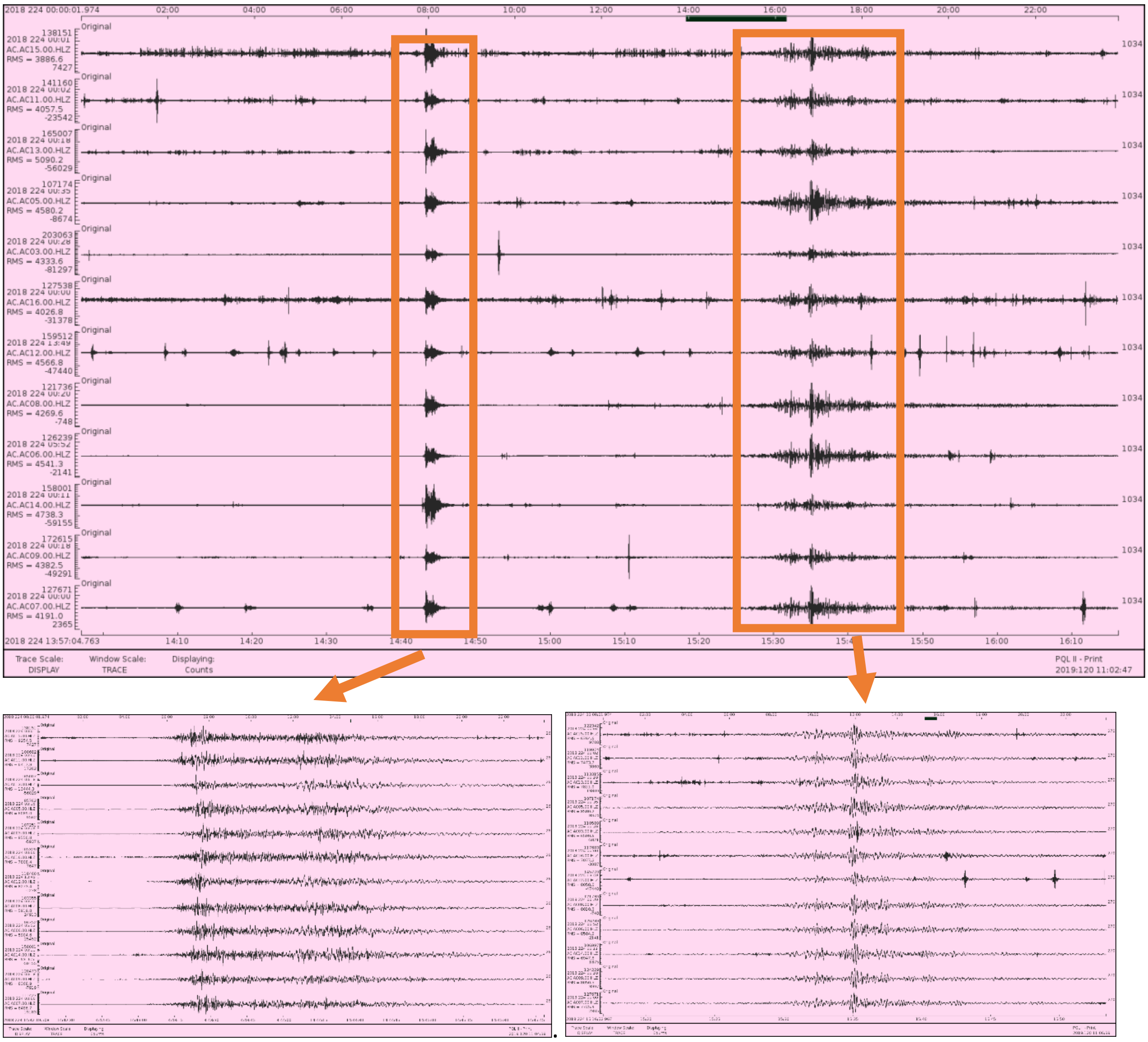

Figure 2 : Examples of regional and teleseismic events.

There is considerable noise in the data, both tremor and spikes. As far as we know, there is no human activity in the area that may cause this except some mining activities. Whether some of these signals originate in the geothermal reservoir is an open question.

The main result from the records so far is that there was no earthquake recorded.

- No local earthquakes were detected or located using ÍSOR's automatic Seiscomp system. The system is optimized for detection and location of local earthquakes in geothermal fields in Iceland. However, some regional earthquakes are detected confirming that the Acoculco seismic network was functional. Consequently, no further seismic analysis on the Acoculco geothermal field can be undertaken.
- Additionally, random inspection of waveform data in PQLX was performed. Confirming the Seiscomp outcome.

As there was no earthquake recorded in Acoculco area, no travel time tomography can be performed.

Only ambient noise study could be performed. The method used in Los Humeros (detailed below) is being used in order to perform ambient noise tomography in Acoculco.

As data are still being acquired, only preliminary results with the first 2 months) could be performed. From all couples between stations, cross-correlation were computed (Figure 3) following the method of Bensen (2007).

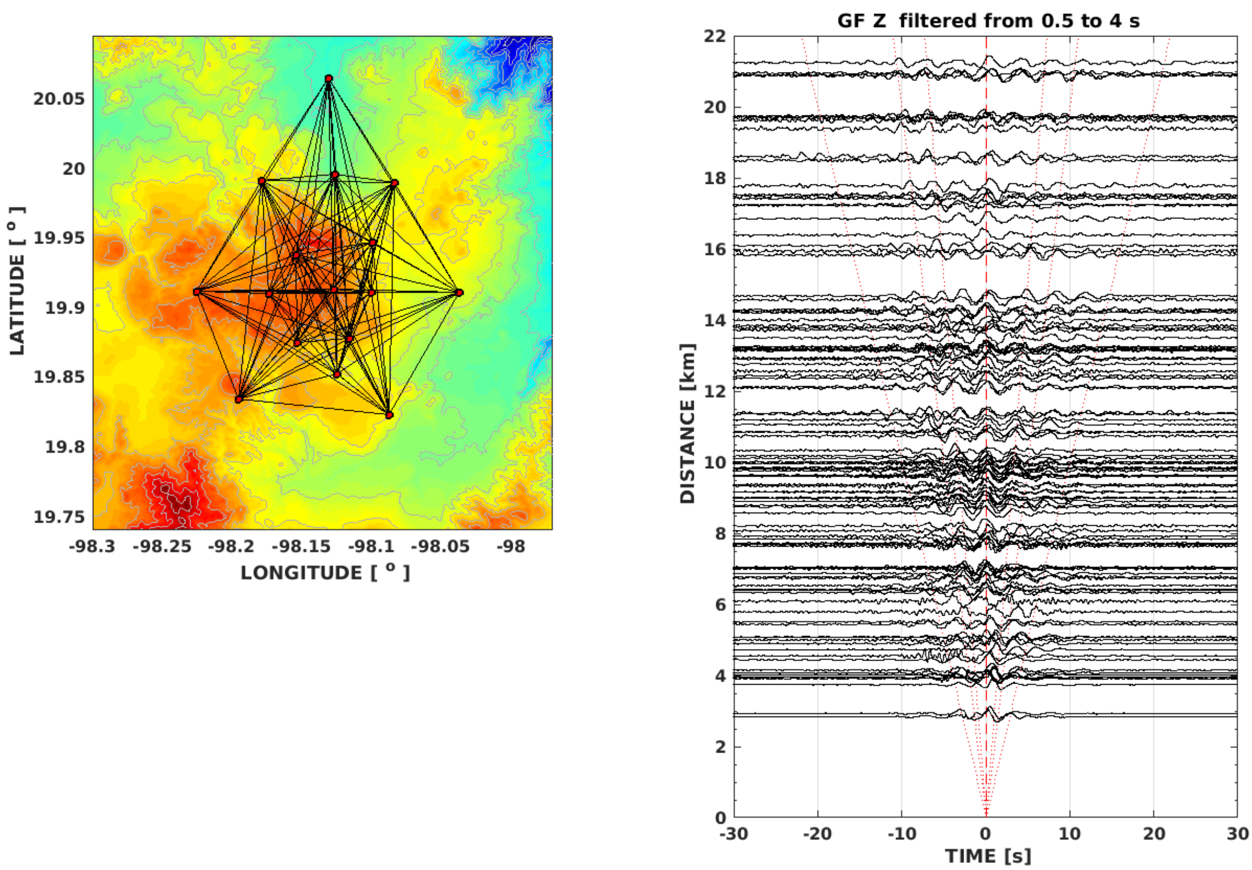

Figure 3 : Cross-correlations (right) are computed for all possible combinations between stations (left). They are then sorted by their inter-station distances (right).

Group velocities are then computed from the dispersion curve for all cross-correlations (Figure 4) on the vertical component.

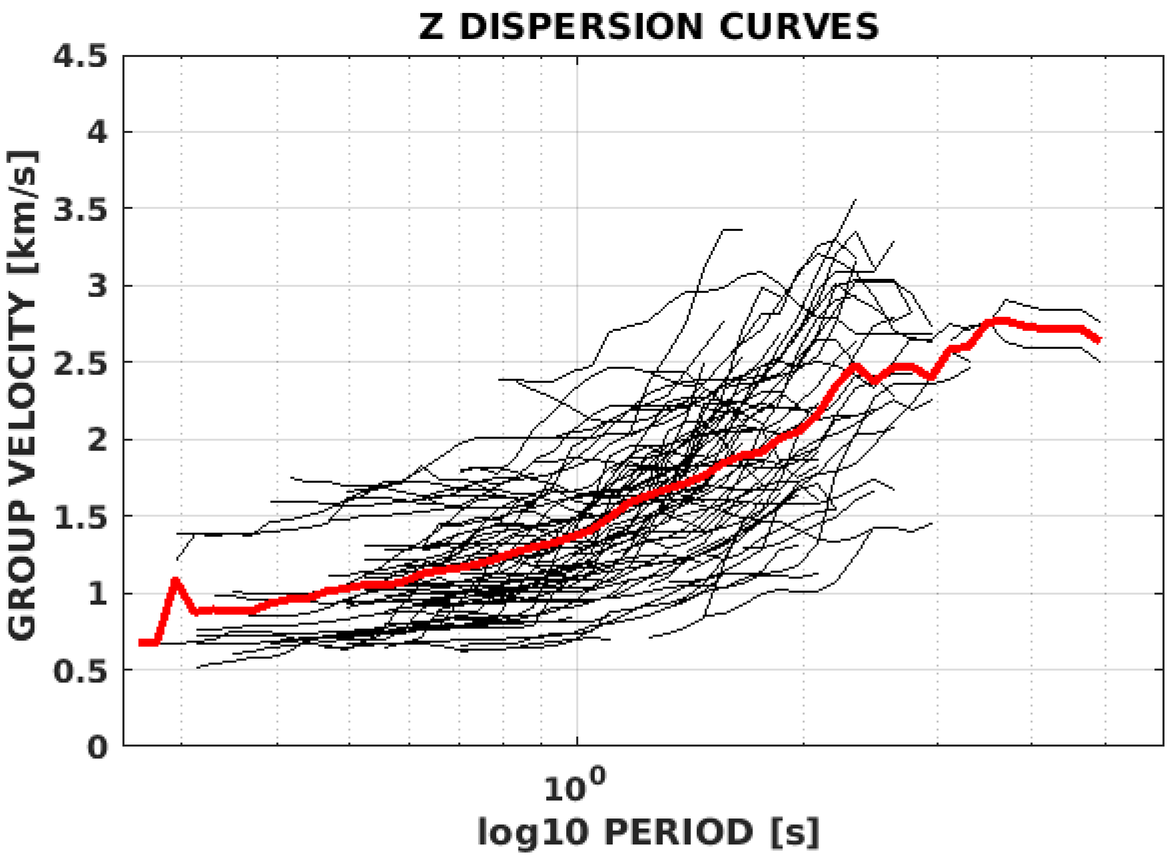

Figure 4 : Dispersion curve of the group velocity given by the vertical (Z) component.

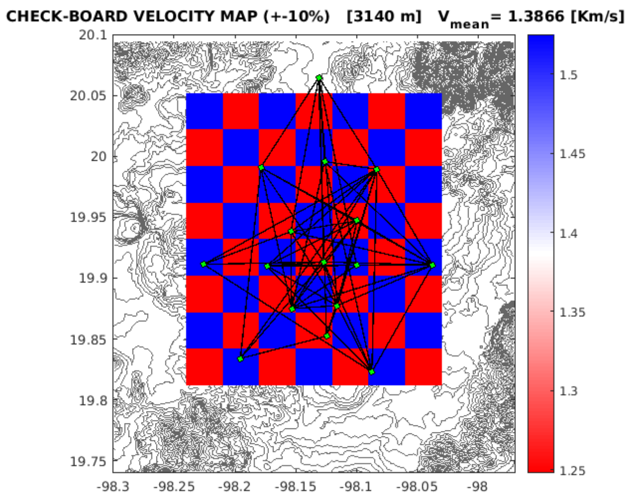

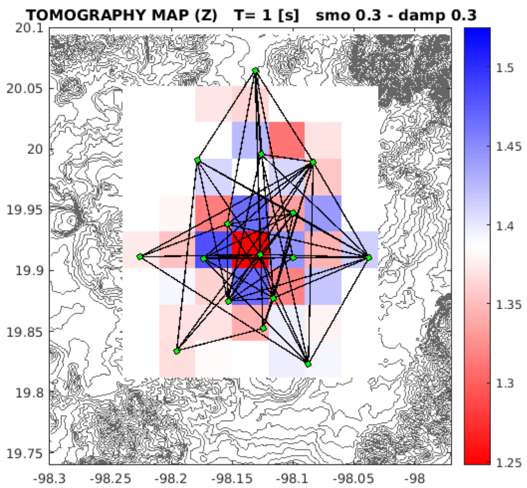

Figure 5 : Checker-board test performed on Acoculco network. (left) initial velocity anomalies introduced. (right) recovered anomalies. Resolution is best in the central area.

In order to check the resolution of the method in Acoculco, a so-called “checker-board test” is applied (Figure 5). This method consists in introducing artificial perturbations in the velocity model with a regular pattern and apply the methodology to recover them. Where good recovery applies, one can recognise the initial pattern.

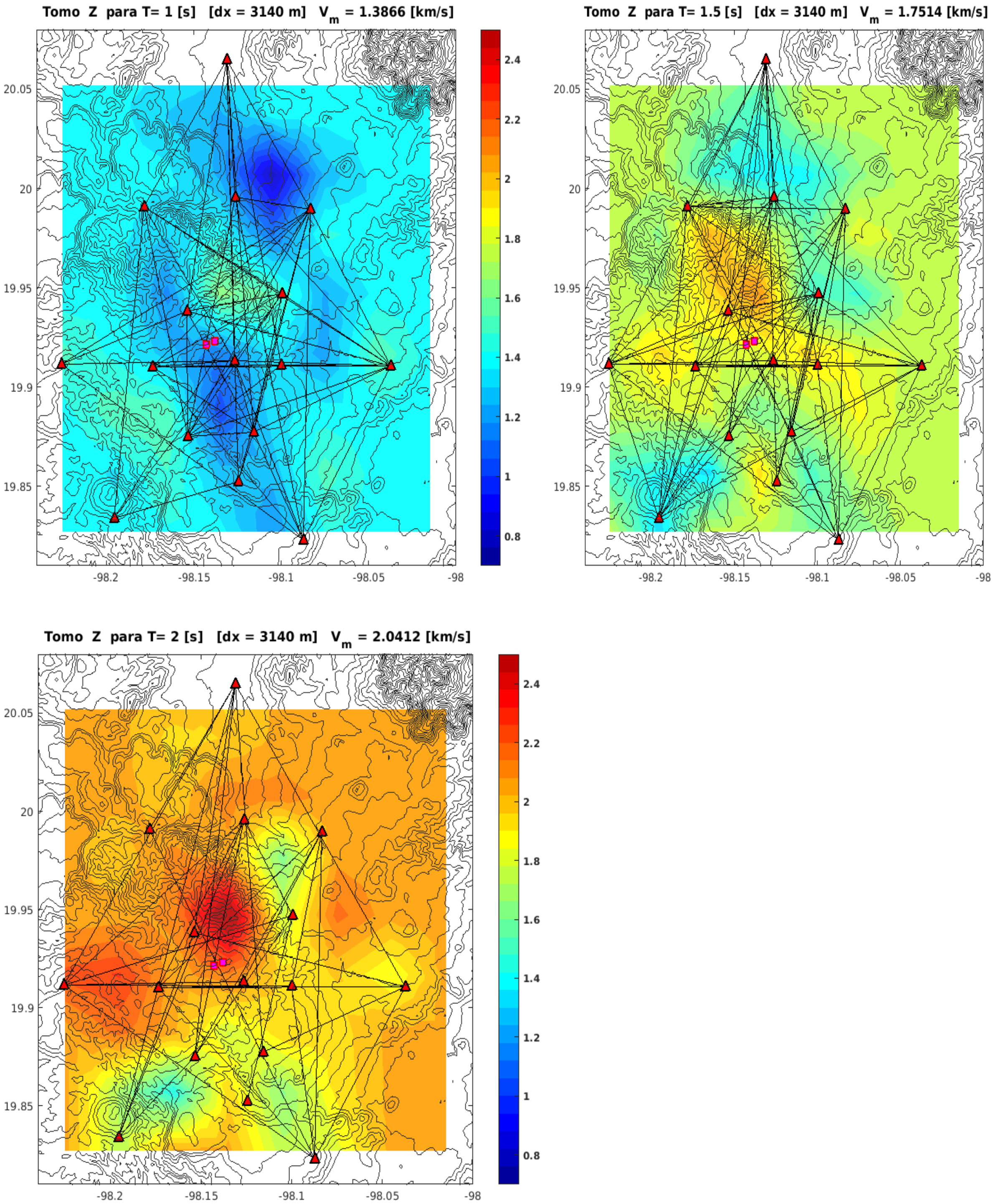

Figure 6 : Group S-wave velocity recovered from ambient noise tomography at Acoculco at different frequencies. Those results should be taken with much care, as they are based on only 2 months of data.

Figure 6 shows very preliminary results for the two first month of data acquired at Acoculco. The interpretation of such result is very hazardous at this stage, as only 2 months of data is compiled. More robust results, i.e., with improve resolution will allow interpretation.

LOS HUMEROS geothermal field

4 Active shot experiment in Los Humeros

Los Humeros is situated in the eastern sector of the Trans Mexican Volcanic Belt (TMVB), forming the northern boundary of the Serdán-Oriental basin. The field is a superhot geothermal system (SHGS) and is operated by the Comisión Federal de Electricidad (CFE). It is currently producing ~ 90 MW, therewith being the third most important geothermal field in Mexico. Los Humeros is geologically characterised by a caldera complex with a complicated evolution.

CFE provided us with active data and also one month records from a local seismic network comprising 6 stations. It allowed to give us an idea of the kind of information we can expect. It was clear from the data, that acquisition conditions in Los Humeros are not ideal due to industrial noise.

4.1 Active shots experiment description

The contribution of active seismic data is relevant to provide detailed information on deep seismic structures, to be integrated with the other geological and geophysical measurements in the local model of Los Humeros.

This subsection describes the work of reprocessing of legacy active seismic data of Los Humeros performed by OGS. The Los Humeros 2D reflection survey consists in four reflection 2D seismic lines: L2, L3, L4, L5, acquired with Vibroseis source in Los Humeros Caldera by Compañia Mexicana de Exploraciones S.A. (COMESA), for Comision General de Electricidad (CFE) in 1998. The position map is shown in Figure 7 .

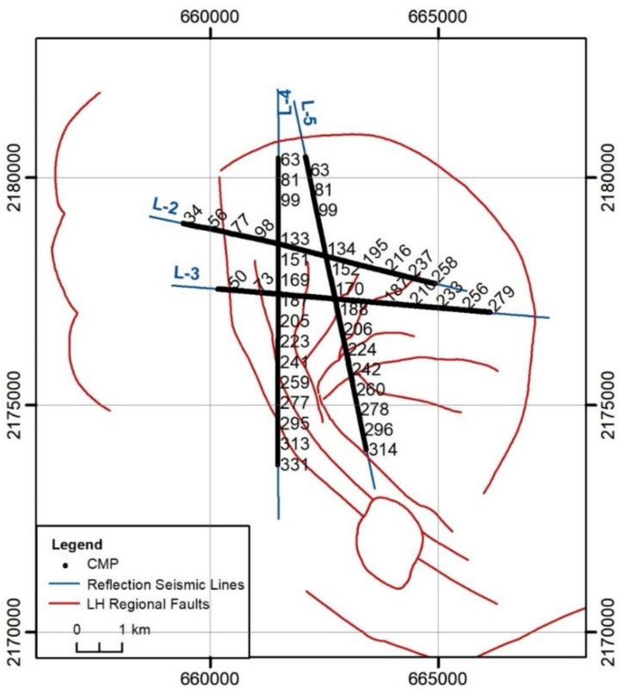

Figure 7 : Los Humeros seismic lines position map. The red lines indicate interpreted faults (Calcagno et al., 2018).

OGS received the complete dataset in February 2018, consisting of single shot files in SEGD format, grouped in a folder for each original tape (named H-12 to H-23), both as regular folder and compressed files in SEG-RODE format. Each SEG-RODE file had its own text files with the files' list (corresponding to field record numbers FFID in seismic file headers). A relevant work was done by OGS to reformat the files and assign the geometry.

4.1.1 Data reformatting and editing

The regular folders contained only few SEGD files, so OGS had to extract the data from SEG-RODE and reformat them to SEGD.

Collecting the information from the headers, i.e., field record number (FLDR), shot point (EP), channel number (TRACF) and geophone number (or receivers) (GRNORS), together with the information text file contained in the SEG-RODE files and the acquisition report, we were able to associate every SEGD files to the corresponding seismic line.

OGS received line L5 in December 2017 in SEGD file format, then L5 together with all the remaining lines (L2, L3 and L4) in February 2018 from UNAM.

In the absence of other maps SEGD files were sorted in FLDR order, and there were one or more FLDR for each shot point (EP). In some cases, for the same shot point (EP) the data were correlated, with time cut to 5120 ms, while others were not correlated and with a length of 21 s. Therefore, we correlated the uncorrelated data of each EP with the vibrator pilot trace and cut to 5120 ms to make all the data uniform, then we stacked together the shots with the same EP. We did this process with Seismic Unix (SU) software.

4.1.2 Geometry assignment

Another step was to assign the geometry, the coordinates of shots and receivers. For the receivers we had XY coordinates files in NAD 27 coordinates system. We converted them to UTM WGS 84 zone 14N to uniform this dataset with the others geological and geophysical information within GEMex project.

Table 1. Main acquisition parameters of Los Humeros active seismic lines.

Parameter	**VALUE**
Line Length	L2 ~ 7145 m, L3 ~ 8293 m, L4 ~ 9444 m, L5 ~ 8695 m
Source	Vibroseis
Sample Rate	2 ms
Record Length	5 s
Sweep Frequency	12 – 64 Hz
Sweep Parameters	4V – 16.7 m – 10 sweeps – 5.5 m 3V – 25M – 13 sweeps – 4.2m 16 + 5 s sweep length
Detection Pattern	N=24 elements; X =4m at constant distance; L=92 m
Receiver Spacing	50 m
No. Of Channels	96
Offset	Min=±300 m Max=±2700 m
Spread	Symmetrical Split, gap 11 traces
Geo Datum	NAD-27 converted to WGS84 Zone 14N
Fold	4800%

We did not have a shot point position list for the lines, so following the EP list from the headers, we used the receivers XY coordinates when EP and GRNORS had the same value, and an intermediate value between adjacent geophones when EP value was ending with .5, e.g., 51.5. In these cases, we multiplied by 10 the EP number to get an integer, and manage more easily the headers with the processing software. Table 1 summarizes the main acquisition parameters.

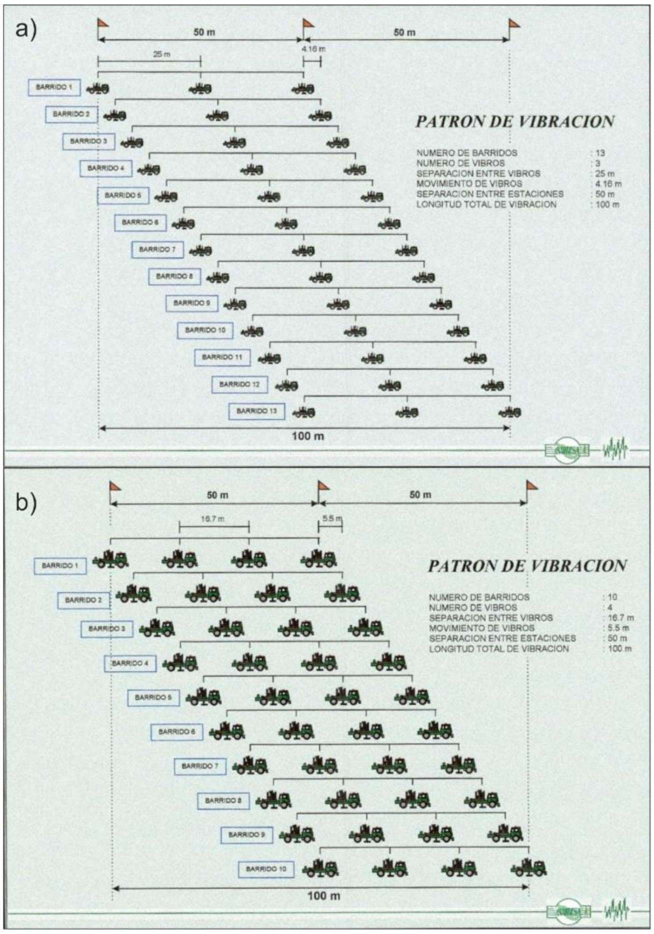

Figure 8: Patterns of seismic vibrators adopted for the Los Humeros active seismic campaign. Modified after COMESA report (1998).

The acquisition report describes two different source patterns. However there are no detailed indications about the distribution of the two acquisition patterns (Figure 8). With these configurations the pattern directivity effects at sources and also receivers (detection pattern of the Table 1) are strong. Radiation and directivity properties of the patterns of vibrator sources and array of geophone receivers are shown in Figure 9.

We observed in the data that the source patterns, although attenuating surface waves, in general generated noisy traces, especially at higher frequencies and positions closer to the shot point (short offsets). In the field shot records there is a 11-traces gap (600 m = 2 × 300 m per side), which probably removes traces with higher noise levels but also information on the shallower layers (see also Section **4.2**). In Section **0** we utilize seismic interferometry to retrieve it in the zone of the offset gap.

Before starting the data processing, we balanced the traces within the single shots to reduce this effect with Seismic Unix. The data set was then converted to SEGY format and processed with VISTA software.

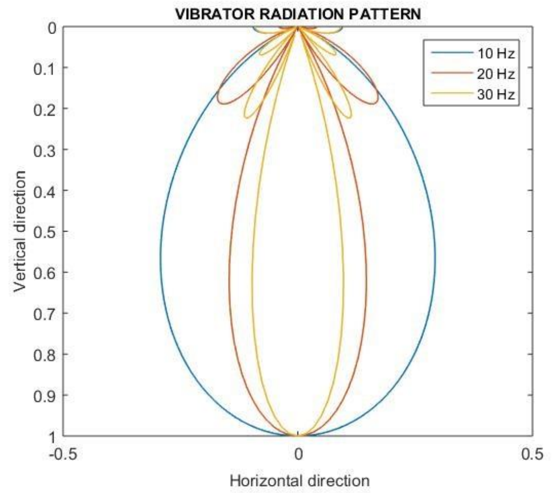

Figure 9: Polar display of the radiation pattern (b) of seismic vibrators of Figure 8 calculated assuming constant velocity 2000 m/s.

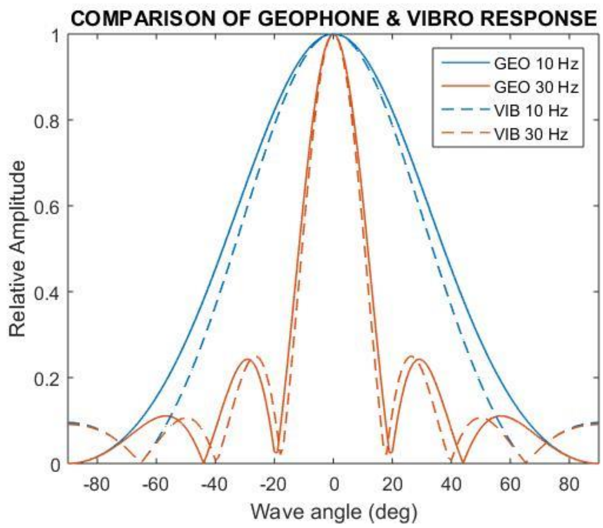

Figure 10: Comparison of radiation pattern (b) of vibrators (Figure 8) and of the geophone array response calculated assuming constant velocity 2000 m/s.

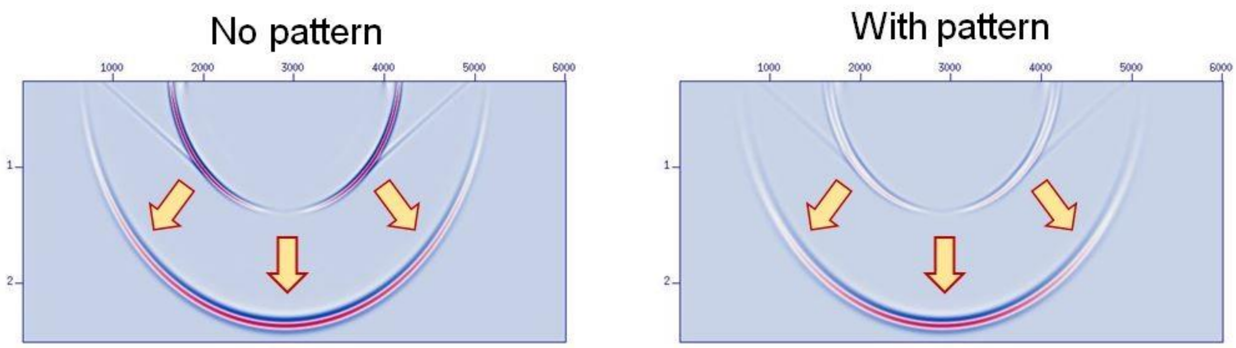

Figure 11: Synthetic snapshots in a uniform half-space calculated (left side) without and (right side) with vibrator and receiver pattern (b). The source-signal peak frequency is 20 Hz. The lateral model dimension is 6 km.

4.1.3 Time-processing flow

After having analysed the data shot by shot for each line, the amplitude / frequency spectrum and run some tests on the different stages of the processing of reflection seismic data set, we decided to use the following processing sequence (Yilmaz, 2001):

- Geometry and CMP (Common Mid Point) position and fold.
- 30 Hz Notch filter, because a constant noise present in all the shots.
- Traces editing with surgical mute, kill of extremely noisy traces and despike tool.
- Static correction to a floating datum, which approximate the topography.
- Passband filter 4/8-30/35
- Spiking deconvolution: Operator length 800 ms, length 20 ms, Pre-Whitening 5%
- Stack velocity analysis.
- Passband filter 4/8-24/28 (from here, see section 3.3.1 for details).
- Kirchhoff Pre-Stack Depth Migration (PSDM): aperture 50 CMP (1250 m)
- Stack
- FX prediction: trace window 100 traces; time window 100 ms; filter length 9 traces.

The target of this task is to obtain information on deep structures. Using the good-quality results from the time and time-migrated processing, we decided to go further to an implementation of the depth velocity analysis, combining it with shallow diving waves tomography and pre-stack depth migration. Both will be discussed in section 4.2.2. Figure 14 to Figure 16 show intermediate processing steps. Figure 17 shows the 3D velocity model converted to depth, after including the tomographic inversion results.

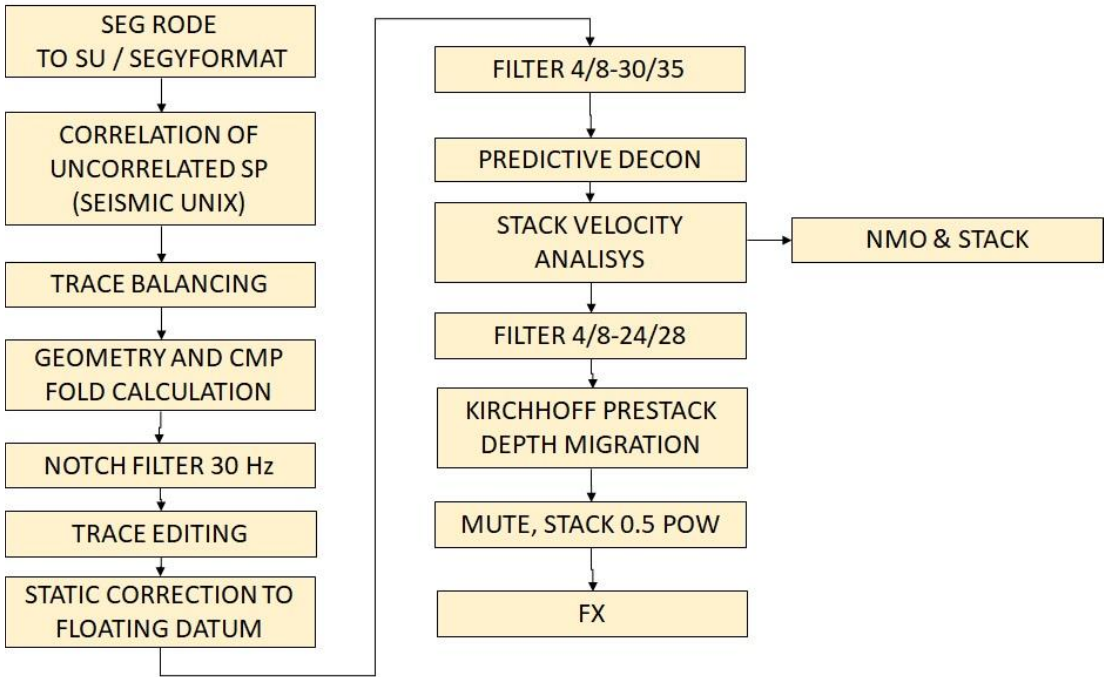

Figure 12: Processing flow adopted for the time processing of the Los Humeros seismic lines, including depth conversion.

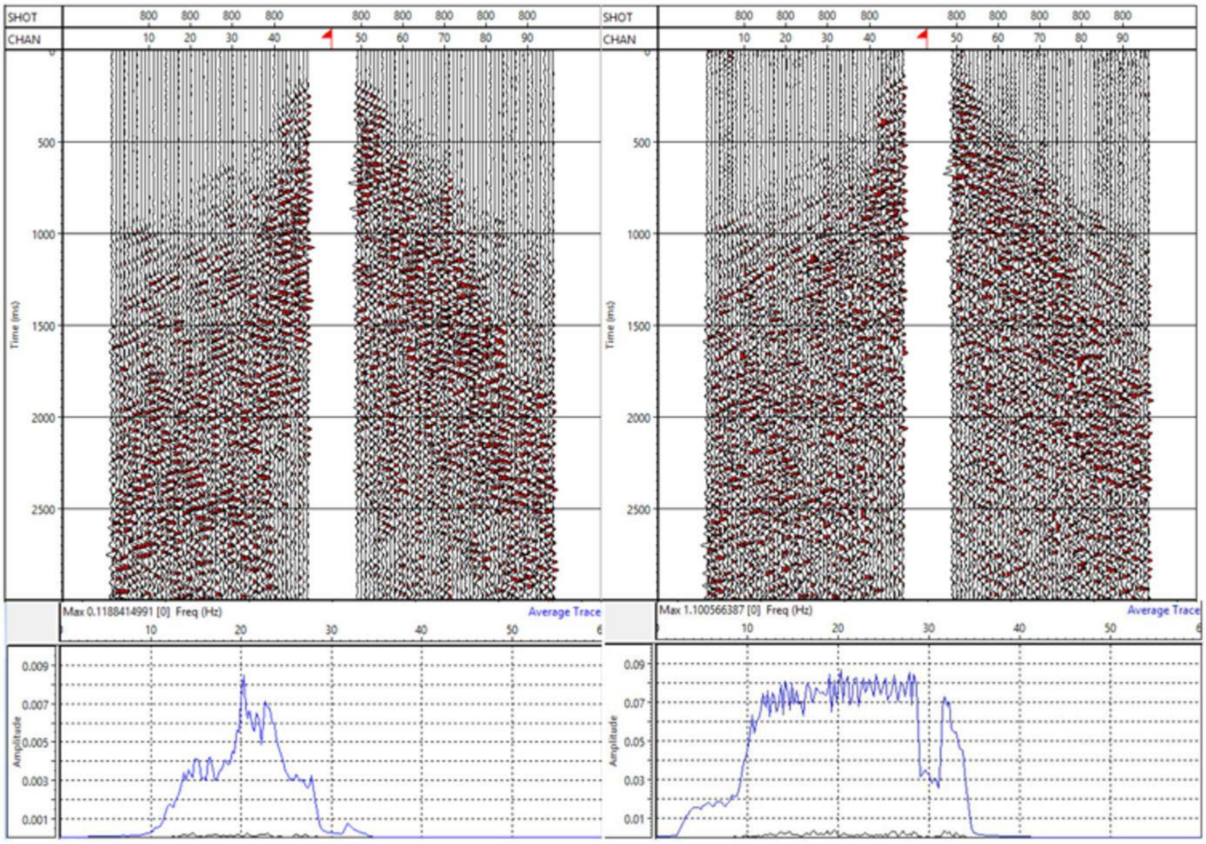

Figure 13: Common-shot time traces and averaged frequency spectra of a Los Humeros record (left side) before and (right side) after signal deconvolution.

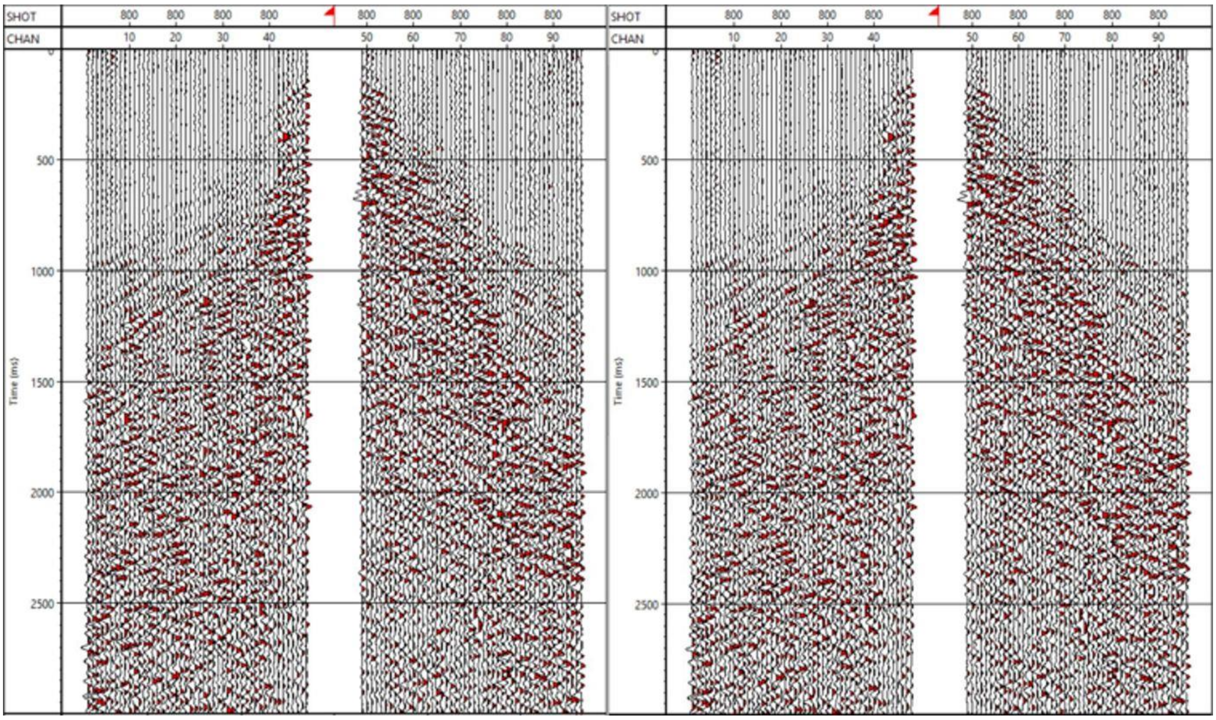

Figure 14: Common-shot signals (left side) before and (right side) after receiver static corrections.

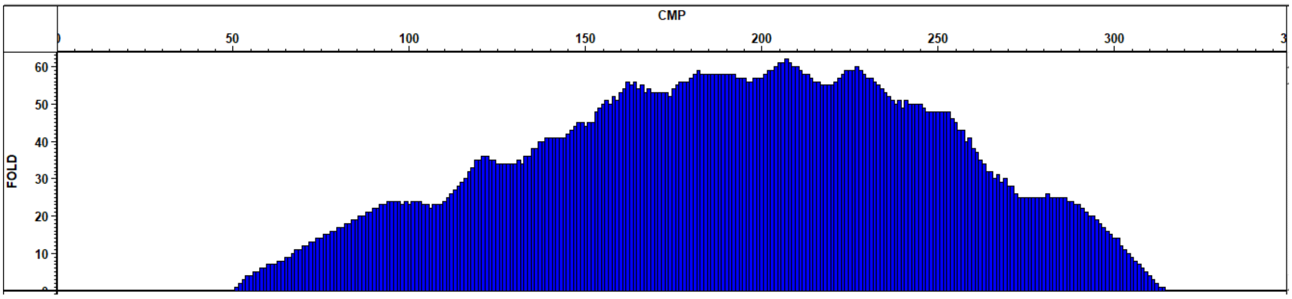

Figure 15: Fold coverage in CMPs of L5 before stacking.

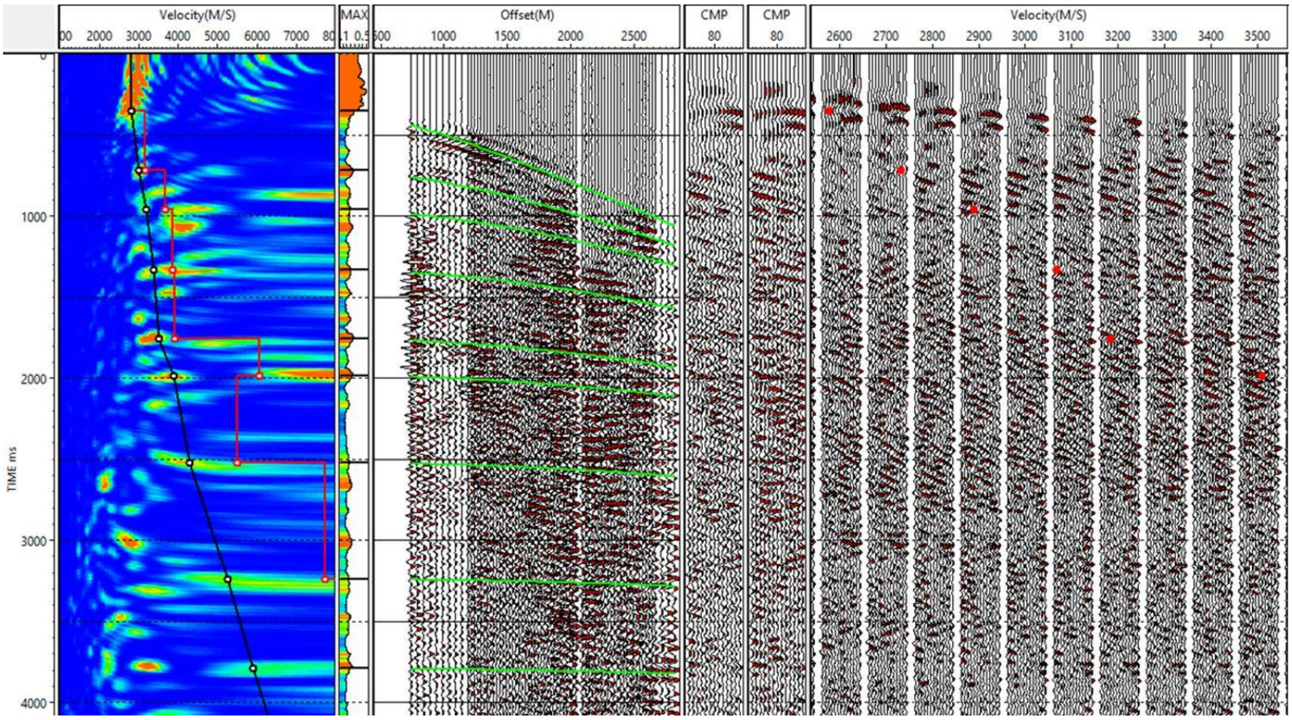

Figure 16: Stacking velocity analysis, with semblance, CMP versus offset gather, common velocity stacks.

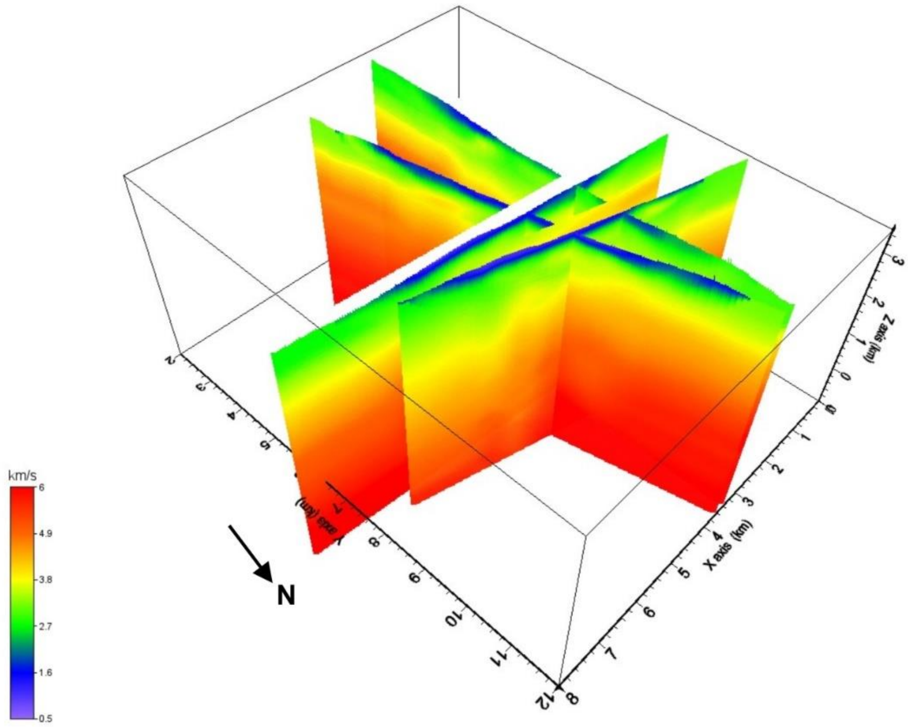

Figure 17: 3D view of the initial seismic velocity model obtained by time-processing, merged with the shallow tomography model (Section 4.2), and converted in depth.

4.2 Tomography and interferometry using existing active-source seismic data

4.2.1 Shallow travel-time tomography using active-seismic direct arrivals

Travel time tomography of the seismic lines

Travel time tomography of the first breaks was computed on the seismic data (4 2D lines). For all the shot gathers of each line the first arrivals were picked and separately inverted for each line by using the diving ray paths (turning ray tomography, Figure 18) (Stefani, 1995). Or this purpose, we used OGS CAT3D software (e.g., Böhm and Petronio 2003). Figure 19 shows an example of picked arrivals in a field shot. With this approach we obtained the corresponding 2D shallow velocity models in depth. (Figure 18 and Figure 21). To enhance the resolution of the tomographic model, staggered grid method was used in the inversion procedure (Vesnaver and Böhm, 2000).

Furthermore, these velocity fields were used to perform the static corrections (Figure 22 and Figure 23) to apply to the seismic data for computing the corresponding stack sections in the initial time-processing phases.

Preliminary analysis of shallow anisotropy effects

The seismic lines L2, L3 and L4, L5 are oriented in different, sub orthogonal, directions. In the next Section, we interpret the velocity models of these lines intersected by faults.

We compare the diving velocity functions in the shallow layers at the crossing positions of the 3D data of Figure 21. We observe different responses in the four panels of Figure 24, in particular for the intersections of L4 with the other lines oriented in sub-perpendicular directions, in particular L3. We consider that these differences are possibly due to local anisotropy effects or to inhomogeneity.

This analysis of shallow seismic properties is preliminary and can be considered for future work integrated with additional shallow surface information, including geological interpretation of faults and their orientation relative to the seismic lines (Figure 25).

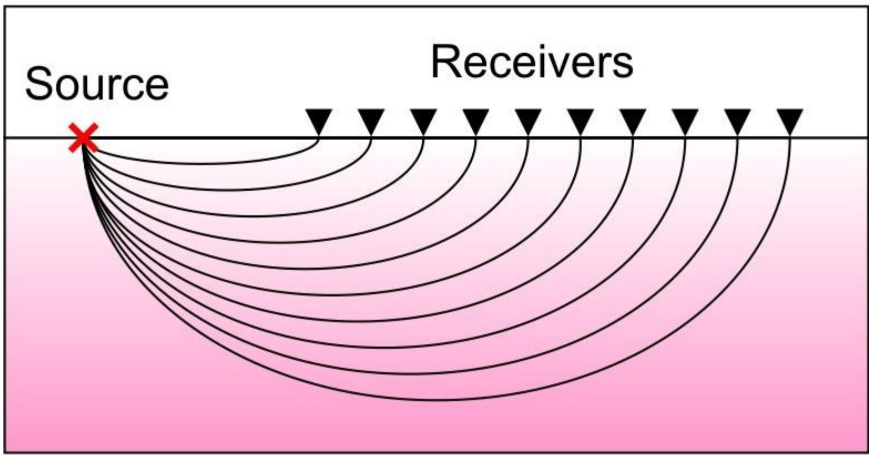

Figure 18: Example of diving waves in a medium with a vertical velocity gradient.

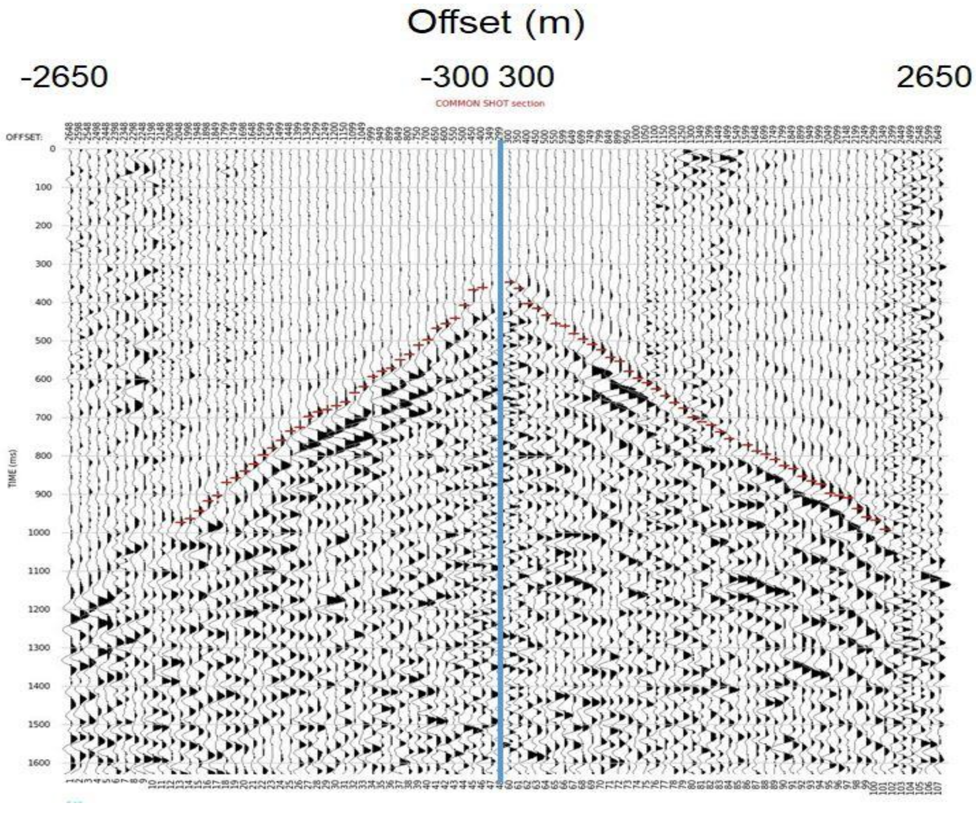

Figure 19: Example of common-shot gather with picked direct arrivals for tomographic inversion.

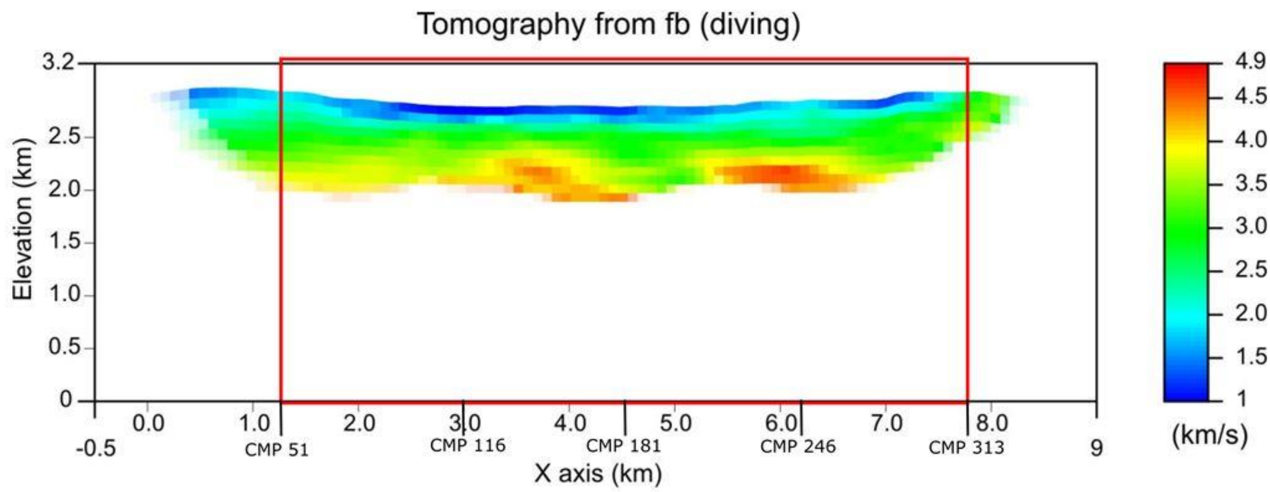

Figure 20: Velocity obtained by tomographic inversion of diving waves along L5. The maximum depth of penetration is of the order of 500 – 700 m.

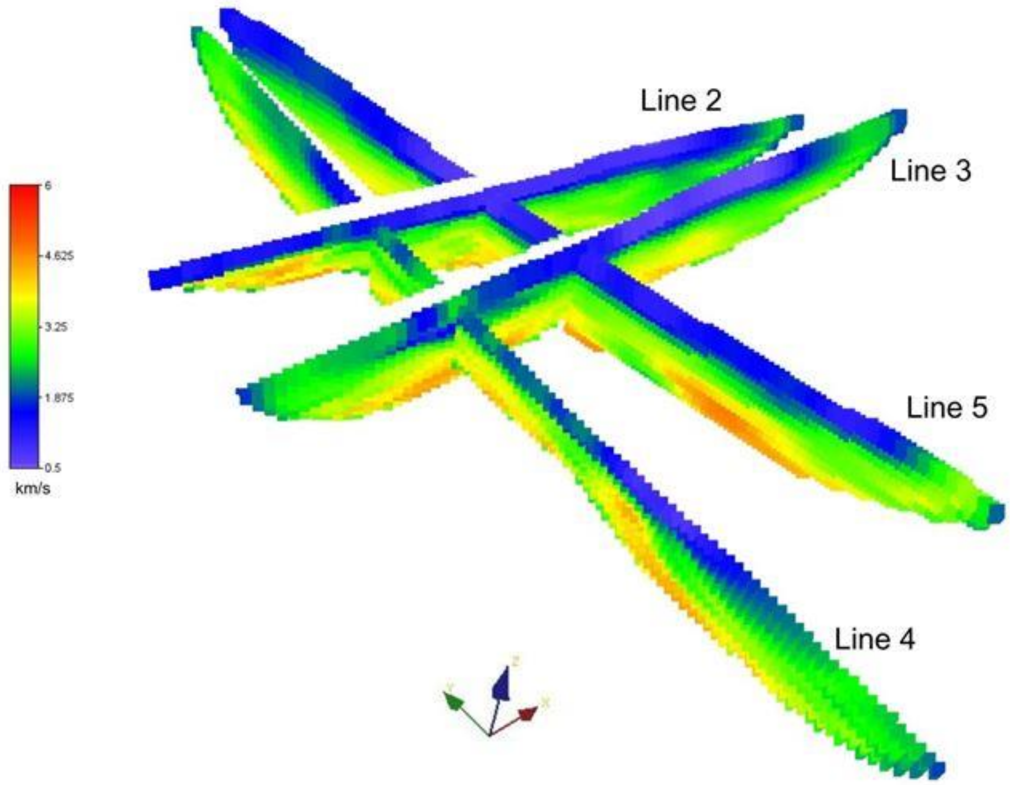

Figure 21: 3D view of the tomographic inversion of the Los Humeros lines.

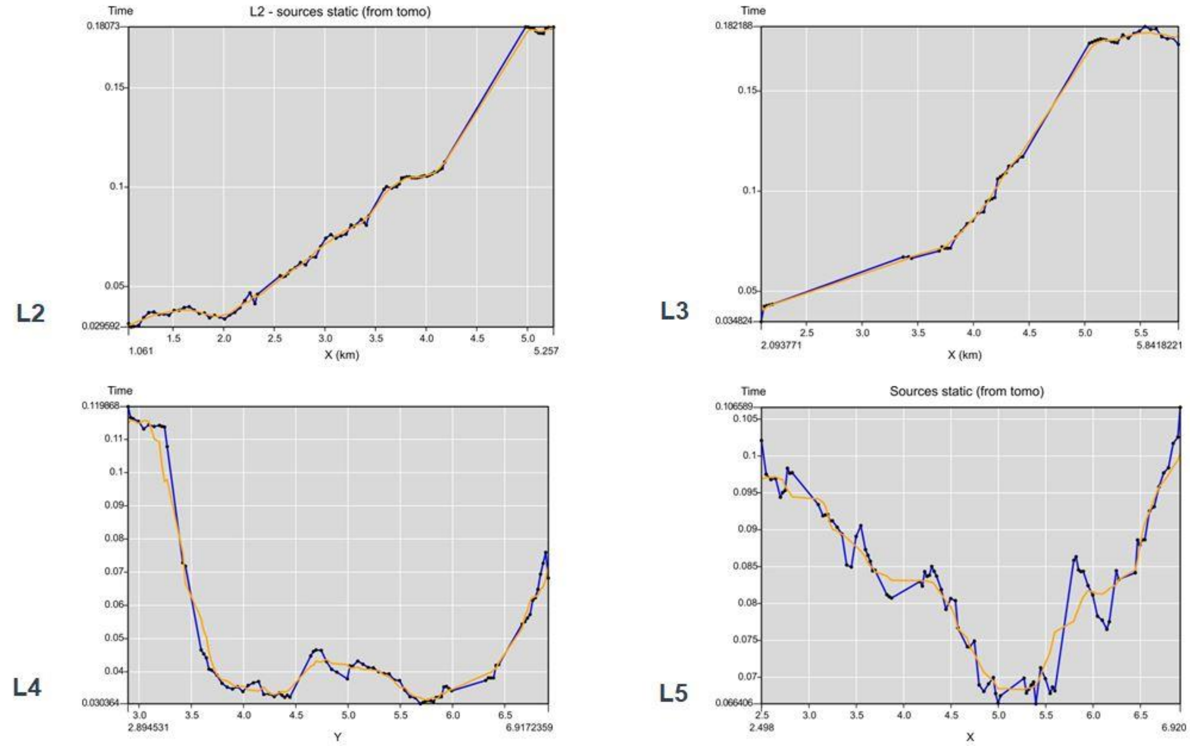

Figure 22: Static corrections at the source calculated with the datum at 2700 m a.s.l. (blue line), and smoothed static values applied on data (yellow line).

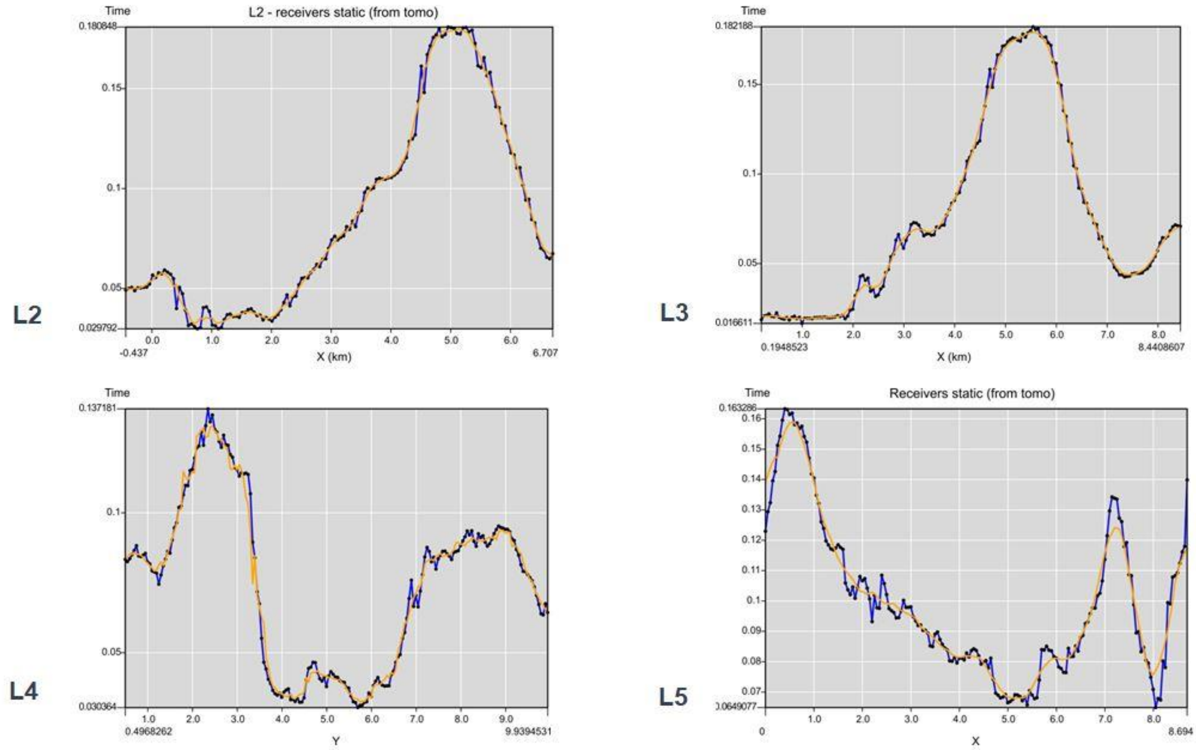

Figure 23 : Static corrections at the receiver calculated with the datum at 2700 m a.s.l. (blue line), and smoothed static values applied on data (yellow line).

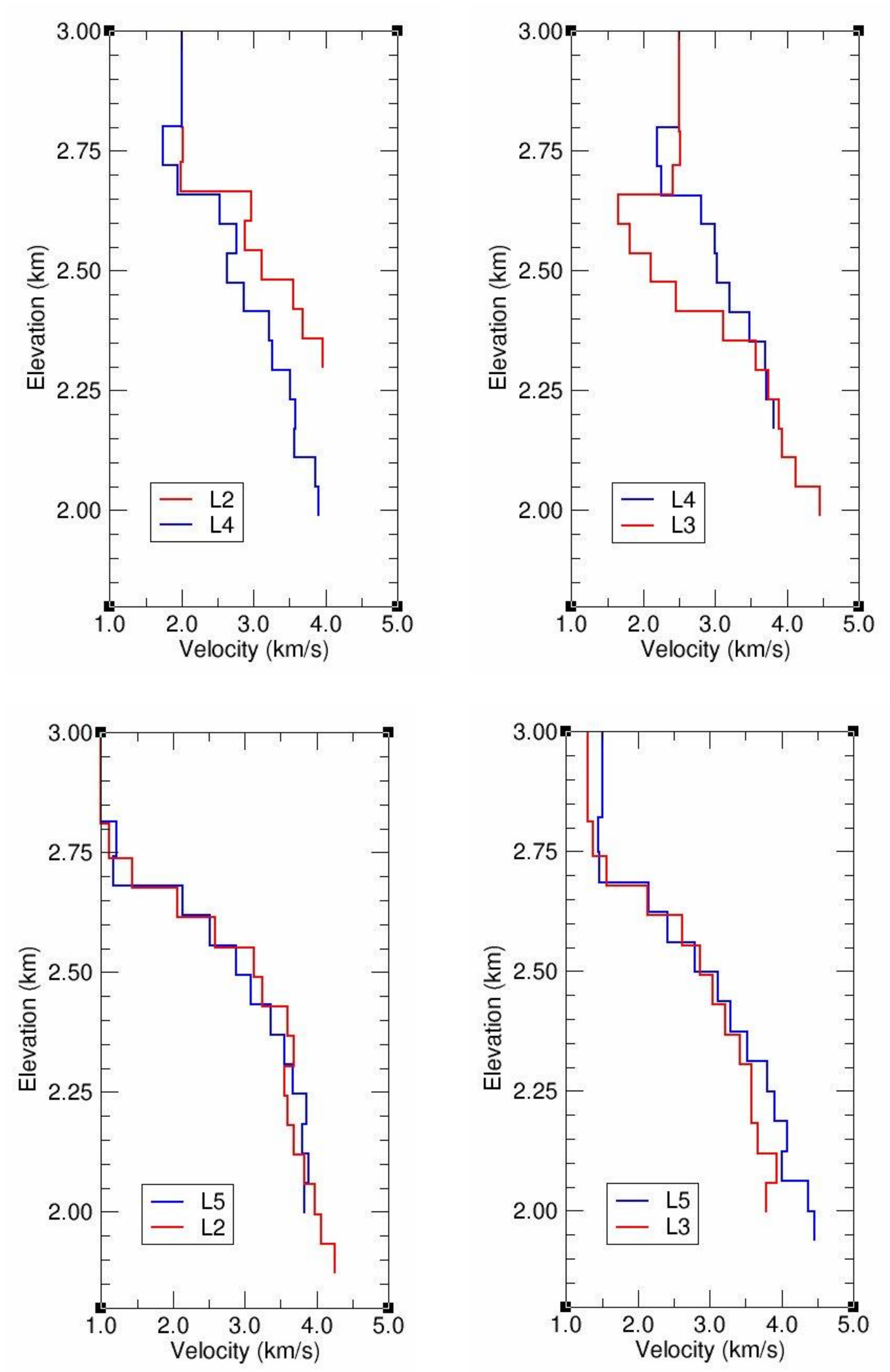

Figure 24: Profiles of the velocities calculated by the diving waves tomography, shown at the intersections between lines.

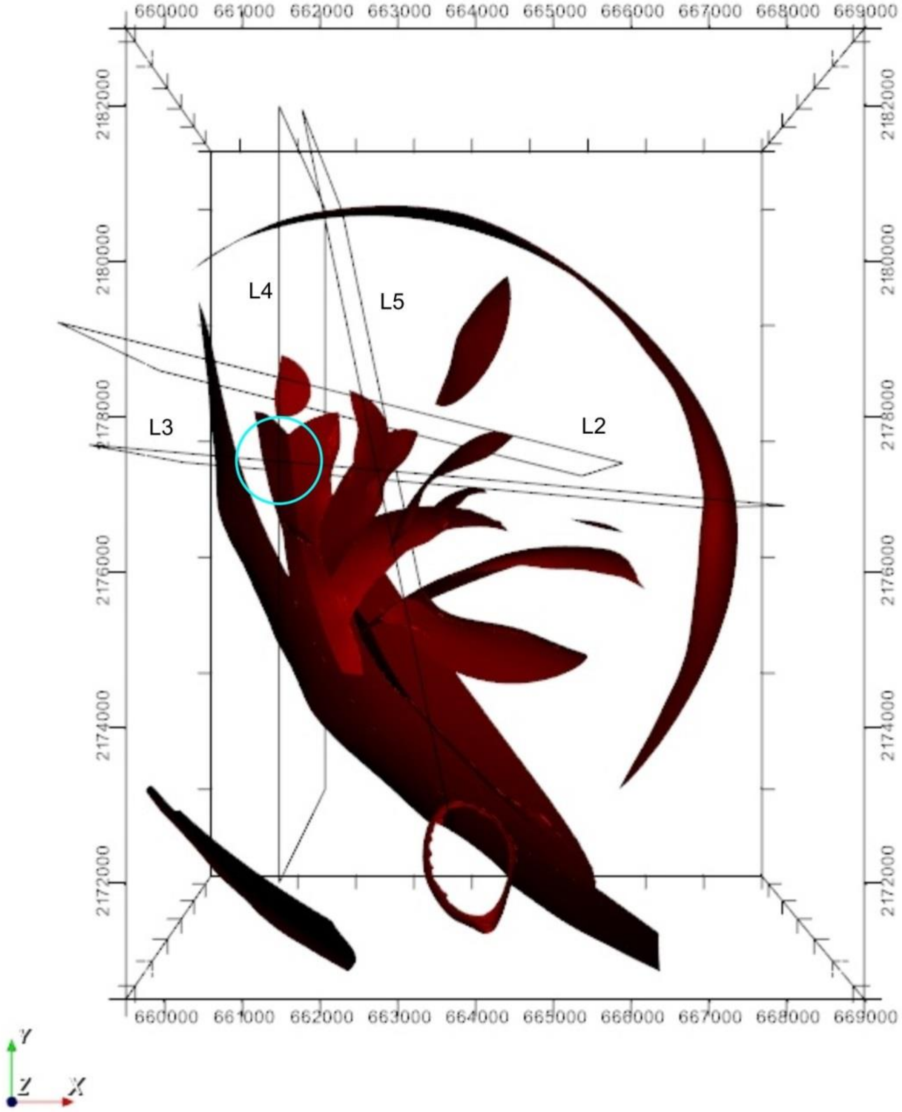

Figure 25: Top view of faults' distribution in the local model of Los Humeros (from GeoModeller WP3). The blue light circle evidences the intersection between L4 and L3, where possible anisotropy effects could be interpreted.

4.2.2 Seismic depth imaging (interpretation, tomography and PSDM)

Data depth processing

The directional properties in the source and receiver patterns used for the acquisition of reflection seismic data focalized the energy on the central traces and downward, so the shallow reflections at large offsets are weak and not easily detectable in the noisy shallow data.

This affected the stack velocity analysis at shallower positions and, consequently, the velocity and seismic sections. Because the shallow reflections weren't detectable. Moreover the 600 m gap between short offset traces removes information by direct arrivals in the shallower part potentially usable for refraction signal analysis. So we decided to fill this shallow velocity information with the velocity resulting from the tomographic inversion of the first arrivals. We converted in depth the time-stack velocity and replaced the upper values with those from first break inversion tomography (Section 4.2).

After the initial processing using the VISTA software, to perform the depth processing for imaging we used the Geodepth tools from Paradigm suite. With this software it is possible to run a residual depth moveout analysis and a 2D Grid-based tomography of depth migrated gathers to improve the depth interval velocity section. This method is also called Common Image Gather (CIG) migration analysis (Figure 26).

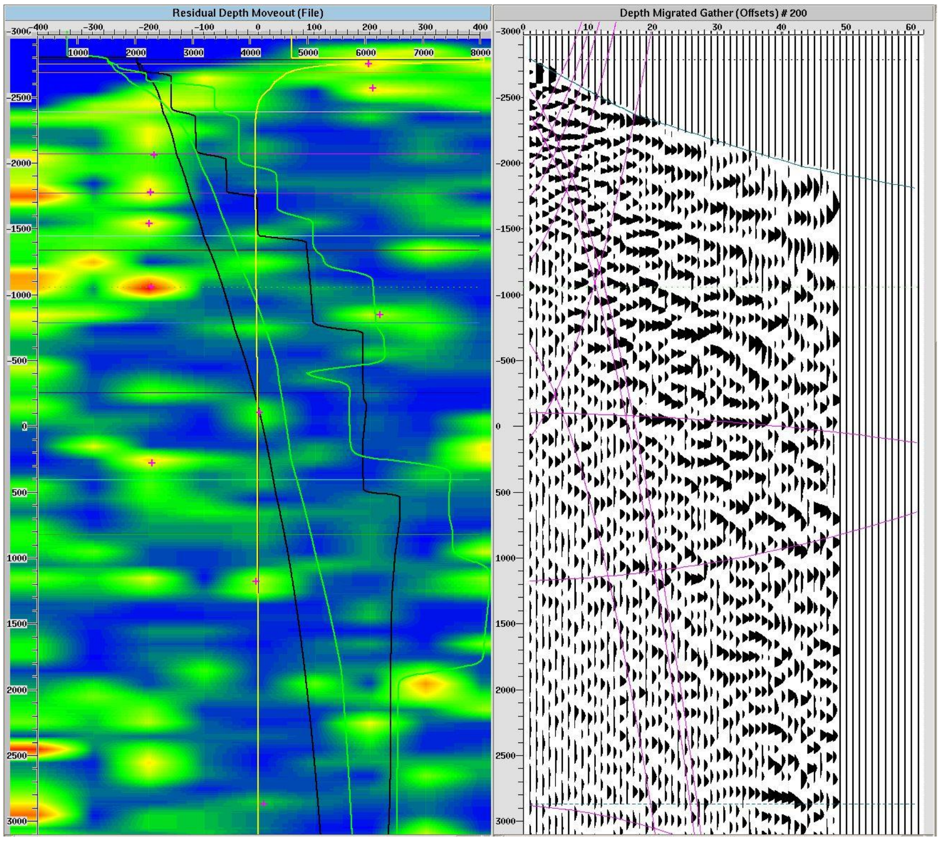

Figure 26: CIG residual velocity analysis for tomographic inversion. In this process the velocity model is updated and subsequently used for PSDM migration.

Tomography of depth migrated image gathers is a method for refining the velocity - depth model when pre-stack depth migration is performed with an incorrect velocity model. The degree of non-flatness is a measurement of the error in the model. Tomography uses this measurement of non-flatness (residual moveout) as input and attempts to find an alternative model which will minimize the errors. An important feature of tomography, as compared to layer stripping, is that it is a global approach. Tomography can attribute an error in time at one location to an error in velocity and depth at another location. It considers the entire model. Layer stripping may result in accumulation of error at the deep parts of the section when there are errors at the shallow parts. Tomography updates the shallow and deep sections simultaneously. 2D Grid-based tomography is a velocity updating procedure for refining and improving your initial velocity section. The output is an updated velocity section, i.e., the tomography updated velocity section which is a grid-type representation of the mode (from Paradigm user manual, 2015).

We used the CIG analysis starting from the combined depth velocity section described before to obtain a first Kirchhoff Prestack Depth Migration (PSDM). After PSDM we applied a frequency-space (FX) prediction deconvolution to enhance the results. The application of the CIG tomography velocity analysis requires and is driven by the identification of a horizon-layers model on the depth seismic section.

We interpreted the depth sections, identifying the main seismic horizons, trying to recognize the GEMex geological interpretation and faults from WP.3 and literature (Calcagno et al., 2018), and taking into account nearby well's information as provided to GEMex consortium (see figures from Figure 27 to Figure 30).

In summary, by an iterative approach, we created a new depth velocity section horizon-based, with which we migrated and interpreted again the data. Then we performed a residual depth moveout analysis on Common Image Gather (CIG) to create a residual depth moveout section. This section and the CIGs are the input for the 2D Grid-based Tomography. The output is an updated velocity section we used to run a new PSDM, we stacked and applied a FX prediction to enhance the results (see Figure). This analysis was applied to all the four seismic lines of Los Humeros.

Figure 27: Legend for horizons interpreted in the depth model.

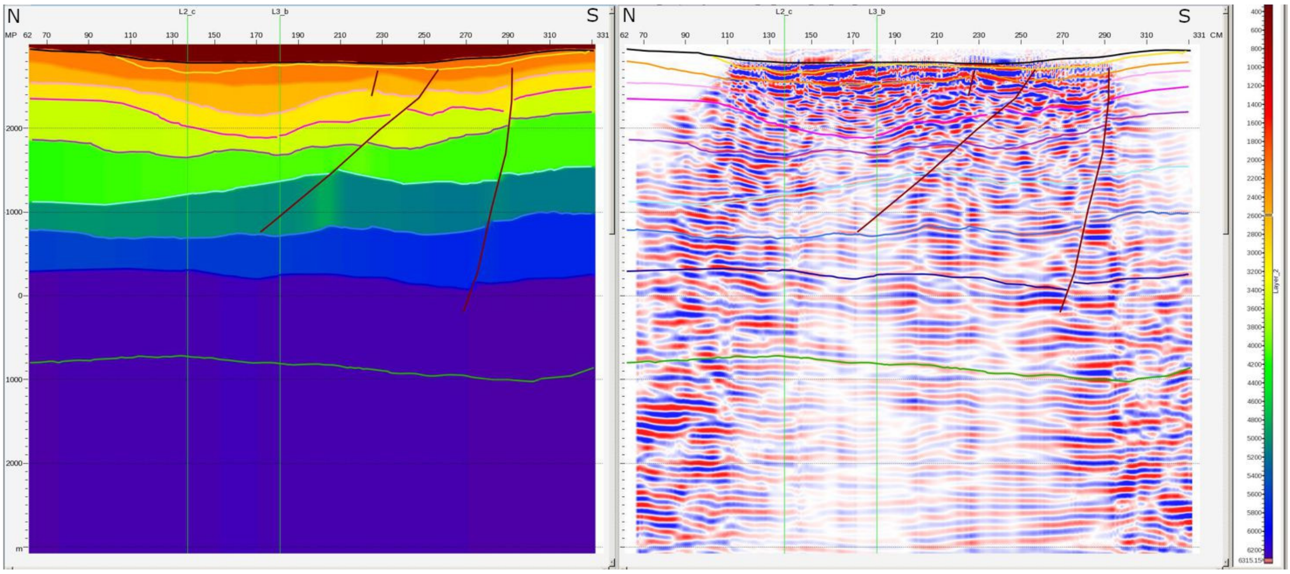

Figure 28: Global view of interpreted seismic section (right side) and velocity model (left side) of line L4. The velocity scale is on the right side of the figure.

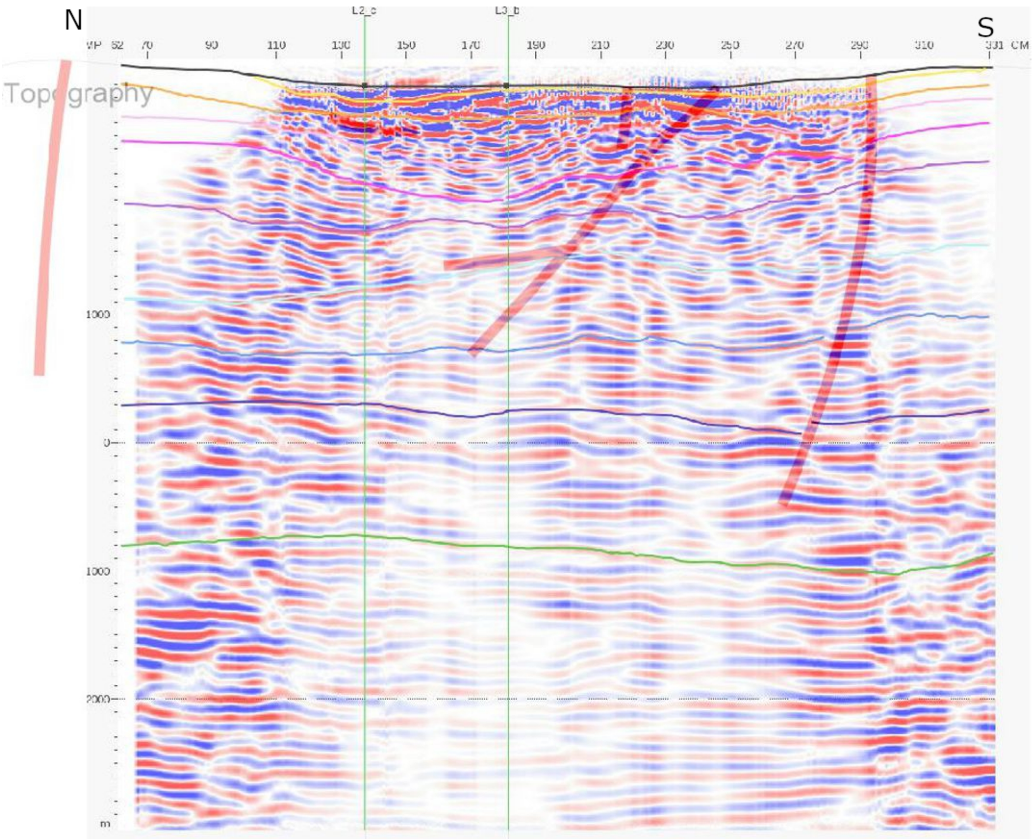

Figure 29: Comparison L4 PSDM and second fault's interpretation by WP3 (Calcagno et al., 2018)

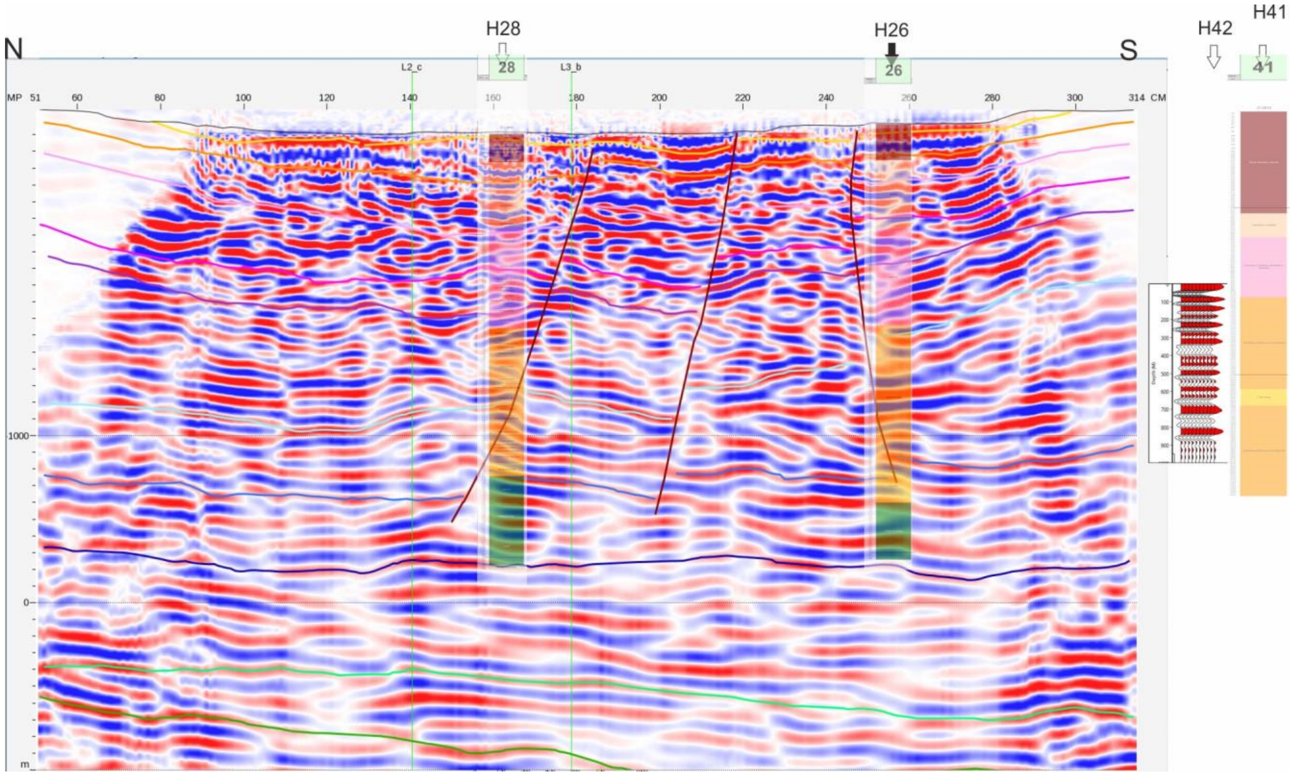

Figure 30: Comparison L5 PSDM and well's results, stratigraphy and synthetic log.

Full waveform elastic modelling

Synthetic full waveform signal analysis supports the interpretation and validation of the results. Figure 31 shows the velocity model of line L4. Figure 32 shows (a) the synthetic shot gather and (b) the real time signal.

The model of the seismic line is discretized with squared pixels of side 10m. To calculate the synthetic seismic data, we use a fourth-order accurate space, second order accurate time, two-dimensional P-SV finite-difference code based on the Madariaga-Virieux staggered-grid formulation. The numerical scheme is developed from the first-order system of hyperbolic elastic equations of motion and constitutive laws expressed in particle velocities and stresses (Levander, 1988).

Velocity and seismic depth results

The velocity and seismic sections and the seismic horizons interpretation presented in this report and loaded into VRE web page are the results of this first iteration. We show also a 3D intersection model and results to highlight the relations among the four lines.

Figure 33 to Figure 36 show (on scale) the depth velocity models of L2, L3, L4 and L5, respectively, with the interpretation of horizons and faults.

Figure 37 to Figure 40 show (on scale) the PSDM seismic sections together with the depth velocity models of L2, L3, L4 and L5, respectively, with the interpretation of horizons and faults.

Figure 41 shows a 3D view of the crossing seismic sections with velocity and interpretation (snapshot from OpendTect). Finally the interpretations of the four lines were extrapolated in 3D to obtain the horizons in the local model (Figure 42).

Conclusions and discussion

These results will be used to update the Los Humeros velocity model, compared with geological results (from WP3 Geomodeller), integrated with geophysical results from other tasks and work packages (seismological data, gravimetric and EM data, in the framework of WP 5.4 with deliverables D5.9, D5.10 and D5.11 and also WP3.1, deliverable D3.1), as well as reservoir modelling (WP6) and for the purposes of the geothermal model simulation with temperature (D5.5).

The analysis performed until now shows that there are confirmations from the comparison between crossing lines, and with well's and geological results (well data and synthetic log). Future updates in the interpretation of these results (**first version** of active seismic line results), with the support of the integrated interpretation, may lead to modifications of the depth sections, and ultimately of the depth images. In particular we might consider as a tentative and provisional the interpretation of the deeper 'intra basement' horizon, corresponding to an event observable in all the four seismic sections, to be further investigated by comparison with other results and evidences of the GEMex project.

To help the integrated interpretation of results of other GEMex partners in the same area, OGS has uploaded on VRE the geometrical maps of the CMP of the seismic sections.

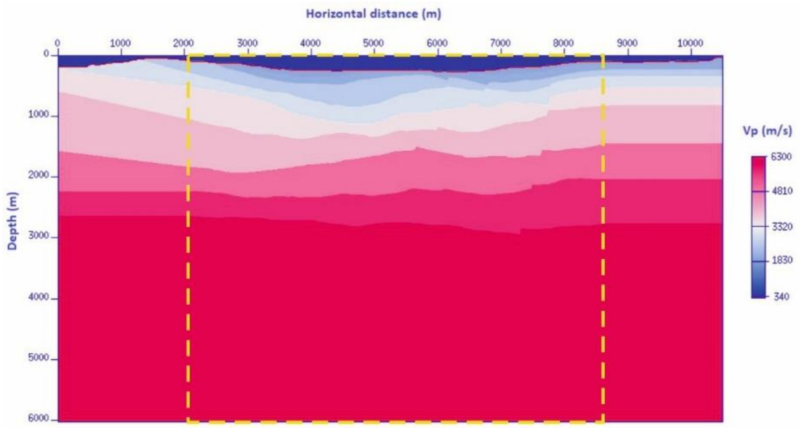

Figure 31: Compressional velocity model of seismic line L4. Sources and receivers are located on the topographic line (red). The yellow dashed line delimitates the area covered by L4 CMP.

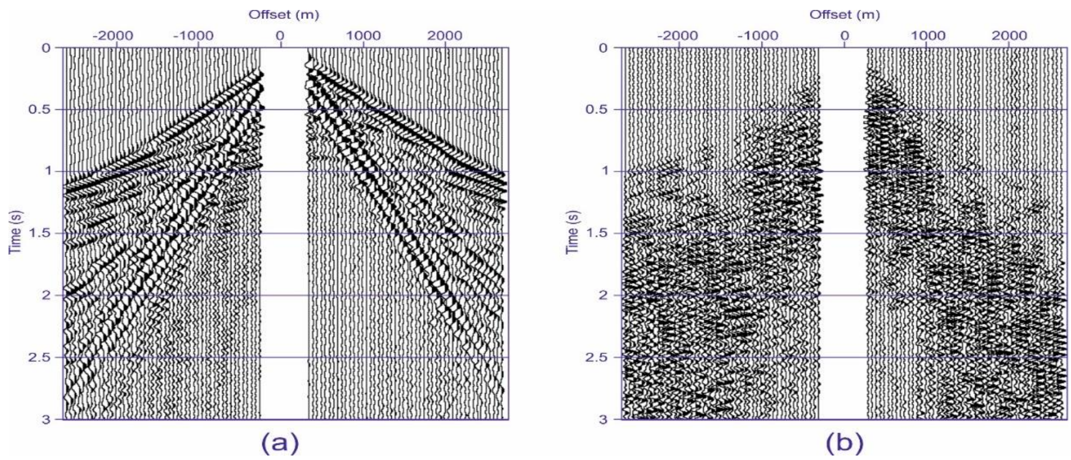

Figure 32: Comparison of synthetic (a) and real (b) data for the shot of L4 at ep=960. The synthetic data are calculated using the model in Figure 31.

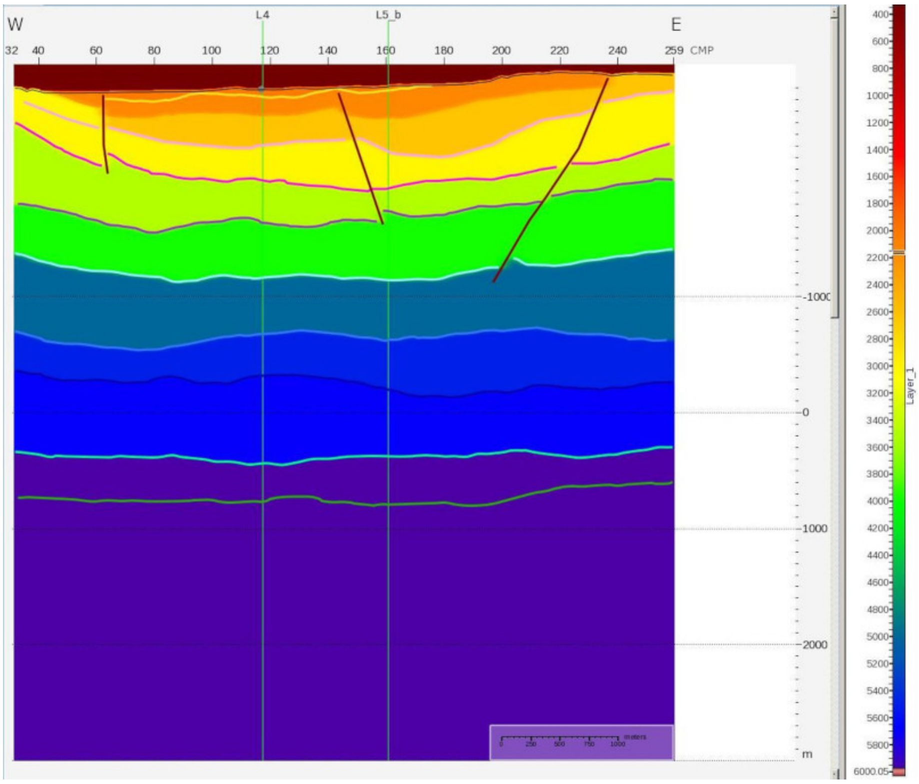

Figure 33: Velocity model of L2 with interpretation.

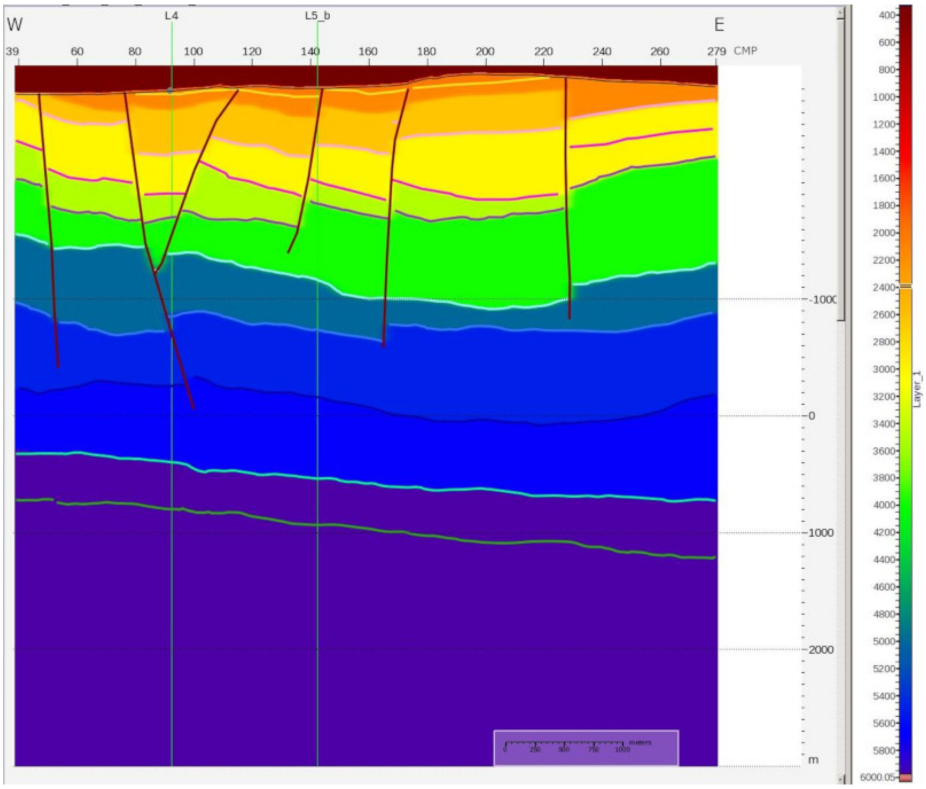

Figure 34: Velocity model of L3 with interpretation.

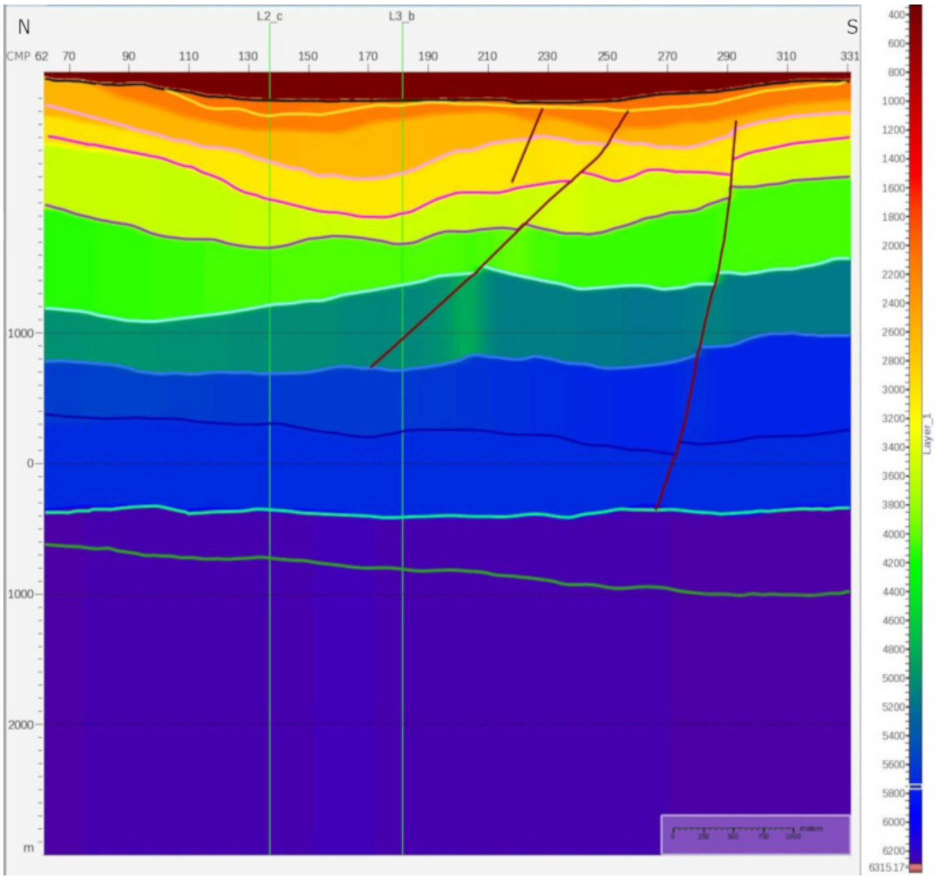

Figure 35: Velocity model of L4 with interpretation.

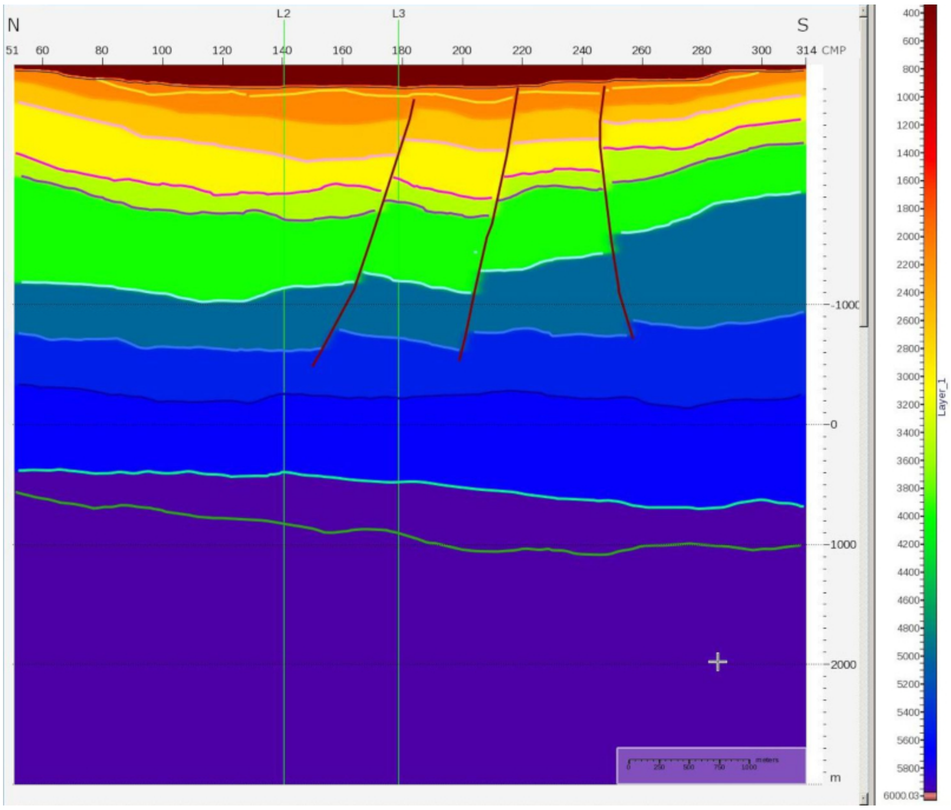

Figure 36: Velocity model of L5 with interpretation.

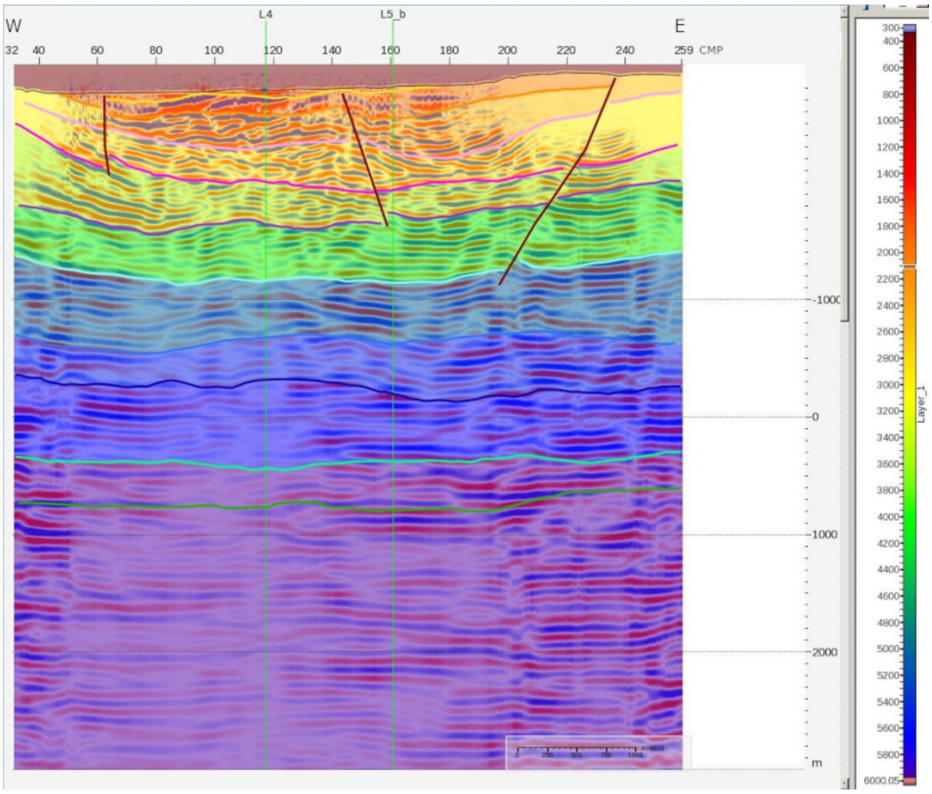

Figure 37: PSDM seismic section of L2 with velocity model and interpretation.

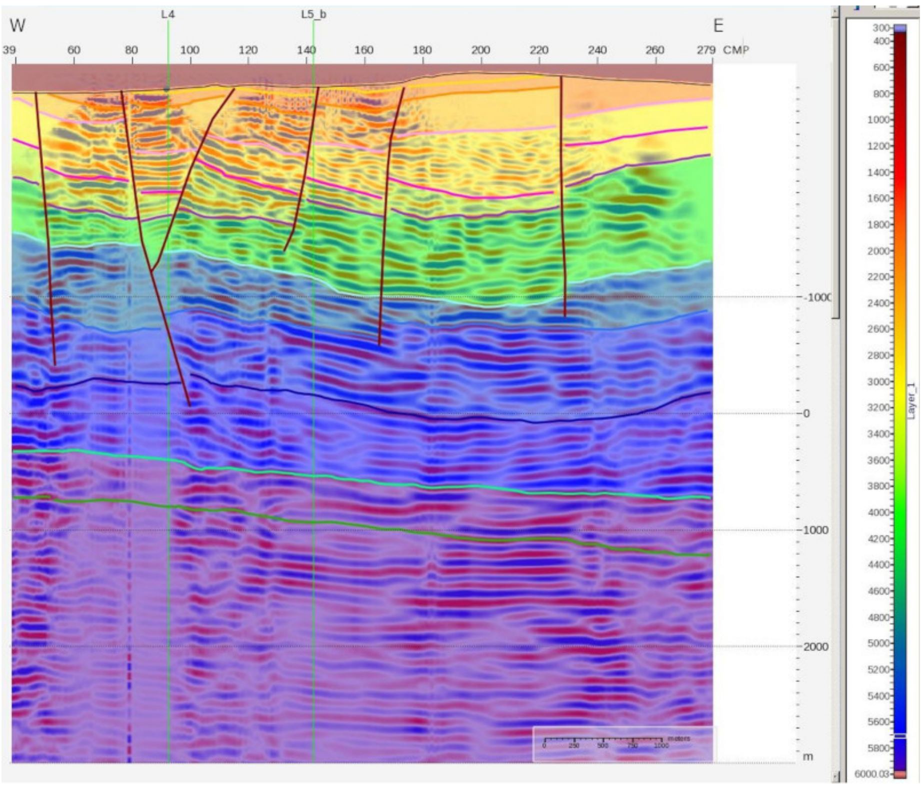

Figure 38: PSDM seismic section of L3 with velocity model and interpretation.

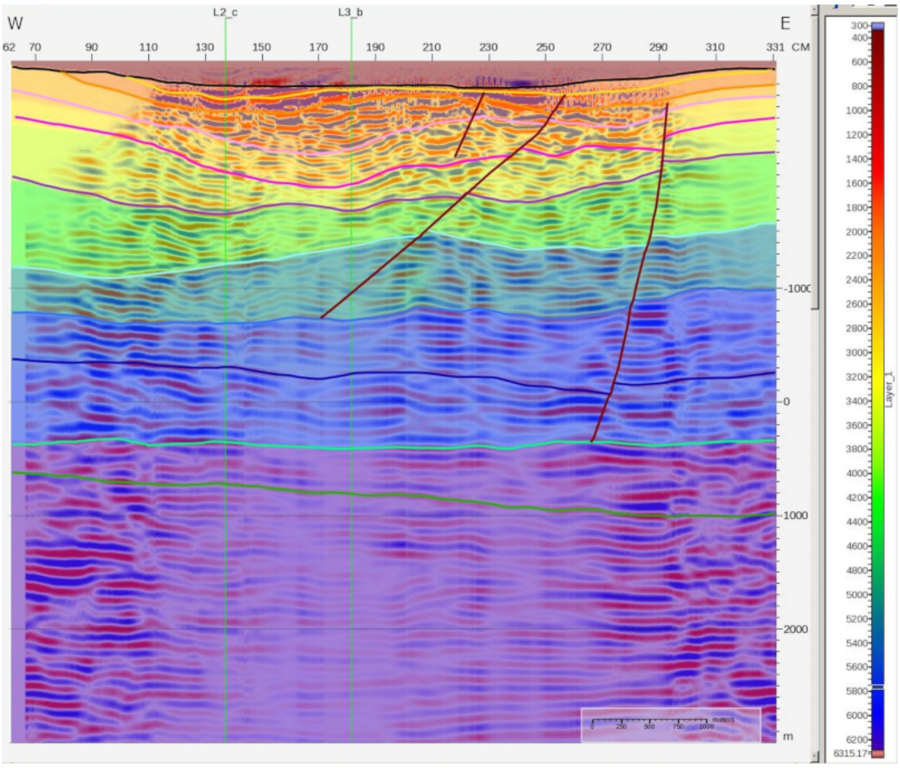

Figure 39: PSDM seismic section of L4 with velocity model and interpretation.

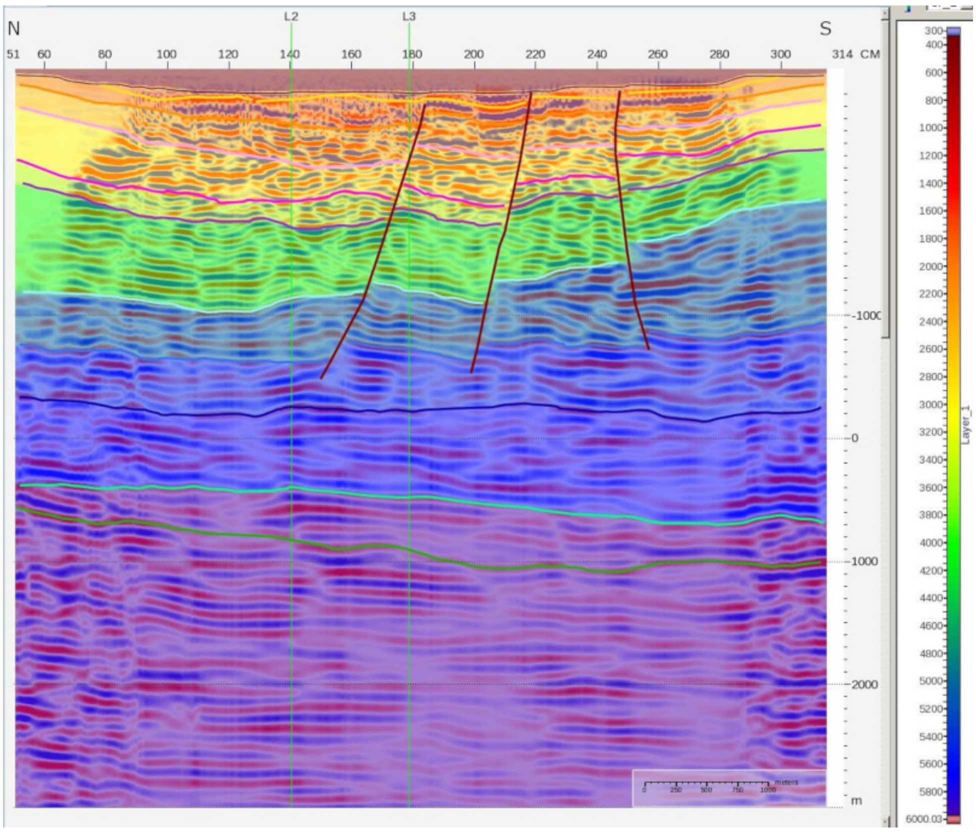

Figure 40: PSDM seismic section of L5 with velocity model and interpretation.

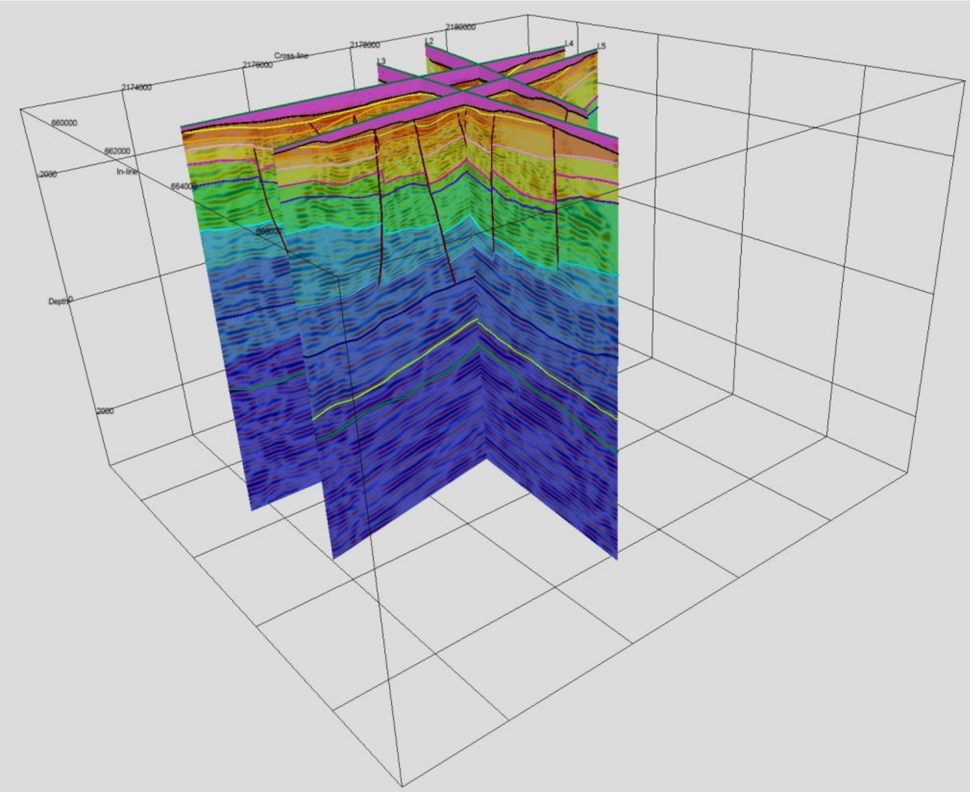

Figure 41: 3D view of crossing lines lines, with observation of the corner between L5 and L3.

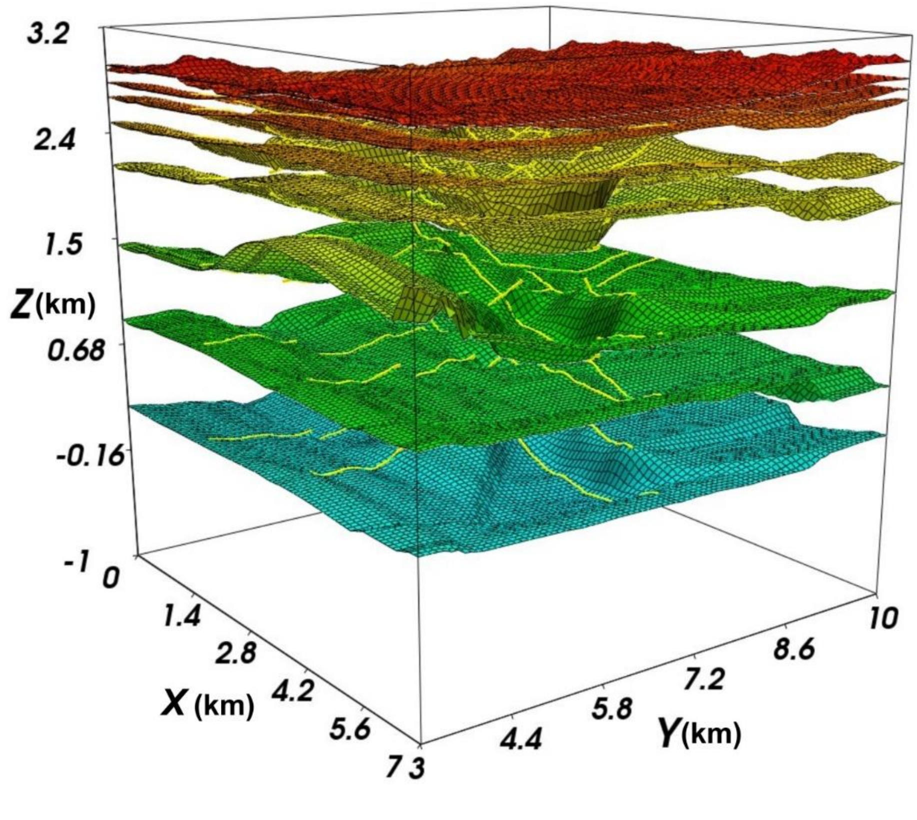

Figure 42: 3D extrapolation of the interpreted horizons in the Los Humeros seismic lines.

4.2.3 Seismic interferometry by active seismic data

The task of recovering deep information at Los Humeros by seismic and seismological methods involves also the issue of recovering near-surface seismic information at locations where the surface measurements are taken. Thus information about shallow layers is important for the purposes of the investigations. The minimum offset in the Los Humeros shot gathers is 300 m (|±300| m) (e.g., Figure 13 and Figure 19). This lack of traces limits the information conveyed by direct and refracted waves, making it difficult to evaluate the behaviour in very shallow layers by direct measurements.

Since the condition of continuity in space with approximately regular spacing is available at the surface for the receiver traces, we adopt the alternative solution to use the seismic interferometry approach by the active seismic data. In this way we create virtual sources for other receivers, also those at shorter offsets, conversely missing in the original data.

The seismic interferometry approach is well known in seismic literature. Among others, we may cite the original concept by Bakulin and Calvert (2006) and also Wapeenar et al. (2008). Considering causal contributions, with the notation of Figure 43, let x_{VS} and and x_R be signals recorded at receivers at the virtual source position and generic receiver at left side position with respect to the source, respectively, and let S_i be sources at the right side. We obtain the left-side virtual source signals by

$$x_{R,VS}^{-} = \sum_{Si>VS} x_R x_{VS}^{*}, \qquad (1)$$

where the signals are in the Fourier frequency domain and '*' denotes complex conjugation. The time signals are obtained by inverse Fourier transforming equation 3.1. Note that equation 3.1 is obtained by summing the signals obtained with sources at positions $S_i > VS$. Limitations can be introduced to avoid shorter and noisier offset traces. As schematically illustrated in Figure 43, this represents an estimate of the Green's function from VS to R. A similar calculation can be performed to obtain the right virtual signals $x_{R,Vs}^{+}$ using energizations at the left positions with respect to the VS position.

We process the data from both the sides using causal and anti-causal signals, which are summed together in the results after time reversing the anti-causal signals. Gating traces to select in time the events in the reference traces is also beneficial. Combining the left side and right side contributions we obtain the virtual traces of a split-offset shot gather, thus also the traces required to fill the offset gap around the real source.

This result is shown by synthetic and real data in figures from Figure 44 to Figure 46. The signals are filtered in a low-frequency bandwidth to remove shallow high-frequency noise and boost the continuity in the signal filtered by the field acquisition patterns, which can be observed in the real merged data in Figure 45 (right side).

The interpretation of spatially continuous events is matter of investigation, to enable the approach to be used for further shallow signal analysis, thus evaluating refraction and direct arrivals. This analysis is ongoing and performed by real and also synthetic shot gathers, as in Figure 46.

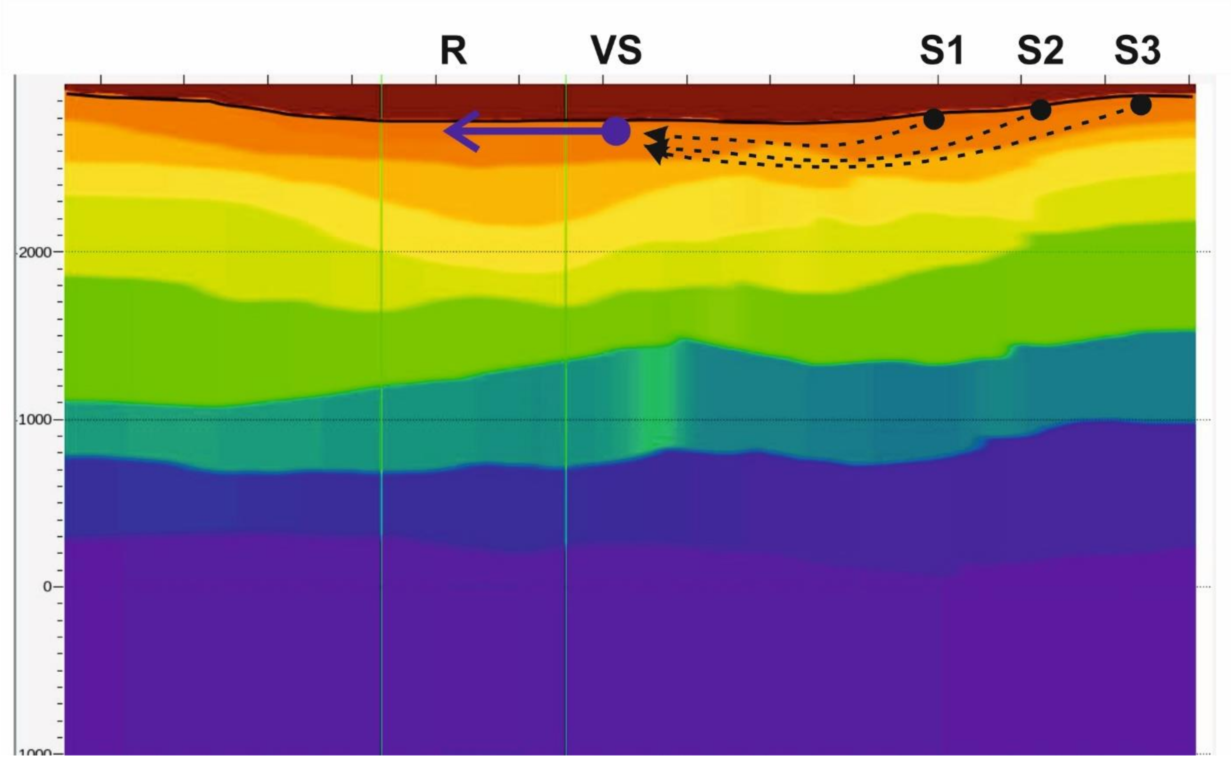

Figure 43: Seismic interferometry using active seismic data. A virtual source (VS) is created for a receiver R using the sources S_i.

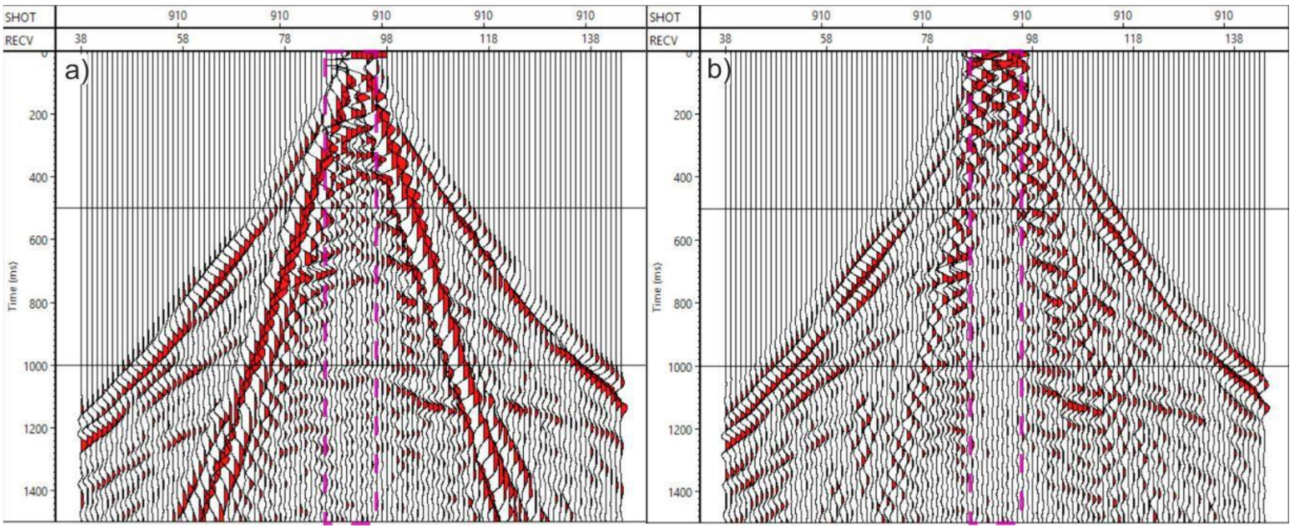

Figure 44: Example of seismic interferometry application to create virtual sources in the gap region (red dashed box) by L5 synthetic signals. a) Full synthetic shot and b) shot with the offset gap filled by interferometry traces. The method provides estimation of wavefields at shorter times.

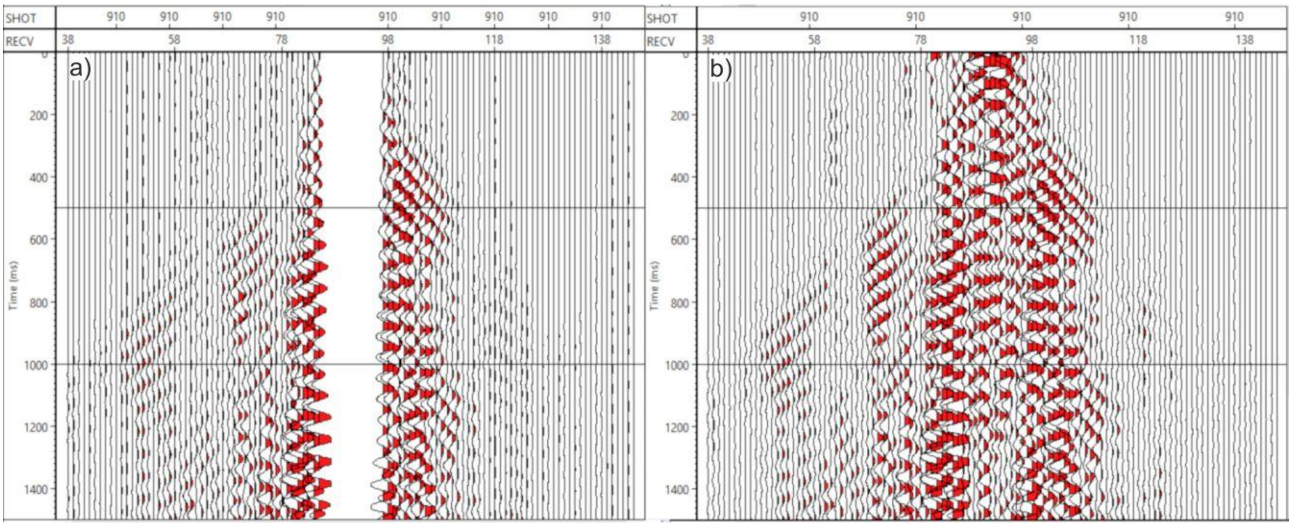

Figure 45: On the left side, real shot of L5 with the acquisition gap between near-offset traces. On the right side, the offset gap is filled by the interferometry traces obtained calculating virtual sources with the real data.

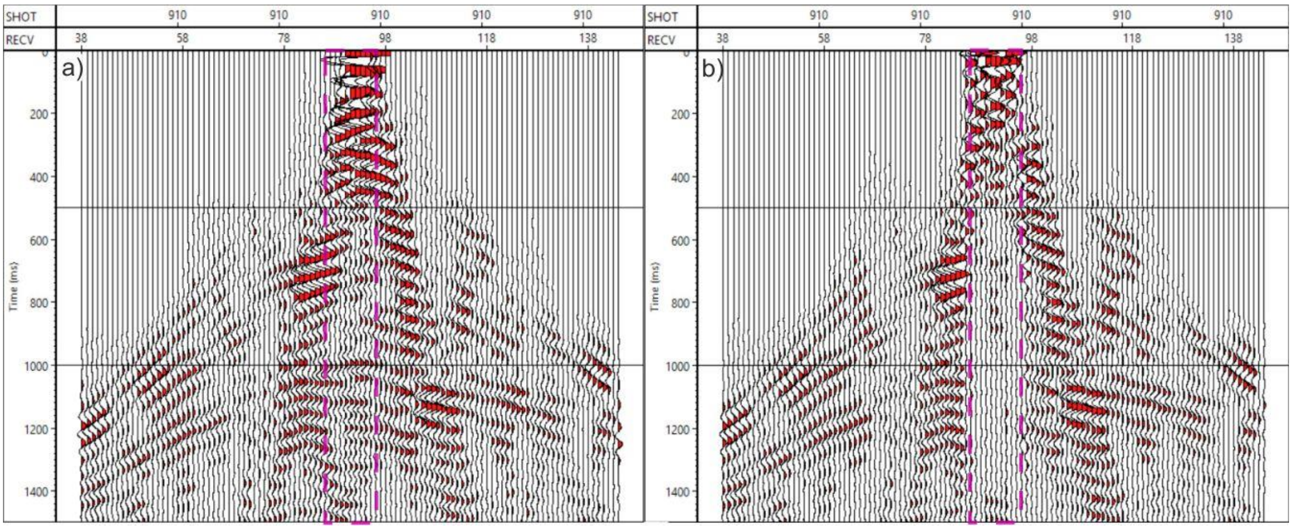

Figure 46: As in Figure 44, seismic interferometry on L5 synthetic signals corresponding to the real data of Figure 45. In this example the synthetic signal is filtered at lower frequencies and with a mix to simulate the vibrator pattern response in the real data. a) Full shot and b) shot with the offset gap filled by interferometry traces. The interpretation confirms the trends observed at shorter times in the real data of Figure 45.

4.3 Attenuation tomography using active seismic data

Reflection attenuation tomography is difficult with the poor-quality and noisy reflections in the active seismic lines of Los Humeros. In this sub-section of the report we investigate the attenuation of the diving waves, by analysing signal wavelets selected in the shallow arrivals. A shortcoming with respect to the attenuation inversion with reflection data, is that the source emission and receiver angles are not negligible in the offset traces, and frequency-dependent directional effects are expected in the data. These can cause bias effects in the attenuation analysis. The source and receiver responses analysis is shown in Figure 47 and Figure 48 for uniform velocity 2000 m/s. Using the angles and the local velocity calculated by tomographic inversion of diving waves, we calculate the responses for the vibrator patterns and receiver arrays, assuming uniform local velocity, and perform the compensation of the pattern response (as in Figure 48) before attenuation inversion.

Then we perform attenuation tomography to obtain the distribution of Q (quality factor) in the model, and attenuation byQ^{-1}. The basic approach to obtain the quality factor *Q* is the following. As the wave propagates the amplitude decreases, pulse broadening occurs and high frequencies are lost. A measure of the frequency shift of the spectrum is the variation of the spectral content of the pulse, ξ, defined as

$$\xi = \frac{f_s - f_r}{\sigma_s^2},$$

where f_s and f_r are the centroid frequencies at the source and receiver, respectively, and σ_s^2 is the spectral variance of the initial pulse. A relation similar to that one used in the travel time tomography can be established between the spectral content and the attenuation factor α in the waves propagated at distance *x* by attenuation $e^{-\alpha x}$, i.e.,

$$\xi = \int_{x_1}^{x_2} \alpha \, ds,$$

where x_1 and x_2 are the position of source and receiver, respectively, and assuming frequency-independent *Q* we have

$$\alpha = \frac{\pi f}{vQ}.$$

Figure 49 shows a) the spectra of the reference wavelet and b) of the signal after propagation. The method is illustrated in Quan and Harris (1997). As pointed out by these authors, the value obtained by the estimation is relative, and some calibration would be beneficial. So we interpret Q = 100 as the minimum value in Figure 50, not as an absolute value but relative in relation to its spatial distribution.

As a preliminary conclusion, further analysis is required to calibrate these attenuation data. Next steps will include the extension of the investigation to the other active seismic lines, to obtain 3D information with evaluation of possible directional effects related to anisotropy.

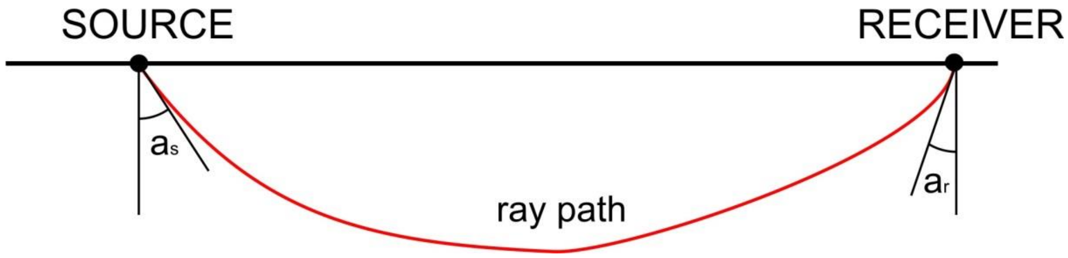

Figure 47: Diving wave, emitted with source emission angle a_s and recorded with receiver angle a_r.

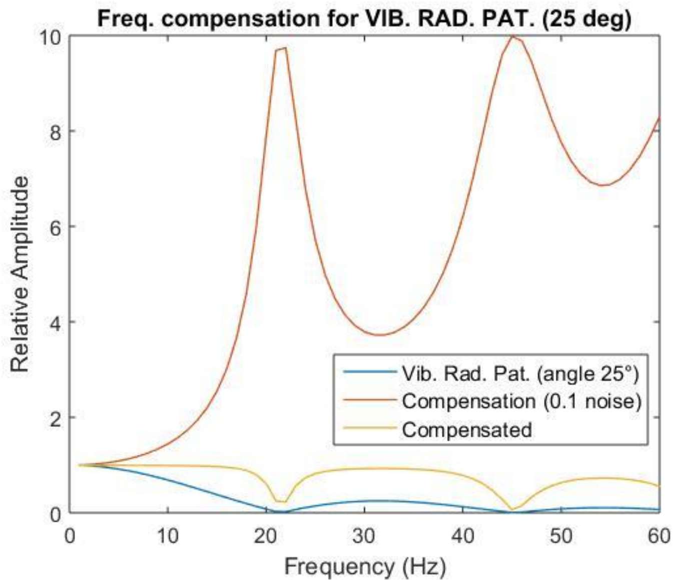

Figure 48: Radiation pattern and compensation curve calculated assuming uniform ground velocity 2000 m/s.

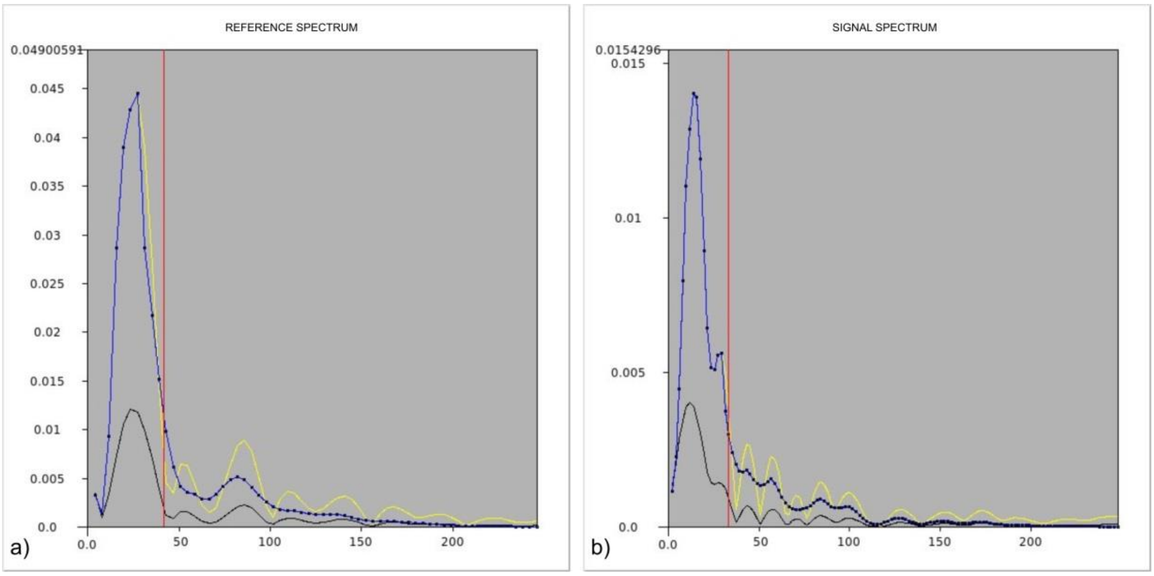

Figure 49: Spectra of wavelets extracted in time and filtered with a Tukey filter. Each figure shows the spectrum of the original signal (black line), of the signal compensated for the radiation patterns (yellow line), and then used for inversion after application of a smoothing function above 35 Hz (blue line), for a) the reference wavelet, and b) the propagated signal. The red line denotes the centroid of the blue spectrum.

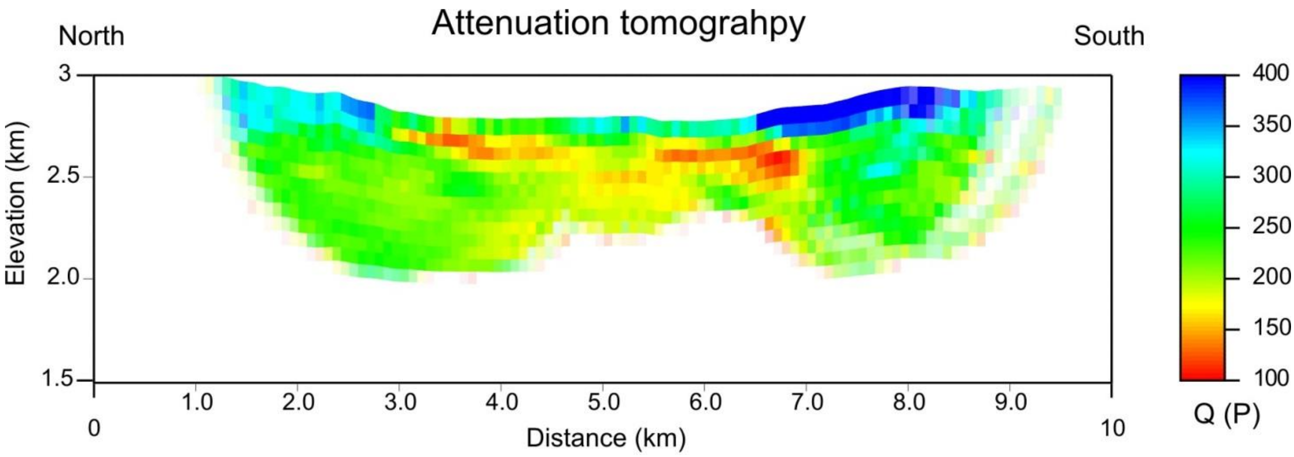

Figure 50: Map of relative Q attenuation tomography calculated along L4.

5 Seismic structure as seen by tomography methods of Los Humeros geothermal field

5.1 Passive seismic permanent network from CFE

Previous studies (Lermo et al. 2007; Urban and Lermo 2013) highlighted the occurrence of local seismic activity in the Los Humeros geothermal field, mainly in the exploited Los Potreros caldera zone. These studies cover different periods (between 1997 and 2008, and 2014 and 2016) during which earthquakes up to moment magnitude 4.2 were recorded. They discuss the possible relationship between the seismicity and the injection operations in the field (Lermo et al. 2016). The analyses are based on a telemetered permanent seismic network of six three-component stations installed by CFE in 1997, and on temporary networks installed in the area for the sake of the studies (Gutiérrez-Negrín and Quijano-León 2004; Lermo et al. 2007). From those studies, a 1D velocity model was derived (see Figure 57). We call this model is this report the “reference model” or “Lermo model”.

For the GEMex project, it was decided to install a dense seismic network for a one-year period. Such a network should provide basic data to image the underground structures with enough details to reach the project objectives.

5.2 Design of the new acquisition network

5.2.1 Synthetic models to design the acquisition network for tomographic analysis

Two different 3D experiments were performed by using different networks of receivers’ stations. In the first one (experiment A) two groups of regular grids were used: 36 stations disposed in a quadrangular area above the cluster of earthquakes, and 21 stations placed externally to the hypocenters area (Figure 51 a). In the second case (experiment B) we used the network proposed and provided by GFZ, which is defined by a sparse distribution of 54 stations (Figure 51 b). In both cases a 3D model was used, with a vertical P-velocity gradient defined on 9 horizontal layers, from 3.0 km/s in the shallower layer (below topography) to 4.6 km/s in the deeper layer (4.5 km depth). Figure 52 shows examples of ray-tracings calculated for these experiments. In the experiment A, defined in a more restricted model (15×15 km), different model grids (regular, irregular and Voronoi based, Figure 53) were used to verify the potential resolution of the inversion. In the experiment B, using a larger model (60×60 km), only regular grids were utilised for the discretization of the model. In both the experiments, the forward and inverse models were computed. Furthermore, for each inversion, the residual analysis (difference between the ‘true’ and the computed travel times) was performed and the null space map were calculated in order to verify the reliability of the results.

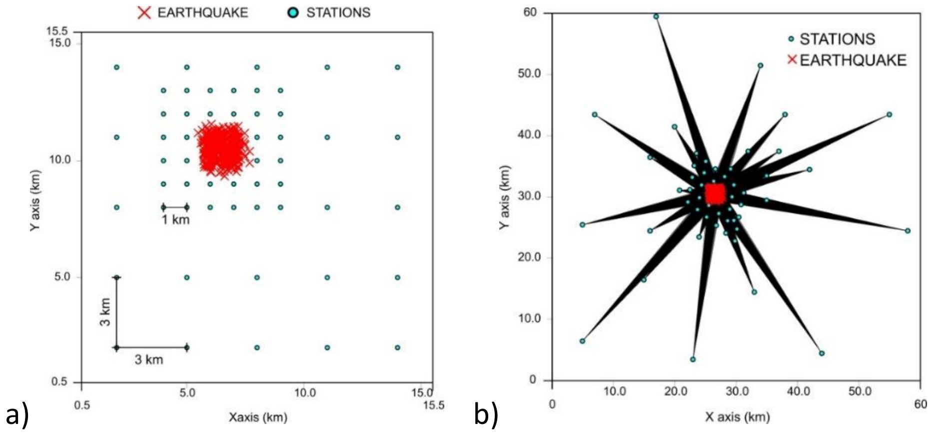

Figure 51 : Plane view of the X-Y positions of the different networks of stations used in the two experiments (a) A and (b) B. In b) the black segments represent the rays connecting each station to the cluster of earthquakes (red crosses).

As final results of the synthetic tests, we observed that, for a tomographic purpose, the regular distribution of the stations in a small area (experiment A), jointly with the use of irregular discretization (Figure 53, grid A3), allows us to reach the best results to define velocity field of the model around the earthquakes cluster. Conversely, the inversion process with sparse distribution of the stations in a large area (as in experiment B) provides average velocity values along the ray band connecting each station to the cluster of earthquakes. These computation of average velocities can introduce local errors in the velocity estimation inside the earthquakes area, and forces to use a lower grid resolution outside of it. This result is due to the fact that the more we consider a large volume to be investigated, the more the earthquakes cluster region approximates a point in the tomographic system. This effect can be seen Figure 54, which shows the ray bands with different thickness relative to the ray distances in the two experiments. Figure 54 shows the misfit of velocity (difference between the true and tomographic velocities) of North-South vertical sections of the two experiments. In the experiment A (top panel), we observe more pixels with low misfit values than in the experiment B (bottom panel), in particular in the area around the earthquakes cluster.

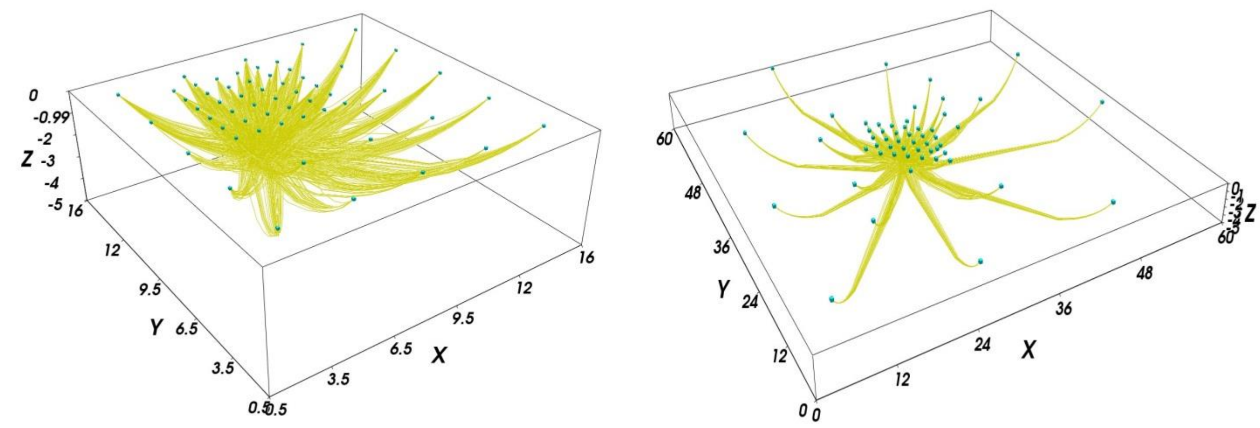

Figure 52: 3D ray tracing related to the experiment A and B in Figure 51 .

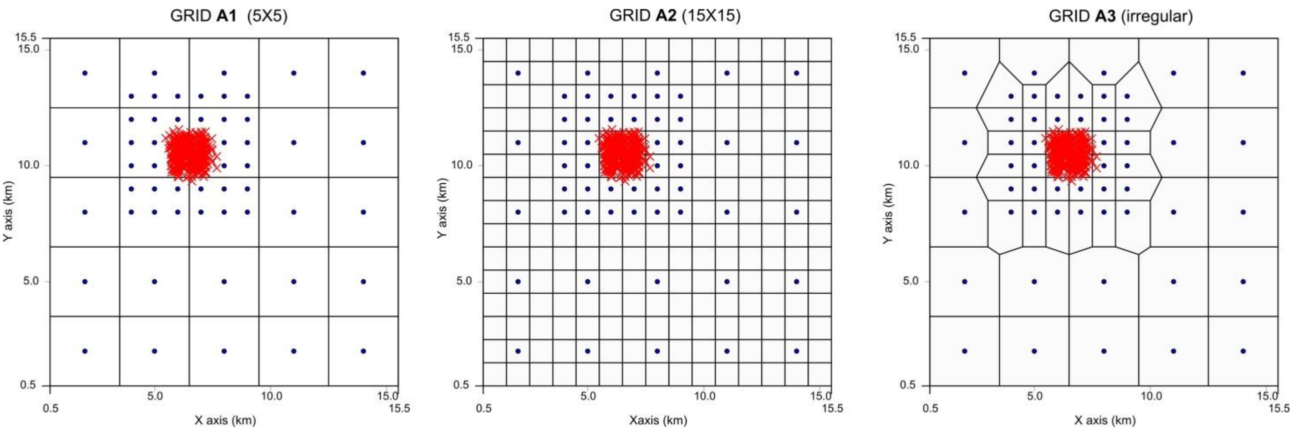

Figure 53: XY grid distributions used in the experiment A. GRID A1 sparse regular grid; GRID A2 fine regular grid; GRID A3 irregular grid using the Voronoi tessellation. In our test, GRID A3 gave us the best result.

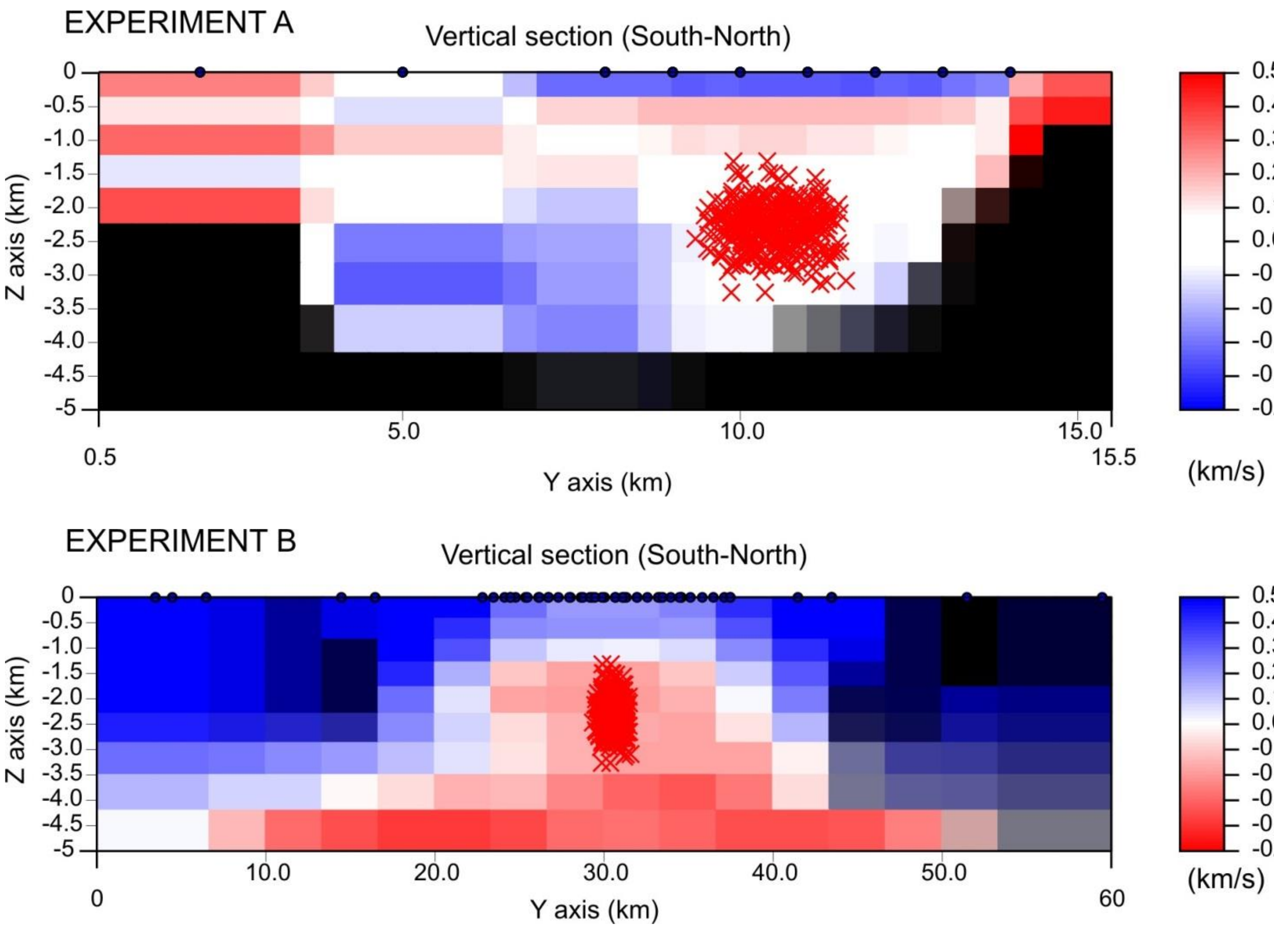

Figure 54: Vertical sections of misfit values on velocity (difference between the true and tomographic velocities) related to the two experiments. Red crosses display the earthquakes positions.

5.2.2 New methodology for network design for best earthquake localisation

We constructed a network optimization scheme based on well-established survey design tools to design and qualify local and regional microseismic monitoring arrays dedicated for geothermal exploration. The optimization routine is based on the traditional minimization of the volume error ellipsoid of the linearized earthquake location problem (D-criterion) with the twist of a sequential design procedure. Seismic stations are removed one by one to obtain networks for constraining the locations of multiple hypothetic earthquakes with varying local magnitudes. The sequential approach is simple and allows the analysis of benefit/cost relations. Cost curves are computed for all hypothetic events to reveal the minimum optimal number of stations given specific design experiment objectives. The scheme was first demonstrated on three test design experiments. Later, we used the routine to augment an existing seismic network for monitoring microseismicity in a geothermal field in NE Iceland (Theistareykir). The resulting 23 station network would become the backbone of a reservoir behaviour and exploitation activity study. Hypothetic event locations and magnitude relations were taken from a previous regional seismicity study and coincide with geothermal injection and production areas. Sensitivities were calculated with a known 1D velocity model profile using a finite-difference back-ray tracer, and body wave amplitudes were computed from known local magnitude relations. Finally, expected earthquake location accuracies were calculated via multiple Monte Carlo experiments. The design routine was later used to qualify an existing seismic network located in SWIceland (Reykjanes). The seismic array was reduced at strategic positions, and benefit and expected accuracies were quantified to observe whether costs could have been optimized had a previous network design experiment been performed. Overall, we explore quick and flexible tools for designing and qualifying networks for many applications at various scales. This methodology is published (Toledo et al., 2019) and has been applied to design the network in Los Humeros.

5.2.3 Network lay-out

Between Sep. 17 and Sep. 18, the GEMex temporary seismic network designed by the previous analyses and decided by a meeting in Postdam was deployed and maintain to monitoring continuously the Los Humeros geothermal field area (Figure 55). Twenty short-period three-components sensors (Mark L-4C-3D) recording at 100 sps and 25 broad-band three-components sensors (Nanometrics Trillium compact 120 s) recording at 200 sps composed the network, which is divided in two sub-networks. The first one, consists of 27 stations spaced every 2 km to cover the producing zone, in the Los Potreros caldera. The second one is sparser, with a 5-km minimum spacing between the remaining stations, and covers an area of about 30 km radius around the centre of the Los Potreros caldera. These sub-networks are complementary and designed to answer specific questions. The dense inner sub-network is intended to focus on the local seismicity and to comply with beamforming and time reverse imaging techniques. The sparser sub-network is dedicated to larger scale imaging techniques, such as seismic ambient noise tomography or interferometry, or regional earthquakes tomography.

Fifty percent of the stations recorded continuously more than 75% of the monitoring period. The site noise levels were, on average, between 2 and 10 dB below the high noise model from 1 to 10 s. For frequencies higher than 1 Hz, the daily varying anthropogenic noise could be observed for several stations.

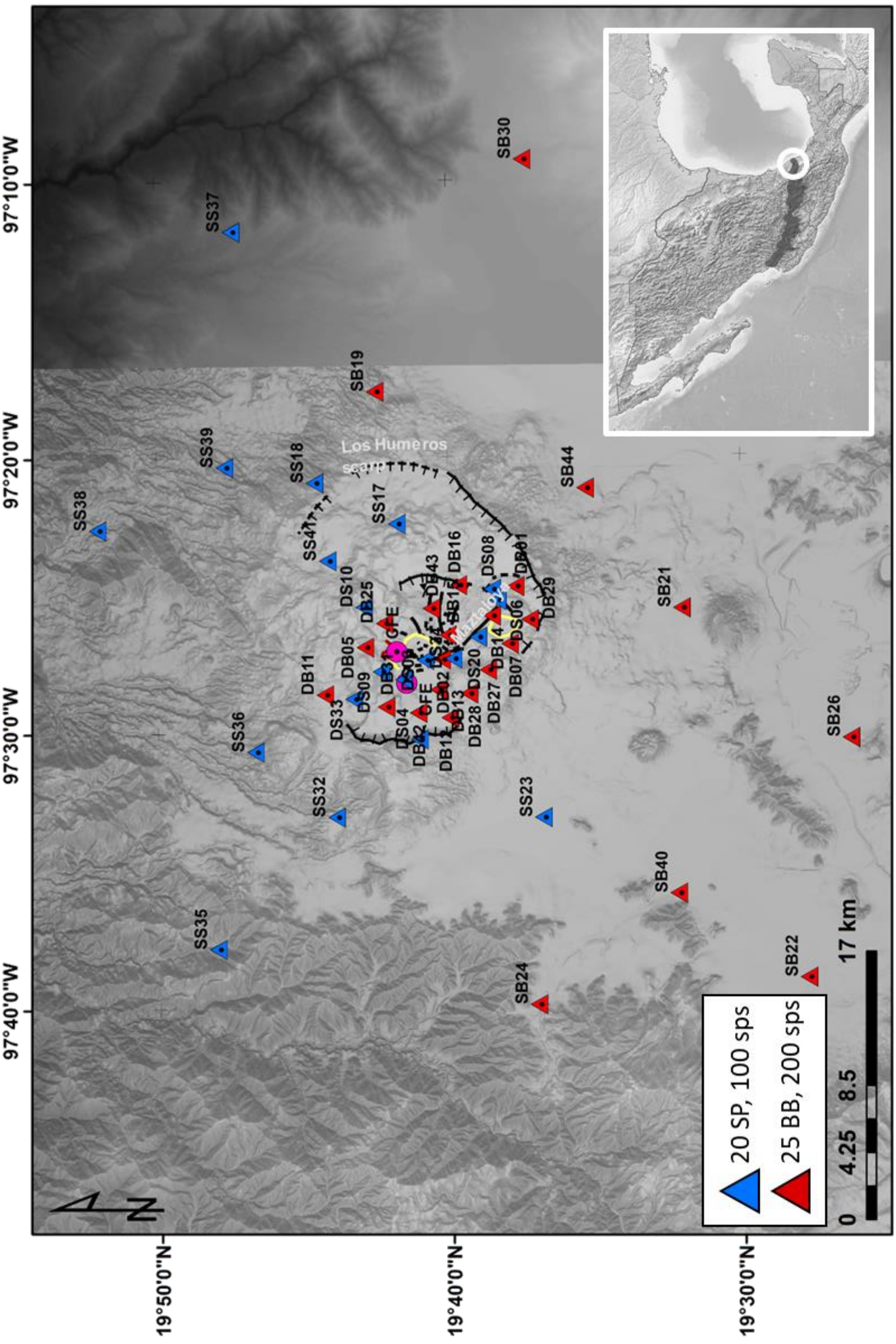

Figure 55: Layout of the passive seismic monitoring network deployed around Los Humeros. The network comprised 3C short-period sensors (blue triangles) and 3C broad-band sensors (red triangles).

5.3 Earthquake detection, initial localisation and basic analysis

5.3.1 Detection of local seismicity

From the continuous recordings, the first task consisted in detecting local seismicity in the Los Potreros area. To do so, we applied a recursive STA-LTA detection algorithm, which was calibrated on local events recorded in 2005 and 2006 by the permanent CFE network, and checked exhaustively on several days of the GEMex seismic database. The optimum detection parameters combine a band-pass filtering between 10 and 30 Hz, STA and LTA windows of 0.2 s and 2 s respectively, an activating threshold for a STA/LTA ratio of 3.5 and a deactivating threshold of 1. In order to detect either on the P- or the S-wave, the STA/LTA ratio was computed on a three-component amplitude trace, which corresponds to the square root of the sum of each squared component. Finally, the detection was applied only on the stations belonging to the dense inner sub-network and validated if at least five stations were triggering. The processing suite applied is developed under the Python programming language and makes use of the numerous capabilities of the Obspy reference library (Beyreuther et al. 2010).

From the continuous records, ca. 1570 possible seismic events were detected. Using the Obspyck software (Megies 2016), they were manually reviewed, classified and picked when relevant. Many of the detections were associated to storms and noise. Regional earthquakes were also identified, part of them being listed in the Mexican earthquake catalogue of the Universidad Nacional Autónoma de México (UNAM). These 88 regional earthquakes typically exhibit P- to S-arrival time difference larger than 10 s. Finally, 481 local earthquakes were isolated, and typically last less than 10 s (Figure 56).

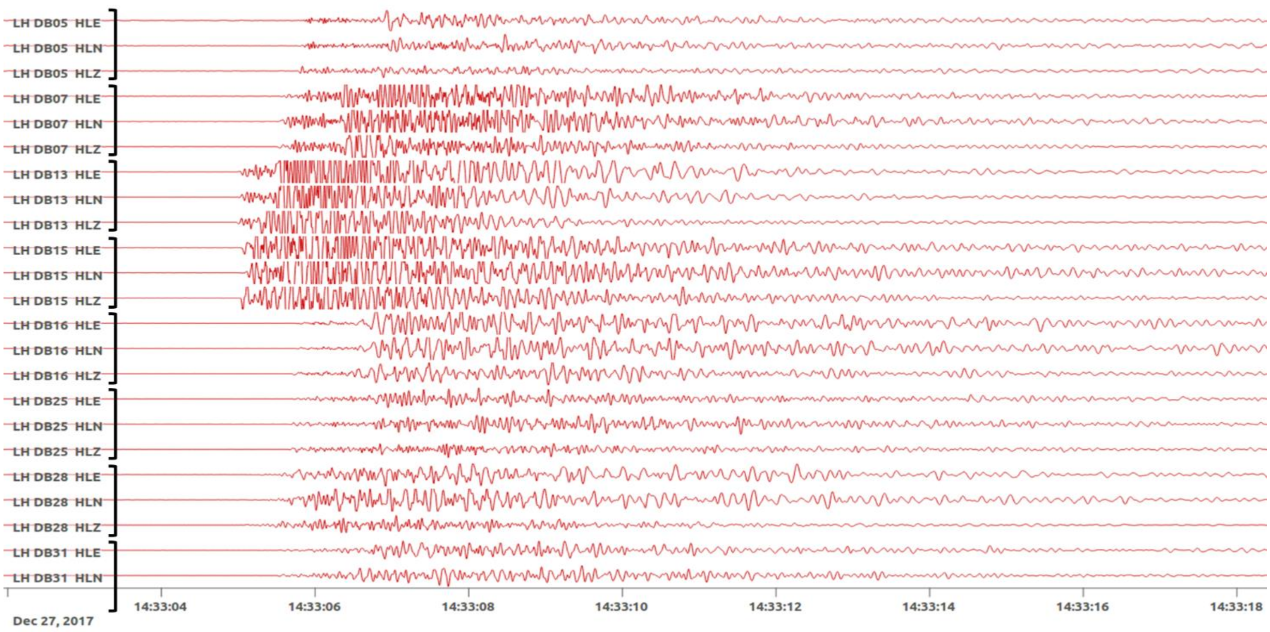

Figure 56: Seismogram of a local earthquake recorded at eight 3C-stations of the dense inner sub-network, for a time window of about 14 s. The traces are sorted East, North, Up for each station. The amplitude scale is common to all traces and chosen to highlight the P- and S-wave arrivals.

5.3.2 Preliminary location of earthquakes: methodology

In order to compute preliminary earthquake hypocentres, a 1D velocity model was used. It is based on the model described and used in several studies of the Los Humeros seismicity (Lermo et al. 2007; Lermo et al. 2016; Urban and Lermo 2013). However, that reference model was smoothed to avoid strong velocity contrasts, at a few interfaces, that would lead to location artefacts. The smoothing preserved the seismic wave propagation time from depth to surface. As in Lermo et al. (2007), the Vp/Vs ratio is taken constant and equal to 1.76. Figure 57 presents the profile of velocity model. However, further tests indicated that this value is too high.

A 1D velocity model is rather a simplistic view within this volcanic geomorphology, as described by Calcagno et al. (2018), but this initial choice is motivated by the fact that several tomography techniques will be applied to better describe the velocity model in 3D.

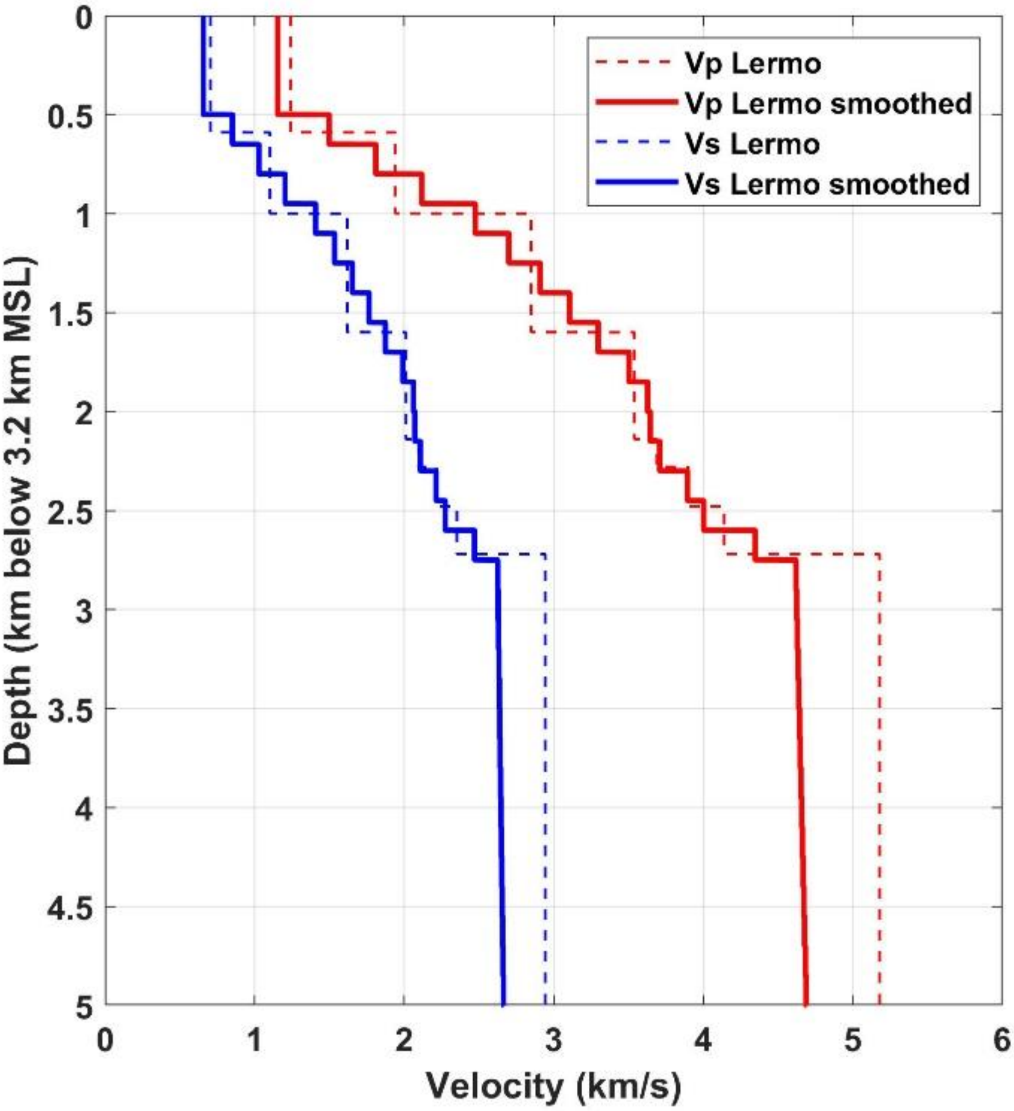

Figure 57: 1D velocity model profile used for preliminary earthquake locations. This model named "Lermo smoothed" results from the smoothing of the original Lermo et al. (2007) model.

To locate the local seismicity, the software NonLinLoc (Lomax et al. 2000; Lomax 2018) is used. It has the advantage to properly take into account the time picking uncertainties and to define the location inverse problem within a probabilistic framework, as described by Tarantola and Valette (1982). This location is made in two runs. In the first run, earthquakes raw hypocentres are calculated and the mean time residuals computed at each station for each body wave is used, in the second run, as station corrections.

Once an earthquake hypocentre is obtained, a local earthquake magnitude (Mlv) is estimated using the Obspy library (Beyreuther et al. 2010), which applies the formula of Bakun and Joyner (1984). This local magnitude is computed from the peak-to-peak amplitude of the vertical components and the associated half-period.

Finally, for a few earthquakes, it was also possible to determine preliminary focal mechanisms using the P-wave polarities and the FocMec software (Snoke 2017).

5.3.3 Local seismicity results and discussion

5.3.3.1 Time and magnitude distribution

Figure 58(top) shows the time distribution of the local seismicity rate computed for five days bins. In average, about six events are detected every five days. A maximum of ten earthquakes was recorded in one day, on the 04/11/17. At a first glance, no specific feature can be observed, however, analysis in parallel with production and injection operations in the field will be done in the near future and may highlight possible links.

The local earthquakes have Mlv ranging between -0.8 and 2.2 (Figure 59, bottom). A first analysis of the magnitude distribution shows that the network reached a magnitude of completeness around 0 and that the b-value is slightly larger than 1 (Figure 59). These are general observations, which will be further investigated in time and space. It must be noticed that these magnitude characteristics may change with improved earthquake locations.

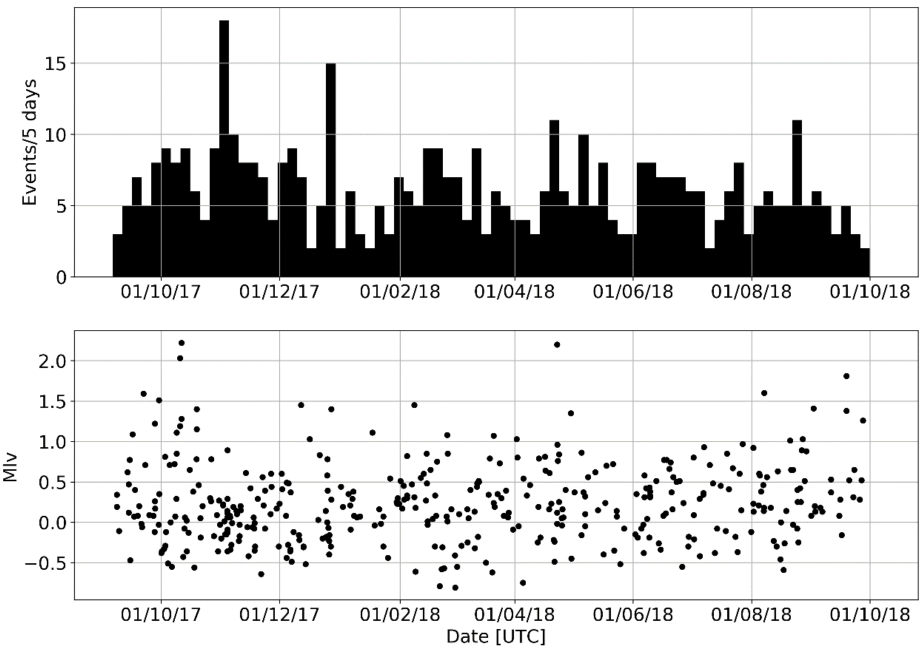

Figure 58: Time distribution of the seismicity: event rate for 5-days bins (top) and event local magnitude (bottom).

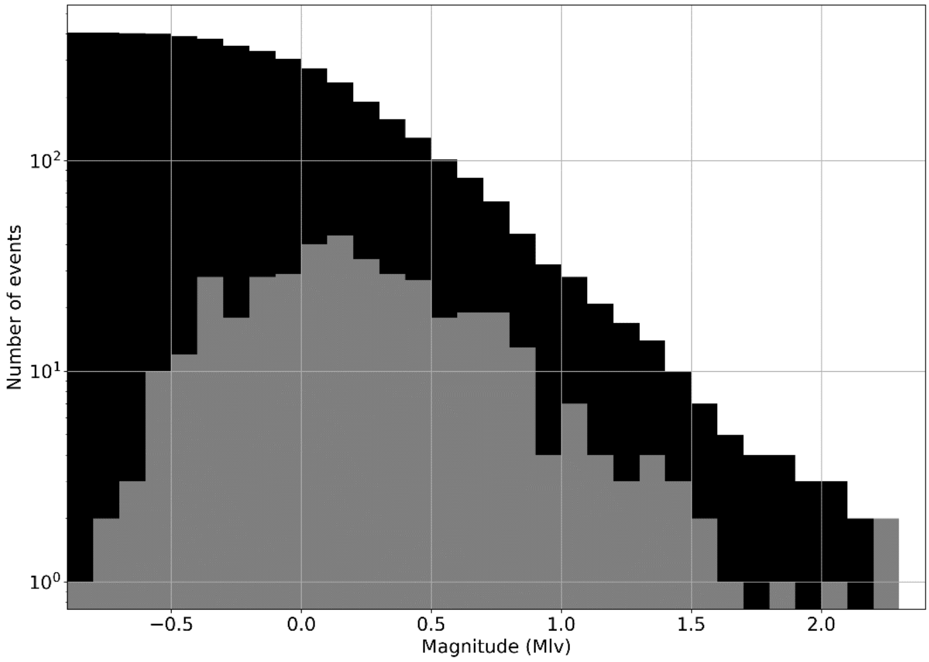

Figure 59: Magnitude distribution of the local earthquakes: cumulative number (black histogram) and number of events (grey histogram). Both numbers are plotted on a log scale.

5.3.3.2 Spatial distribution

Figure 60 shows a map of the epicentres of the local earthquakes. As observed, the recorded seismicity is not sparse but rather distributed in clusters, well within the coverage of the dense inner network. Three main clusters can be identified and are located in the central and North zone of the Los Potreros caldera.

The cluster, which contains most of the seismicity, is the northern one. It is located in the central collapse, between the La Cuesta and Loma Blanca faults. This zone was already seismogenic, as noticed by the previous studies of Lermo et al. (2007), Gutiérrez-Negrín and Quijano-León (2004) and Lermo et al. (2016). It is located at the level of two injection wells (H29 and H38). A second cluster is located to the west side of the Los Humeros fault, at the level of the wells H-40 and H-7, near station DB02. As far as we know from available bibliography, seismicity was not observed in this area. Finally, the third cluster, which is a bit more spread, is located between the central collapse to the west, the Las Papas fault to the south and the Las Viboras fault to the north. Seismicity was observed by Lermo et al. (2016) to the west of this zone. There, the local earthquakes do not seem directly related to geothermal wells. Hence, the GEMex dataset highlights a new seismogenic zone besides existing ones.

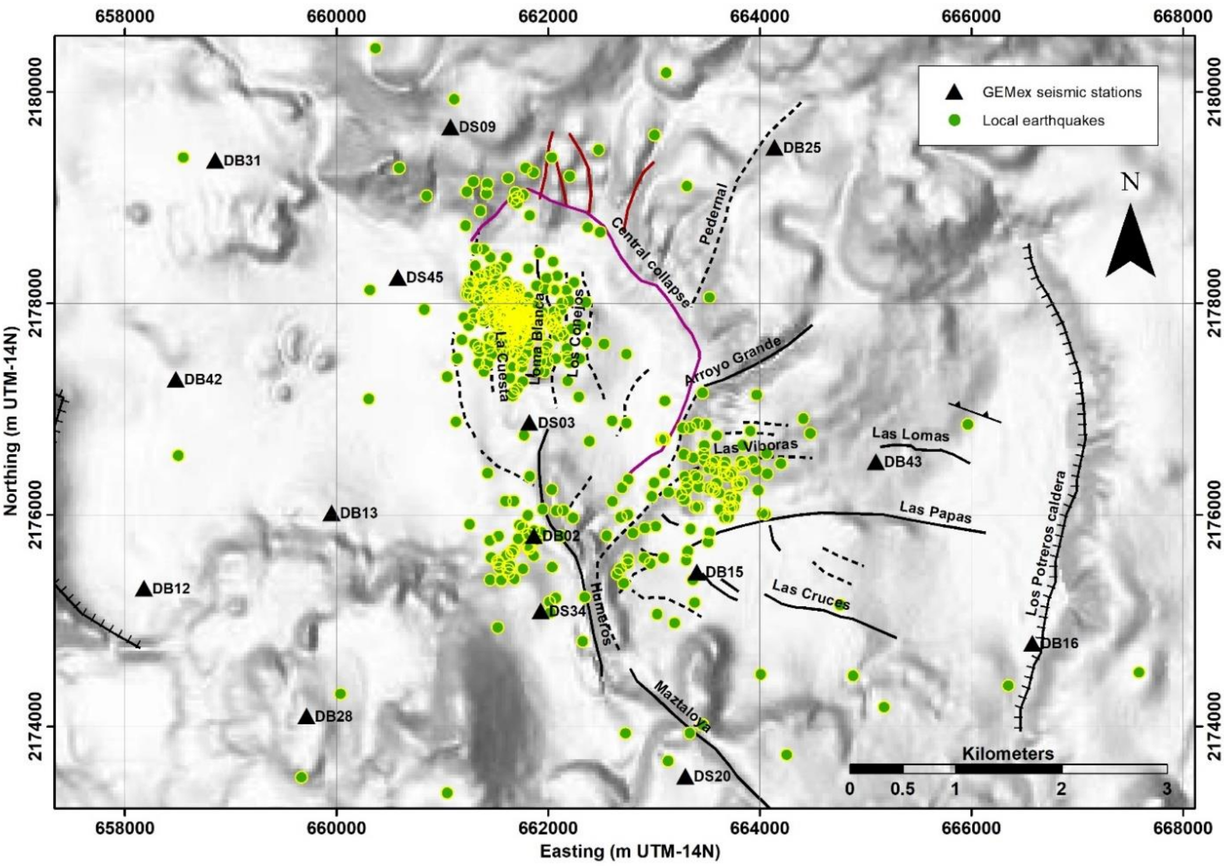

Figure 60: Epicentre map of the local seismicity (green with yellow contour circles) recorded at Los Humeros on top of the topographic map. The temporary seismic stations are displayed as black triangles.

In depth, most of the seismicity is located between 1 and 3 km, with the largest distribution at 2.5 km depth (below 3200 m TVD MSL). This depth range corresponds to the currently exploited reservoir interval. To further investigate the depth distribution of the seismicity, it is necessary to benefit from the tomography results that would provide reliable absolute depths values. As a matter of fact, the simplistic 1D velocity model taken here for preliminary earthquake location may provide relatively certain earthquake epicentres, thanks to the seismic network density; however, it does not constrain the event depth. Hypocentres uncertainties in depth are in average ±350 m, about twice as large as the average horizontal uncertainties.

More detailed analysis of the spatial evolution of the seismicity with time will require improved data processing of our current dataset and information about the production history of the field.

5.3.3.3 Preliminary focal mechanisms

Preliminary focal mechanisms of several of the largest recorded earthquakes have been computed (Table 2). Results are plotted on Figure 61. For several mechanisms, many solutions are consistent with the P-wave polarities (Table 2 only provides the most likely solution).

As observed, many shearing modes apparently occur in field: strike-slip faulting, reverse and normal faulting. However, many strike directions are NNW to NNE, which is consistent with the direction of geological features close to the seismicity. The dipping angles range mainly between 30 and 70°. These preliminary results should be assessed once the earthquake locations have been improved.

Table 2. List of the local earthquakes for which focal mechanisms have been computed. The hypocentre coordinates are given in meters in the UTM Zone14N, WGS 1984, and coordinate system. Depth is relative to 3200 m TVD MSL. The uncertainty is the largest half-length of the hypocentre uncertainty ellipsoid. The strike, dip and rake are the double-couple angles of the most likely focal mechanism plane, under the standard angle convention.

Origin time	North (m)	East (m)	Depth (m)	Mlv	Uncer (m)	Strike (°)	Dip (°)	Rake (°)
2017-10-11T12:09:16	2176232	663572	3023	2.2	148	135.8	67.5	-62.8
2018-04-22T21:03:50	2177763	661781	3005	2.2	73	158.5	46.9	-69.2
2017-10-10T18:11:44	2175523	661642	2375	2.0	57	340.0	60.0	-90.0
2018-08-07T13:17:45	2177545	661351	3691	1.6	205	325.0	55.0	-90.0
2017-09-21T22:41:52	2177553	661606	2936	1.6	95	338.2	31.5	70.6
2017-09-29T22:45:56	2175492	662678	3027	1.5	49	150.0	40.0	90.0
2017-12-12T00:02:17	2175837	663527	2657	1.5	82	0.0	65.0	90.0
2018-02-08T09:09:38	2177263	661758	2678	1.5	104	190.1	7.1	44.9
2017-10-19T09:01:47	2176251	663309	3151	1.4	64	299.4	52.8	-16.0
2017-12-27T14:33:04	2175546	661533	2450	1.4	78	20.0	40.0	90.0
2018-04-29T22:49:57	2175500	661540	2500	1.4	79	265.0	45.2	-83.0
2017-09-27T20:14:05	2175758	661447	1998	1.2	36	45.0	45.0	90.0
2017-10-10T18:12:54	2175640	661653	2418	1.2	54	345.0	75.0	-90.0
2017-09-16T07:43:40	2172156	665010	3739	1.1	201	337.1	57.2	-40.1
2018-02-25T07:06:36	2177752	661664	2788	1.1	106	65.0	30.0	90.0
2017-11-04T03:47:56	2179185	661619	1994	0.9	50	340.8	14.1	44.6
2018-04-16T15:03:26	2176374	663390	3125	0.8	100	12.1	66.6	68.1

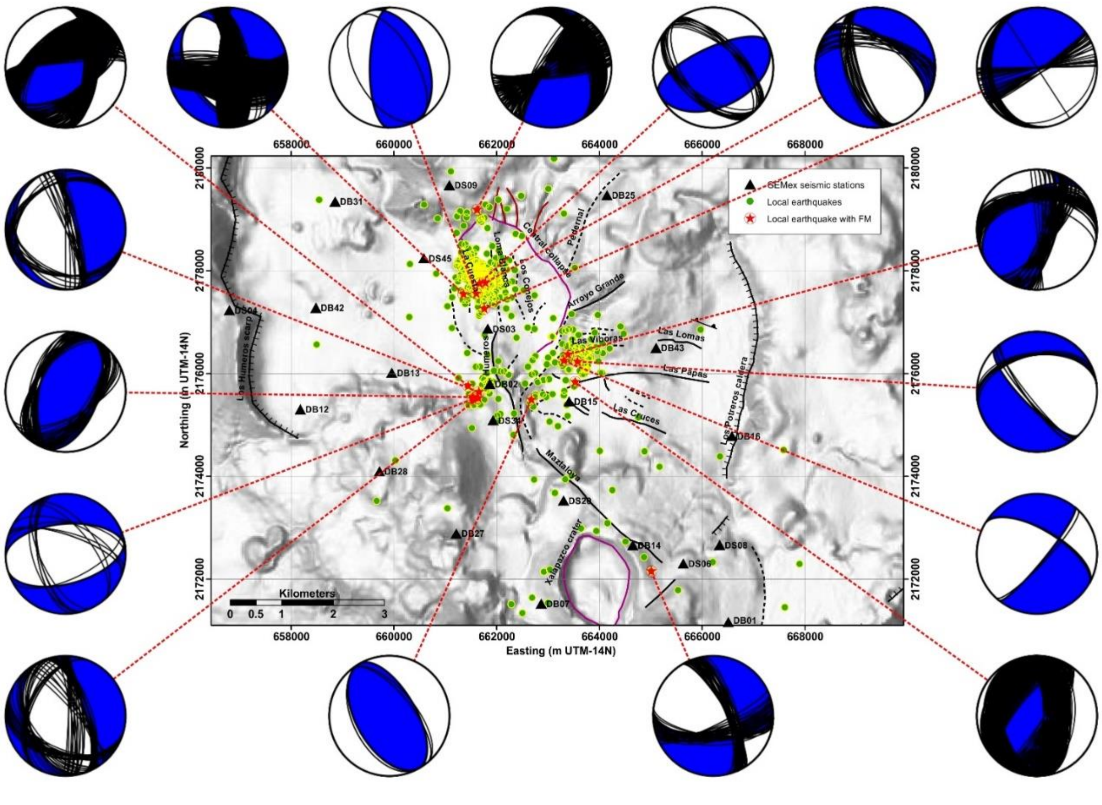

Figure 61: Location and representation (on the lower hemisphere) of the focal mechanisms inverted for the largest magnitude local earthquakes.

5.3.4 Conclusion and outlook

The temporary monitoring network deployed for one year around the Los Humeros geothermal field, in the framework of the GEMex project, was fruitful. Local earthquakes were regularly detected, at a rate of about 1.2 events per day. The network was able to record earthquakes of local magnitude ranging between -0.8 and 2.2, with a magnitude of completeness close to 0. The magnitude distribution, taken as a whole, is consistent with a b-value slightly smaller than 1.

Around 470 events have been located, almost exclusively below the central part of the network. The seismicity takes place exclusively in the Los Potreros caldera, which is currently exploited. The hypocentres are located in the central and northern parts of the production area and are clustered horizontally and in depth at the reservoir level. Three main clusters have been identified and are located in the vicinity of geothermal wells or known geological structures.

Further work to improve the structure imaging from the local earthquakes is necessary. The first next step will consist in performing multiplet analysis and relative locations to provide more details on the clusters identified so far. Analysis in combination with focal mechanism is also foreseen. The spatial and temporal behaviour of the local seismicity must be investigated in detail in the light of geothermal well locations and production and injection operations. This is of main interest to better understand the interaction between the field operations and the seismicity, and thus the impact of the exploitation on the stability of the underground structures. Finally, these results should be integrated and compared to other results obtained within the framework of the GEMex project, especially the complementary geophysical investigations (tomography, magneto-telluric, gravity), the geochemical and geological ones, but also reservoir modelling results.

5.4 Earthquake based travel-time tomography

Travel time tomography method allows to invert jointly for both earthquake locations and velocity model. This is a highly non-linear problem, and it can be solved only by linearization. It is therefore very important to be as close as possible to the final model to find the accurate final model… Therefore, it takes time and patience to find the best parameters that lead to the most realistic model that would explain data best, taking into account the numerous uncertainties coming from errors from picks, from the inaccurate a priori information, errors in the theory applied for wave propagation, etc. So far, the procedure is the following:

- From arrival times of the P and S waves recorded by the seismic stations a 1D velocity model is derived and a preliminary location of earthquakes is obtained.
- Because the results is strongly dependent on the initial model set up as apriori information, test is performed on a large number of initial models (Figure 62)
- Once the 1D velocity model is found (Figure 63 and Figure 64), a 3D inversion is performed, which will give results on the horizontal variation of the 1D results, building velocties anomalies in both horizontal directions. The final earthquake location is updated and different from the initial location found in the 1D model. Bad picks can be found using the Wadati diagram (Figure 65).
- The inversion result should fit as much as the data, however not at the expense of the reality of the model. Therefore a damping parameter is introduction in the inversion computation, which is initially defined by trial and errors. Once this parameter found, the inversion is performed initially with large grid spacing and refinement to a denser model.

5.4.1 1D velocity model using VELEST

In order to define the 1D velocity model, a large number of initial velocity models with varying gradients were tested. The final 1D velocity model is then selected by the smallest RMS value, and verified by their associated station corrections, and hypocentre and model variations per iteration.

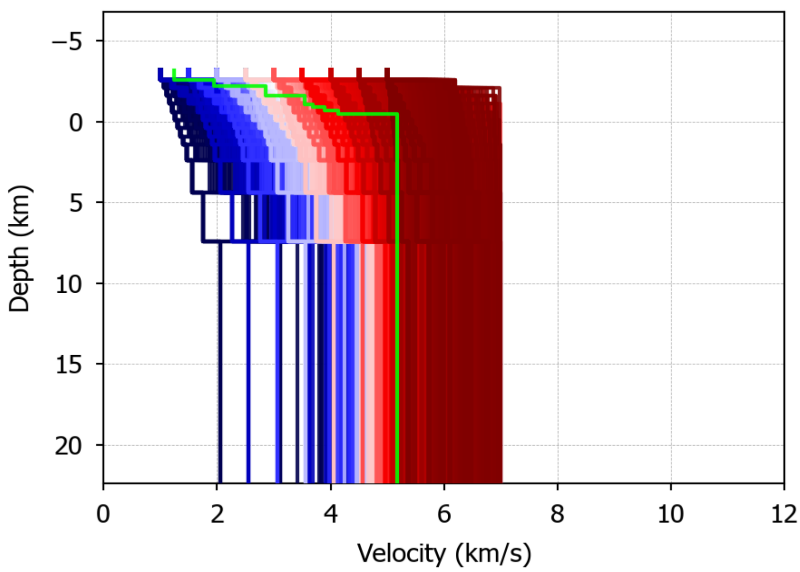

Figure 62: Set of initial velocity models tested to invert for the 1D velocity model. Several initial velocities at surface and depth, and velocity gradients were tested. Colors have no meaning in this plot.

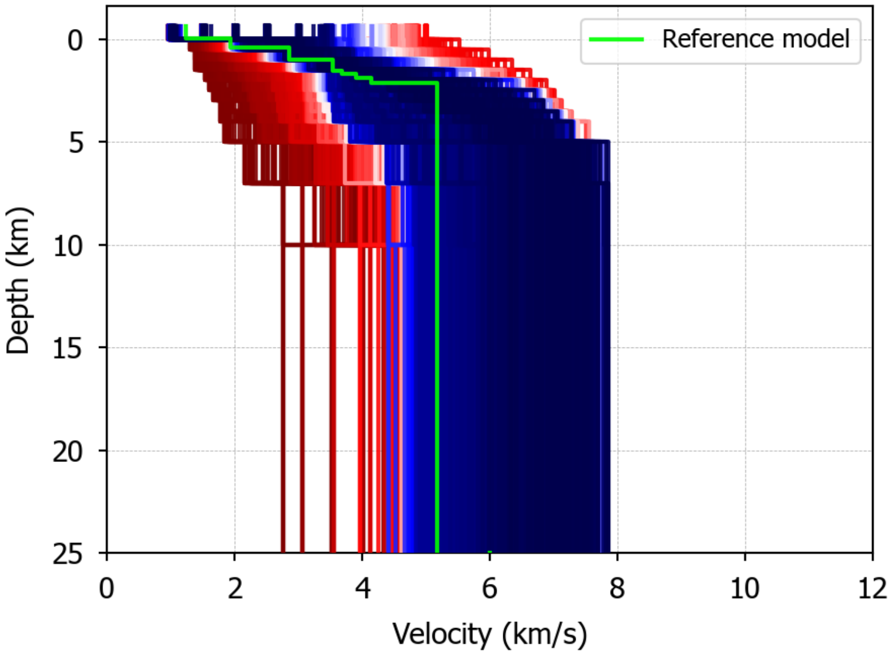

Figure 63: Final 1D velocity models obtained from the inversion of the initial velocity model data set. Blue color represents a higher probability to be the right model, in the sense that the RMS obtained between computed and observed travel times is minimum.

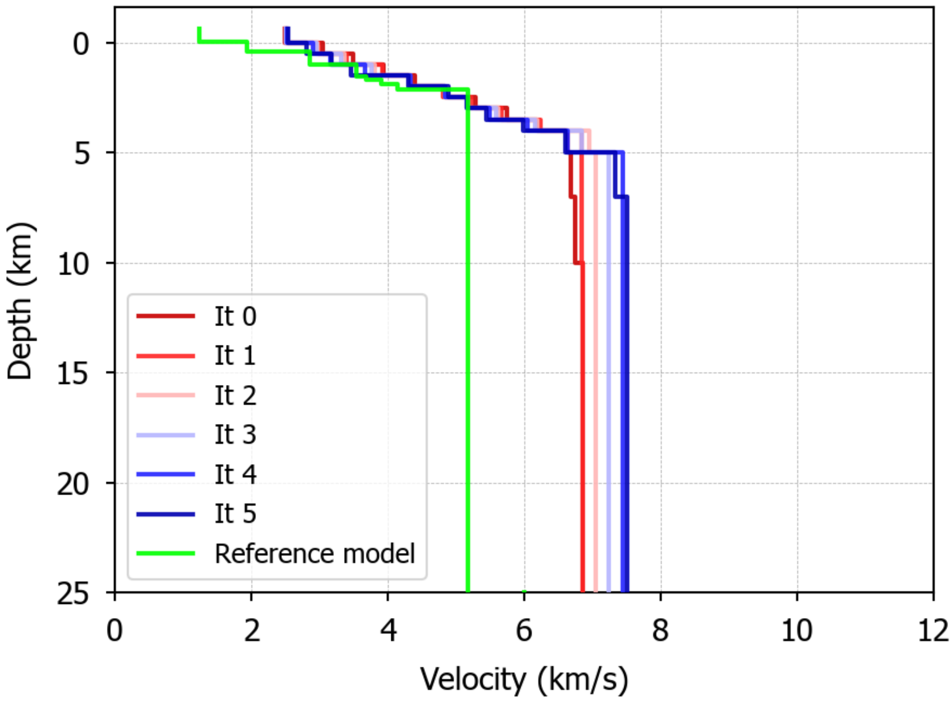

Figure 64: Best 1D velocity model obtained from the inversion of the data set. For each inversion, several iterations were performed. The "reference model" corresponds to Lermo, 2008.

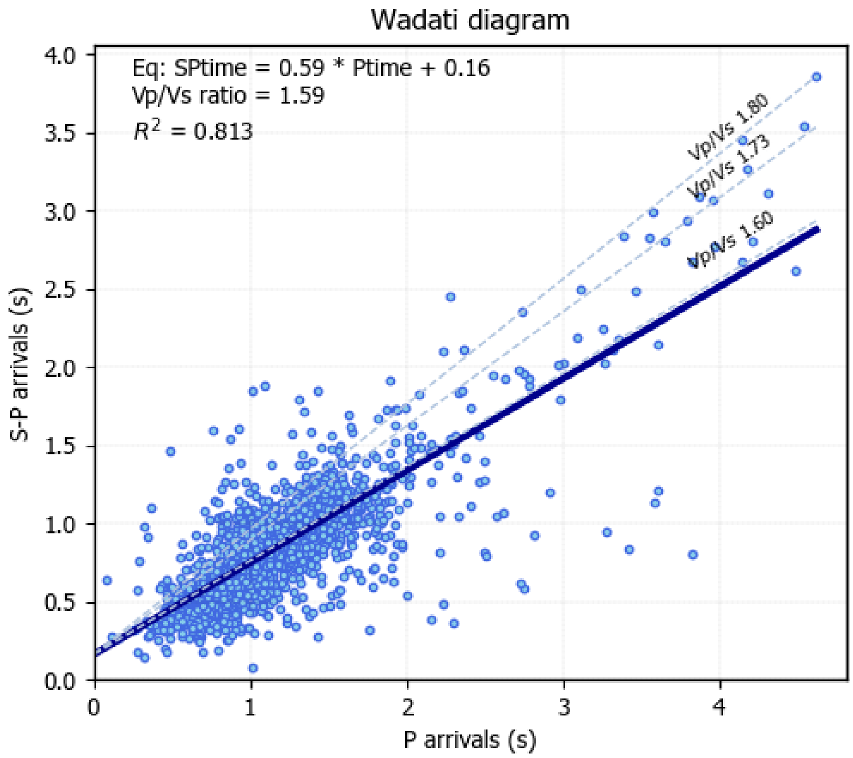

Figure 65: The Wadati diagram (Wadati, 1933) allows us to check whether there are wrong picks and to derive a first Vp/Vs ratio, useful for the 3D inversion.

The seismic event hypocentre location is given in Figure 66, Figure 67 and Figure 68. Most of the seismic events detected are located at the depth of the injection wells, suggesting that most of them are probably induced by the exploitation of the geothermal reservoir, and in particular the injection of used fluids. The zero reference hereby used corresponds to 2600 m above sea level.

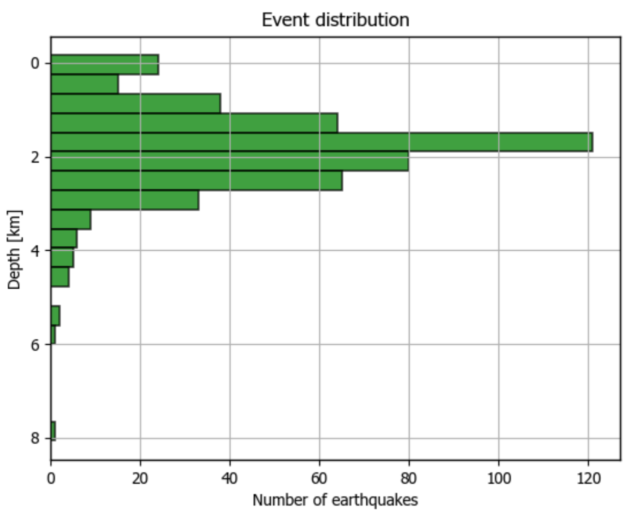

Figure 66: The seismic event distribution with depth

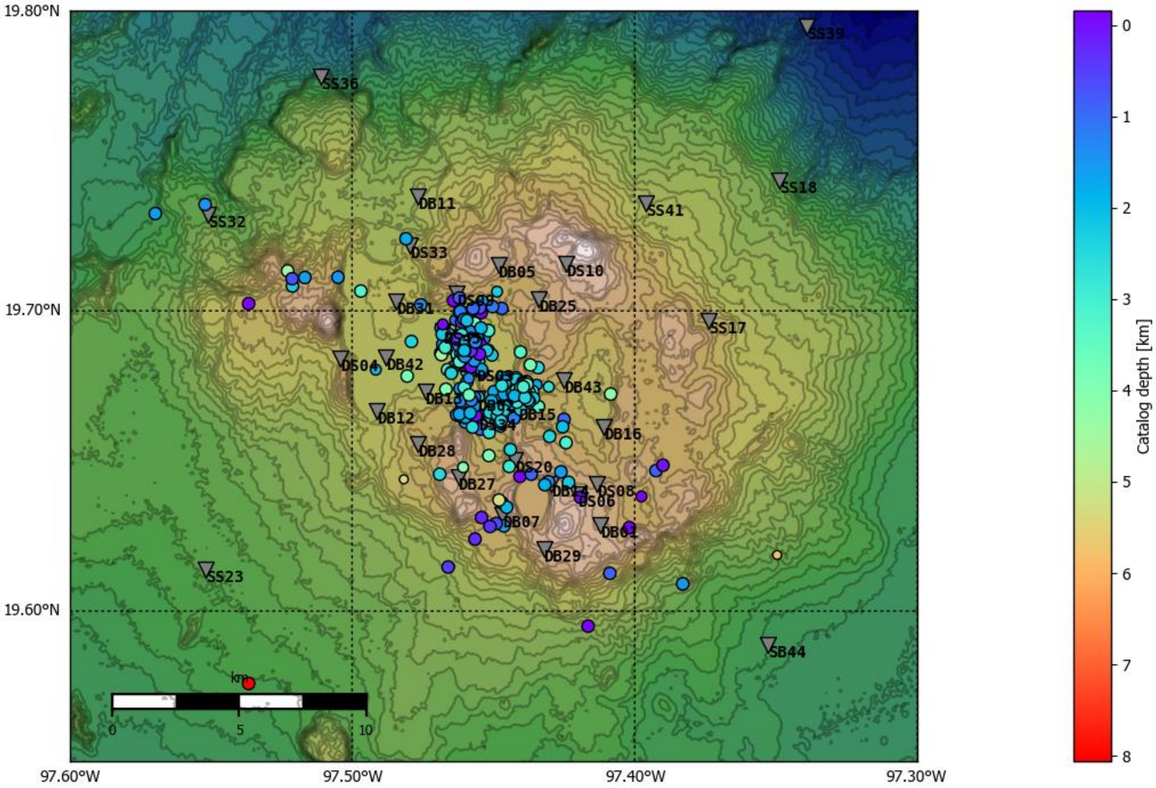

Figure 67: Map of the seismic event distribution

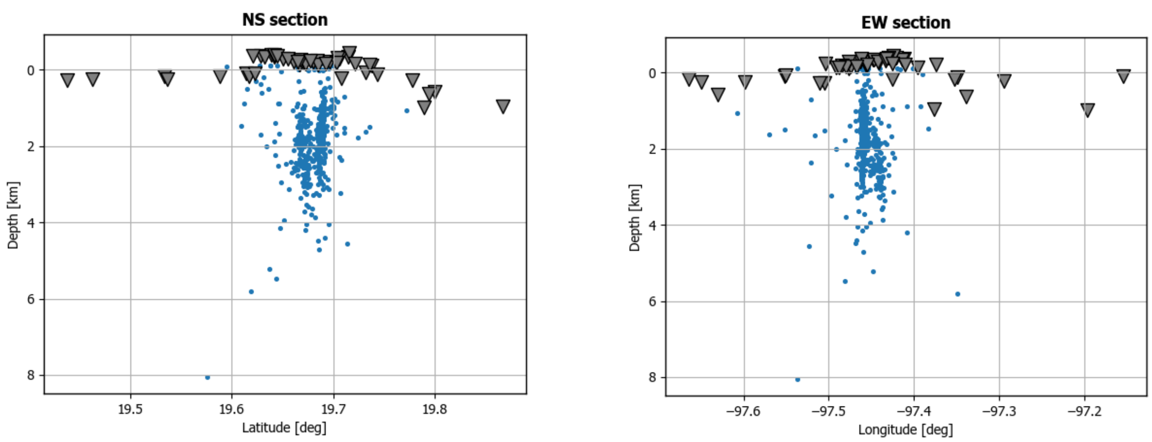

Figure 68: Two cross-sections showing the distribution of earthquakes with depth.

5.4.2 3D velocity model using SIMULPS

The 3D travel time tomography consists in finding lateral velocity variations that best explains the data after each cell of the underground parametrized by a 3D grid. The accuracy and resolution for each cell of the model depend on the number of rays (hypocentre-station) that crosses each cell. The rays for all earthquakes are plotted in Figure 69.

To prevent inversion instabilities a damping value is introduced. To determine the optimum damping values, a trade-off test is performed.

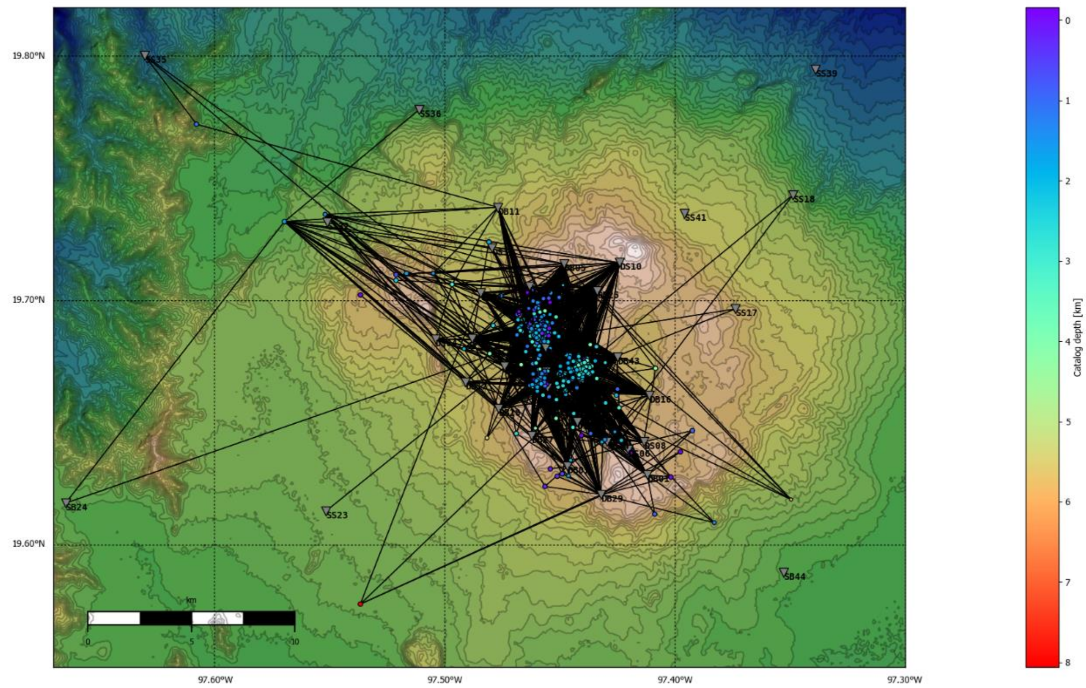

Figure 69: Ray paths computed from all earthquake position to all stations. From this figure, we may expect good resolution in the central part of the network, where the geothermal field resides.

The concept of a trade-off curve consists in adjusting and selecting a damping parameter that reduces the data variance as much as possible, without deteriorating the model validity. If we try to explain the data as good as possible, then the model would fit perfectly data, which makes the RMS (Root Mean Square) of the data very low, however the model found may be unrealistic (too large oscillations in velocities that do not correspond to geological reality). On the other hand, damping too much the inversion may help finding a model that is more realistic, but data may not be explained satisfactorily.

We performed the trade-off curve for 2 inversion steps. First, we perform this to find the Vp model, while holding the Vp/Vs ratio constant (large damping value). Then once the Vp model is found, we perform a Vp/Vs ratio inversion or Vp and Vs inversion by computing a trade-off curve once more. Both the Vp model and the Vp/Vs ratio are indicative parameters for structures and presence of fluids.

A catalogue of 472 earthquakes (reported on the VRE website) is used as input, with 2970 P-picks and 3871 S-picks. The number of S picks is larger, which is typical for geothermal reservoir seismic observations.

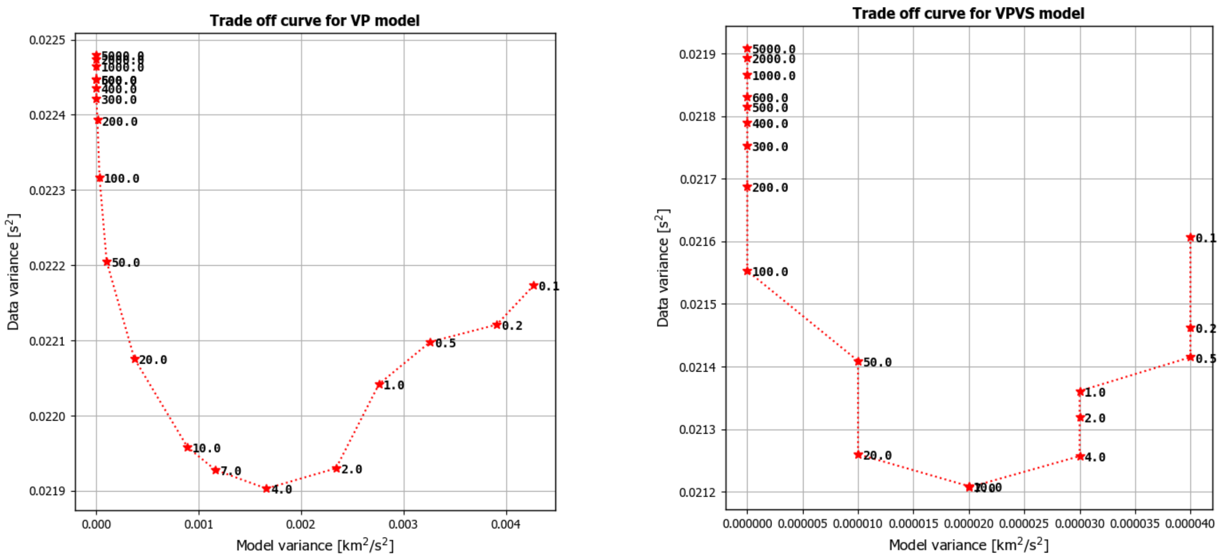

a. b.

Figure 70: a. Trade-off curve between data variance and model variance for different damping values, indicating that the damping value that need to be taken for the inversion for Vp is around 4 to 7. b. Trade-off curve between data variance and model variance for different damping values, indicating that the damping value that need to be taken for the inversion of Vp/Vs ratio is around 10 to 20.

The results obtained after the inversion are a distribution of P-wave velocity, Vp/Vs values, and earthquake locations, that jointly minimizes the misfit between observed and computed arrival times, in the least square sense. The computed travel times between hypocenter and stations are obtained using ray theory (e.g., Cerveny, 2005).

Figure 71 to Figure 75 represent the results of the travel time tomography for Vp. Dots are earthquake hypocenters. Figure 71 is the Vp distribution at different depths. We see a clear distinction between the North-West and the South-East of the area. In the North-West a high Vp anomaly is observed with velocities for example 5300 m/s at 2 km depth. In the South-East the anomalies are lower velocities for example 4800 m/s at 2 km depth. Resolutions are given in Figure 72. The resolution is fine within the area (delimited by the red line) where the resolution is good. The spread value in Figure 73 indicates how the values are focused and accurate in space. The larger the spread value is, the lower accurate in space the results are. The spread value is lower in the centre of the area, where more rays are present. Finally, Figure 74 and Figure 75 show a cross section and a 3D view of the tomographic results.

Figure 76 to Figure 81 represent similar observations for the resulting Vp/Vs ratio. The Vp/Vs results are also concentrated in the central area where earthquakes occurred. Similarly than for the Vp anomalies results, Vp/Vs ratio slices at different depth reveal a similar structure, i.e., a North-West area where Vp/Vs is higher, around 1.76, and a South-east where Vp/Vs is smaller, i.e., 1.72.

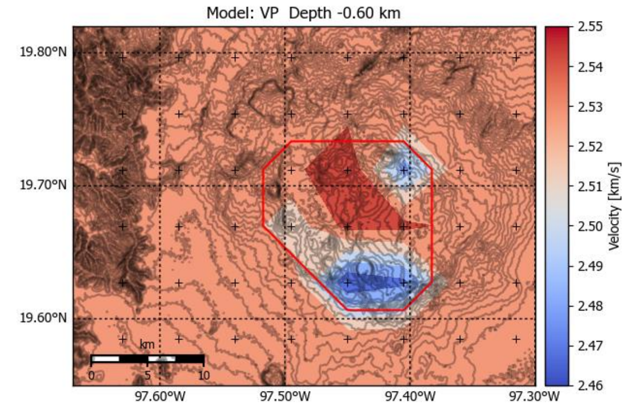
Model: VP Depth -0.60 km
19.80°N
19.70°N
19.60°N
97.60°W
97.50°W
97.40°W
97.30°W
km
0 5 10
Velocity [km/s]
2.55 2.54 2.53 2.52 2.51 2.50 2.49 2.48 2.47 2.46

a.

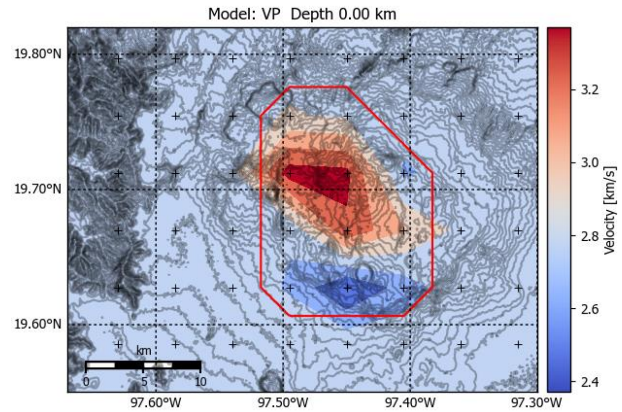
Model: VP Depth 0.00 km
19.80°N
19.70°N
19.60°N
97.60°W
97.50°W
97.40°W
97.30°W
km
0 5 10
Velocity [km/s]
3.2 3.0 2.8 2.6 2.4

b.

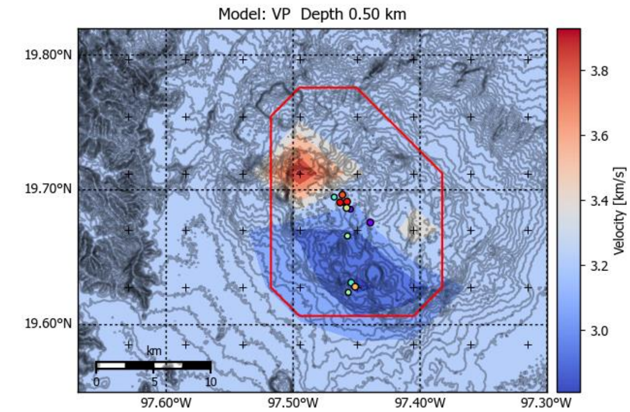
Model: VP Depth 0.50 km
19.80°N
19.70°N
19.60°N
97.60°W
97.50°W
97.40°W
97.30°W
km
0 5 10
Velocity [km/s]
3.8 3.6 3.4 3.2 3.0

c.

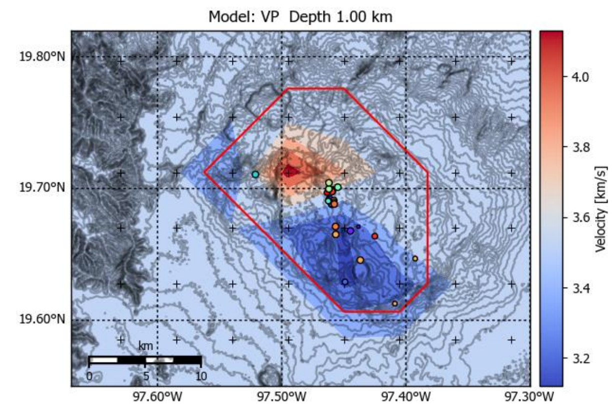
Model: VP Depth 1.00 km
19.80°N
19.70°N
19.60°N
97.60°W
97.50°W
97.40°W
97.30°W
km
0 5 10
Velocity [km/s]
4.0 3.8 3.6 3.4 3.2

d.

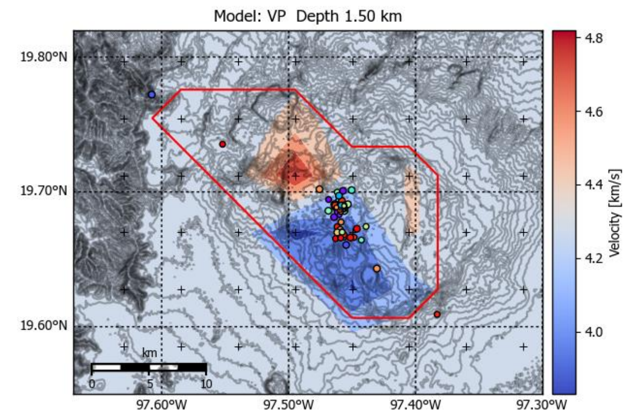
Model: VP Depth 1.50 km
19.80°N
19.70°N
19.60°N
97.60°W
97.50°W
97.40°W
97.30°W
km
0 5 10
Velocity [km/s]
4.8 4.6 4.4 4.2 4.0

e.

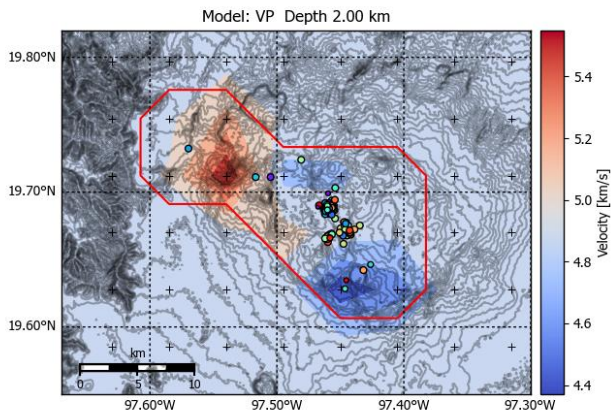
Model: VP Depth 2.00 km
19.80°N
19.70°N
19.60°N
97.60°W
97.50°W
97.40°W
97.30°W
km
0 5 10
Velocity [km/s]
5.4 5.2 5.0 4.8 4.6 4.4

f.

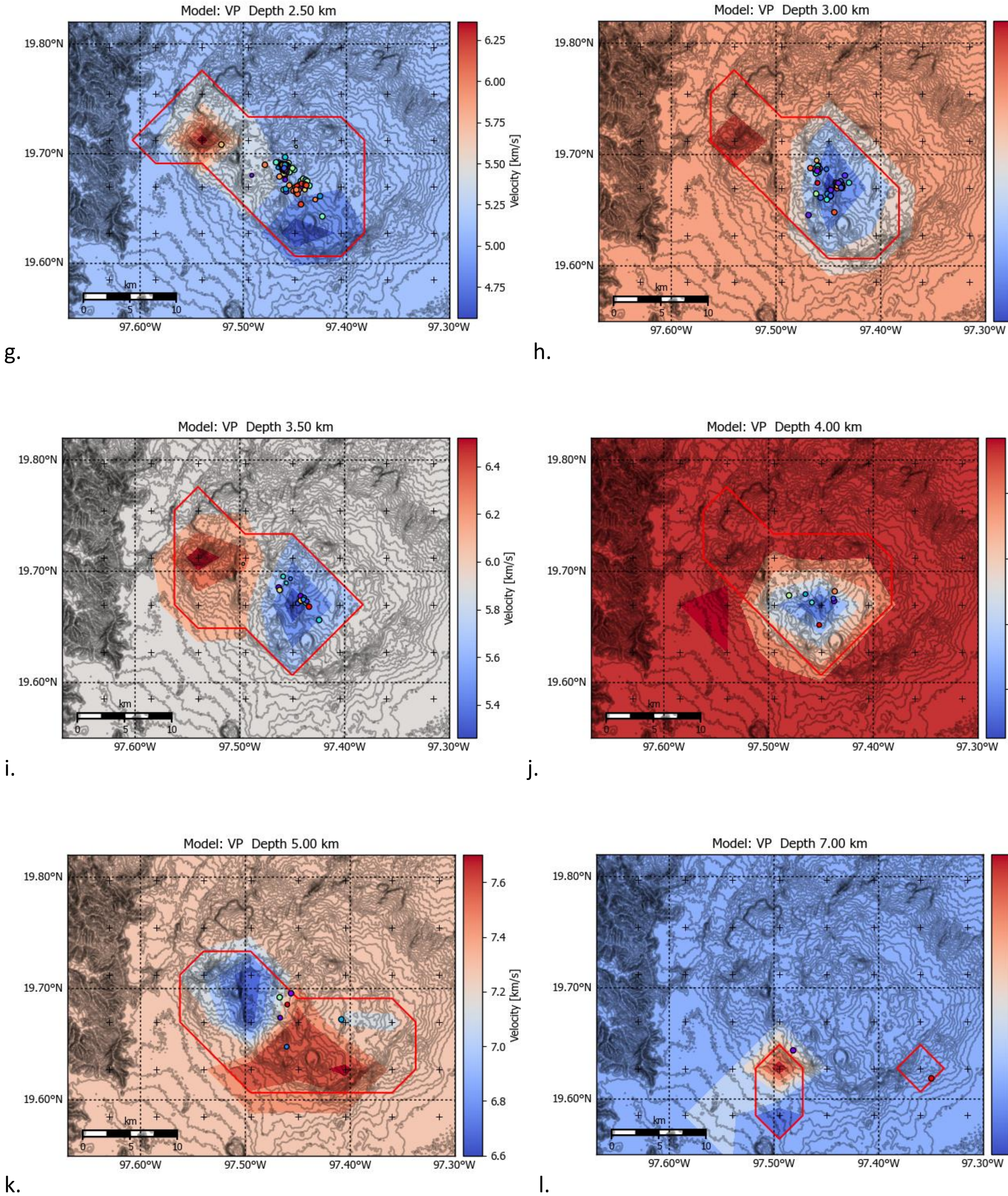

Figure 71: Results of the 3D travel time tomography for several horizontal slices. The resolutions are given in the Figure 72 and Fehler! Verweisquelle konnte nicht gefunden werden.**. We find that there is a high Vp anomaly in the north-west of the area and a low Vp anomaly in the South-east for most depths. a. to l.: different depths. The red line represent the limit where the resolution is the highest. In this area, results can be trusted, whereas outside the area, the resolution is low. The black crosses indicate location of the grid of the parametrisation of the model (every 5 km in this case).**

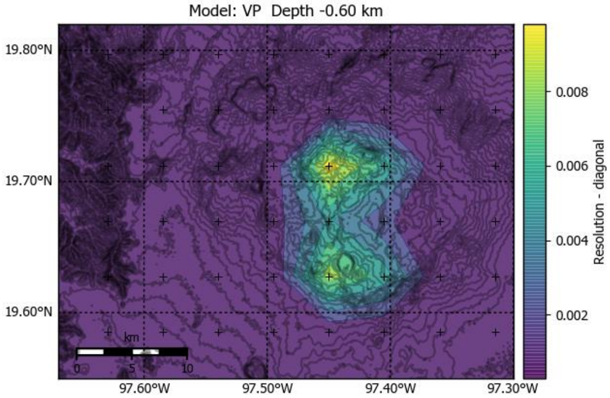
Model: VP Depth -0.60 km
19.80°N
19.70°N
19.60°N
97.60°W
97.50°W
97.40°W
97.30°W
km
0
5
10
0.008
0.006
0.004
0.002
Resolution - diagonal
a.

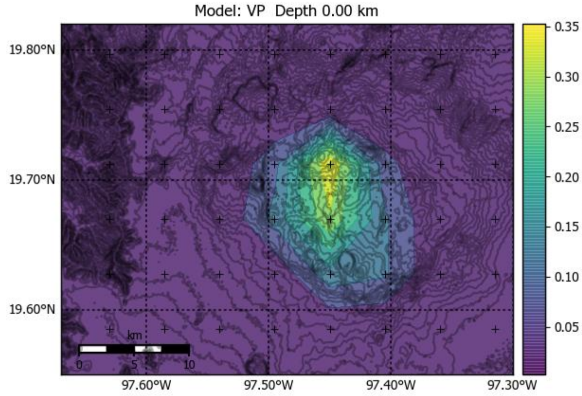
Model: VP Depth 0.00 km
19.80°N
19.70°N
19.60°N
97.60°W
97.50°W
97.40°W
97.30°W
km
0
5
10
0.35
0.30
0.25
0.20
0.15
0.10
0.05
Resolution - diagonal
b.

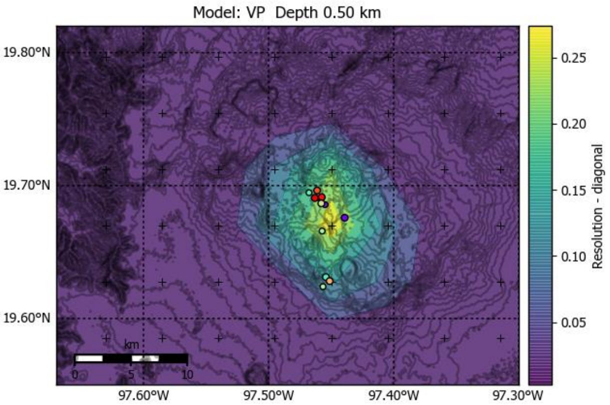
Model: VP Depth 0.50 km
19.80°N
19.70°N
19.60°N
97.60°W
97.50°W
97.40°W
97.30°W
km
0
5
10
0.25
0.20
0.15
0.10
0.05
Resolution - diagonal
c.

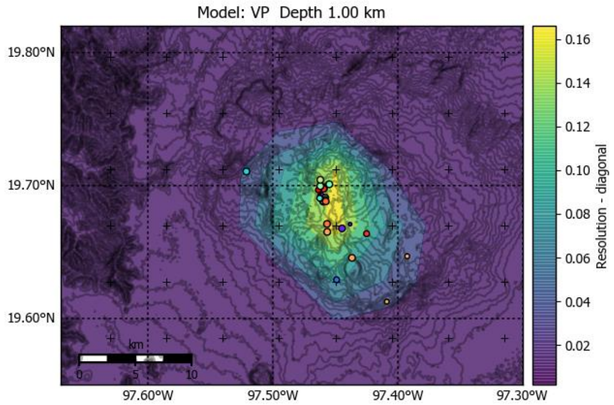
Model: VP Depth 1.00 km
19.80°N
19.70°N
19.60°N
97.60°W
97.50°W
97.40°W
97.30°W
km
0
5
10
0.16
0.14
0.12
0.10
0.08
0.06
0.04
0.02
Resolution - diagonal
d.

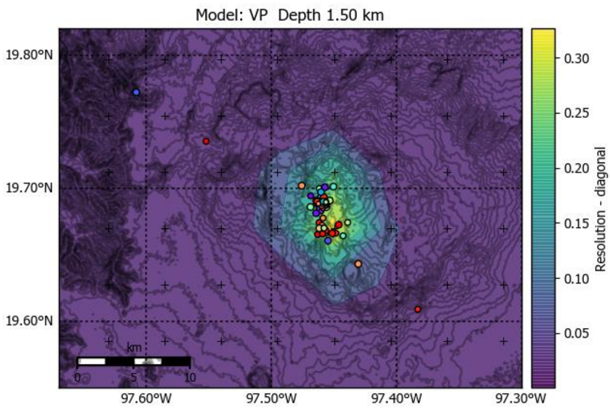
Model: VP Depth 1.50 km
19.80°N
19.70°N
19.60°N
97.60°W
97.50°W
97.40°W
97.30°W
km
0
5
10
0.30
0.25
0.20
0.15
0.10
0.05
Resolution - diagonal
e.

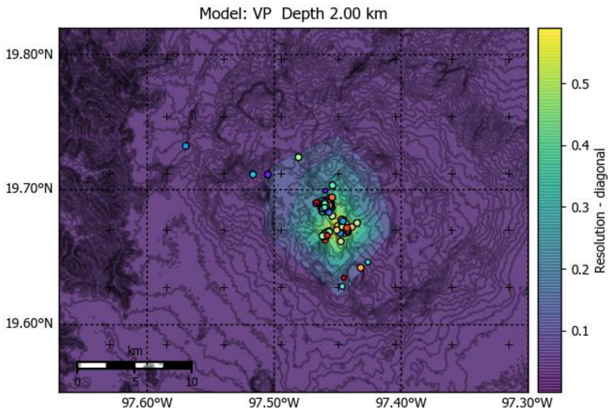
Model: VP Depth 2.00 km
19.80°N
19.70°N
19.60°N
97.60°W
97.50°W
97.40°W
97.30°W
km
0
5
10
0.5
0.4
0.3
0.2
0.1
Resolution - diagonal
f.

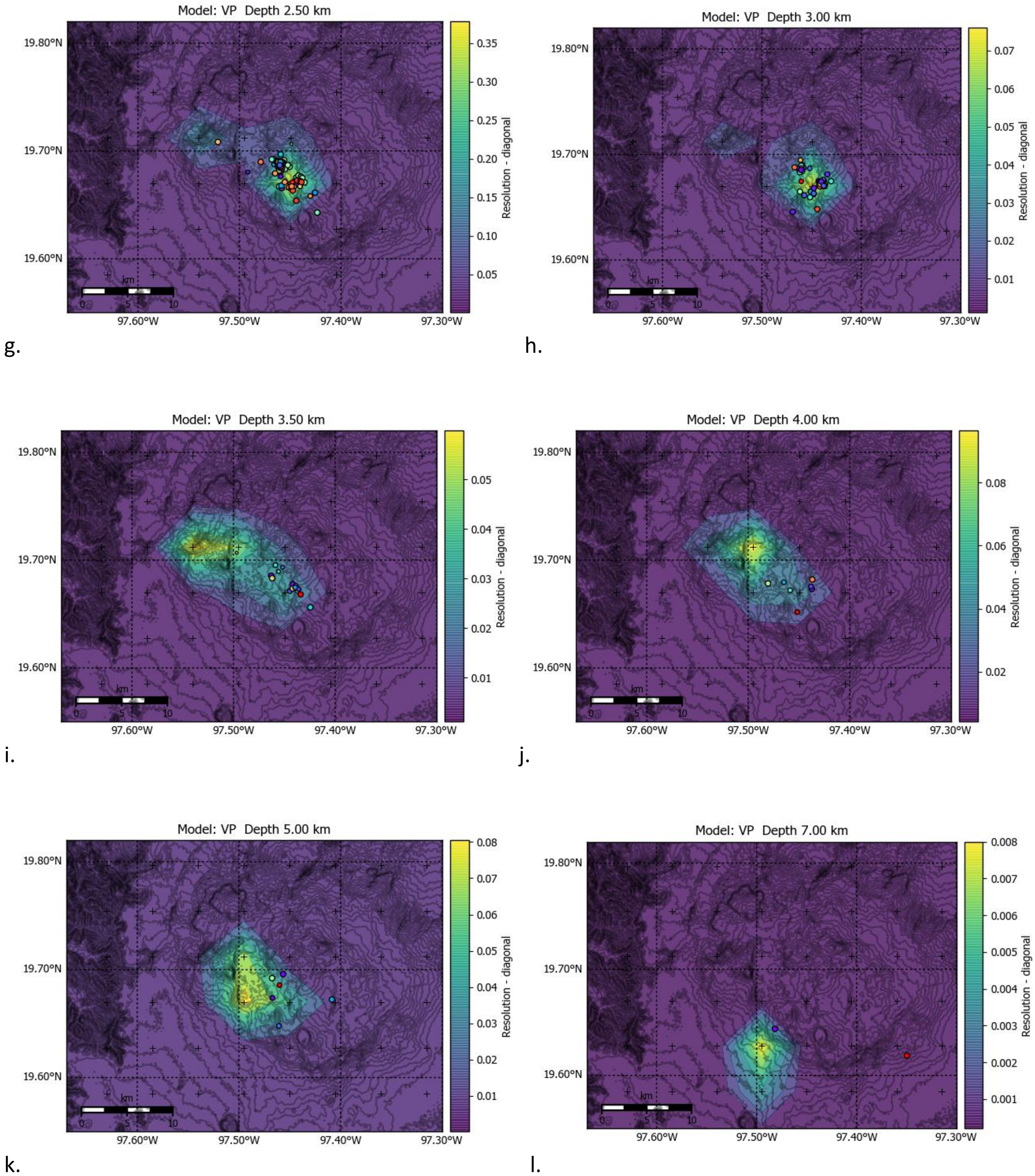

Figure 72: Diagonal values of the resolution matrix for the velocities maps obtained in Figure 71.

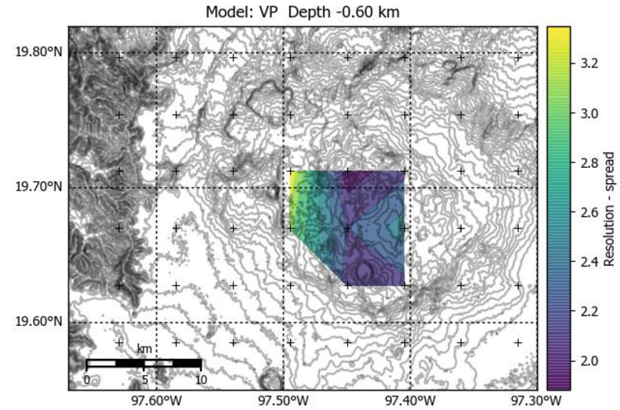
Model: VP Depth -0.60 km
19.80°N
19.70°N
19.60°N
97.60°W
97.50°W
97.40°W
97.30°W
km
0
5
10
Resolution - spread
3.2
3.0
2.8
2.6
2.4
2.2
2.0

a.

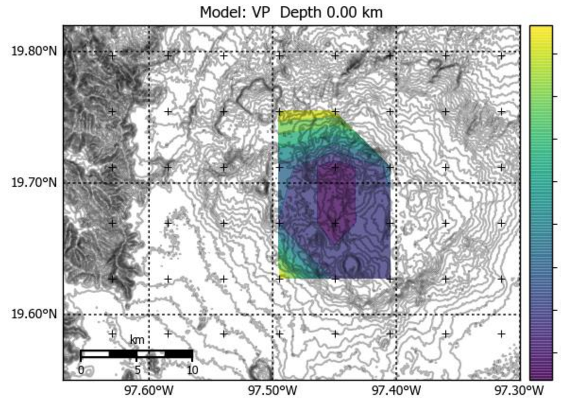
Model: VP Depth 0.00 km
19.80°N
19.70°N
19.60°N
97.60°W
97.50°W
97.40°W
97.30°W
km
0
5
10
Resolution - spread
2.6
2.4
2.2
2.0
1.8
1.6
1.4
1.2

b.

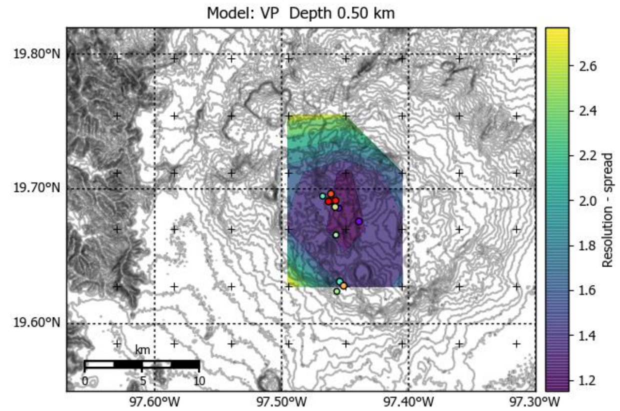
Model: VP Depth 0.50 km
19.80°N
19.70°N
19.60°N
97.60°W
97.50°W
97.40°W
97.30°W
km
0
5
10
Resolution - spread
2.6
2.4
2.2
2.0
1.8
1.6
1.4
1.2

c.

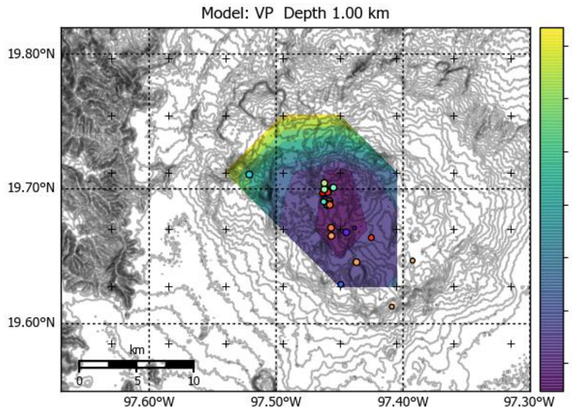
Model: VP Depth 1.00 km
19.80°N
19.70°N
19.60°N
97.60°W
97.50°W
97.40°W
97.30°W
km
0
5
10
Resolution - spread
2.6
2.4
2.2
2.0
1.8
1.6
1.4

d.

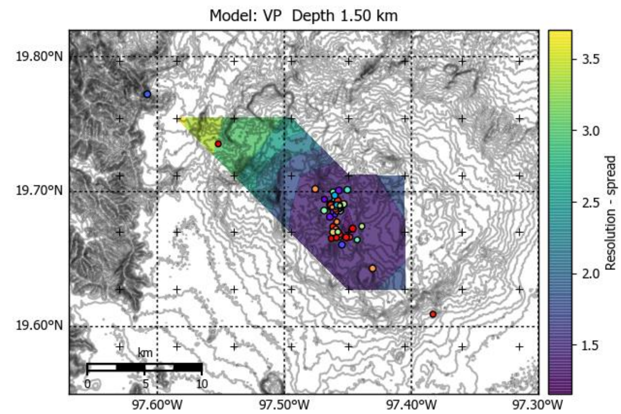
Model: VP Depth 1.50 km
19.80°N
19.70°N
19.60°N
97.60°W
97.50°W
97.40°W
97.30°W
km
0
5
10
Resolution - spread
3.5
3.0
2.5
2.0
1.5

e.

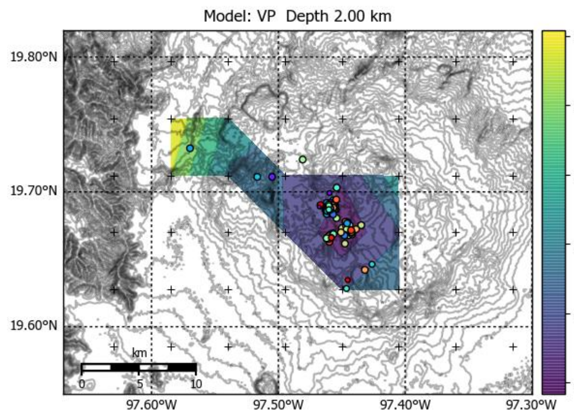
Model: VP Depth 2.00 km
19.80°N
19.70°N
19.60°N
97.60°W
97.50°W
97.40°W
97.30°W
km
0
5
10
Resolution - spread
3.5
3.0
2.5
2.0
1.5
1.0

f.

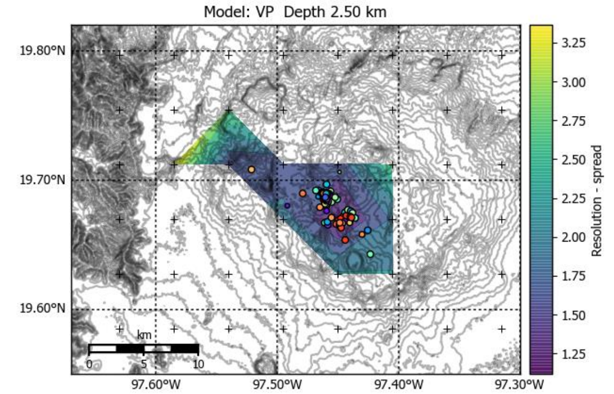

g.

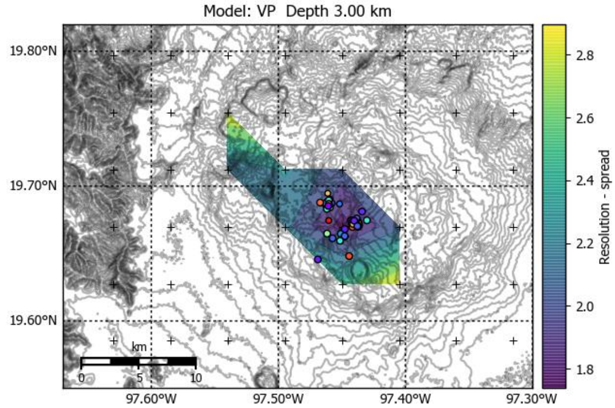

h.

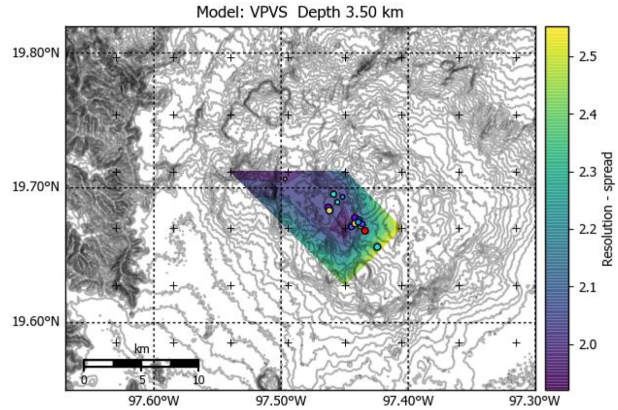

i.

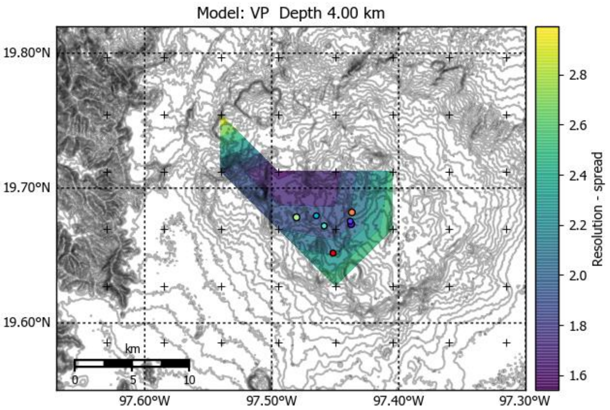

j.

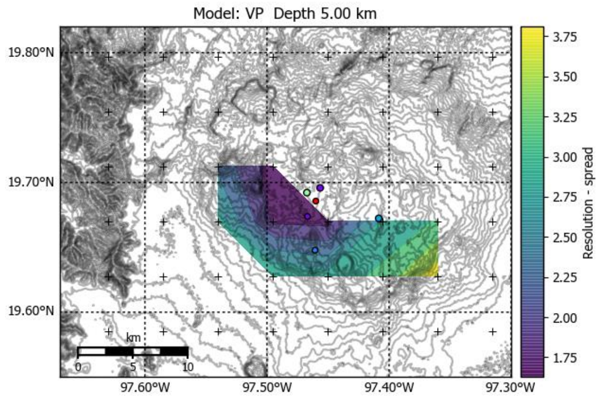

k.

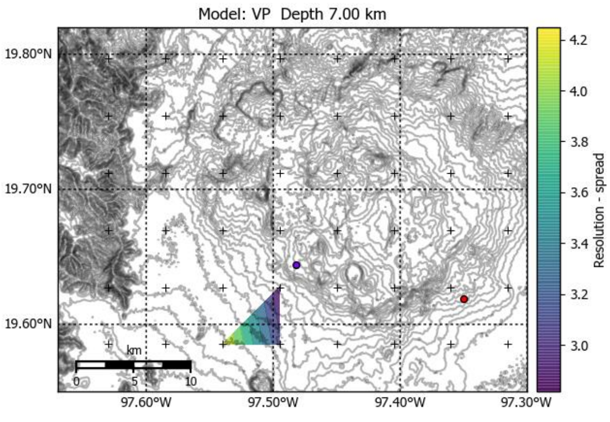

l.

Figure 73: Spread value (off diagonal terms) obtained from the tomography.

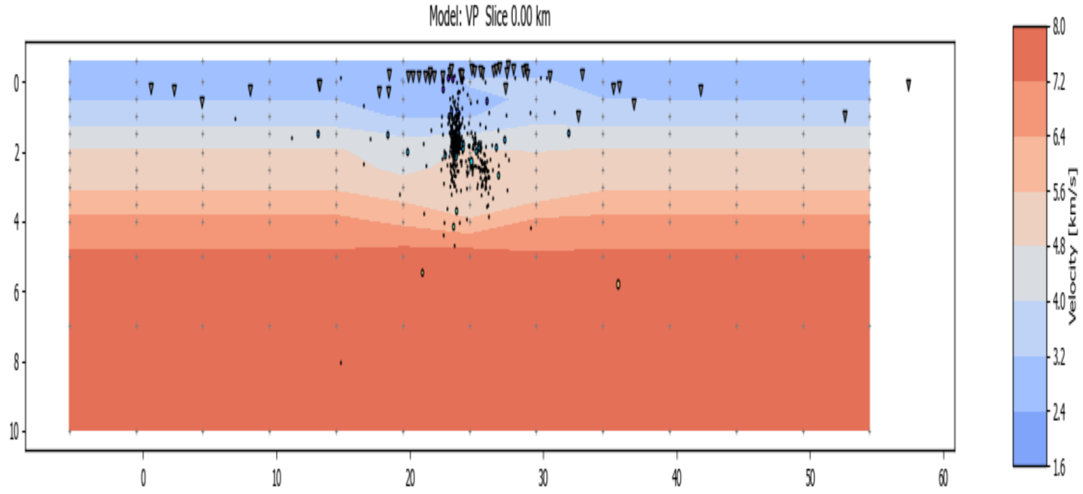

Figure 74: Cross-section of the 3D VP model (NS)

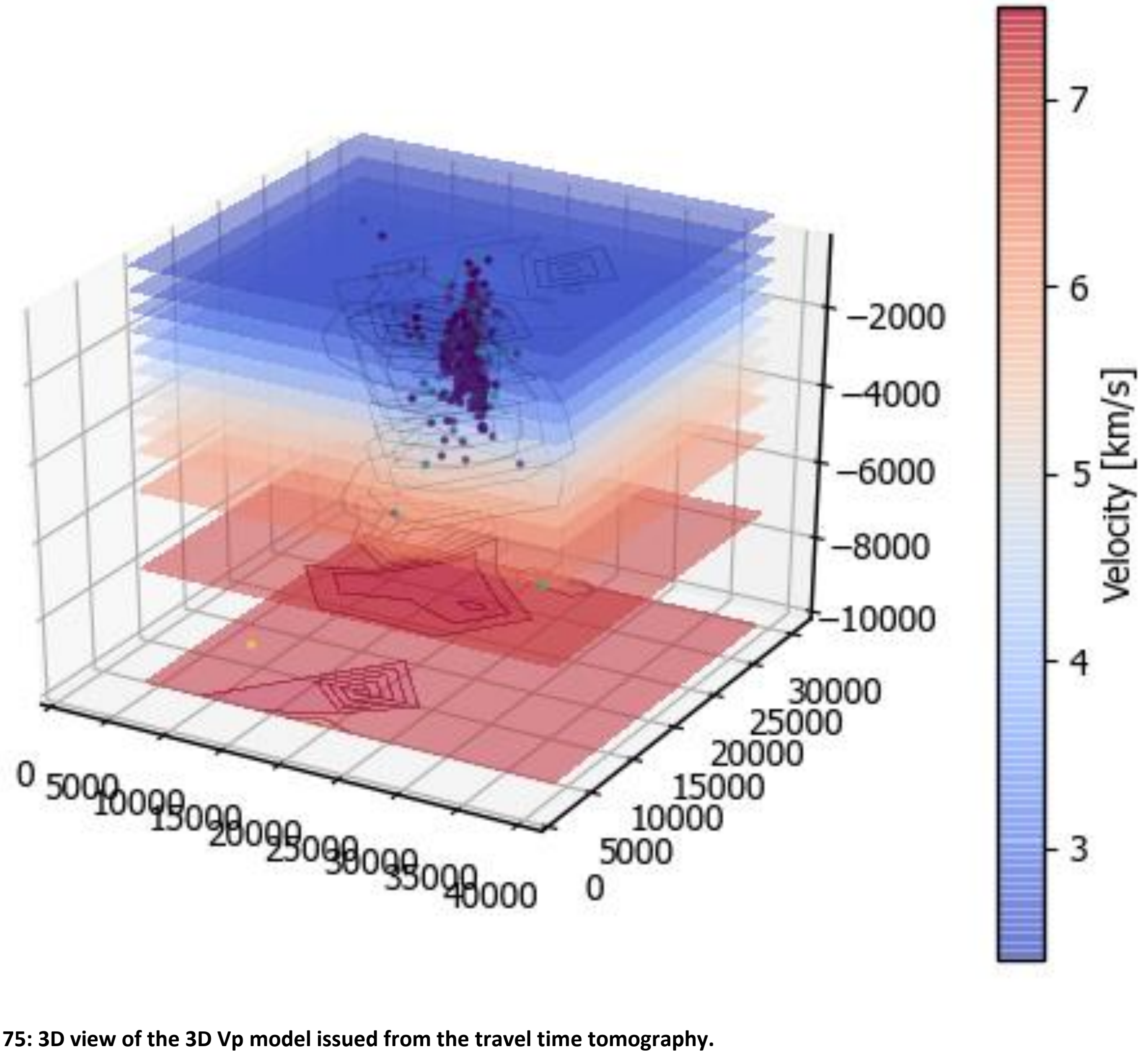

Figure 75: 3D view of the 3D Vp model issued from the travel time tomography.

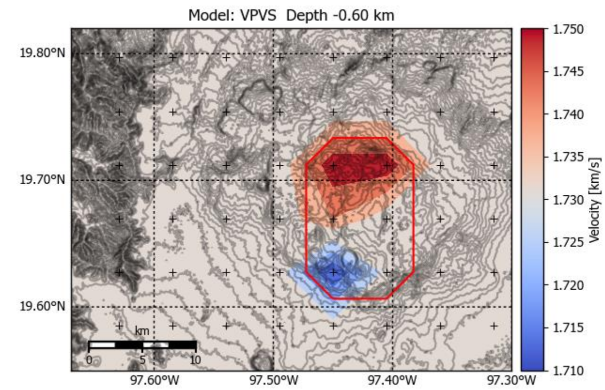
Model: VPVS Depth -0.60 km
19.80°N
19.70°N
19.60°N
97.60°W
97.50°W
97.40°W
97.30°W
km
0
5
10
1.750
1.745
1.740
1.735
1.730
1.725
1.720
1.715
1.710
Velocity [km/s]

a.

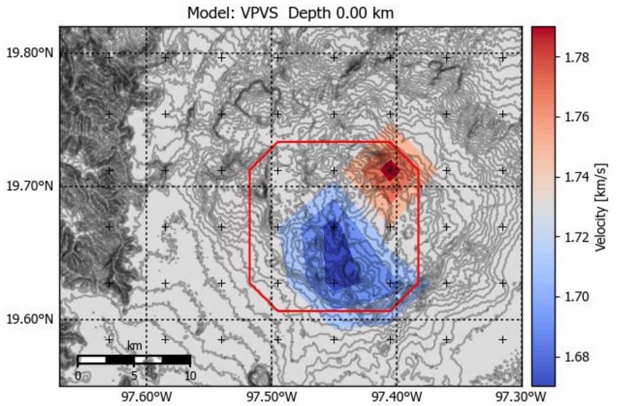
Model: VPVS Depth 0.00 km
19.80°N
19.70°N
19.60°N
97.60°W
97.50°W
97.40°W
97.30°W
km
0
5
10
1.78
1.76
1.74
1.72
1.70
1.68
Velocity [km/s]

b.

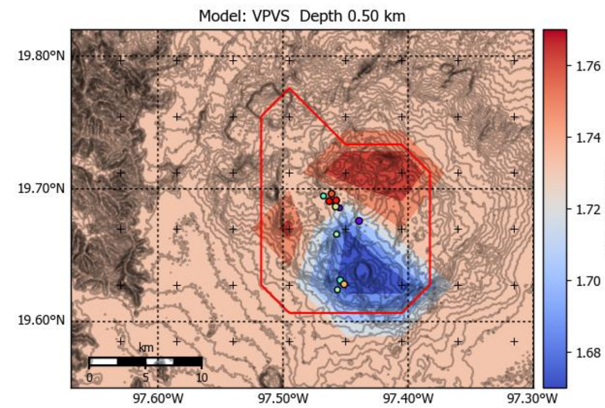
Model: VPVS Depth 0.50 km
19.80°N
19.70°N
19.60°N
97.60°W
97.50°W
97.40°W
97.30°W
km
0
5
10
1.76
1.74
1.72
1.70
1.68
Velocity [km/s]

c.

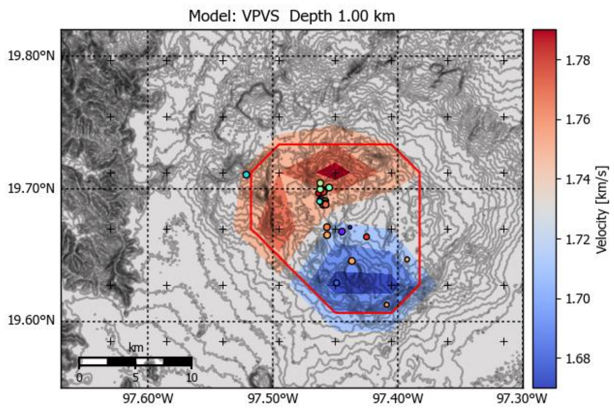
Model: VPVS Depth 1.00 km
19.80°N
19.70°N
19.60°N
97.60°W
97.50°W
97.40°W
97.30°W
km
0
5
10
1.78
1.76
1.74
1.72
1.70
1.68
Velocity [km/s]

d.

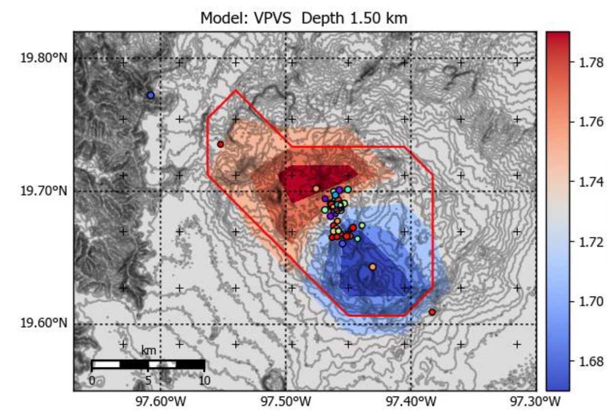
Model: VPVS Depth 1.50 km
19.80°N
19.70°N
19.60°N
97.60°W
97.50°W
97.40°W
97.30°W
km
0
5
10
1.78
1.76
1.74
1.72
1.70
1.68
Velocity [km/s]

e.

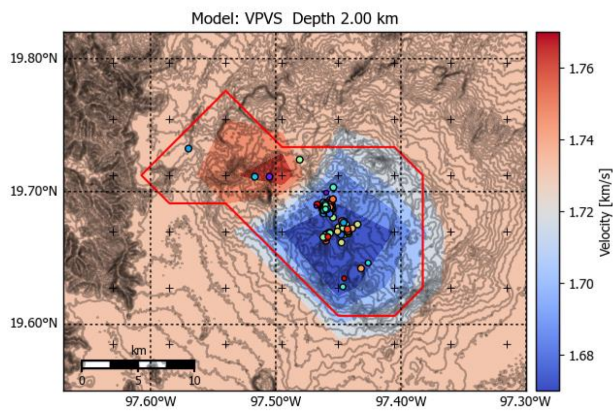
Model: VPVS Depth 2.00 km
19.80°N
19.70°N
19.60°N
97.60°W
97.50°W
97.40°W
97.30°W
km
0
5
10
1.76
1.74
1.72
1.70
1.68
Velocity [km/s]

f.

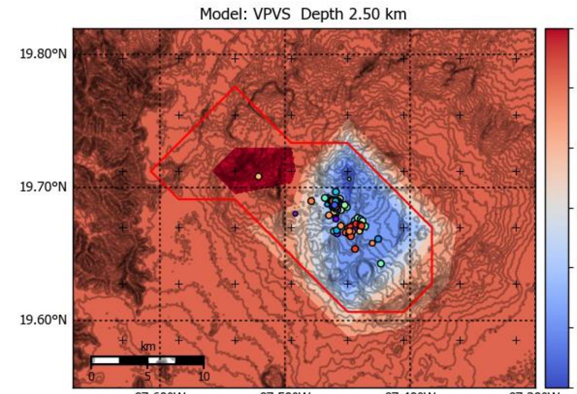

g.

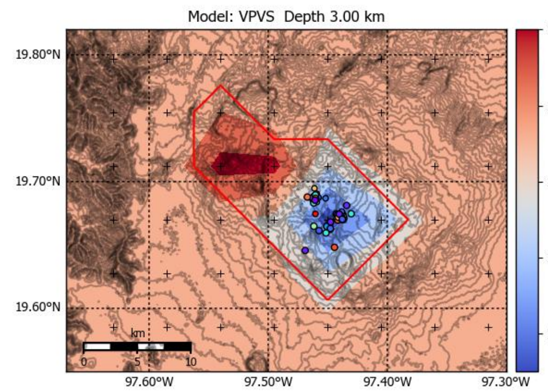

h.

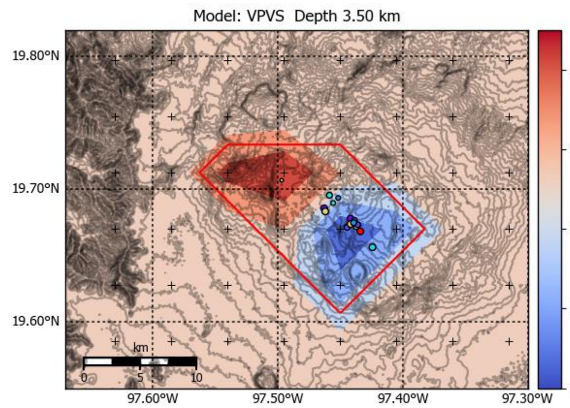

i.

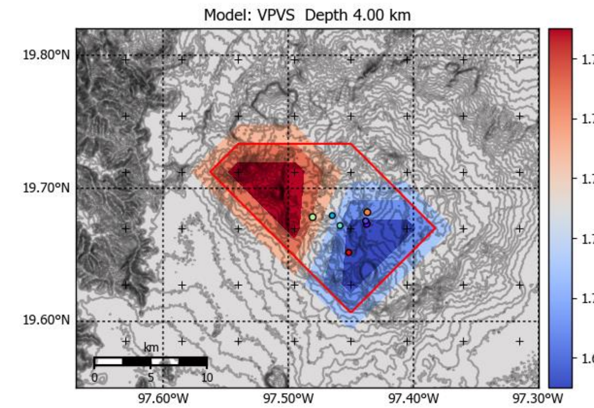

j.

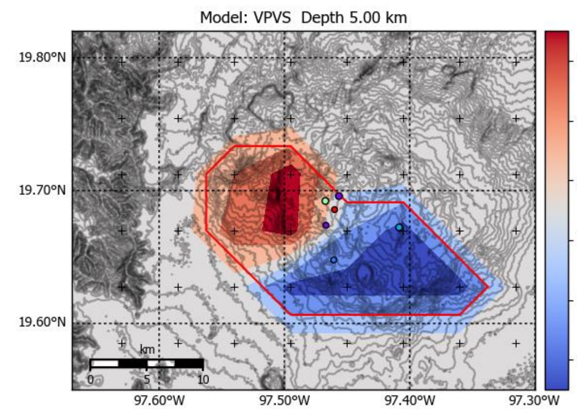

k.

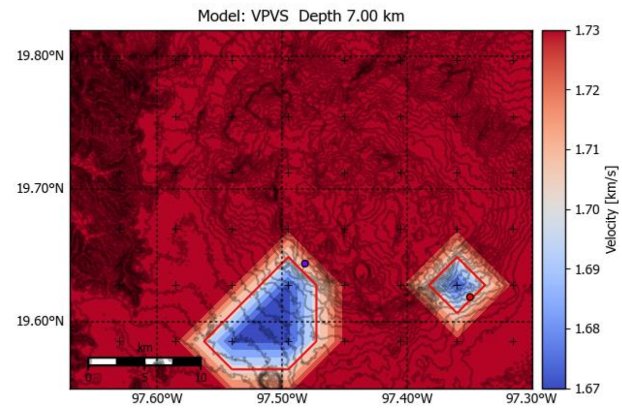

l.

Figure 76: Results of the 3D tomography for VP/VS ratio. The lines represent the area where the resolution is good.

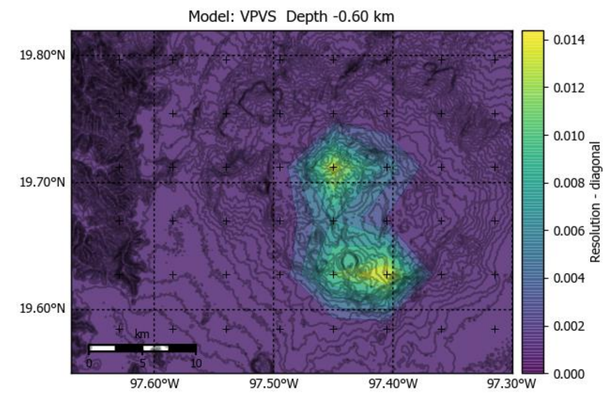
Model: VPVS Depth -0.60 km
19.80°N
19.70°N
19.60°N
97.60°W
97.50°W
97.40°W
97.30°W
Resolution - diagonal
0.014
0.012
0.010
0.008
0.006
0.004
0.002
0.000
km
0
5
10

a.

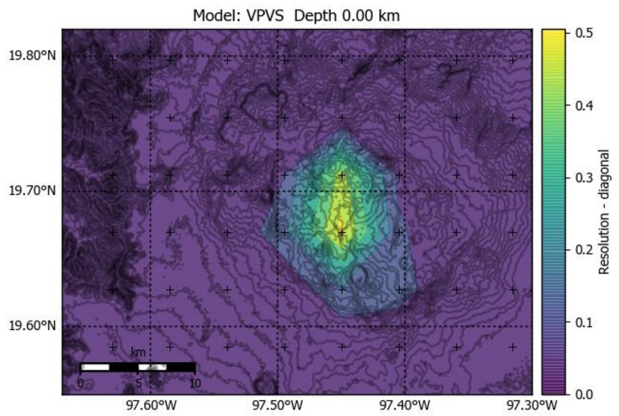
Model: VPVS Depth 0.00 km
19.80°N
19.70°N
19.60°N
97.60°W
97.50°W
97.40°W
97.30°W
Resolution - diagonal
0.5
0.4
0.3
0.2
0.1
0.0
km
0
5
10

b.

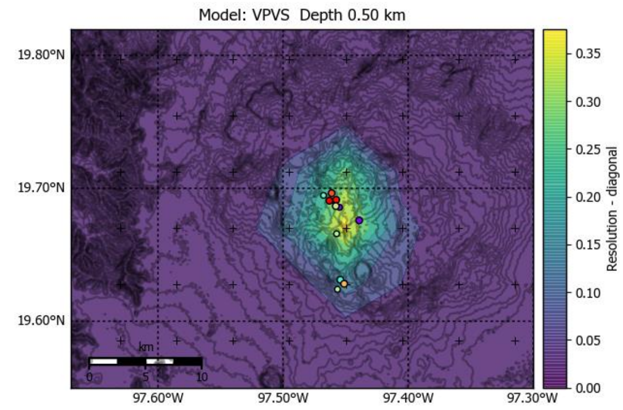
Model: VPVS Depth 0.50 km
19.80°N
19.70°N
19.60°N
97.60°W
97.50°W
97.40°W
97.30°W
Resolution - diagonal
0.35
0.30
0.25
0.20
0.15
0.10
0.05
0.00
km
0
5
10

c.

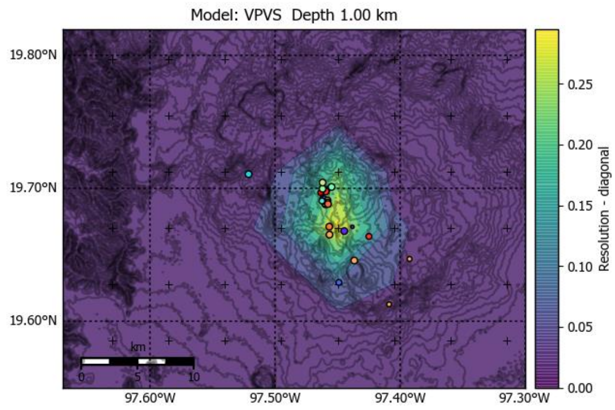
Model: VPVS Depth 1.00 km
19.80°N
19.70°N
19.60°N
97.60°W
97.50°W
97.40°W
97.30°W
Resolution - diagonal
0.25
0.20
0.15
0.10
0.05
0.00
km
0
5
10

d.

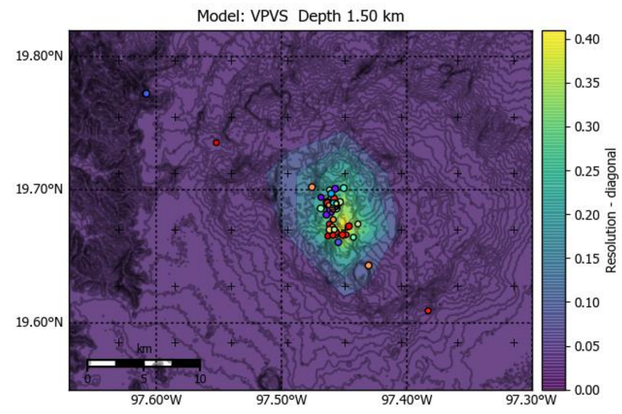
Model: VPVS Depth 1.50 km
19.80°N
19.70°N
19.60°N
97.60°W
97.50°W
97.40°W
97.30°W
Resolution - diagonal
0.40
0.35
0.30
0.25
0.20
0.15
0.10
0.05
0.00
km
0
5
10

e.

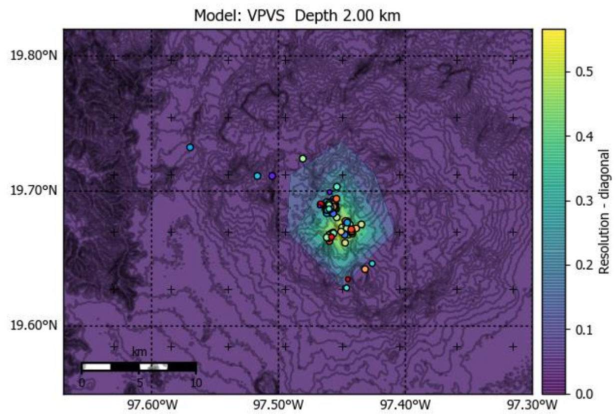
Model: VPVS Depth 2.00 km
19.80°N
19.70°N
19.60°N
97.60°W
97.50°W
97.40°W
97.30°W
Resolution - diagonal
0.5
0.4
0.3
0.2
0.1
0.0
km
0
5
10

f.

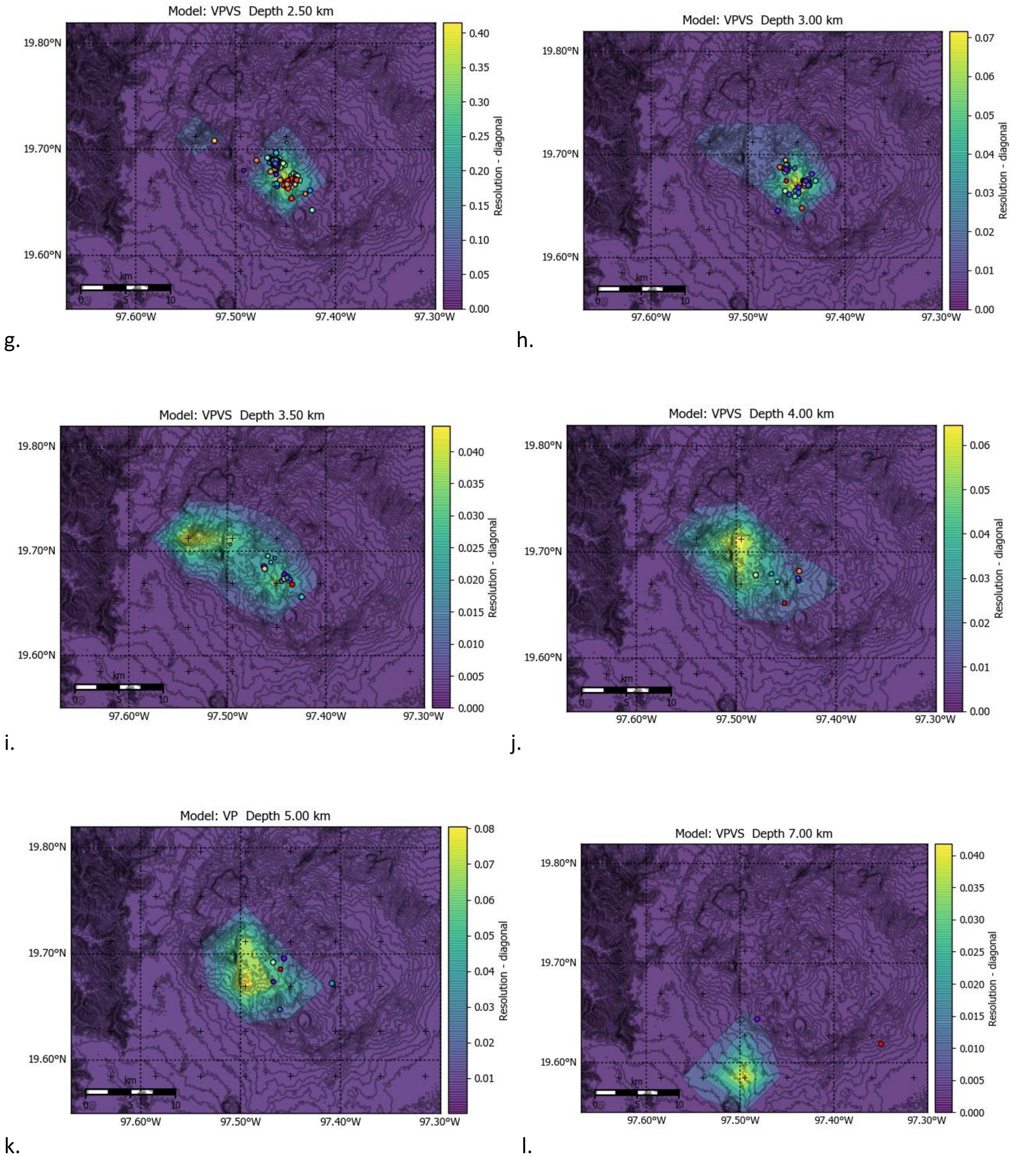

Figure 77: Diagonal values of the resolution matrix for similar depths as previous figures.

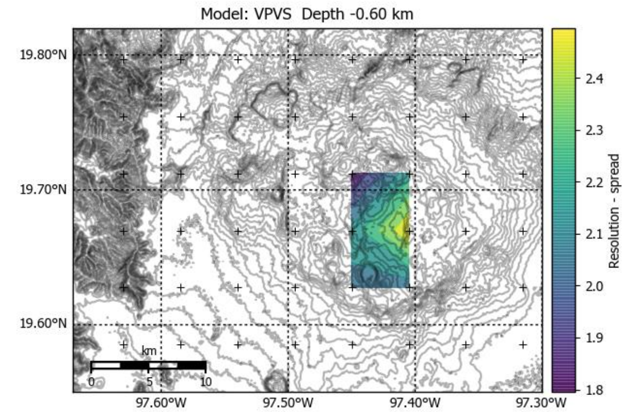
Model: VPVS Depth -0.60 km
Resolution - spread
km

a.

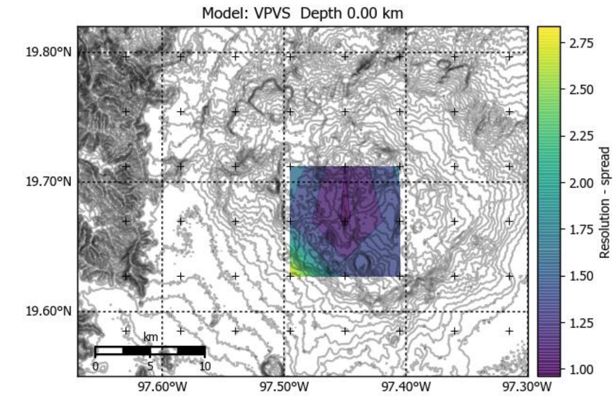
Model: VPVS Depth 0.00 km
Resolution - spread
km

b.

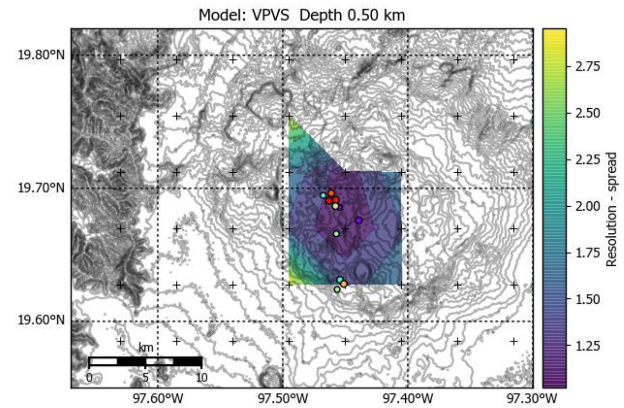
Model: VPVS Depth 0.50 km
Resolution - spread
km

c.

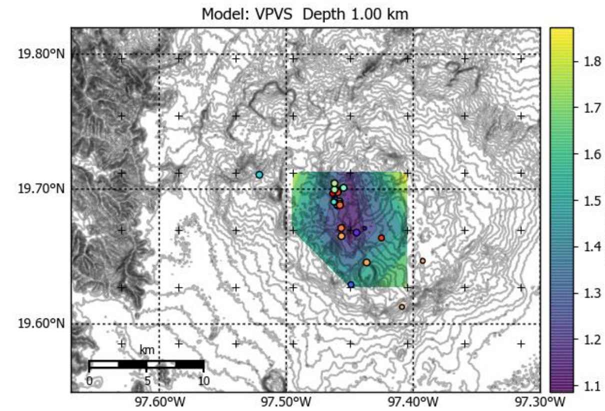
Model: VPVS Depth 1.00 km
Resolution - spread
km

d.

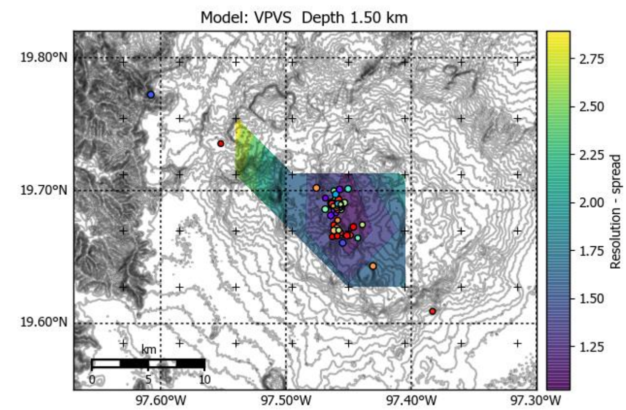
Model: VPVS Depth 1.50 km
Resolution - spread
km

e.

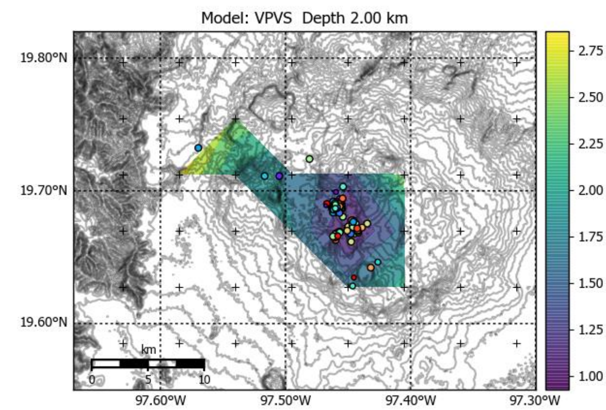
Model: VPVS Depth 2.00 km
Resolution - spread
km

f.

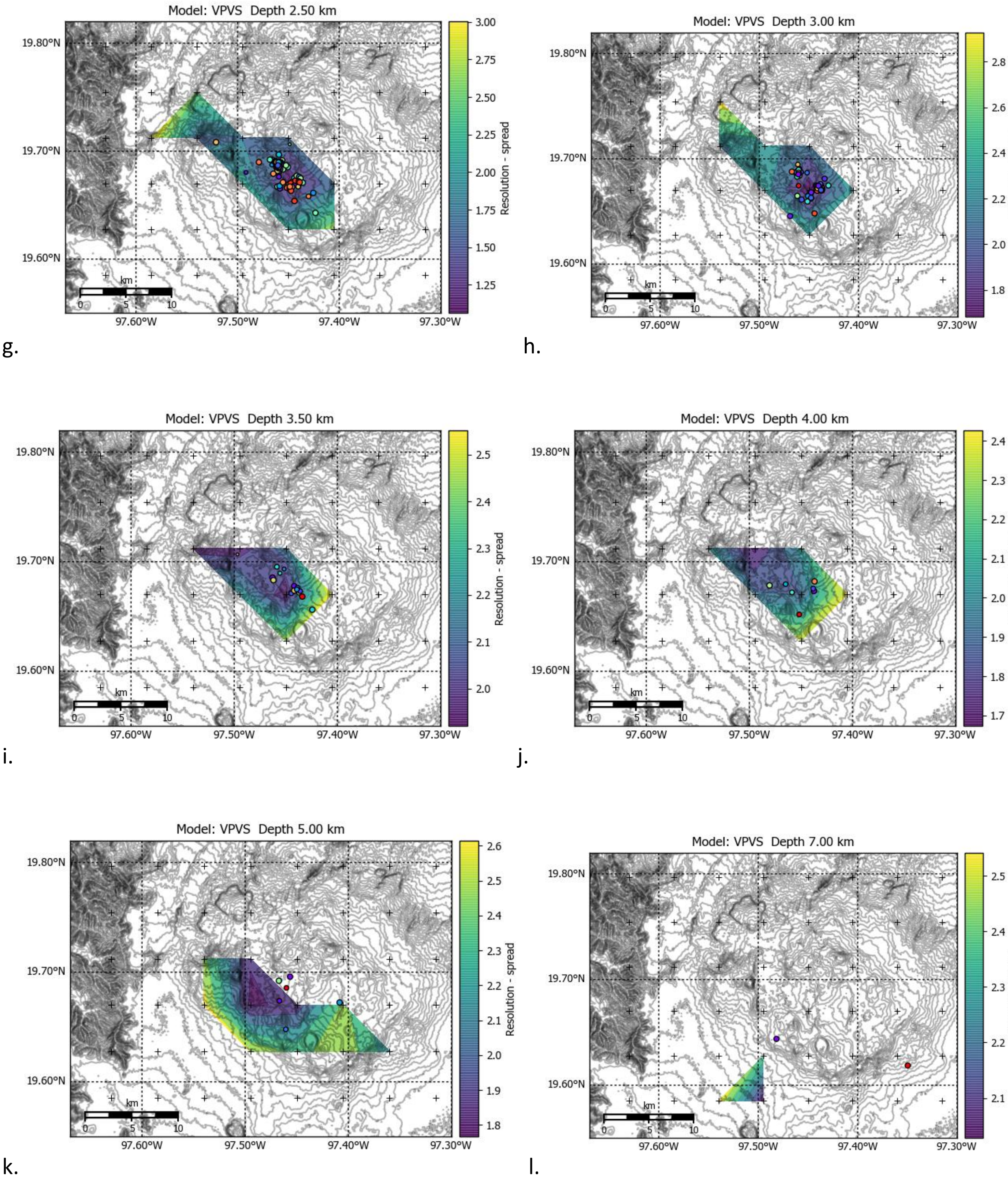

Figure 78: Spread values (off diagonal terms) for the Vp/Vs ratio.

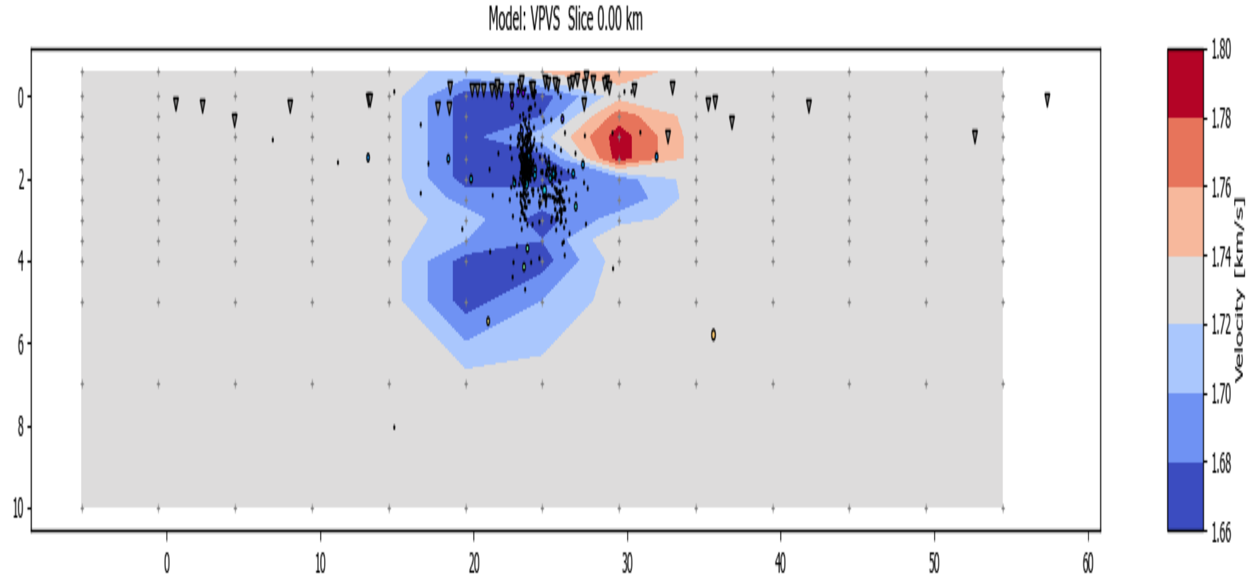

Figure 79: Cross section (NS) of the Vp/Vs ratio issued from the 3D travel time tomography.

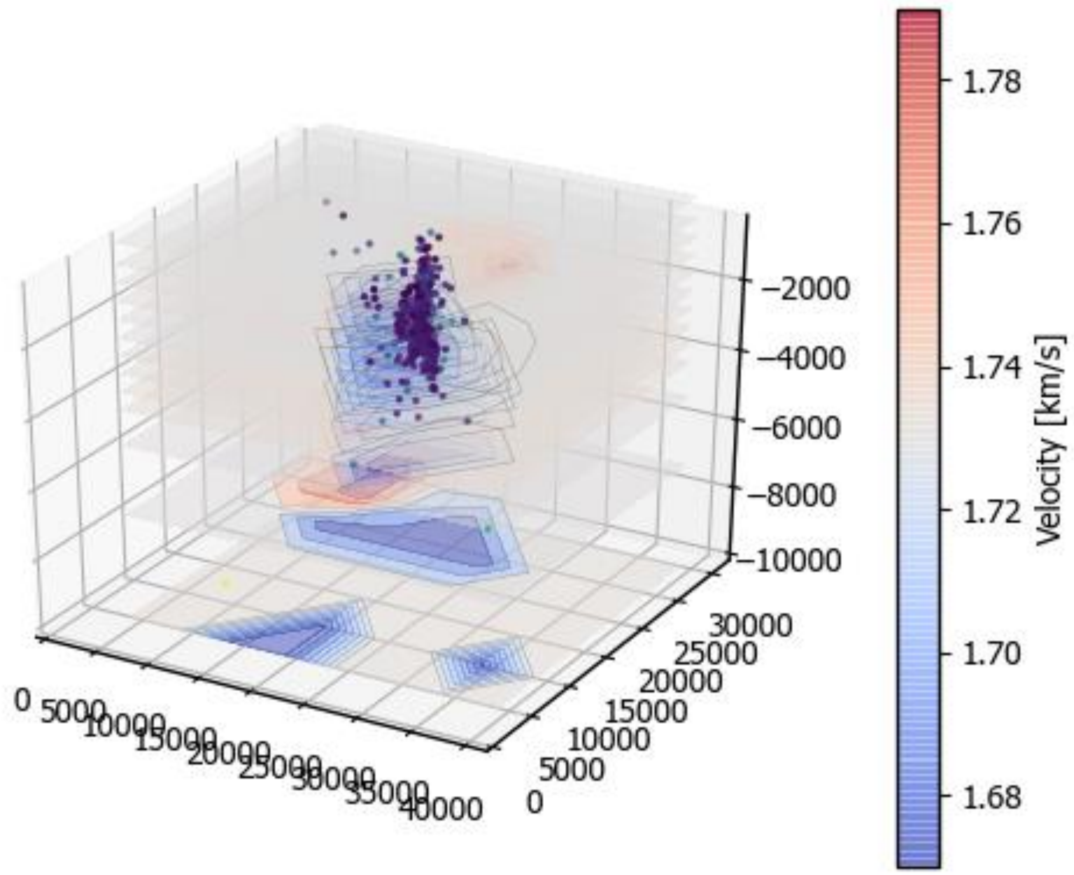

Figure 80: 3D view of the Vp/Vs ratio.

In order to test whether the results depend on the orientation of the parametrization grid, we have tested results for different grid rotations (Figure 81). We see that there is not much influence, which points to the validity of the results, independently to the grid orientation.

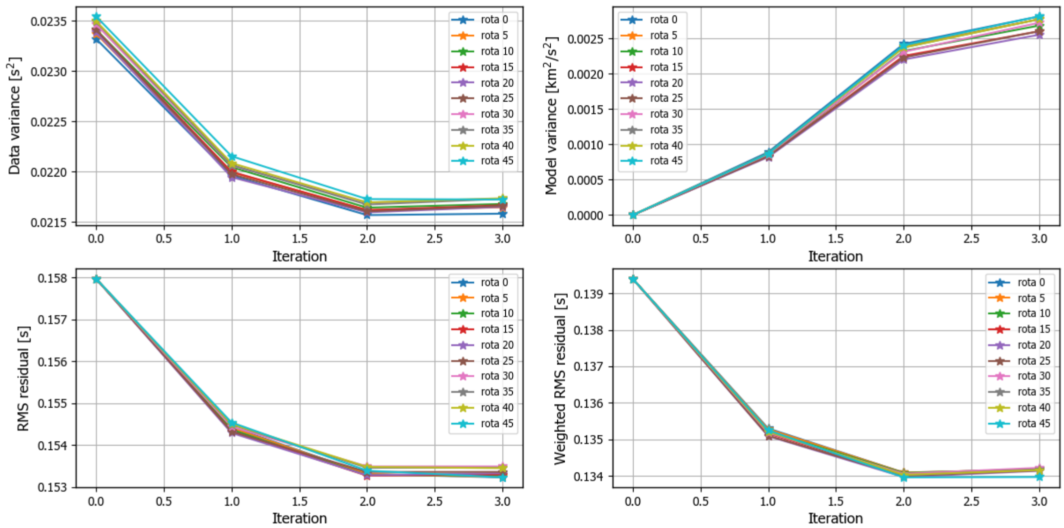

Figure 81: RMS obtained for various grid rotated around the central part of the model. Those results demonstrate that the rotation of the grid does not bring anything better.

Interpretation

Those results alone do not allow to understand the boundaries of the geothermal reservoir, as velocity variations may be linked to many possible reasons. For instance, higher pressure increases Vp, which is the main reason of the velocity increase with depth. High temperatures also contribute to a decrease of Vp velocity, but the presence of water or vapour may also influence the values. Additionally, the rock composition may affect the velocity distribution. The interpretation therefore requires a comparison with other geophysical methods, which could confirm interpretations.

Next steps

Starting from the previously assembled catalogue of 472 events, a pre-selection data criteria was applied to ensure inversion stability. Local events with azimuthal gap less than 180° (within the seismic array) and with at least 6 readings were selected as input, however all seismic events were relocated with the obtained 1D velocity model. The extracted 1D velocity model is related to position 19.6700°N and 97.450°W, which corresponds approximately to the centre of the dense seismic array and the extracted local seismicity.

Further steps involve and will be included in a publication in preparation (Toledo et al., in prep).

- Checkerboard test/modelling main features and inverting for them
- Sequentially refining the model grid and/or combining different results from rotated initial grids.
- Cross-checking with Resistivity results
- Cross-check with geochemistry, gases, fluids, cores…

5.4.3 3D velocity model CAT3D

In this section, we report the results obtained with passive seismological data recorded in the Los Humeros regional area. We obtained a $V_\mathrm{P} - V_\mathrm{S}$ velocity volume by inverting the picked P-S arrivals generated by GFZ team. The map of the seismic stations is shown in Figure 82a (UTM coordinates). For the inversion, we applied a tomographic iterative procedure using the OGS software Cat3D.

In summary, the main steps of the Cat3D tomographic procedure are:

1. Creation of the initial $V_\mathrm{P} - V_\mathrm{S}$ model for the first hypocenters localization, from the P-S picked arrivals (travel times). The P-velocity model is defined by the vertical function shown in Figure 82b. This vertical velocity gradient comes from an average estimation of the regional velocity model (see also Section 5.2.1). The corresponding initial S-velocity values are computed using a constant $V_\mathrm{P}/V_\mathrm{S} = 1.73$.
2. First hypocenters localization.
3. Tomographic inversion using the hypocenters positions and the P-S picked arrivals from the associated stations.
4. Calculation of the time residuals (difference between the picked times and the computed times) and exclusion of the records with high residuals (higher than a prefixed threshold) from the input picked data.
5. New tomographic inversion using the new input picked times obtained in step 4.
6. Hypocenters localization using the P-S velocity volume obtained by the previous inversion.
7. Return to step 3 until the time residuals and the velocity model do not change appreciably.

The final velocity model (Figure 84, Figure 85 and Figure 86) was obtained after 3 iterations of the procedure. For the hypocenters localization, we used the nonlinear location approach NLloc (Lomax et al., 2000). In the tomographic steps (3 and 5), we used the SIRT (Simultaneous Iterative Reconstruction Technique) algorithm for the travel time inversion (Gilbert, 1972), and the "staggered grid" method (Vesnaver and Böhm, 2000) to enhance the resolution of the tomographic grid.

The corresponding V_S and $V_\mathrm{P}/V_\mathrm{S}$ results of the tomographic inversion are shown in Figure 87, respectively.

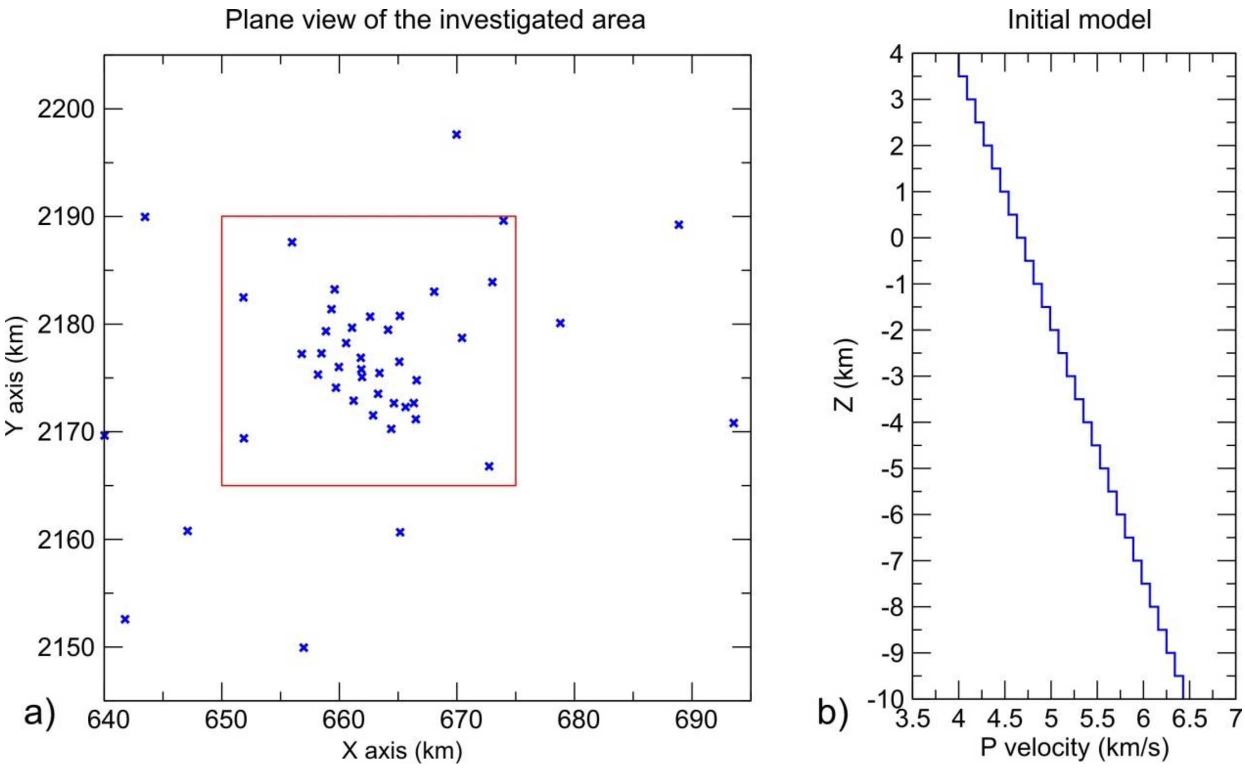

Figure 82: a) Plane view of the area interested by the tomographic inversion (UTM coordinates). The red rectangle indicates the detailed area represented in Figs 2 and 3 . b) P velocity model used to compute the earthquake localization in the first step of the procedure.

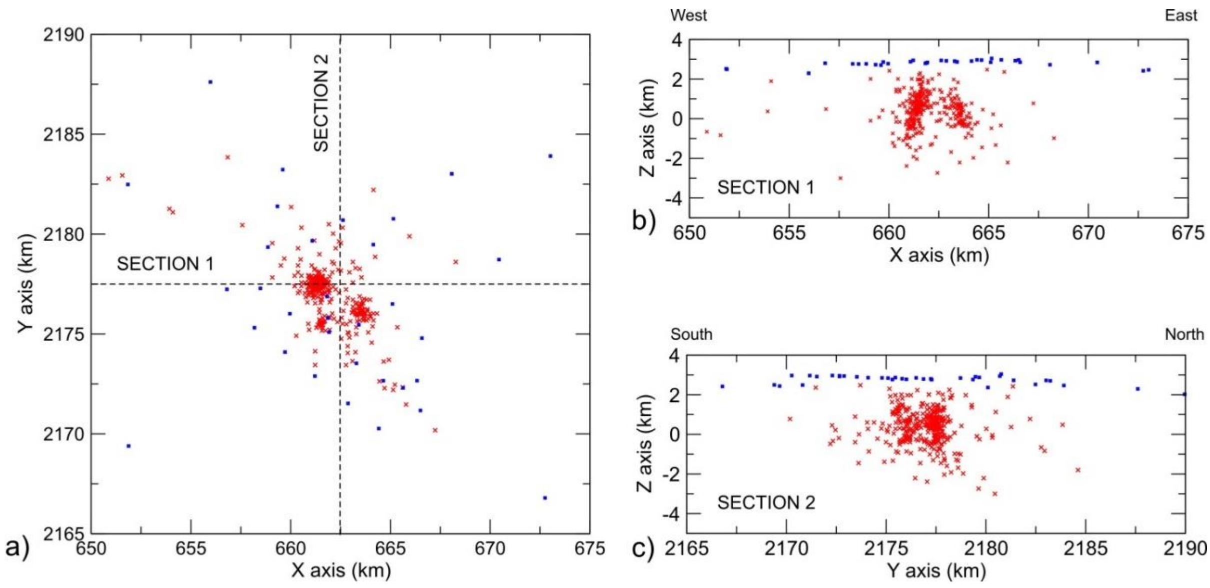

Figure 83: Earthquakes location (red crosses) at the final step of the iterations, with the used stations (blue points). a) Plane view, b) West-East section, c) South-North section.

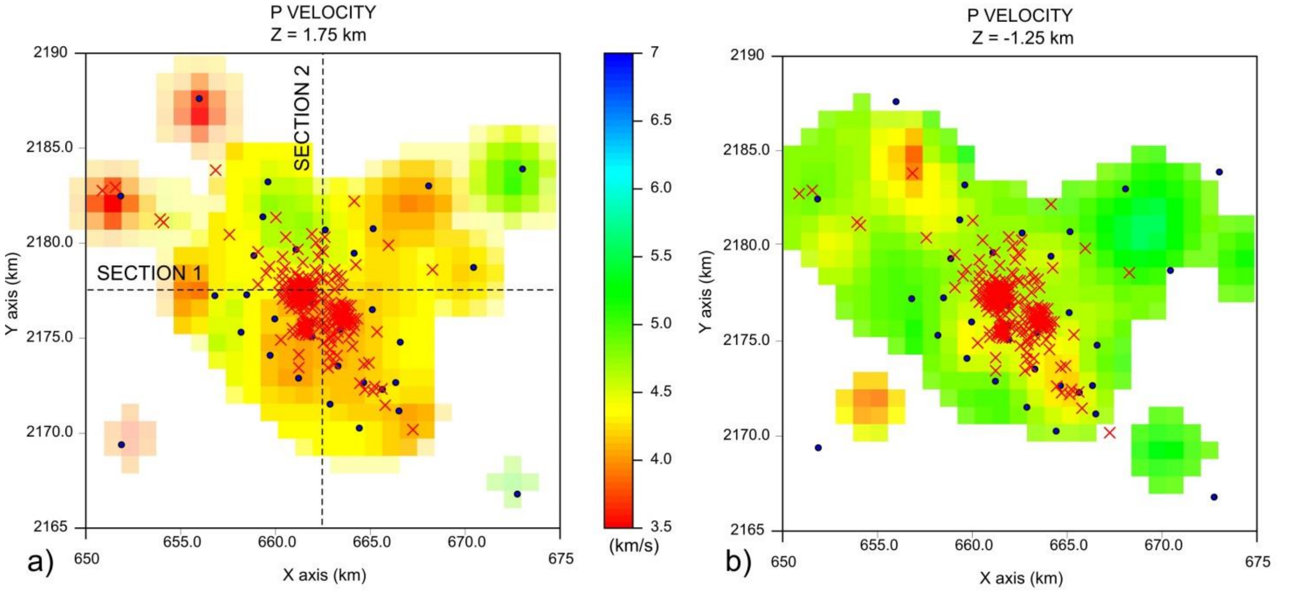

Figure 84: Horizontal slides at different depths of the P-velocity volume obtained by tomographic procedure at final step. The white zones represent those parts not affected by the inversion (not covered by rays). The dash lines in a) indicate the position of the vertical sections of Figure 85 and Figure 86.

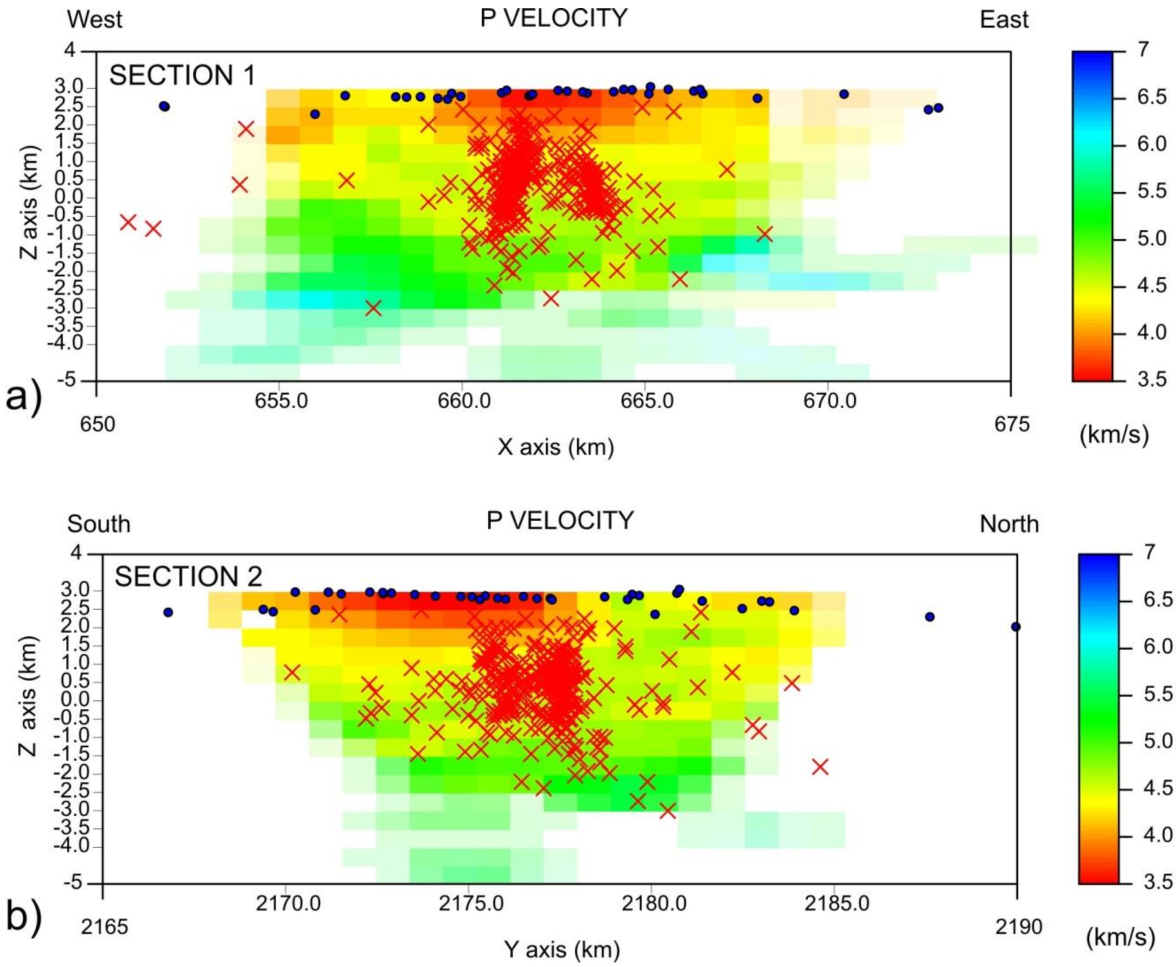

Figure 85: Vertical sections of the P-velocity volume obtained by tomography at final step. a) West – East section; b) South – North section. Blue dots are stations at the surface.

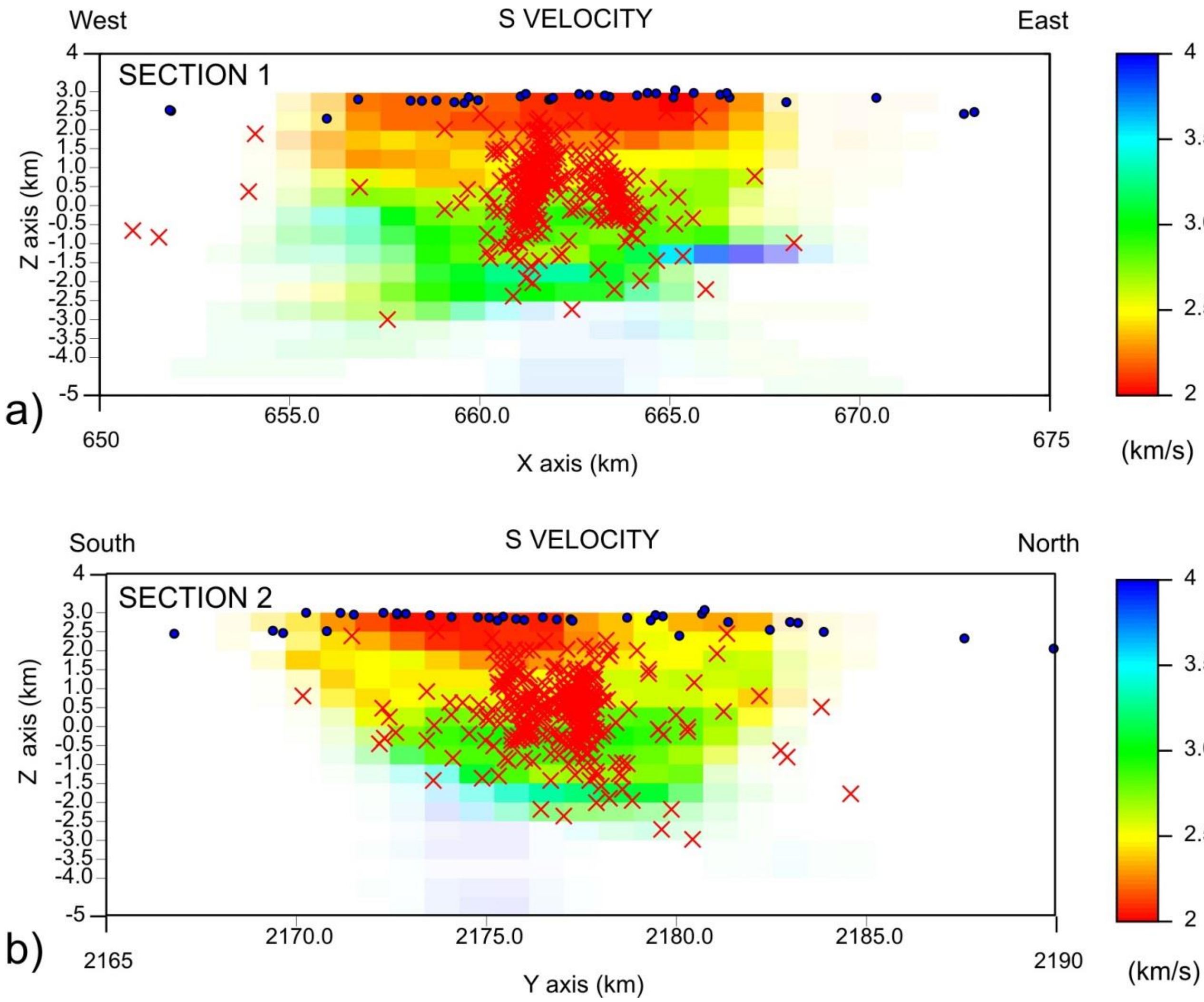

Figure 86: Vertical sections of the S-velocity volume obtained by tomography at final step. a) West – East section; b) South – North section. Blue dots are seismic stations.

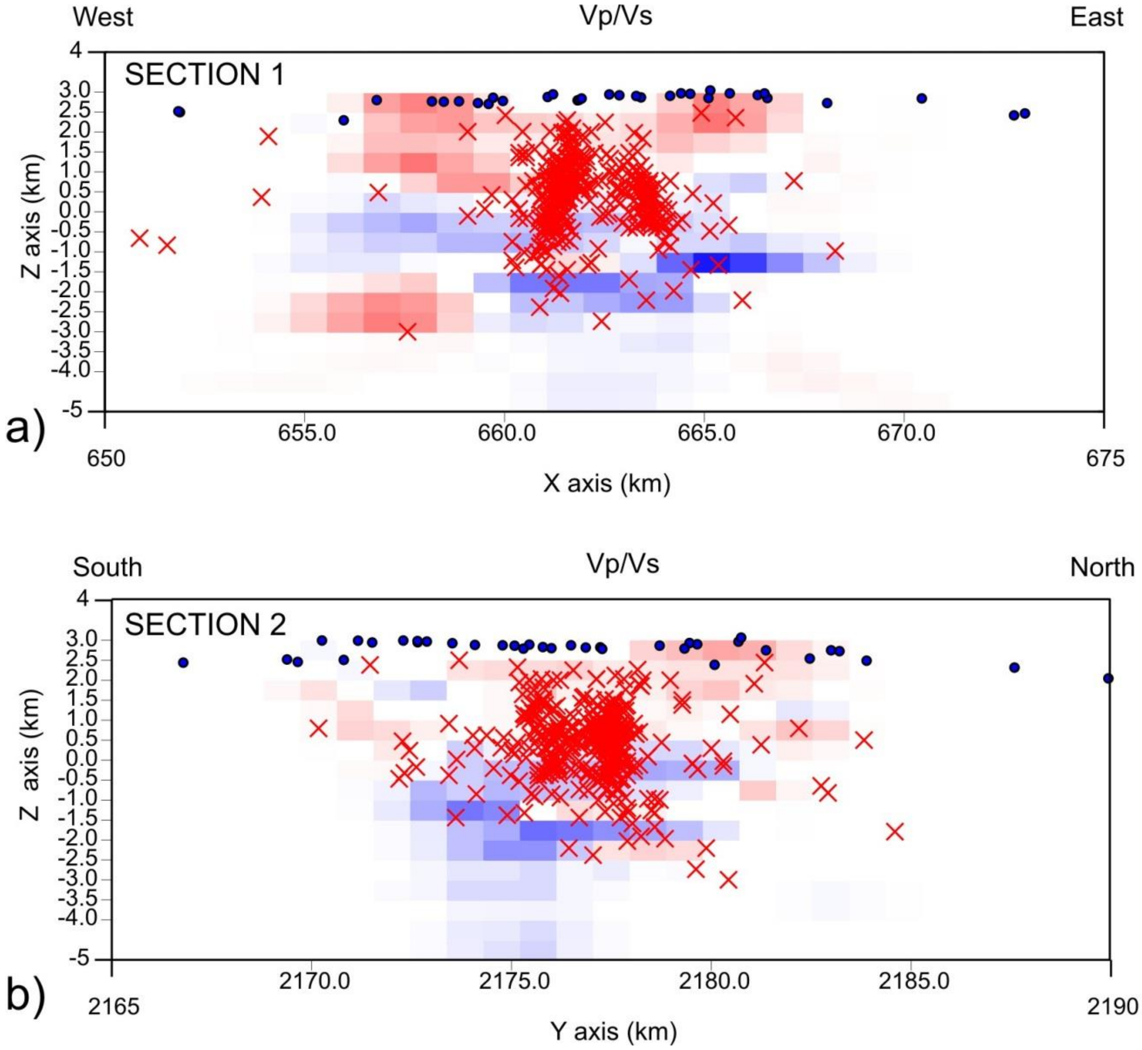

Figure 87: Vertical sections of the V_P/V_S volume obtained by tomography at final step. a) West – East section; b) South – North section. Blue dots are seismic stations.

5.4.4 Comparison of results

In this part, a tentative qualitative comparison is performed between the models obtained from the travel time tomography from Simulps and CAT3D. In both models, we can see similar anomalies associated with earthquake locations and the main features match. Figure 88 shows a comparison of the anomalies of Vp and Vp/Vs ratio faults plotted at the surface.

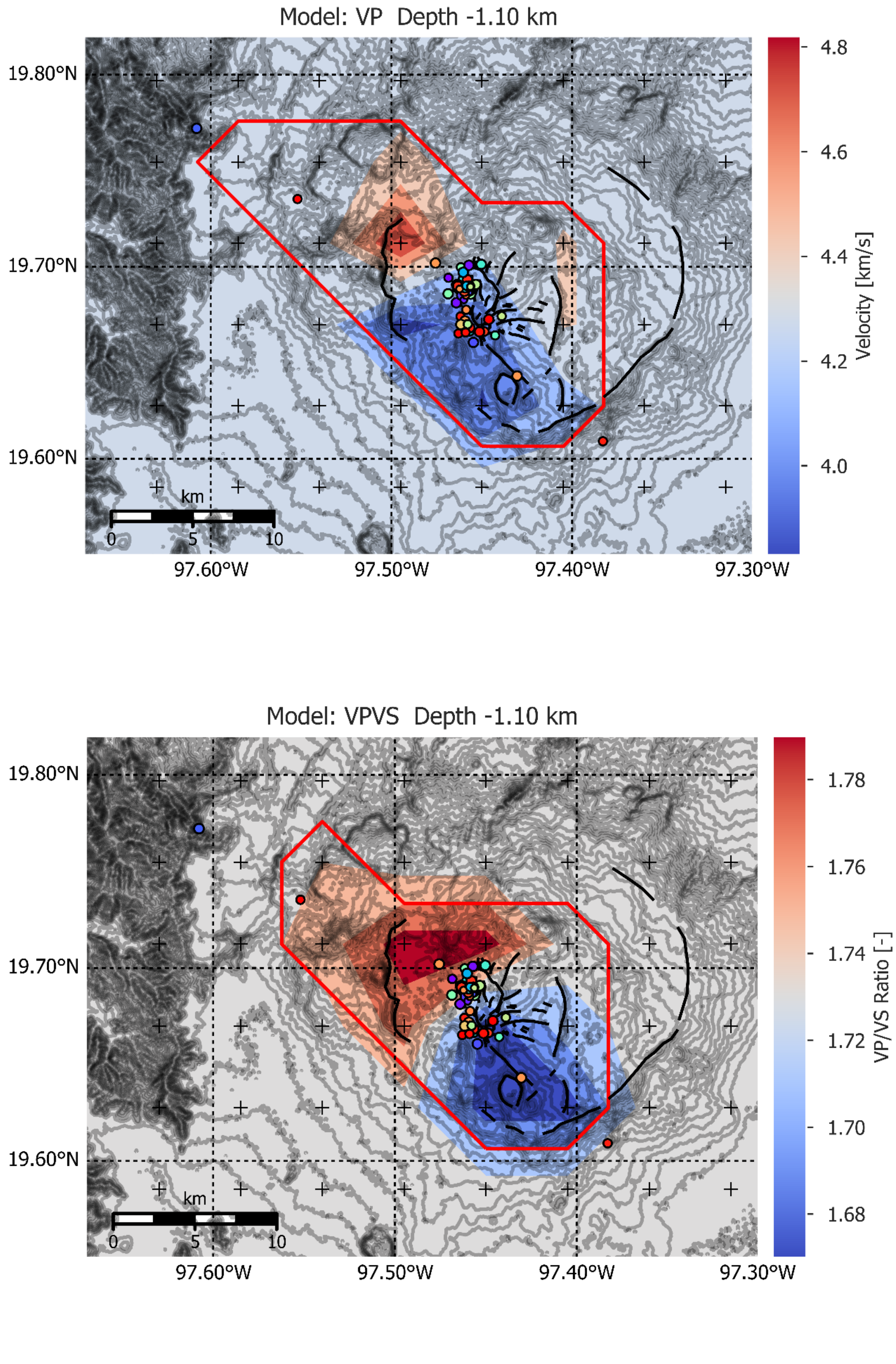

Figure 88: Comparison of Vp and Vp/Vs ratio slices at 1.1 km depth and faults plotted at the surface. Dots are earthquakes hypocenters.

5.5 Ambient noise correlation methods

5.5.1 Ambient noise tomography

Since the successful retrieval of surface-wave responses from the ambient seismic field via cross-correlation (Shapiro & Campillo, 2004), noise-based interferometry has been widely used for high-resolution imaging of the Earth's lithosphere from all around the globe (e.g. Shapiro et al. 2005). Further applications on geothermal fields reveal the potential of ambient noise techniques to characterize the subsurface velocity field and understand temporal evolution of the velocity models due to field operations. Examples of applications to producing fields like Soultz-sous-Forêts (Calò and Dorbath, 2013a and Calò et al., 2013b), St. Gallen geothermal site in Switzerland (Obermann et al., 2015), Alsace in France (Lehujeur et al., 2015) and Iceland's Reykjanes Peninsula (Weemstra et al., 2016; Martins et al., 2019b) have been boosting in recent years.

This section summarizes the results of ambient noise tomography (ANT) techniques over the Los Humeros geothermal field. The goal of the application of ANT is to derive a 3D S-wave velocity field from the deployed seismic network deployed under the GEMex project (Figure 55).

From the ambient noise recorded at the deployed seismic network, we extract surface-waves after the computation of the empirical Green's functions (EGF) by cross-correlation techniques. The extracted surface-waves are dispersive, and as such their velocity is a function of frequency, which by its turn is a function of depth. From the retrieved surface-waves, we can estimate both group and phase velocities, which are not always the same. Phase velocities, at which the peaks or troughs move, are usually faster and monotonically increase inversely with frequency (dispersion properties). Group velocities, at which the wave energy moves, can oscillate. Group velocities can be defined by $U = d\omega/dk$ (where ω is the wave's angular frequency and k is the angular wavenumber) and the phase velocities by $c = \omega/k$. Their independency arises from the fact that the surface-wave sensitivity kernels (Zhou et al., 2004) for both phase and group velocities dependency with depth are different. From a processing point of view, group velocities are usually easier to pick than phase velocities especially for higher frequencies, allowing better sampling at shallower depths. Here, we use both phase and group velocities to obtain a better constrained inversion from frequency to depth.

We used the vertical component of the data recorded by the seismic network active from September 2017 to September 2018 (Figure 55). The total network is composed of 45 seismometers from which 25 are Broadband (BB) and the remaining short-period stations (see section 5.2). Figure 89 shows the spatial distribution of the stations (All stations vs BB only) and all the possible station pair combinations. Not all the station pairs displayed in the figure will be available for all frequencies, so the picture is only representative of frequencies which will use all the station-pair combinations (see Figure 89 for the effect of frequency on the number of used ray-paths).

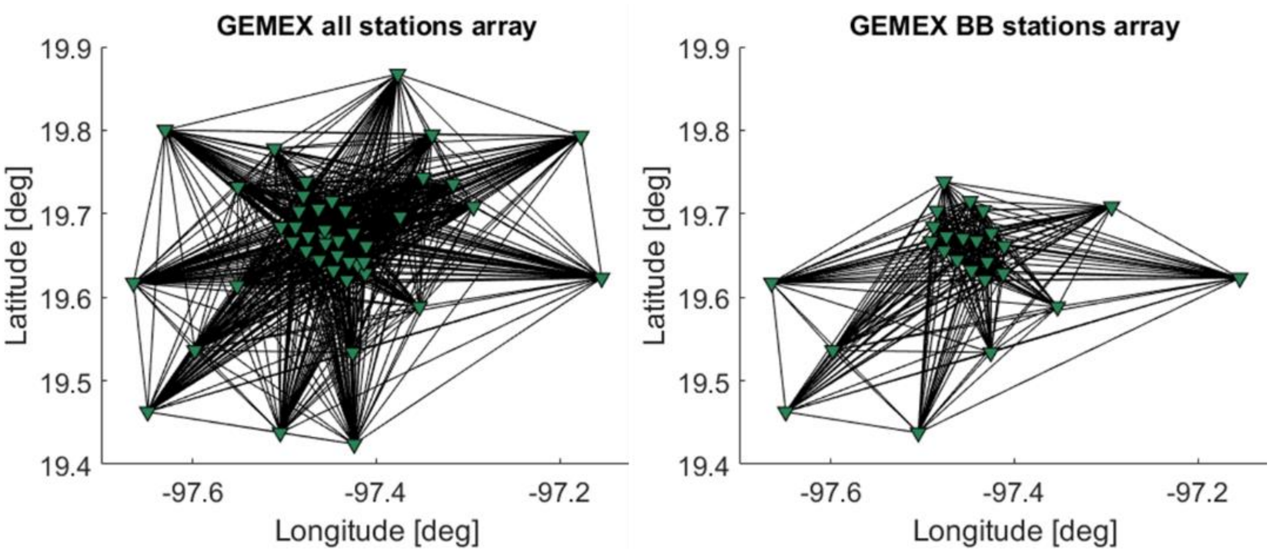

Figure 89: Spatial distribution and all possible ray-path combination of the full seismic network (left) and broadband (BB) seismometers only (right). The lines connecting the station pairs of each figure provide an indication of the spatial coverage of the ray-paths for which we estimate the phase and group velocities.

5.5.2 Methodology

The methodology we apply is depicted in a flowchart form (Figure 90). Here, we use the potential of phase and group velocity pickings for a better constrained inversion of phase and group velocities from frequency to depth. The reasoning for each analysis step and quality control is explained in the corresponding section of this document.

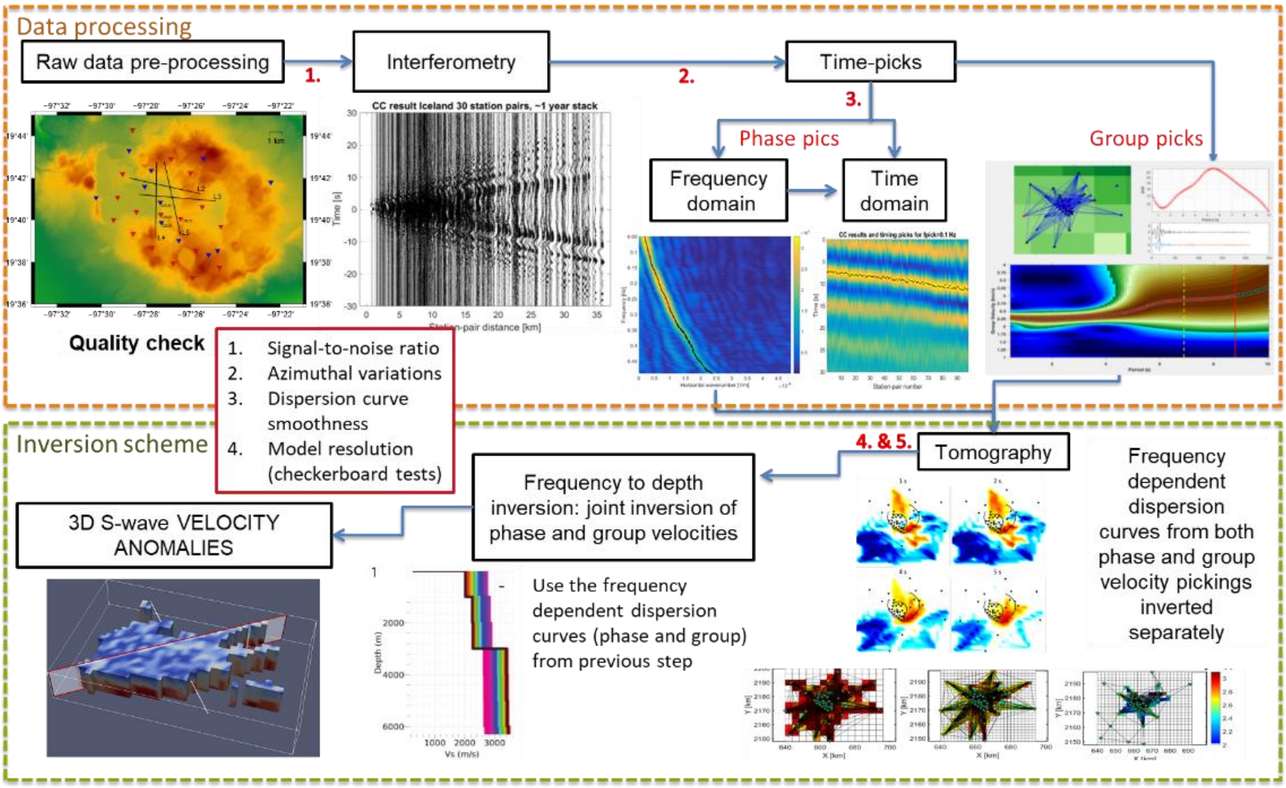

Figure 90: In this study, we extend the tomographic imaging workflow applied in EU-project IMAGE (adapted after Martins, et al. 2019a).

5.5.2.1 Raw data and pre-processing

We analyzed the continuous noise records from the vertical component. Prior to the calculation of the cross-correlations (CC), we apply the following processing steps: instrument response deconvolution; resampling of the data to a sampling frequency of 5 Hz; elimination of 2 h signal segments that show amplitudes greater than 10 times the standard deviation of the daily trace; spectral whitening of the amplitude from 0.5 to 20 s, a second elimination of 2 h signal segments that show amplitudes greater than 3 times the standard deviation of the daily trace (e.g. due to local earthquakes) (Bensen 2007).

5.5.2.2 Auto- and Cross-correlations

We calculate the CCs between all station pairs for the remaining two-hour segments (Courtesy Anne Obermann, ETH Zürich). Prior to the stacking, we use the autocorrelations to verify if there are problems with the individual stations during certain periods. For e.g. in station 'SS18', we observed temporary problems due to noise amplification in certain days (low SNR in Figure 91b). While in other stations, we observe potential clock errors (mismatch between the GPS and the internal instrument clock) throughout the recording period (Figure 92).

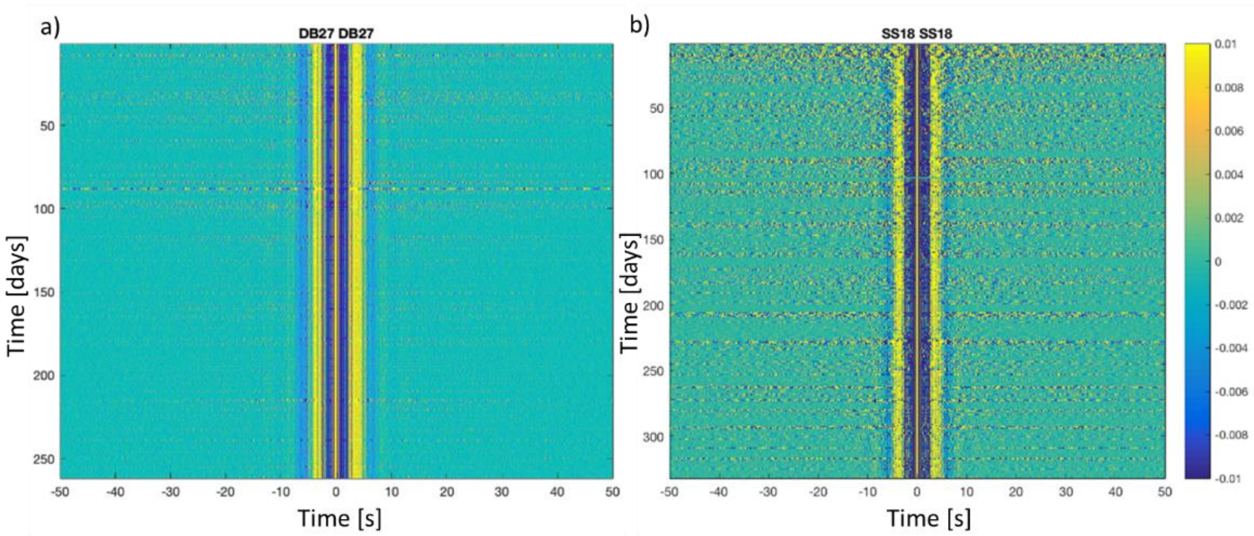

Figure 91: Auto-correlation panels for single stations in time. a) Auto-correlation for the whole acquisition period (from September 2017 to September 2018) of station '*DB27*' a BB seismometer. b) Auto-correlation for the whole acquisition period of station '*SS18*' a short-period seismometer. Color scale represents amplitude.

In general, and as expected for the short-period stations, the signal-to-noise ratio (SNR) is lower than for the BB seismometers. Figure 91 shows a specific example of an auto-correlation panel for a BB station and an auto-correlation panel of one of the short-period stations with the lowest SNR.

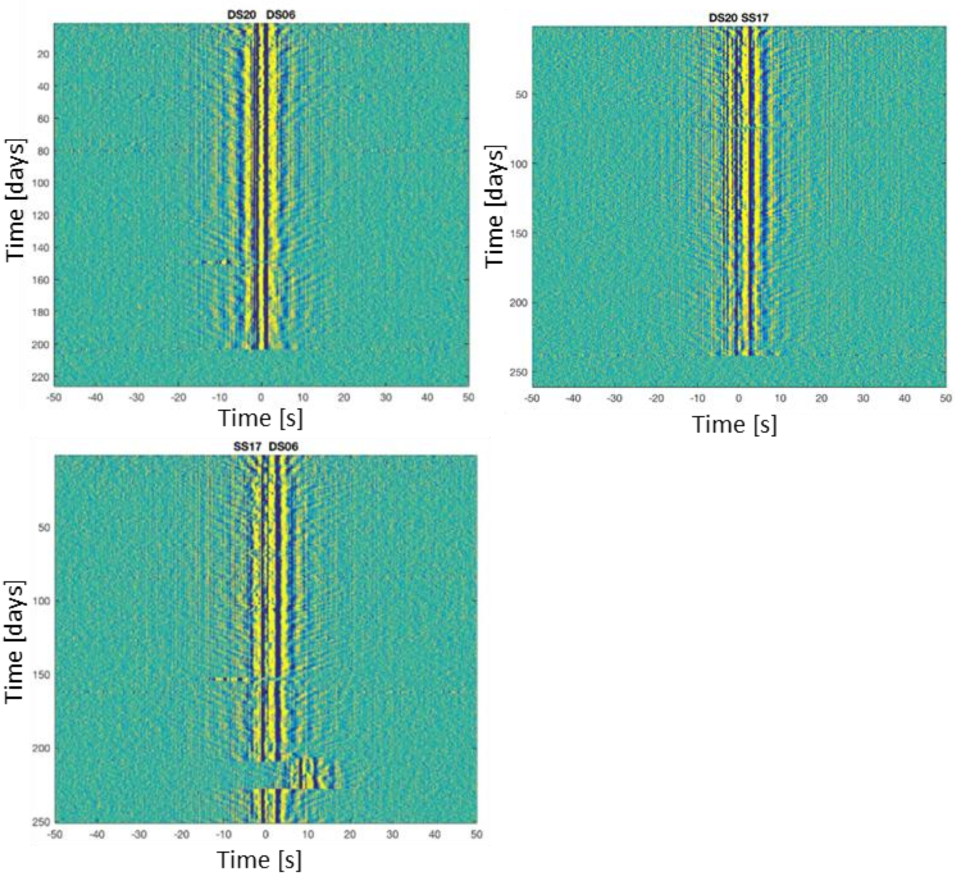

Figure 92: Cross-correlation panels of the combination of three stations: 'SS17', 'DS06', 'DS20'. The cross-correlation panels show the estimated cross-correlation per day (y axis) with the causal and a-causal time arrival estimation.

In Figure 92, we show the cross-correlations for some of the stations with better and worse time arrival retrieval. Please note that the y axis stops according to the data availability. Prior to stacking we eliminate the data records with the identified problems for all the cross-correlated pannels (e.g. the ~20 days shift of the cross-correlation panel between 'SS017' and 'DS06'). We then average positive and negative lag-times to enhance the part of the signal that is symmetric. This procedure slightly increases the signal to noise ratio which helps to homogenize the noise sources distribution (Mordret et al., 2015).

As a side check, we processed separately the BB seismometers to check if there would be abrupt changes during phase velocity pickings. Figure 93 displays the CC using the complete seismic network and the BB seismometers only with the corresponding interstation distances. For all stations the average station-pair sampling (average distance between each CC line) is 65.6 m while using the BB only it is 170m ensuring the Nyquist wavenumber, half the spatial sampling distance ($k_{NY} = 1/(2dR)$ with $dR = (R_{max} - R_{min})/n_{pairs}$) of 0.0076 m^{-1} and 0.0030 m^{-1}, respectively for all the stations and the BB only. Where R_{max} and R_{min} are the maximum and minimum interstation distances per frequency, and n_{pairs} is the number of station pairs for each frequency. The Nyquist wavenumber is significantly larger than the extent of the wavenumber axis for both examples in Figure 93, meaning that we are not aliased.

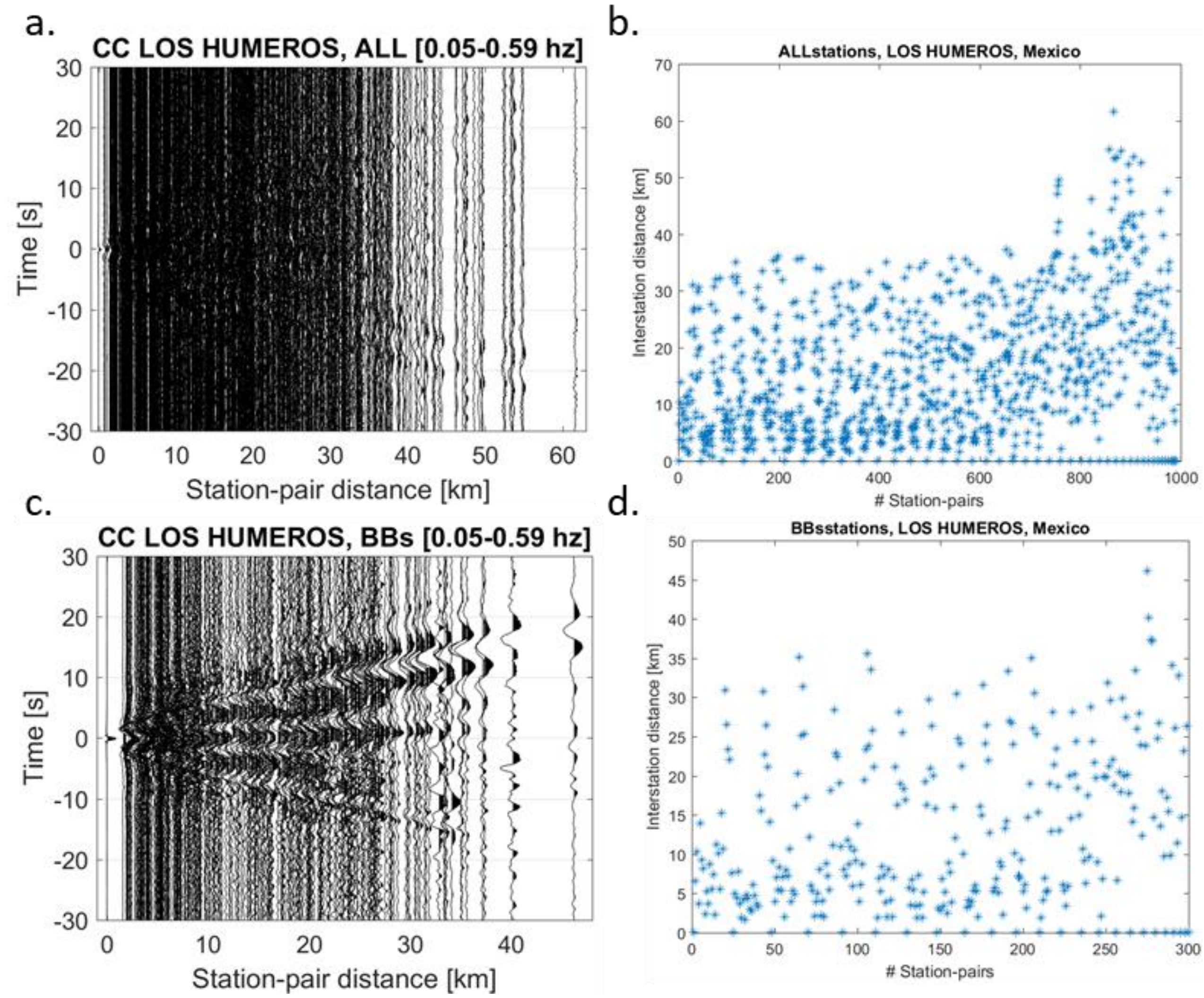

Figure 93: a and c: Retrieved surface-waves at positive and negative times in the corresponding frequency range (from 0.05 Hz to 0.59 Hz) for all stations (top) and for the BB only (bottom). b and d: Station-pair distances for all stations (top) and for the BB seismometers only (bottom).

Figure 93 shows how better retrieved the direct wave arrival using the BB seismometers is with comparison with using the whole seismic network. For this reason, throughout the remaining processing and until the inversion from frequency to depth, we keep a separate analysis of the BB only. This way we ensure a reliable cross-check of the estimated values throughout the processing chain.

5.5.2.3 Phase velocity picks

We adopted the methodology of Martins et al. (2019) for the phase velocity pickings. First, we estimate an average phase velocity picking in the wave number-frequency domain using the multichannel surface wave method (MASW) described in (Park et al., 1998) and (Park et al., 1999). The average dispersion curve is then used to guide the path dispersion in the time domain (Martins et al., 2019) using narrower frequency bands.

5.5.2.4 Average phase velocity picks

Figure 94 displays the MASW wave number-frequency pickings for all the seismic stations from the network (left) and for the BB stations only (right).

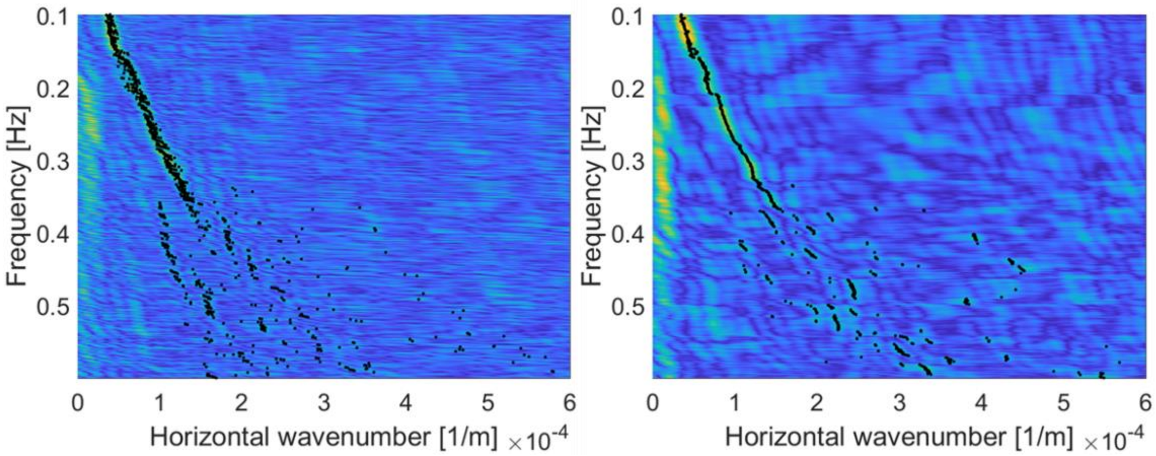

Figure 94: a) Picking in frequency-wavenumber domain using MASW algorithm using all the seismic stations. b) Picking in frequency-wavenumber domain using MASW algorithm using the BB seismometers only, between 0.1 Hz and 0.6 Hz.

We observe that the picking is more smooth while using the BB seismometers only, allowing a more certain phase velocity picking. We see that for frequency values above 0.4 Hz it is difficult to extract a reliable average phase pick. Therefore we decide to drop out phase velocity picks above 0.4 Hz.

The same can be observed in Figure 95(left), where the average velocity is depicted as function of frequency. Above 0.4 Hz the average velocity estimation is cluttered and therefore difficult to estimate an average velocity. Because we need a good estimation of the average phase velocity for individual phase picks, we restrict our phase measurements to frequencies below 0.4 Hz.

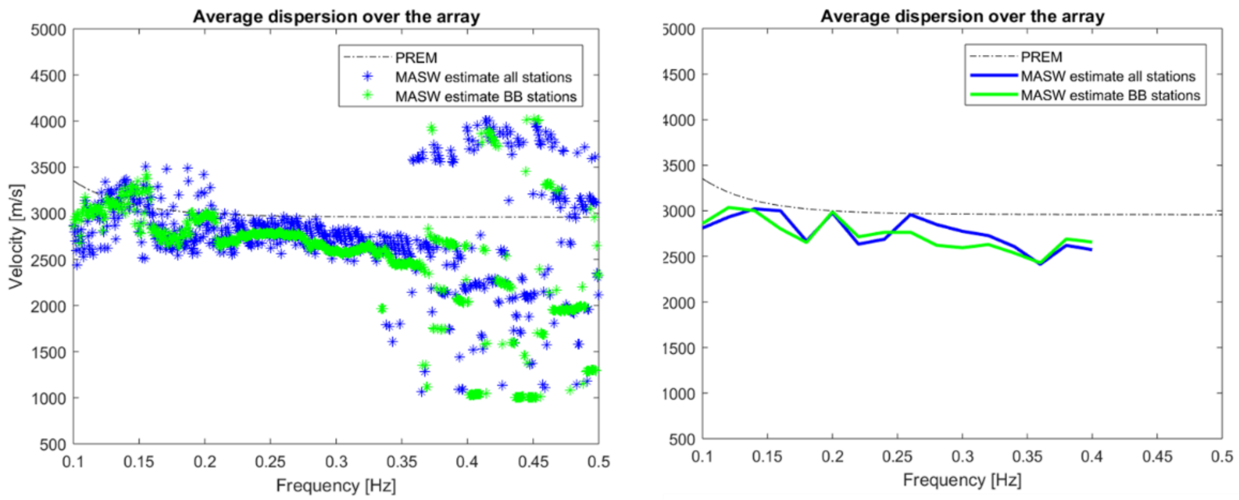

Figure 95: Left: MASW pickings using the whole seismic network and using only the BB seismometers and PREM as a reference. Right: Interpolated MASW pickings using the whole seismic network and using only the BB seismometers and PREM (Preliminary Reference Earth Model) as a reference (Dziewonski et al., 1981).

We filter out the velocity values that do not seem realistic under quite strong assumptions. We select the average velocity values which continue (between 0.3 and 0.4 Hz) immediately below the PREM taking advantage of the fact that the phase velocity values decrease monotonically with frequency. Then we interpolate the values in between to obtain the green (using all seismometers) and blue (using the BB seismometers only) average velocity estimations in Figure 96. We see that both MASW velocity estimation using all seismometers and the BB seismometers only follow the same trend, indicating that even though the short-period seismometers have lower SNR, it is still possible to use them.

5.5.2.5 Station-pair phase picks

After selecting an average velocity per frequency from the MASW estimation, we use that average velocity to guide the phase velocity pickings in the time domain.

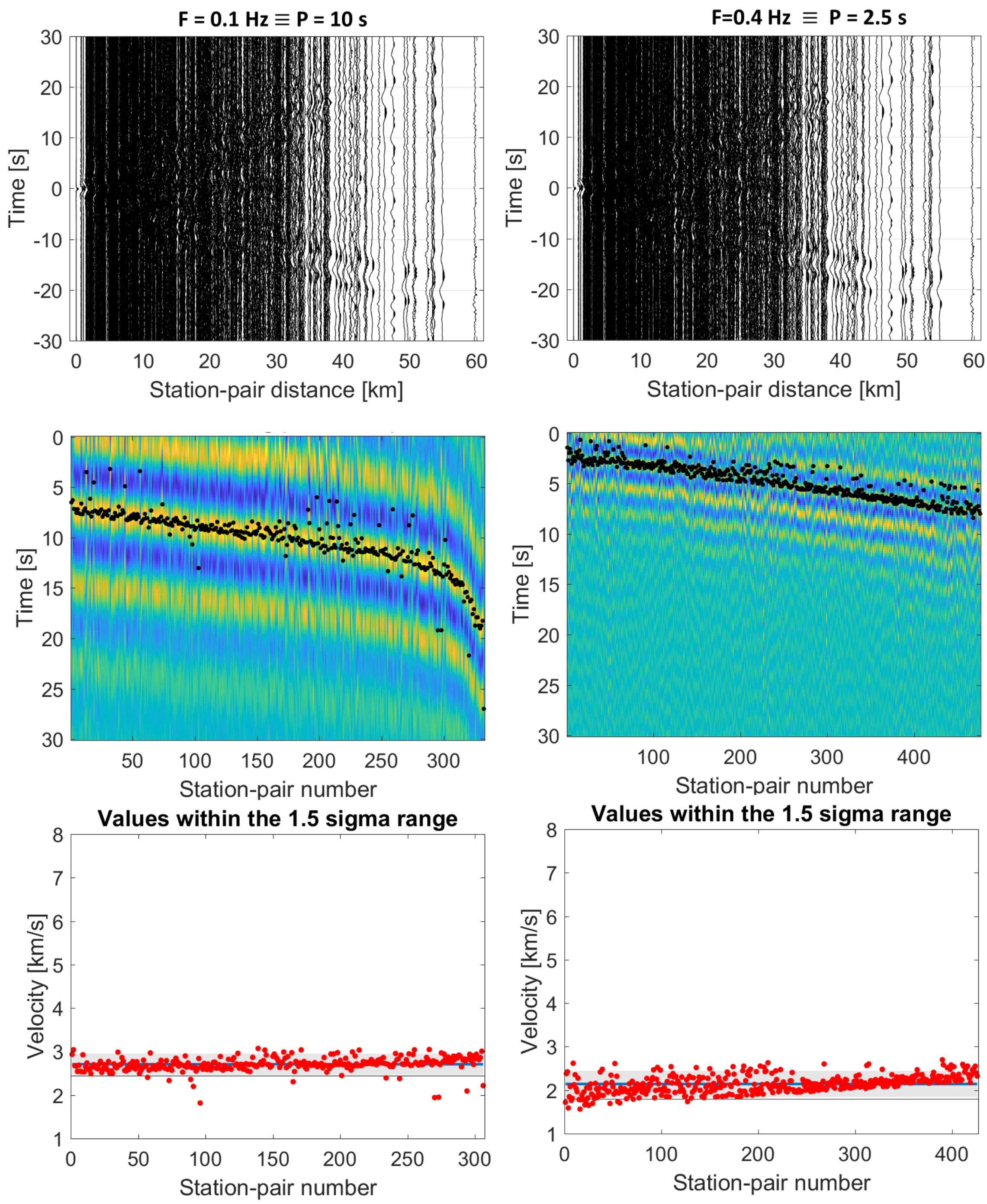

Figure 96: Top: Retrieved surface-waves at positive and negative times in the indicated centre frequency/period for all stations within a narrow frequency band. Middle: Station-pair phase pick for the corresponding frequencies. Bottom: estimated velocity

between each station pair number ranked by interstation distance. Grey shadow locates the corresponding 1.5 σ confidence interval around the estimated mean velocity.

Figure 96 shows an example of two picks using two different centre frequencies (centre frequency of +/-0.01 Hz and corresponding centre period) and the corresponding station-pair phase velocity estimation. Station-pair pickings outside the 1.5σ deviation from the average velocity are dropped out. The same quality control selection is performed for all the frequencies. Here, we display specifically two period centres at the edges of the frequency bandwidth (0.1 Hz and 0.4 Hz), to show that the assumption made on the average frequency in the previous section seem to be reasonable given the estimated velocities.

Because the phase picks were performed in the frequency domain up to this point we refer to the picks in the frequency domain. However, because referring to period is somehow more intuitive, from now on we will use period by convention. From the phase velocity picks we conclude that it is possible to retrieve reliable phase velocity picks between 2.5 and 10 seconds.

5.5.2.6 Group velocity pickings

We estimate the group velocity dispersion curves with a frequency-time analysis from 0.5 to 15 s (Levshin et al., 1989; Ritzwoller and Levshin, 1998). We use a graphical user interface that involves analyst validation of the dispersion curves (Mordret et al., 2014). Figure 97 shows an example of such graphical interface, with the picking of the average group velocity as function of period for the whole array. Group velocities from inter-station distances smaller than 1.5 wavelength and SNR<10 are not considered.

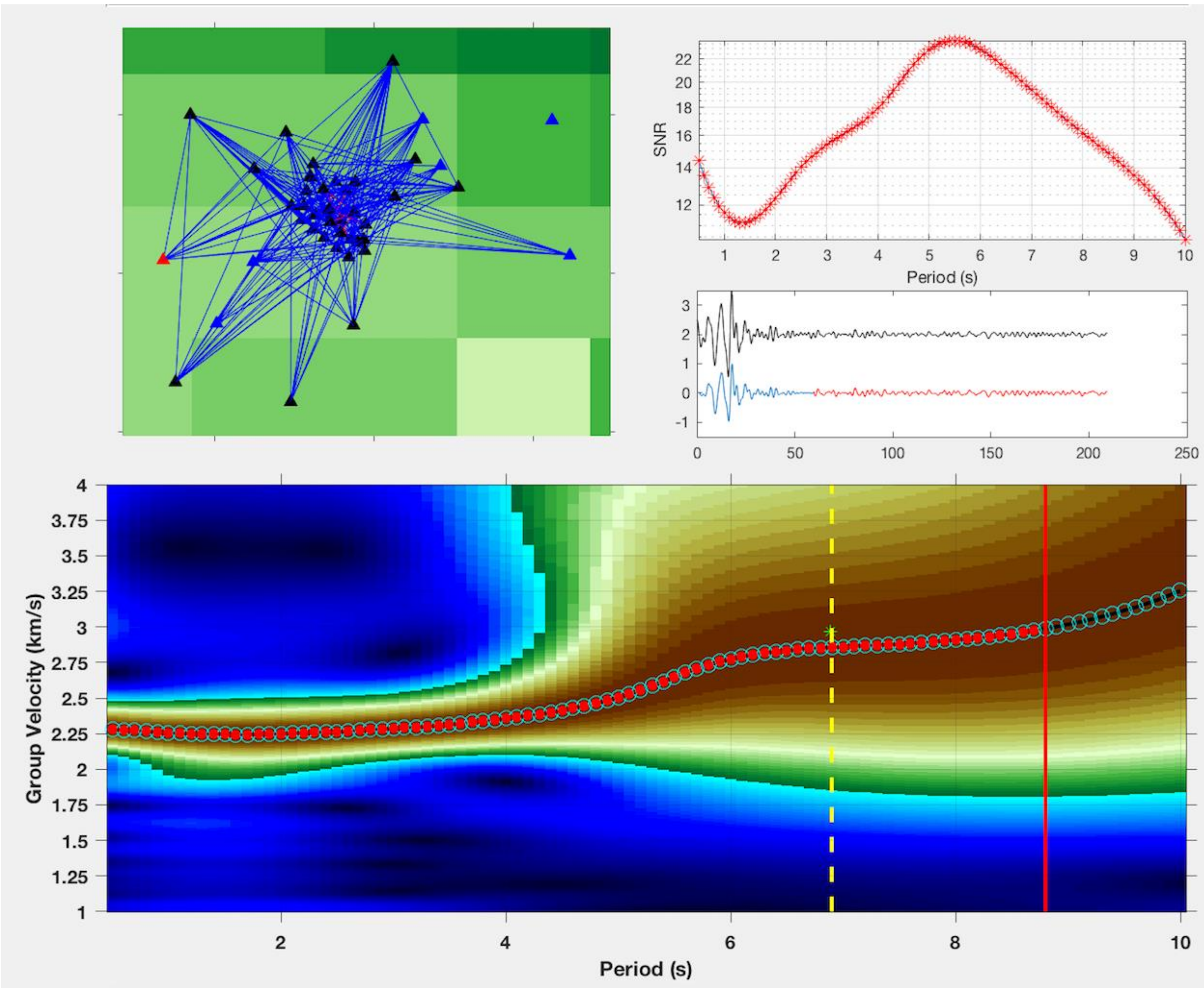

Figure 97: Example of group velocity picking using only the first 6 months of data.

Figure 98a shows the final set of group velocity dispersion curves calculated for this study. Figure 98b shows the number of measurements as a function of period. We limit our analysis to reasonably covered period ranges with at least 100 measurements, which restricts us to periods between 1 and 7 seconds.

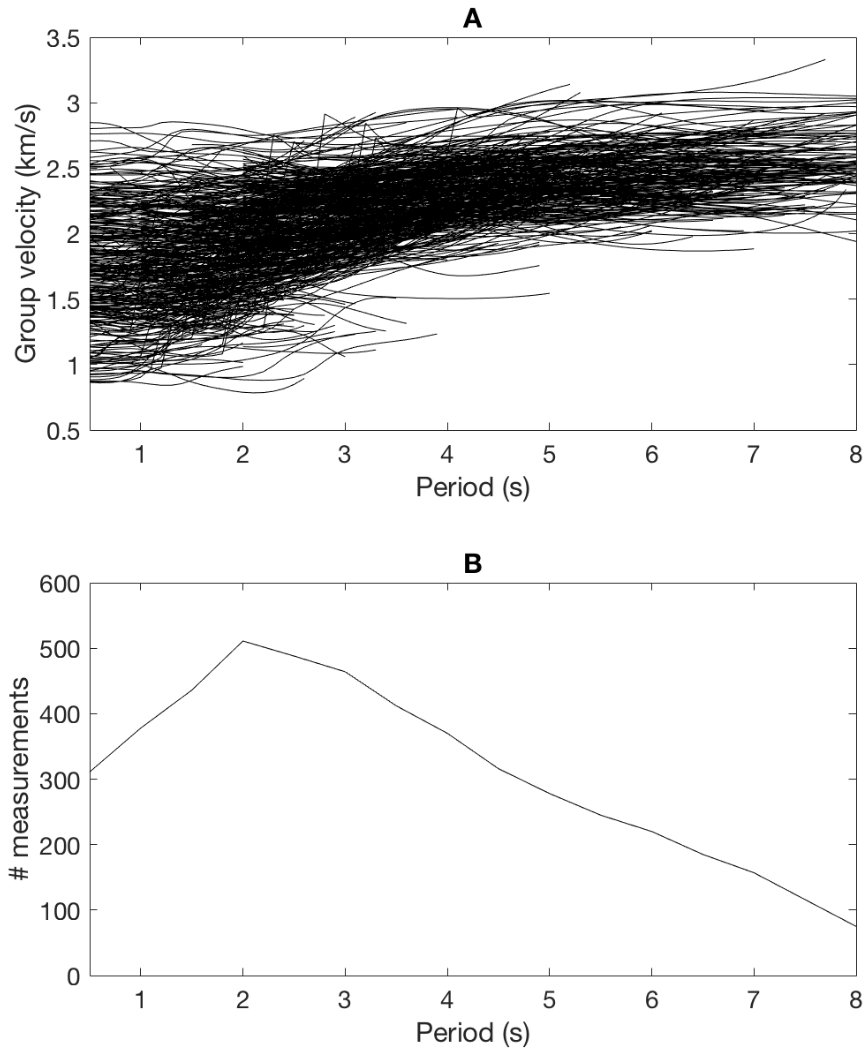

Figure 98: A) Rayleigh wave dispersion curves used in this study. B) Number of measurements as a function of period.

5.5.3 Tomographic Results

5.5.3.1 Checkerboard tests

The checkerboard tests are performed to assess, in a forward modelling way, if the chosen spatial sampling of the station network can reproduce the simulated checker. In other words, to understand if the seismic network configuration allows the complete recovery of the simulated checkerboard test. We tested different combinations of checkerboard anomaly sizes and solve for different resolutions. The checkerboard tests show good performance for resolutions up to the highest tested horizontal resolution (2 km). The area where the checker is better reproduced is outlined by the polygon and corresponds to the area of higher station density, inside the Los Humeros volcano caldera. Because of computational reasons we left out the horizontal resolution of 1km, but we think that 1km resolution is still achievable with good results within the defined polygon.

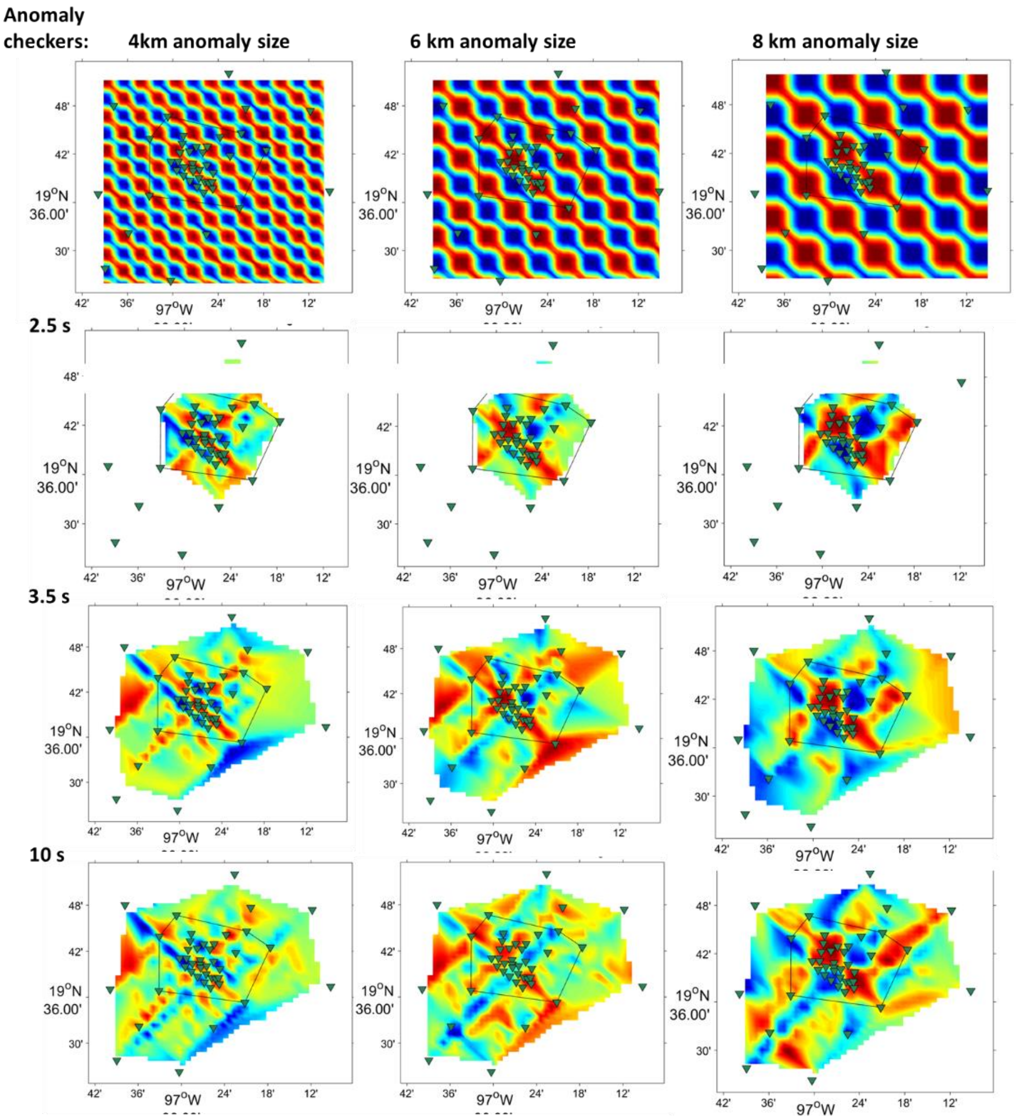

Figure 99: Checkerboard tests for combinations of three anomaly sizes and the higher tested resolution for periods of 2,5 s, 3.5 s and 10 s. The black polygon defines the area where visually the tested checkerboards are better reproduced.

The checkerboard results (Figure 99) indicate that the seismic network configuration is not optimal for results within the seismic network aperture. The area outside the defined polygon does not have enough ray path coverage for a constrained tomographic result. For a better sampling of the whole area it would be preferred to decrease the density of the inner network stations and place then outside the polygon.
For this reason, we exclude any tomographic result outside the defined polygon.

5.5.3.2 Phase and group velocity tomography

We perform the phase and group tomography using the methodology of Martins et al. (2019a). We use a Tikhonov regularization to deal with the ill-posed tomographic inversion and the regularization parameter is estimated using the cross-validation algorithm (Golub et al., 1979).

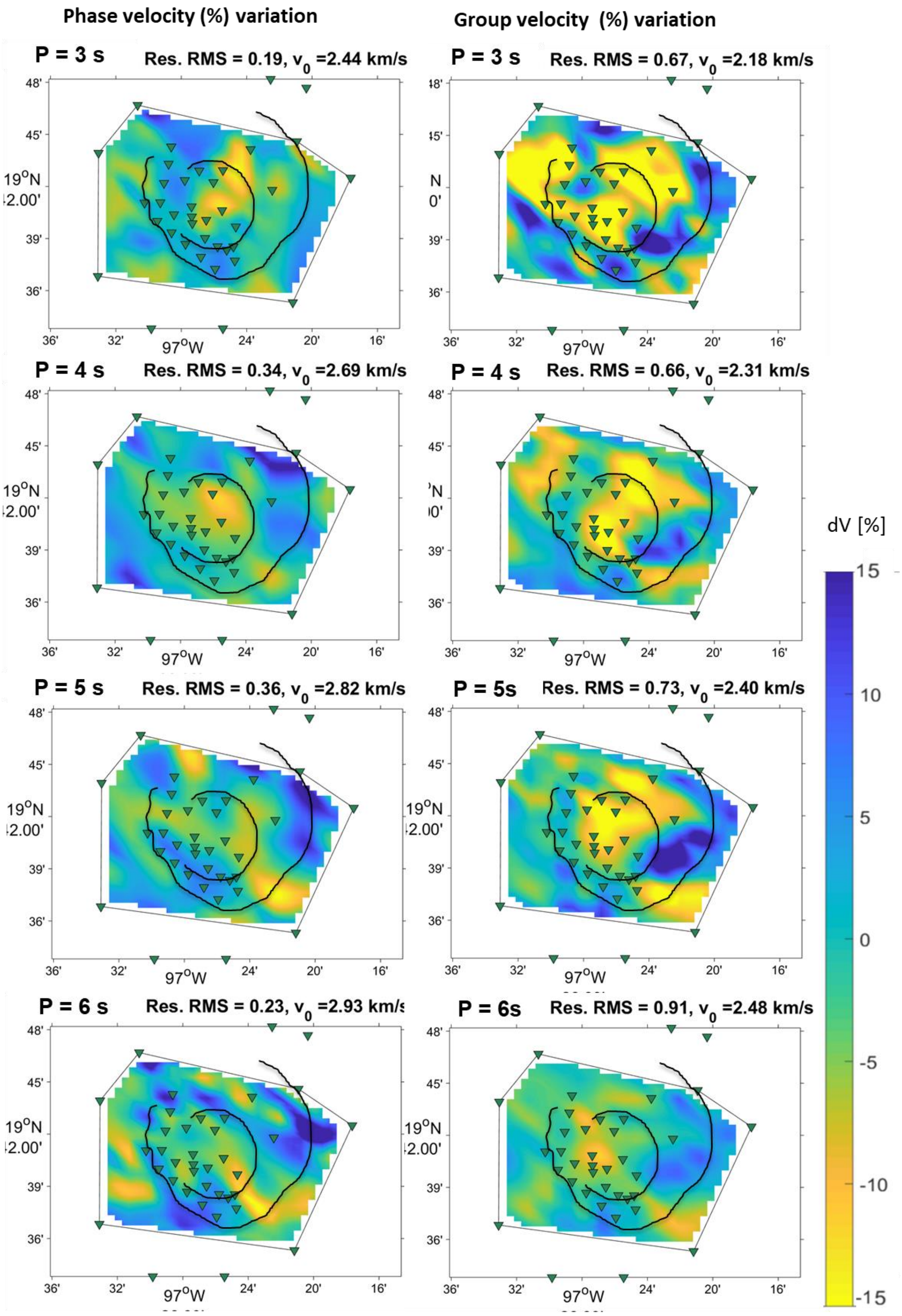

Figure 100: Tomographic results of Rayleigh phase and group velocity variations. The results show velocity variations between -15% and 15% from the reference estimated mean velocity (v_0) per period. The polygon locates the area selected after the checkerboard tests as the area of better reproduced checkers. The black this semi-circles locate the outer and inner caldera of the Los Humeros geothermal field.

In Figure 101, we show the results of both phase and group tomographic results for 5 different periods. We drop all the grid cells outside the pre-defined polygon to avoid misinterpretations due to interpolation over non-existing or not well constrained grid cells. We identify positive and negative velocity variations from an average velocity between -15% and 15%. The velocity variations seem consistent for the phase and group velocities except for the 4 s period. The average group velocities are in general lower than the phase velocities, as expected. However, we find that the group velocity anomalies are more pronounced than the phase velocity anomalies.

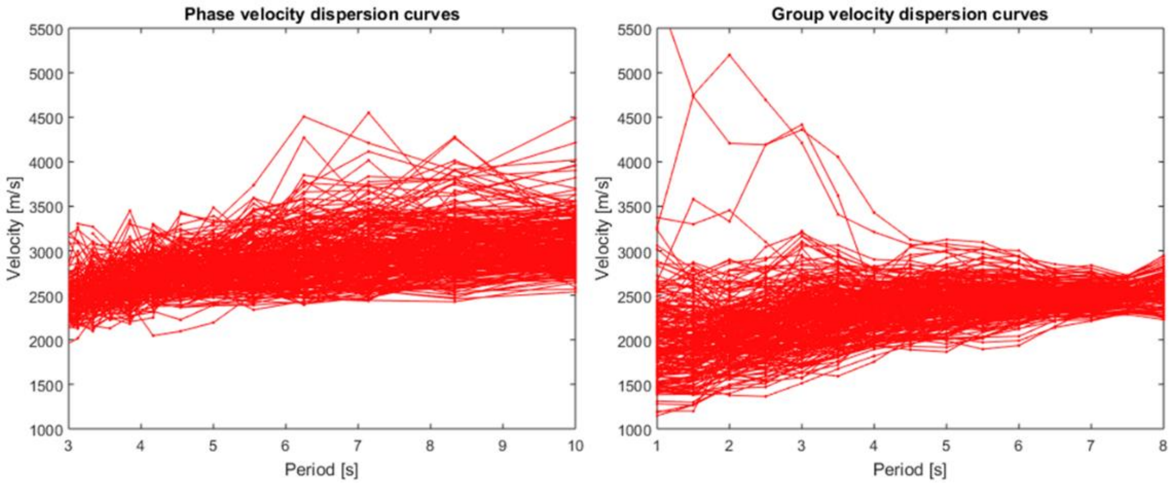

Figure 101: Phase and group dispersion curves per grid cell.

In Figure 101, we show the dispersion curves of the period dependent phase and group velocities for each grid cell for a resolution of 2 km. With few grid-cells as exception (which are removed before the depth dependent inversion), both phase and group velocity dispersion curves are smooth. As expected the velocity of the phase dispersion curves is higher than the group. For both phase and group velocity estimations we limit our analysis to reasonably covered period ranges with at least 100 measurements, which restricts us to periods between 3 and 10 seconds for phase and between 1 and 8 seconds for group. As hypothesized, while the phase velocity sample better higher periods (equivalent to higher depths), group velocity have the advantage of sampling lower periods (shallower depths) constraining each other in the overlapping periods and using the one or the other to sample higher or shallower depths.

5.5.4 Discussion and next steps

In this study we have retrieved the approximate empirical Green's functions from ambient noise by cross-correlations. We extract the surface wave part of the empirical Green's functions and estimate the phase and group velocities of the fundamental mode of the Rayleigh waves, for which we derive the corresponding phase and group tomographic results.

The data quality in general is not as good as expected. In the short-period stations there are shifts identified for some couples which are indicative of bad data quality. For some stations, especially the short periods, the noise is so amplified that even in the autocorrelations, the direct wave is barely visible. If these days "meet" other days with a lot of noise, that part of the signal correlates stronger than the surface wave that we are looking for. Therefore, most of these stations pairs are dropped by our quality control analysis.

A reliable tomography seems to be achieved with the proposed methodology (see phase pickings section), as station pairs with destructive interference are dropped out during the processing scheme. We identify velocity variations between -15% and 15% from a frequency dependent average velocity using phase and group velocities estimated independently. The phase and group velocity tomographic results displayed here can only be compared up to some point, as phase and group velocities are in essence different. In general, there is a good agreement between the estimated low-velocity anomalies in both phase and group tomographic results. Lower velocity anomalies are identified in the centre of the seismic array as opposed to higher velocities located outside the volcano caldera. This is consistent with the surface temperatures measured at the Los Humeros caldera. The group velocity tomography tends to identify a more pronounced and persistent lower velocity anomaly within the inner caldera throughout the whole frequency bandwidth.

Both estimated tomographic results should be inverted jointly in a follow up study to obtain a well constrained 3D S-wave velocity field.

5.6 Ambient noise correlation methods: Body wave retrieval

Integration of results from active seismic, passive seismic and well data reduces the uncertainties of several subsurface parameters that are of interest for cost-effective geothermal production operations in Los Humeros. In this study, we present results from the application of ambient noise seismic interferometry (ANSI) to retrieve zero-offset reflected P-waves from continuous seismic data recorded at the Los Humeros geothermal field, Mexico.

This study is inspired by encouraging results from the application of ANSI for body wave reflection retrieval that were reported in 2016 for a geothermal field located at Reykjanes peninsula, Iceland (Verdel *et al.*, 2016). Continuous broadband and short-period seismic recordings provided insightful reflection information that corresponded well, in relevant depth intervals, with reflectivity retrieved from the correlation of coda waves from a distant but very strong earthquake. That work was carried out within the context of EU's Seventh Framework research and innovation program IMAGE.

Encouraged by these findings, it was decided to conduct a new study following a similar approach within the context of the GEMex project, a European-Mexican collaboration. The purpose of GEMex is to gain improved understanding of geological structure and geothermal reservoir behaviour for two geothermal fields: Los Humeros and Acoculco.

In the following, we address data selection and processing aspects related to retrieval of reflected P-waves from Los Humeros seismic noise recordings. The retrieved reflections are compared with modelled reflectivities at two station locations at a close distance from the location where the seismic interval velocities that are used in the modelling were available from literature. The reflected P-wave information provides structural detail about the field at locations directly underneath the employed seismic stations.

5.6.1 Reflection retrieval from ambient noise

In the past two decades, a limited but steadily growing number of publications can be found on successful retrieval of P-wave reflections from ambient seismic noise. Subsurface reflection images can provide higher structural detail as compared to velocity images from tomographic inversion of surface waves extracted from ambient noise. But the challenge to provide reflectivity information with sufficient fidelity from ambient noise is generally much larger than producing useful images from noise tomography because the retrieved body waves are orders of magnitude weaker than surface waves.

Ambient noise seismic interferometry (ANSI), used in geophysical exploration and monitoring, is known to provide valuable reflection information for the shallow crust: body-wave reflections up to depths of ~1 km were successfully retrieved with ANSI-autocorrelations by e.g. Draganov *et al.* (2007, 2009, 2013) and Boullenger *et al.* (2015). But also at much larger depths, ANSI can provide valuable reflection information: Moho-reflected P-waves (PmP) were retrieved from ANSI-crosscorrelations by Ruigrok *et al.* (2011) and Poli *et al.* (2012) and Moho-reflected S-waves were retrieved by Zhan *et al.* (2010). Autocorrelations of ambient noise for frequencies up to 0.55 Hz were used by Oren & Nowack (2017) to retrieve crustal thickness and frequencies up to 1 Hz were used by Tibuleac & von Seggern (2012) to retrieve Moho-reflected P and S from autocorrelations. Crustal thickness was mapped also by Becker & Knapmeyer-Endrun (2018) with the same technique, using frequencies in the range 1.0-2.0 Hz, and more high-frequent (2.0-4.0 Hz) ambient noise was autocorrelated by Gorbatov *et al*. (2013) and Kennett *et al*. (2015) to identify PmP. The same frequency band (2.0-4.0 Hz) was used by Saygin *et al*. (2017) to determine basin-depth; their results provided indeed reflection information at shallow crustal scale. Higher frequencies, up to 8 Hz, were used by Heath et al. (2018) to determine internal volcano structure and, finally, Romero & Schimmel (2018) employed even higher frequencies than that (up to 18 Hz) to map the basement of the Ebro basin with autocorrelations from ANSI. From the here provided brief overview of ANSI examples, it can be concluded that the frequency band for which ANSI can be applied successfully for delineation of intra-crustal reflectors has broadened largely. In particular, the frequency-band has widened for ANSI-autocorrelations, and applications now range from exploration scale (up to a few km depth) at the high-frequency end to mantle scale depth at the low frequency end.

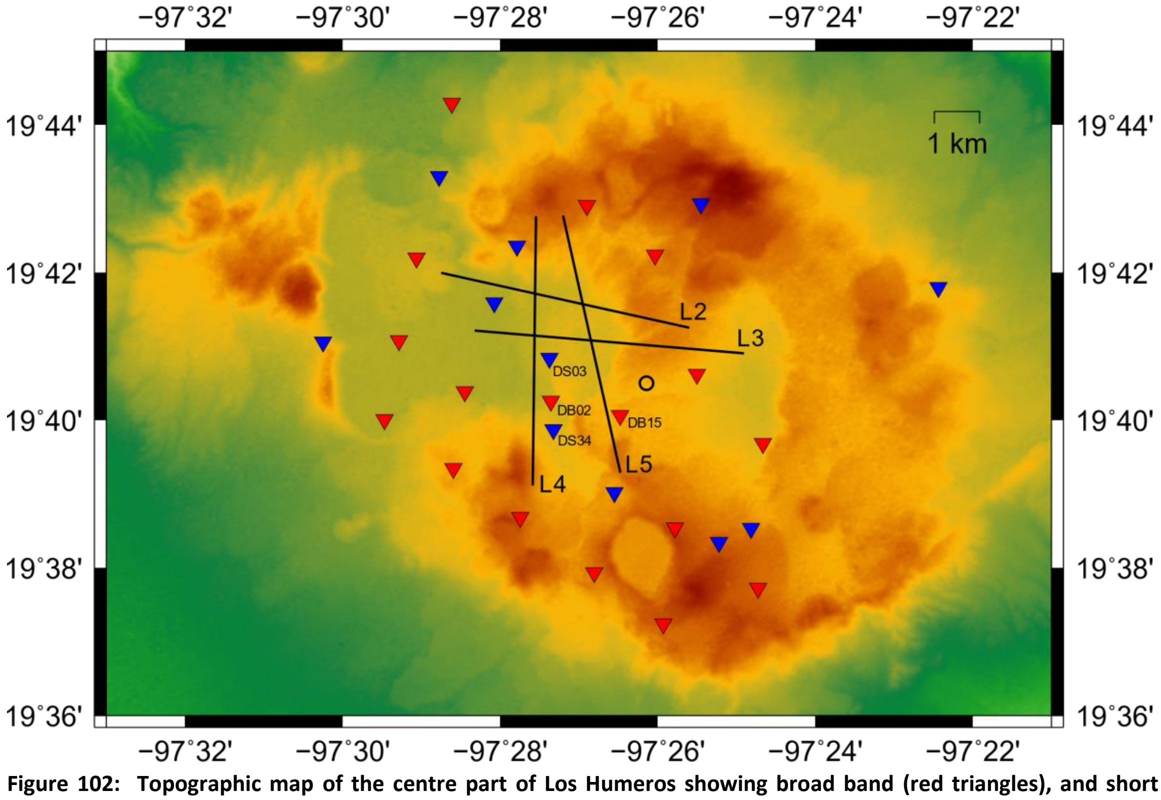

Figure 102: Topographic map of the centre part of Los Humeros showing broad band (red triangles), and short period (blue triangles) seismic station locations, the four active-source vintage seismic lines L2-L5 and the location of well H-27 (black circle).

5.6.2 Seismic and 1D reference model

Figure 102 shows the topographic map of the centre area of Los Humeros, the seismic station locations of the inner part of the deployed network, the locations of four old active-source seismic lines L2-L5 from the eighties and the location of well H-27 (black circle). The seismic network deployed for this study recorded continuously from September 2017 until September 2018. In the following, we will only discuss results from data recording during 2017. A 1D reference velocity model is used for comparison of modelled reflectivities with those retrieved from ambient noise. The blocky seismic velocity profile shown in Figure 103 was derived years ago using a reflection seismic profile produced by COMESA using Dix' formula in the vicinity of well H-27, see Figure 102 and also Figure 6 of Lermo (2008). This location more or less coincides with the centre of the derived seismic profile discussed in that paper. We select two seismic stations from the current network for which we describe ANSI reflectivity results: Trillium Compact broadband station DB15 and short-period Mark Sensor station DS03 (see Figure 102). Based on this selection we take an average of 2800 masl (metres above mean sea level, green line in Figure 103) for constructing an initial reference velocity model for finite-difference (FD) modelling, which is 400 m below the reference level used for the original model referred to in Lermo's 2008-paper. These two stations were selected based on position (neighbourhood of active seismic lines for later comparison), seismic data availability, and a lack of instrument-related problems.

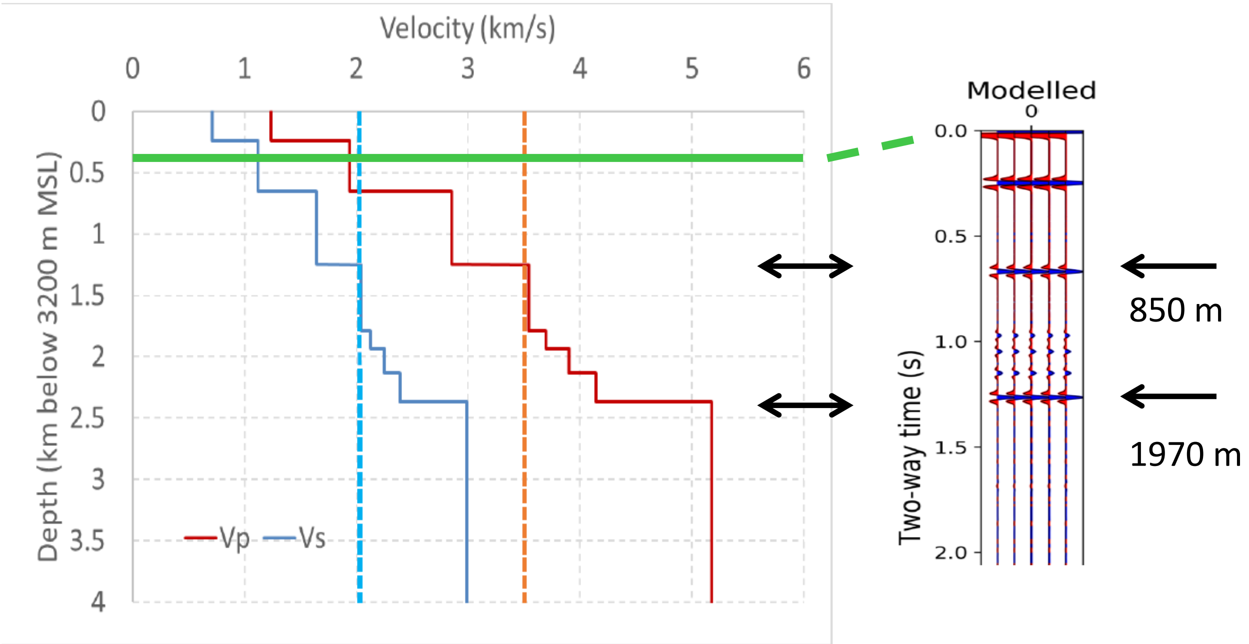

Figure 103: Left: 1D P-wave (red) and S-wave (blue) blocky velocity profiles derived from seismic data at a location close to well H-27 (see Figure 102). A constant Vp/Vs is assumed: 1.732. After Hurtado (2001) and Lermo (2001). Right: FD-modelled reflectivity trace with 15 Hz Ricker wavelet and density taken constant at 2.85 g/cm3.

5.6.3 Passive Seismic data Analysis

In order to obtain an impression of the variability, for an arbitrary day (selected was 16 November 2017, viz. Julian day 320), of the spectral ambient noise characteristics of stations DS03 and DB15, we show in Figure 104 two 1-hour power spectral density (PSD)-displays for each station: one at 3 am local time and the other at 3pm. Clipping levels are constant per station. Notice the relatively constant 'background' noise level for frequencies below ~20 Hz. It can be clearly observed that strong short-lasting (in the order of minutes) noise bursts occur for both stations in the entire frequency band at daytime (frequencies lower than 5 Hz are tapered off).

This suggests that there are two categories of ambient noise that should be distinguished: one for frequencies lower than 20 Hz and the other for all frequencies in the studied spectral band (up to 50 Hz).

In Figure 105, we show the autocorrelation panel for station DB15, which is located at a distance of approximately 1 km from well H-27, the assumed location close to which the 1D seismic interval velocity model was derived. Each trace represents a single day-stack (the horizontal axis represents Julian days). In addition, the FD-modelled 1D reflectivity-trace for the model shown in Figure 103 is presented (modelled trace is repeated for convenience). Ideally, under perfect subsurface noise illumination conditions, each auto correlated trace represents the global 1D zero-offset reflection response, viz. the primary reflection response plus all internal and free-surface multiples. We can see a strong variability from day to day in the stacked autocorrelations, but we fortunately also can observe continuity in the panel at various two-way-reflection times, showing up as horizontal alignments. Two strong shallow reflections are highlighted, that are taken from the modelled reflection trace, and that correspond with two large acoustic impedance contrasts that are indicated with arrows in Figure 103. Both reflections show an encouraging match for a large majority of day-stack-traces, meaning that for long periods of time (weeks to months) the autocorrelation-stacks for this station at least suggest to carry useful reflection information. The same holds true, but to a somewhat lesser extent, if we filter the data (the field data for this seismic station as well as the modelled data) in the frequency band 3-9 Hz, see Figure 106. Figure 107 and Figure 108 show the comparable results for short-period station DS03, which is located at a distance of approximately 2 km from well H-27 (see Figure 102). We can observe similar phenomena as for station DB15, albeit that the variability of the single-day autocorrelation stacks is somewhat larger in the low-frequency band (Figure 108). On the other hand, the shallow strong reflector (highlighted in green) stands out even more clearly in the 10-40 Hz panel (Figure 107).

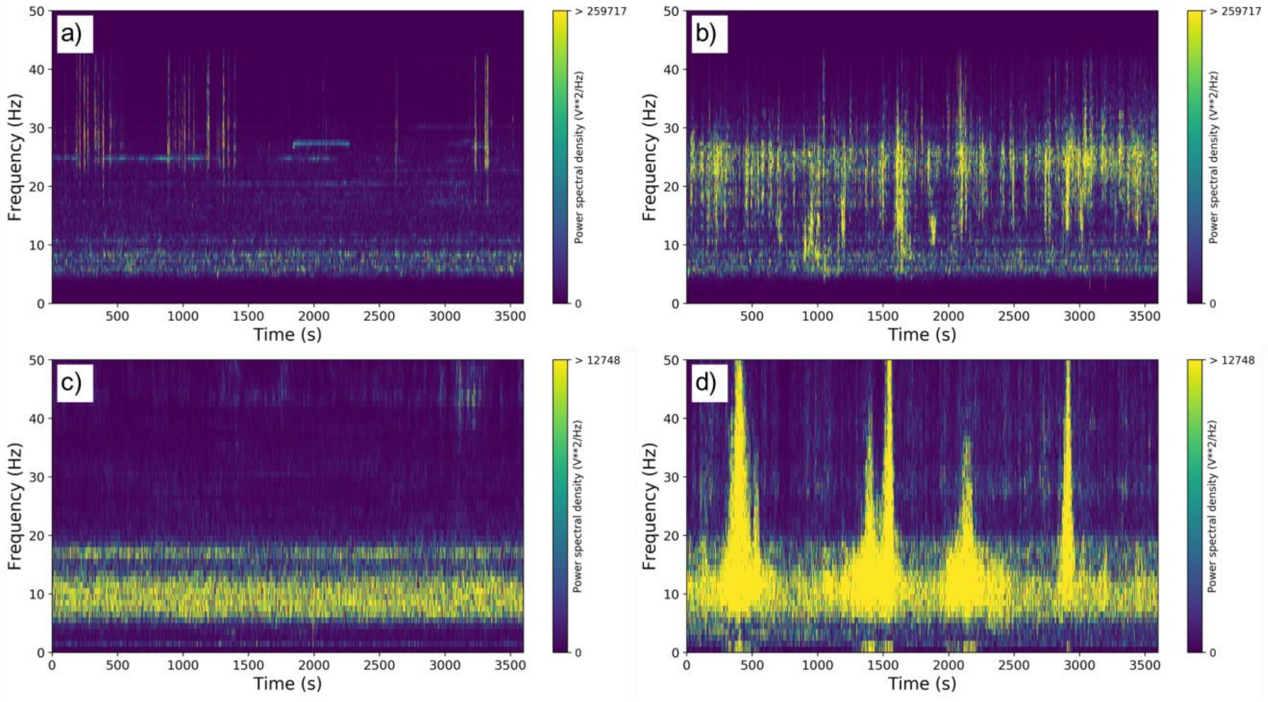

Figure 104: Power spectral density (PSD) displays showing ambient noise variability for two one-hour time windows of station a) DS03, UTC9, 3am local time, b) DS03, UTC21, 3 pm local time, c) DB15, UTC9, 3am local time, and d) DB15, UTC21, 3pm local time. The clipping level per station is constant. Notice the relatively constant 'background' noise level for frequencies below ~20 Hz.

We performed a simple 1D ambient noise reflection interferometry study using passive seismic data recorded during the second half of 2017 from only two selected seismic stations from the Los Humeros seismic network that was installed within the context of the combined European-Mexican project GEMex. The stations were selected based on data-availability and -quality as well as proximity to a location at which seismic interval velocity information was available from literature.

We observe clear correspondence between modelled reflectivities and single-day autocorrelation stacks produced from the field data. We consider these results as indications that passive station data contain valuable subsurface reflection information that may be used in a possible future follow-up study. In such a study, additional ANSI-processing should be performed to improve the quality of the day-stacks, such as source-wavelet deconvolution to sharpen the reflection events. Also, additional effort should be spent on 1) removal of undesired noise (bursts), 2) use of data from more stations and 3) comparison with active-seismic imaging results for lines L2-L5. Our results suggest that the locally derived 1D seismic interval velocity profile close to well H-27 in the shallow interval up to ~2 km depth, viz. up to and within the producing geothermal reservoir, can be laterally extended in the directions of DB15 (at ~1 km lateral distance) and DS03 (at ~2 km distance), which is relevant for the understanding of the geothermal reservoir that is located in the 1500–2500 metres depth range.

The ANSI auto-correlation technique applied for zero-offset reflectivity retrieval can be regarded as a promising technique, with relatively high vertical subsurface image resolution, for obtaining near-vertical velocity contrast information, corresponding with location information (depths) of near-horizontal reflectors.

As such, results from the presented passive-seismic method may partially complement and partially confirm subsurface information derived from active-seismic, that can only be acquired at a higher cost, which is more labour-intensive and which has more impact on the environment.

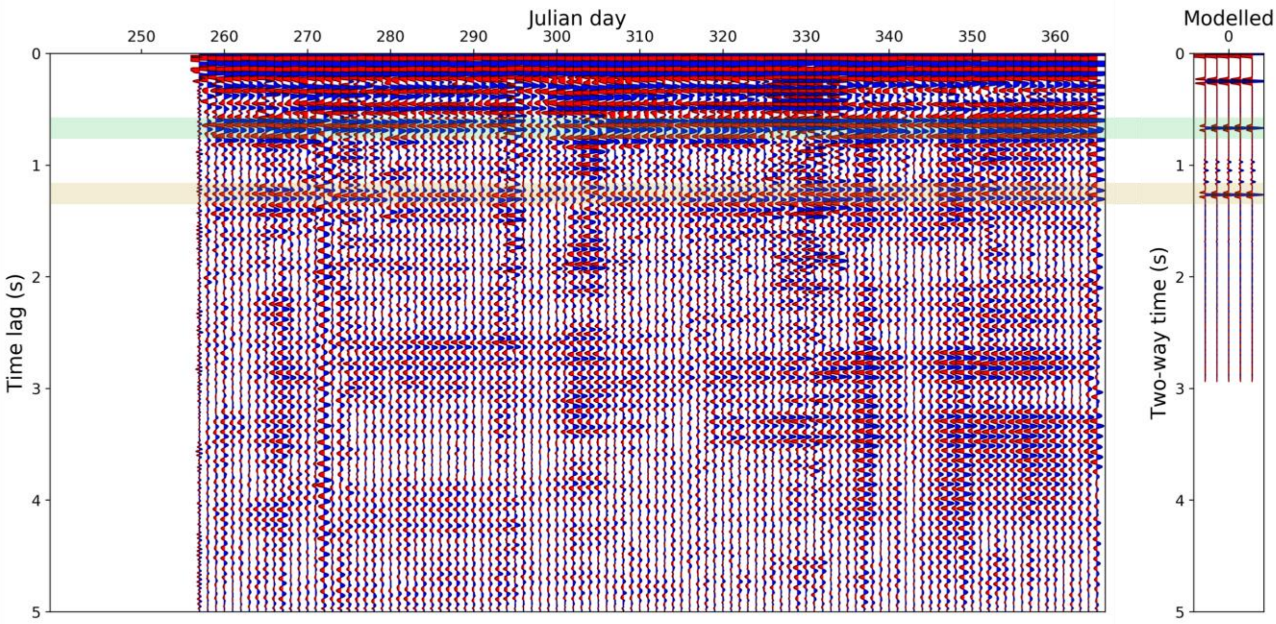

Figure 105: Panel of 10-40 Hz bandpass-filtered day-stacks of auto-correlated ambient noise (vertical component) recorded at station DB15 throughout year 2017 (from September onwards) in a combined display with FD-modelled 1D reflection response (bottom). Two key reflectors are highlighted in green and orange.

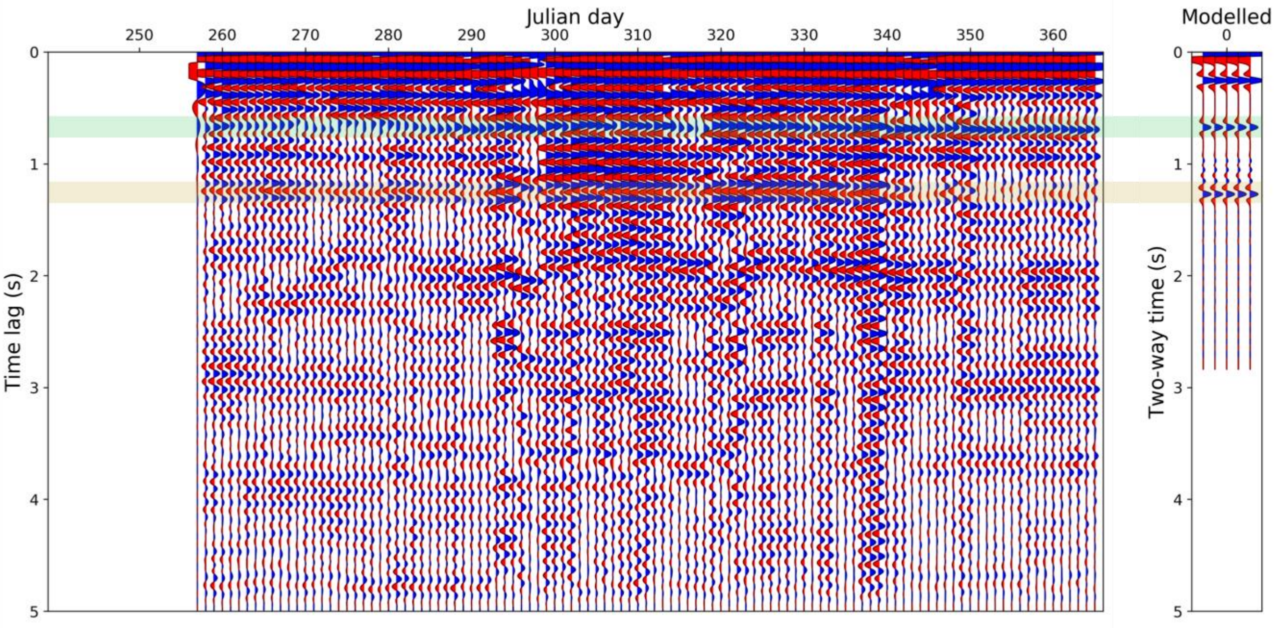

Figure 106: Panel of 3-9 Hz bandpass-filtered day-stacks of auto-correlated ambient noise (vertical component) recorded at station DB15 throughout year 2017 in a combined display with FD-modelled 1D reflection response (bottom). Two key reflectors are highlighted in green and orange.

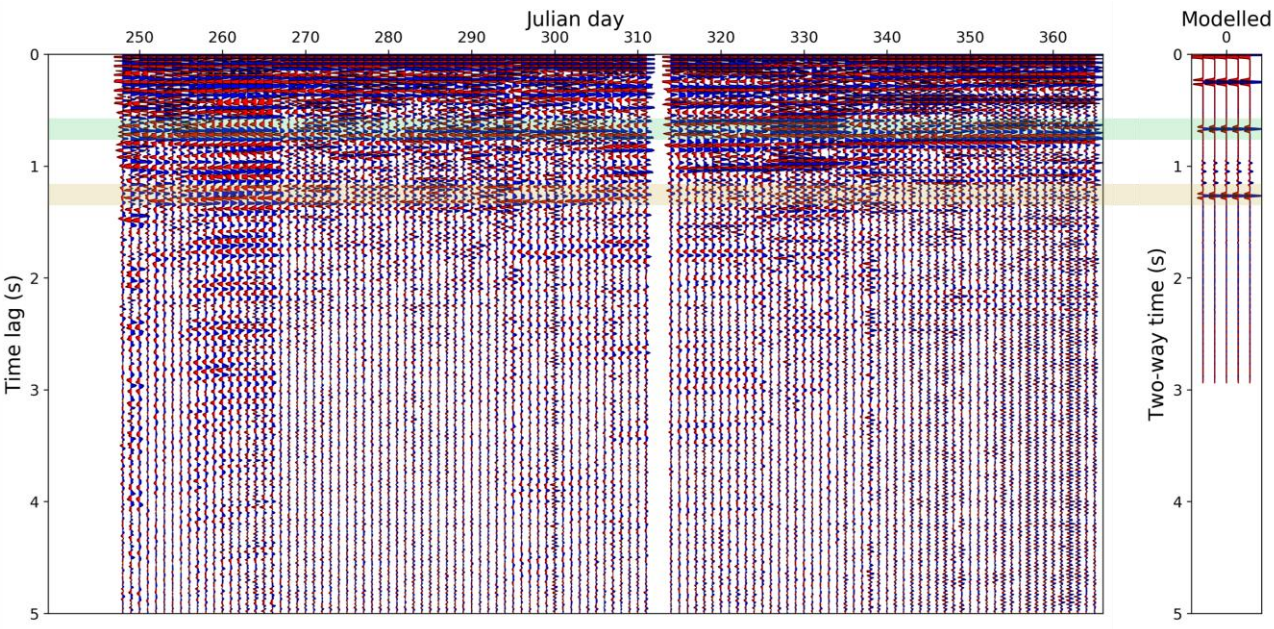

Figure 107: Panel of 10-40 Hz bandpass-filtered day-stacks of auto-correlated ambient noise (vertical component) recorded at station DS03 throughout year 2017 (from September onwards) in a combined display with FD-modelled 1D reflection response (bottom). Two key reflectors are highlighted in green and orange.

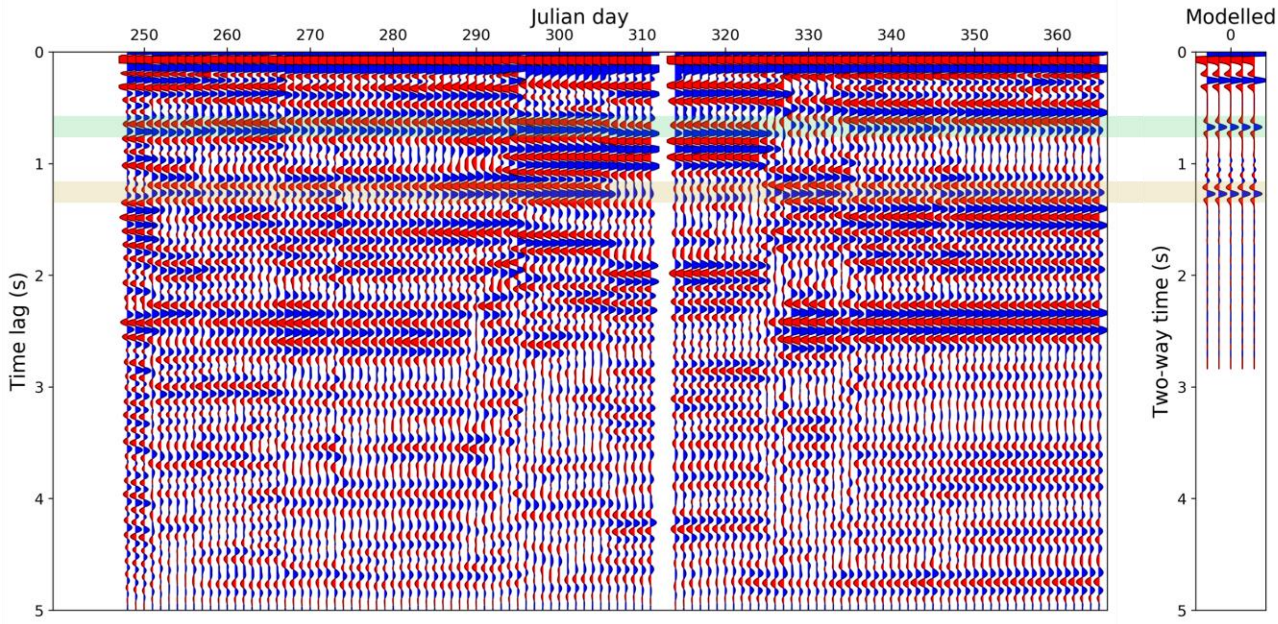

Figure 108: Panel of 3-9 Hz bandpass-filtered day-stacks of auto correlated ambient noise (vertical component) recorded at station DS03 throughout year 2017 in a combined display with FD-modelled 1D reflection response (bottom). Two key reflectors are highlighted in green and orange

5.7 Beamforming method

5.7.1 Introduction

We perform three-component (3C) beamforming, a seismic array technique that provides the polarization, direction of arrival (DOA), velocity, and incidence angle of a seismic wave crossing the array in a given time-frequency window. Applied to ambient seismic noise data, it allows us to extract the dominant wave mode (e.g. Rayleigh or Love wave) in subsequent time windows and the corresponding propagation parameters as a function of frequency (Riahi et al., 2013; Löer et al., 2018).

The suitable frequency-wavenumber range is defined by the array geometry. As a rule of thumb, we apply an approximation by Tokimatsu (1997)

$$2d_{min} < \lambda < 3d_{max} \qquad (5.1)$$

where, d_{min} and d_{max} are the minimum and maximum station spacing. Since wavenumber $k = 1/\lambda$ and $f = k \cdot v$, the corresponding limits can be derived from Eq. 1 by considering a minimum and maximum velocity value. Additionally, the so-called array response function (ARF), which gives us the theoretical beam response of a wave coming from directly below ($k = 0$), also allows us to estimate the resolution range of the array by considering the width of the central maximum and the occurrence of sidelobes (Rost & Thomas 2009). In general, the array aperture controls the width of the central maximum (large aperture – sharp maximum, small aperture – wide maximum) and the station spacing controls the location of sidelobes (dense spacing – far out sidelobes, sparse spacing – close sidelobes).

For surface waves, the sampled depth depends on the respective wavelength and can be estimated for Rayleigh waves (Lowrie, 2007) as $z_R = 0.4\,\lambda_R$. Hence, Eq. (1) also allows us to approximate the minimum and maximum depth we can investigate with a given array geometry.

Finally, from 3C beamforming we obtain estimates of surface wave dispersion curves (1D-average over the whole array), frequency-dependent anisotropy, i.e., velocity as a function of DOA, and frequency-dependent wavefield composition.

5.7.2 Results

We use ambient seismic noise data recorded at the broadband (BB) stations deployed in Los Humeros. The restriction to broadband stations is due to the fact that we are interested in the low frequency range well below 1 Hz to which short-period stations are less sensitive. Analysing the ARF of the complete BB-array, we find that it contains unfavourable sidelobes close to the main maximum (Fig. 1a) due to the incoherent station spacing within the array. We thus decided to split the BB-array into two subarrays containing (1) the dense broadband stations (DB; up to 16 stations) and (2) the sparse broadband stations supplemented by three stations of the DB-array (SBx; up to 10 stations) to fill a central gap. The corresponding ARFs are shown in Fig. 1 (b) and (c). Note that both arrays cover different wavenumber ranges and while being processed separately are meant to complement each other in the analysis. Station spacings and corresponding frequency ranges are summarized in Table 1 for $v_{min} = 1.5\ \mathrm{km\ s^{-1}}$ and $v_{max} = 5.0\ \mathrm{km\ s^{-1}}$.

Table 3. Minimum and maximum station spacing of the two subarrays DB and SBx and the corresponding depths and frequency ranges.

Array	d_{min}	d_{max}	z_{min}	z_{max}	f_{min}	f_{max}
DB	1.6 km	13.9 km	1.3 km	16.7 km	0.12 Hz	0.47 Hz
SBx	7.2 km	54.9 km	5.8 km	65.9 km	0.03 Hz	0.10 Hz

We have performed 3C beamforming for data recorded on the DB-array during 18 days in 2017 (277 and 284-300), when at least 14 stations were operating. The analysis, as conducted so far, concentrates on the maximum peak in each beam response and therefore extracts the strongest mode only. Figure 110 shows slowness-frequency histograms for fundamental Rayleigh waves (a), its first overtone (b), and Love waves (c). Figure 110 (d) shows the corresponding dispersion curves derived as the median of each distribution. Note that higher mode Rayleigh waves travel much faster than the fundamental mode and thus the derived frequency limits in Tab. 1 do not apply. Figure 111 gives an overview of the DOA (Direction of Arrival) for fundamental mode Rayleigh and Love waves at selected frequencies. Despite the vicinity of the array to the Gulf of Mexico (GoM), we find that especially for frequencies around $f = 0.16$ Hz surface wave noise arrives predominantly from the Pacific ocean and only for frequencies above 0.22 Hz noise from the GoM provides a noticeable contribution. Figure 112 demonstrates that for most frequency bands the azimuth range covered by the dominant DOA is very limited and thus an anisotropy analysis is not applicable. We show an example for Rayleigh waves at $f = 0.25$ Hz where the azimuth range is broader and anisotropy parameters can be derived by fitting a curve to the slowness-frequency histogram (Figure 113; to be completed). Finally, Figure 113 gives an idea about the frequency-dependent modal composition of the maximum picks within the noise wavefield. As expected, Rayleigh waves are the dominant mode peaking around the secondary microseism, while the contribution of body waves increases with higher frequencies. We have to note, however, that the range of resolvable frequencies provided in TAB is not yet adapted to body waves, which have incidence angles $i < 90°$ and thus higher apparent velocities.

5.7.3 Outlook

The analysis will be complemented by data from 2018 and the SBx array. Dispersion curves are to be inverted for a 1D velocity profile that describes a lateral average over the region covered by both arrays. This will include depths down to 17 km for the DB-array only and down to 70 km – albeit at a lower resolution – for the SBx-array. A time-lapse analysis of anisotropy data in suitable frequency bands is supposed to investigate correlations between geothermal production and amplitude or direction of measured anisotropy.

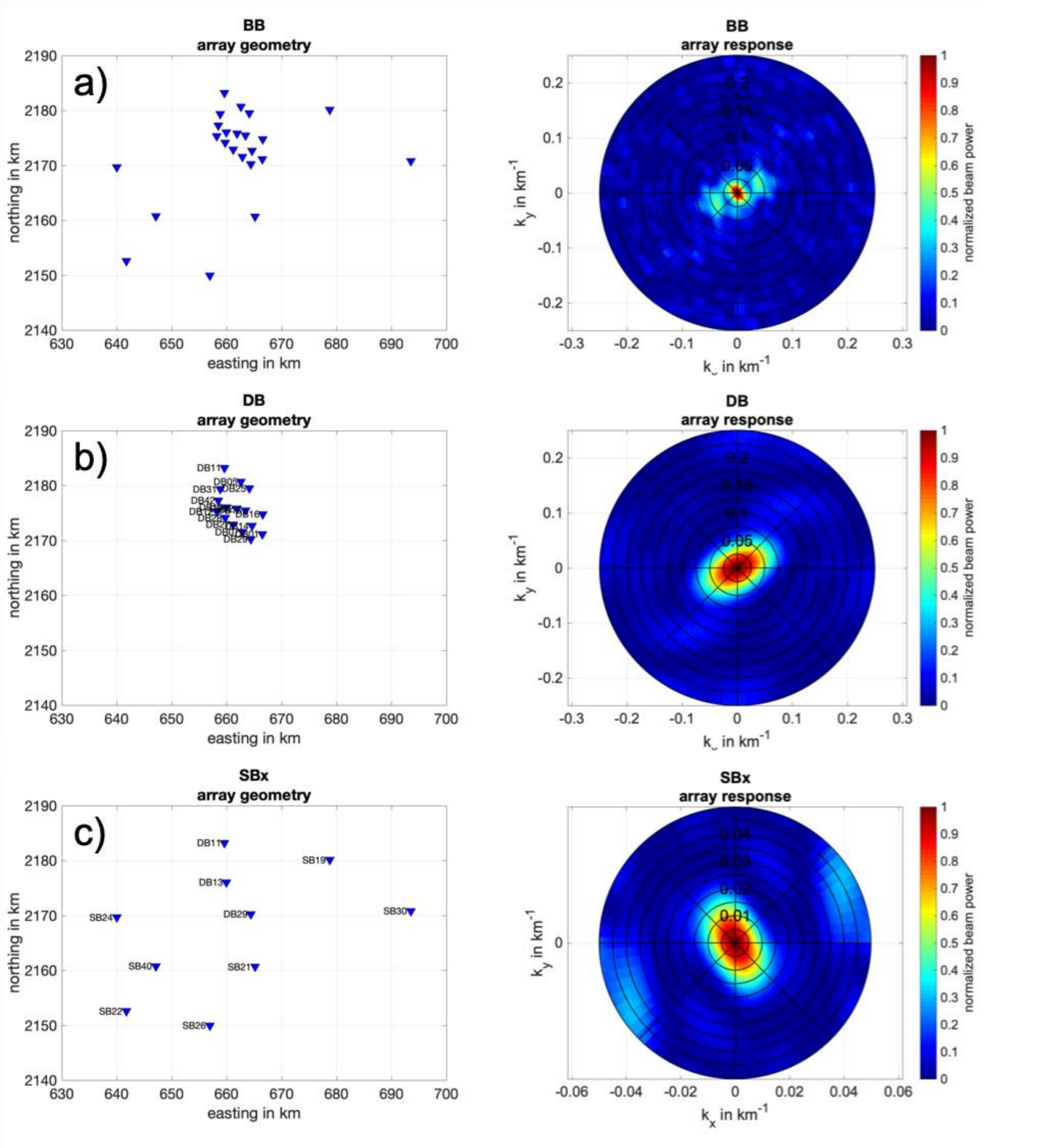

Figure 109: Array geometries and array response functions (ARFs) of (a) all broadband stations (BB), (b) the dense broadband stations (DB) and (c) the sparse broadband stations plus three DB-stations (SBx). The resolvable wavenumber range is $\mathbf{0.03 - 0.30\ km^{-1}}$ for the DB-array and $\mathbf{0.01 - 0.07\ km^{-1}}$ for the SBx array.

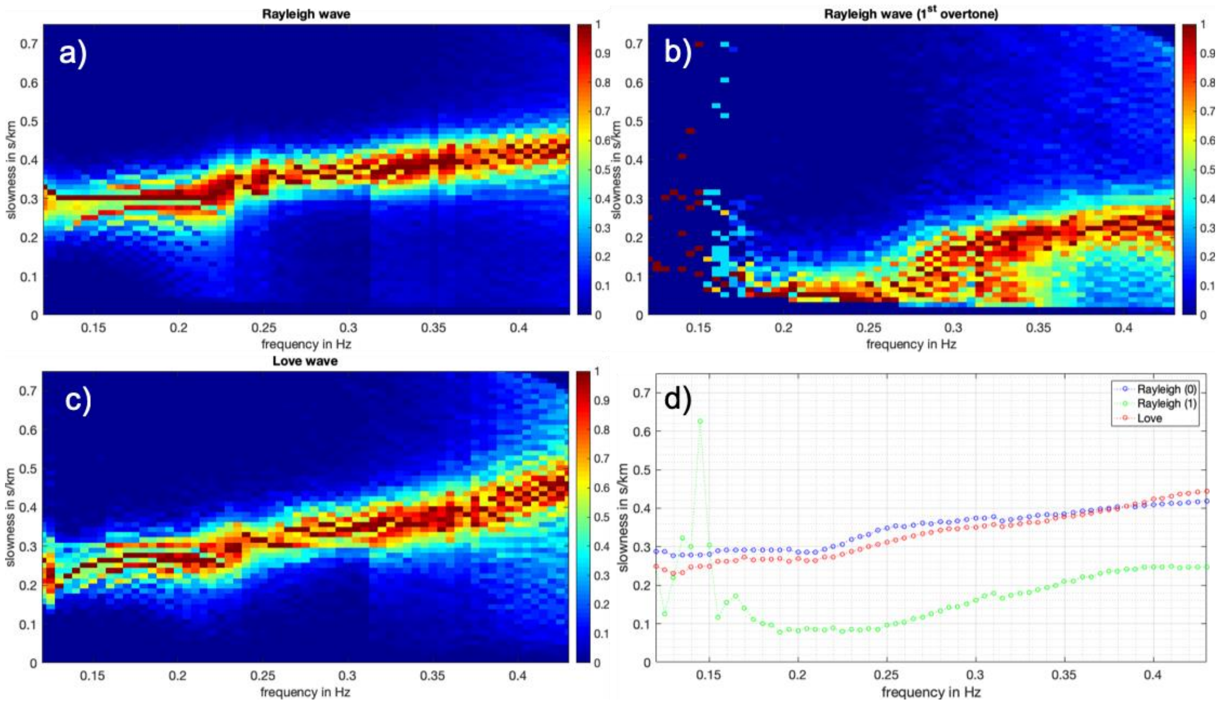

Figure 110: Slowness-frequency histograms for (a) fundamental mode Rayleigh waves, (b) first higher mode Rayleigh waves, and (c) Love waves. The slowness sampling is $0.013\ \mathrm{s\ km^{-1}}$and was adapted to the lowest frequency. (d) shows the corresponding dispersion curves extracted as median of the distributions in (a), (b), and (c).

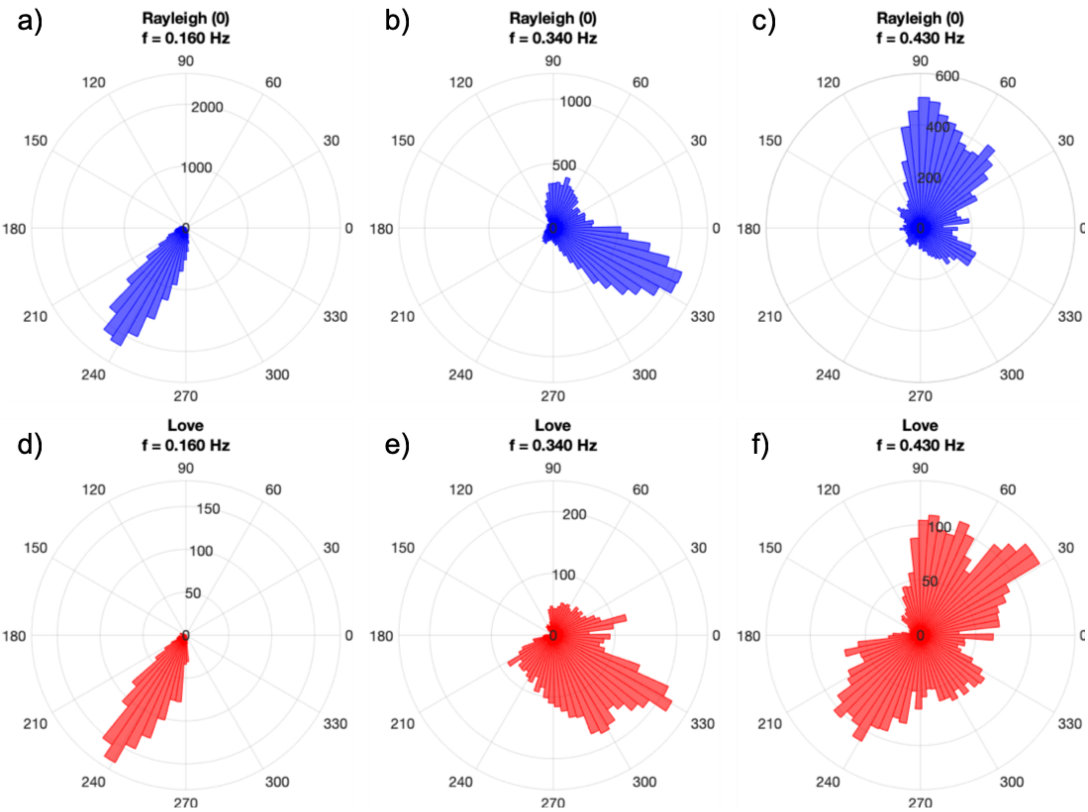

Figure 111: Direction of arrival for fundamental mode Rayleigh waves (a-c) and Love waves (d-e) for frequencies 0.16 Hz, 0.34 Hz and 0.43 Hz.

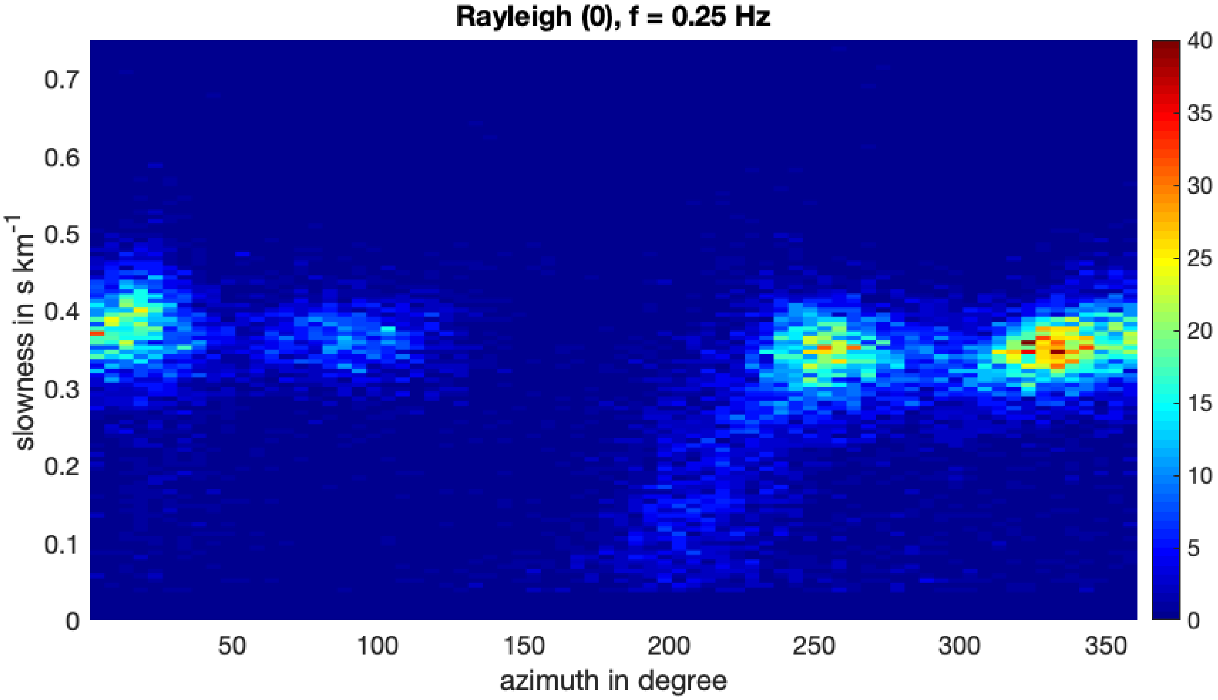

Figure 112: Slowness-azimuth histogram of fundamental mode Rayleigh waves at 0.25 Hz.

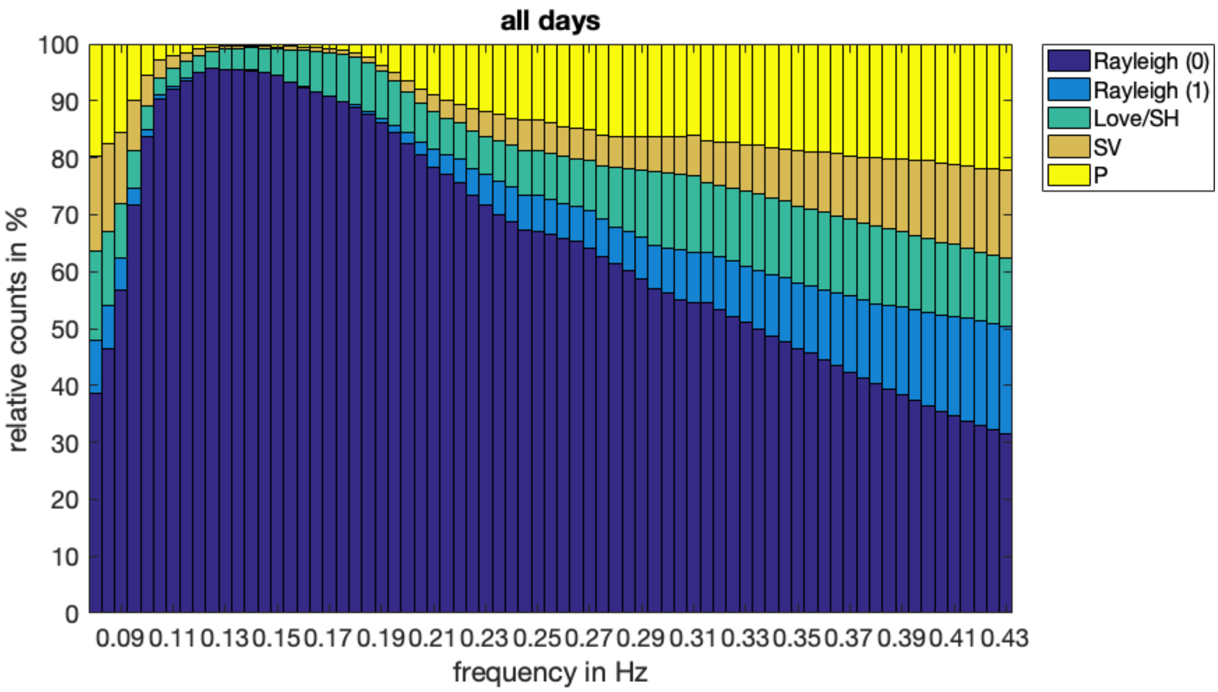

Figure 113: Modal wavefield composition derived from maxima of beam responses.

5.8 Time-lapse attributes

5.8.1 Introduction

Low-frequency effects associated to hydrocarbon reservoirs were first described in Soviet/Russian literature where seismic stimulation was used to enhance oil recovery (Beresnev & Johnson, 1994; Nikolaevskiy et al., 1996). Signals of higher amplitude were recorded at the surface above hydrocarbon-bearing zones, both during the active source emission period and, more surprisingly, also after it stopped (Kurlenya & Serdyukov, 1999, see Fig. 1.3a). Low-Frequency Passive Seismic, in the sense of hydrocarbon exploration using ambient noise amplitude spectra, appeared as a subject with the discovery by Dangel et al. (2003) of amplification anomalies in the ambient noise spectra measured above 15 hydrocarbon reservoirs throughout the world. The affected frequency range was considerably lower than in the active case: 1.5-4 Hz (Fig. 1.3b).

Dangel et al. (2003) used the term “tremor” to describe the supposed hydrocarbon signature in the ambient noise spectrum because of an “astonishing similarity” with volcanic tremors. This analogy lead to a preliminary interpretation of the “hydrocarbon micro-tremor” (HMT) as a result of oil/gas bubble oscillation within water-wetted pores of the reservoir rock. In the context of hydrocarbon exploration, this method looked promising, since it could allow to get a hydrocarbon potential map at low cost, without using any active source of seismic emission. In the late 2000s - early 2010s, a technology based on HMT was widely promoted by the Spectraseis company under the name HyMas (hydrocarbon micro-tremor analysis, Graf et al., 2007). Several aspects of this technology were patented (Saenger, 2008; Saenger et al., 2009; Saenger, 2009; Podladchikov et al., 2010; Kelly et al., 2013), mainly concerning particular ways of extracting relevant attributes from the ambient noise, statistically treating them, and converting them into hydrocarbon potential maps. Another patent concerned reservoir imaging based on the time-reverse imaging (TRI) exploiting the HMT signals in the time domain (Saenger et al., 2010).

In 2009, Spectraseis launched a wide consortium (Low-Frequency Seismic Partnershift) in close collaboration with the Swiss Federal Institute of Technology (ETH Zürich). The aim of the consortium was to assess the physical nature of HMT, through numerical modelling, sample tests in laboratory and repeated field surveys. This gave rise to a significant number of publications (e.g. Steiner et al. 2008; Lambert et al., 2009; Saenger et al., 2009; Quintal, 2012; Lambert et al., 2013). The subject rapidly became controversial, as some authors reported failures of the method for individual hydrocarbon fields. An intense debate arised on the pages of Geophysical Prospecting after the publication by Lambert et al. (2009) of the results of a passive survey above the Voitsdorf oil and gas field, Austria, and concluding to some degree of correlation between the ambient noise amplitude attributes and the actual location of hydrocarbon-bearing zones. The methods and conclusions of Lambert et al. (2009) were severely criticized by Green & Greenhalgh (2010), according to whom the claimed HMT was in fact a combination of artificial noise and shallow layer effects. Lambert et al. (2010) then replied to this criticism, insisting that neither the effects mentioned by Green & Greenhalgh (2010), nor the hydrocarbon-related nature of the “microtremors” could be excluded.

It is reported that the signature of a geothermal reservoir (Kazantsev et al. 2017) appears quite different from what was observed at hydrocarbon reservoir sites (reported so far). Instead of the amplification of the vertical component, they observe an attenuation of all the components. Since the attenuation for the horizontal components is stronger than for the vertical one, the resulting signature is an increase of the V/H ratio. In fact, this is similar to the simulation results of Lambert et al. (2013). Compared to the hydrocarbon context, higher fluid-related attenuation may be expected in the geothermal context because of a higher matrix heterogeneity (fracture porosity), and a thicker fluid system (Grab et al., 2017b), which gives more validity to the simulation parameters used by Lambert et al. (2013).

5.8.2 Methods

5.8.2.1 PSD-IZ Value

The PSD-IZ value was introduced by Saenger et al. (2009). Here, PSD is the Power Spectral Density and IZ stands for the Integral of the vertical component. Originally this method was developed to characterize the Power Spectral Density of a passive seismic wavefield over a hydrocarbon reservoir. Figure 114 shows an example of a PSD curve and how the PSD-IZ value is determined.

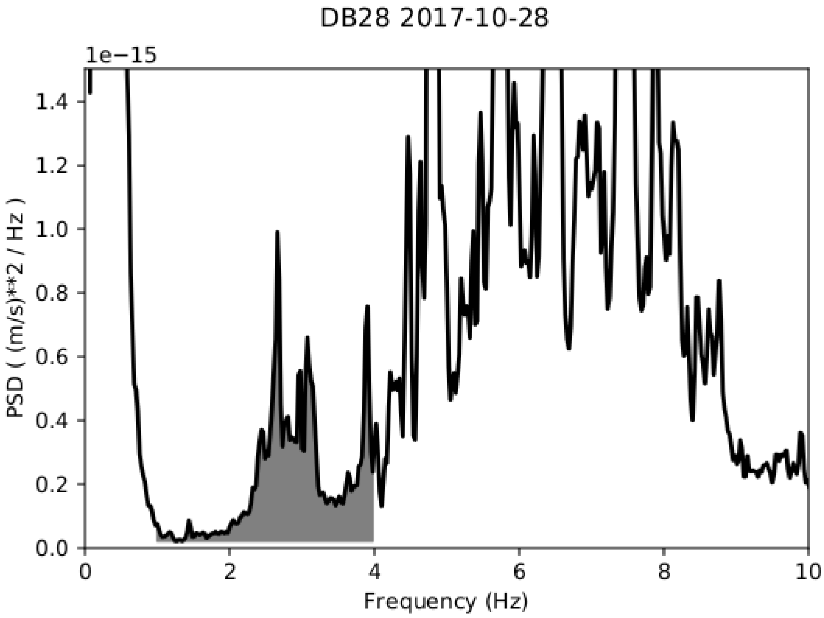

Figure 114: Example for the PSD-IZ value at the 29th of October 2017 at station DB28. The grey area between 1 and 4 Hz illustrates the PSD-IZ value. Due to fact that the PSD curve is estimated from the lowest 10 % of all PSD curves, all resulting curves are highly similar in the lower frequency range.

Welch's average periodogram method (Welch, 1967) is a standard method to determine the PSD of a time series. This method is implemented in the Python library Matplotlib (Hunter, 2007). To get rid of any artefacts, the time series of each day is divided into 60 s long subwindows. Welch's method is applied on each detrended subwindow and the instrument response is removed in the frequency range. Afterwards, the resulting PSD is saved in an array. Finally, the average of each PSD in a frequency range from 1 to 10 Hz is estimated to get the lowest 10 % of all PSD curves of one day. These PSD curves are used to get the final average PSD curve of one day, excluding artefacts e.g. by human activities. At last, the minimum of the PSD curve around 1 Hz is taken. The integral above this minimum defines the PSD-IZ value. For this site, the PSD-IZ value is estimated in a frequency range from 1 to 2 Hz and from 1 to 4 Hz. This procedure is repeated for each day and station.

5.8.2.2 V/H-Ratio

The V/H-Ratio is used as a second attribute to characterize the site. Spectral ratios are more stable in time than the absolute spectra of each component (Bard, 1999). To determine the spectral ratios without any artefacts in the time series, the subwindows of the 10 % lowest PSD curves are used. The 60 s long time series of each component (one vertical and two horizontal) is detrended and the mean is removed. To avoid side lobe leakage a 5 % cosine taper is applied on both sides of the time series. The time series are Fourier transformed and the horizontal components are merged by

$$H(f) = \mathrm{sqrt}((H_N(f)^2 + H_E(f)^2)/2), \quad (5.2)$$

where $H_N(f)$ and $H_E(f)$ denote the Fourier transform of the north and the east component, respectively. The final spectral ratio S(f) is given by

$$S(f) = H(f)/V(f), \quad (5.3)$$

where V (f) denotes the Fourier transform of the vertical component.

To compare and to map the V/H-Ratios of each station, the full integral from 1 to 2 Hz and from 1 to 4 Hz is taken into account. Figure 115 shows an example of the spectral ratio. The integral in both frequency ranges is computed for each day and station.

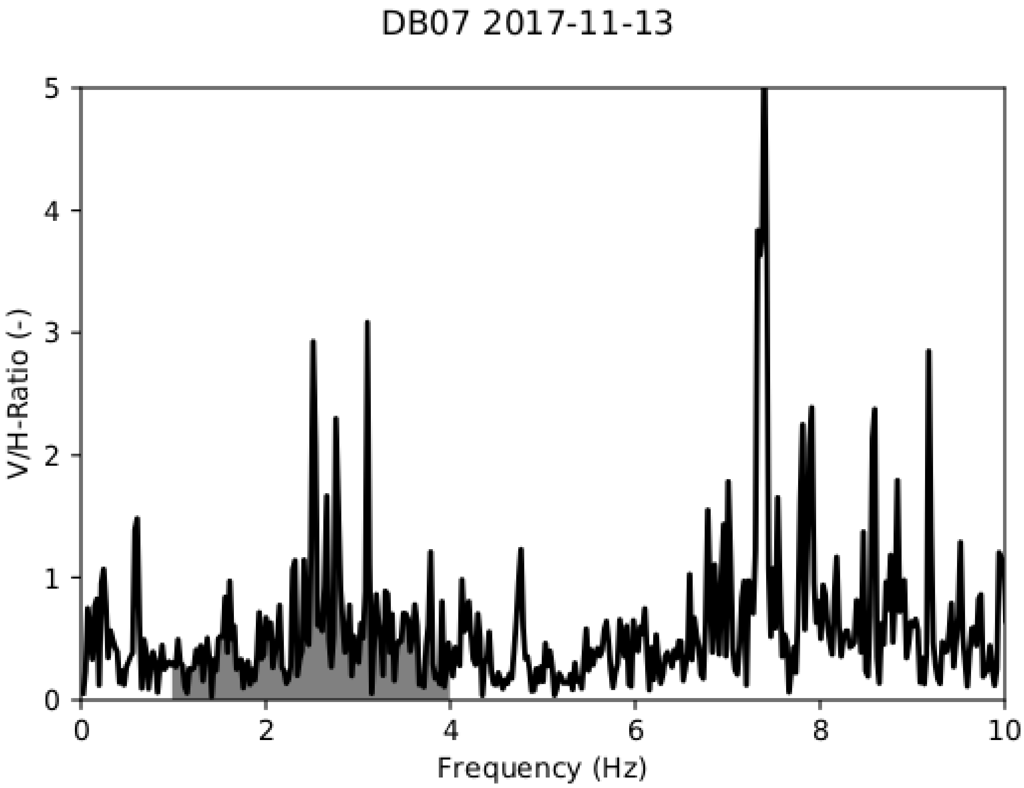

Figure 115: V/H-Ratio between 0 and 10 Hz of station DB07 at 2017-11-13. The ratio has no physical unit and the grey shaded area illustrates the full integral under the spectral ratio curve between 1 and 4 Hz.

5.8.2.3 Results

The PSD-IZ value and full integral of the spectral ratio of each station is plotted into a topographic map. The values between the stations are interpolated over a 2D grid, using a cubic spline interpolation from the Python library Scipy (Jones et al., 2001). Note, not all stations are used for mapping due to some data gaps.

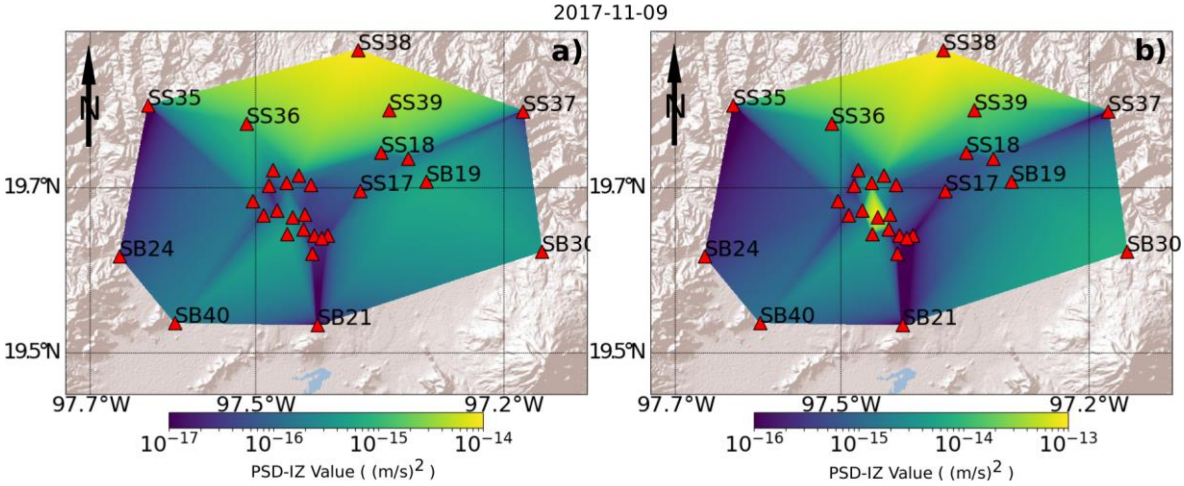

Figure 116: Maps of the interpolated PSD-IZ value at 2017-11-09. a) Map for the frequency range 1 to 2 Hz. The PSD-IZ value increases in northern direction. b) Map for the frequency range 1 to 4 Hz. The PSD-IZ value increases in northern direction but it has its maximum in central part of the site. Note, due to data gaps, not every stations is displayed in the map. The PSD-IZ value does not change significantly over time at this site.

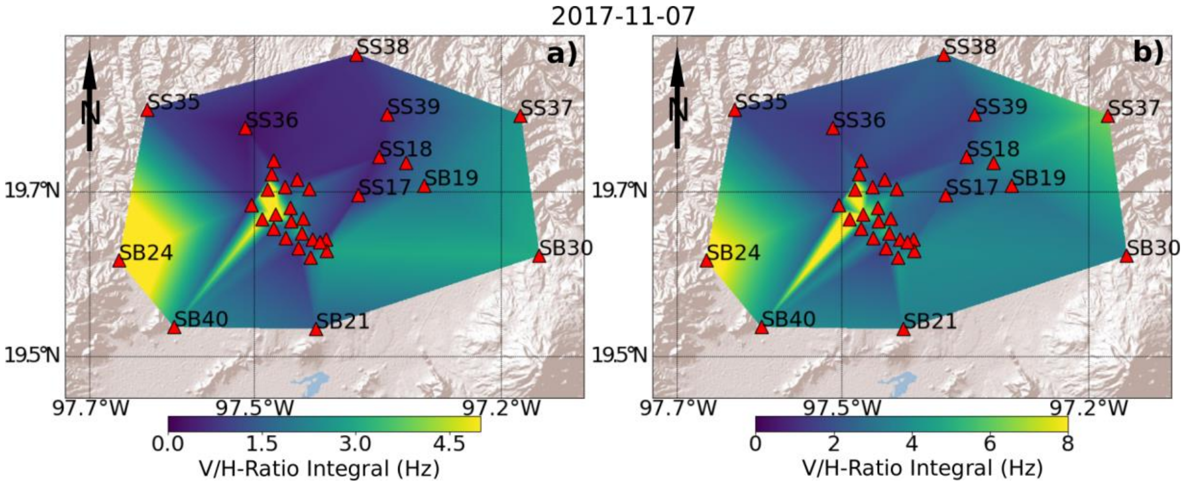

Figure 117: Map of the full integral under the V/H-Ratio curve in a frequency range from a) 1 to 2 Hz and b) 1 to 4 Hz. The value of the integral changes slightly over time but in areas with a high value, the integral does not change significantly. Note, due to data gaps not all available stations are used at this site.

5.8.2.4 Interpretation

A full interpretation regarding the observations displayed in Figure 116 and Figure 117 is challenging. We plan to check other frequency ranges and may will apply additional filtering. However, in the centre of the array we obtained relative high V/H values as well as relative high PSD-IZ values. This may be indicative for an underlying geothermal reservoir. On the other hand this observation is only true for a limited number of stations in the central area. To predict any possible reservoir extensions a more stable pattern should be achieved with a more detailed analysis of so far unknown local noise sources (pumps, streets, etc.).

6 Conclusion

6.1 Main results achieved – milestones of the task

Table 4. List of Milestones

Milestones	Due date /data of achievement	Status
M5.2 Seismic network deployed	21.11.2017	MS reached succesfully

6.2 Scientific knowledge increased

The study presented here confirms that seismic data is of great use for a better understanding and quantification of the structure of geothermal fields.

We used a large range of seismic methods and demonstrated that the results are significant, comparable with each other and complementary. Most results obtained concern Los Humeros, as the deployment occurred earlier in the project and seismic events could be detected, allowing the comparison between a larger number of seismic methods.

Concerning the active seismic data set. The analysis of the seismic lines L2, L3 and L4, L5 indicate clear structural features related to faults. The faults delineate block which also have different velocities. We interpreted the velocity models of these lines intersected by faults. The different responses in the four panels are different, which are possibly due to local anisotropy effects or to inhomogeneity. This analysis of shallow seismic properties is preliminary and can be considered for future work integrated with additional shallow surface information, including geological interpretation of faults and their orientation relative to the seismic lines.

Concerning the passive data set, the choice of the unconventional seismic network and preliminary study for designing the network proved to be very valuable, as the deployment performed was a good choice as results of all methods are satisfying for all methods and also as results of different method tend to converge, which in geophysics is not always so common. In particular, in the results of the synthetic tests, we observed that, for a tomographic purpose, the regular distribution of the stations in a small area, jointly with the use of irregular discretization allows us to reach the best results to define velocity field of the model around the earthquakes cluster. Conversely, the inversion process with sparse distribution of the stations in a large area provides average velocity values along the ray band connecting each station to the cluster of earthquakes.

The seismic activity was related to the location of earthquakes, suggesting the injection of used fluids from the geothermal wells is suggesting that there is a relation between the injection of used fluid from the geothermal wells and local seismic events. Those events are small (magnitude 0-2) located at shallow depth (between 1 and 3 km) and occur as clusters of earthquakes, with main occurrence in the central and north tone of Los Potretos Caldera. The focal mechanism of the largest seismic event could be determined and reveal many shearing modes. Strike-slip faulting, reverse and normal faulting. However, mains directions of strikes are NNW to NNE, direction consistent with the main geological features and the anomalies direction revealed in all tomography results. Long period events have also been observed and some of them triggered by regional large earthquakes (e.g., Caló et al., 2019). They occur also at the boundaries between the different velocity anomalies.

All tomography results point to similar features. The travel time tomography image shallow structures (0 to 4 km depth) and ambient noise tomography image deeper structure, although with less resolution, but wider area. The autocorrelation method result point to high frequency resolution of reflectors. A detail analysis is still under process, but from the results it appears that reflectors match also boundaries between velocity anomalies.

The main features concern a high velocity anomaly visible in all topographies in the north within the Caldera and a low velocity anomaly in the south.

The next step concern publications. The following publications are already in preparation envisaged:

- Conventional analysis of the earthquake detected (KIT, GFZ, Mexican partners)
- Earthquake base travel time tomography (GFZ, KIT, Mexican partners, Toledo et al., 2019)
- Ambient noise tomography (TNO, ETH, Mexican partners)
- Time reverse imaging (Werner and Saenger, 2019).
- Beamforming method for structural imaging (Loerr et al., 2019)
- Near-surface geophysical investigation for characterization of a volcanic geothermal reservoir by active-seismic-data tomography and attenuation analysis (Böhm and other, 2019, Submitted to NSG 2019)
- Offset-gap compensation by seismic interferometry for shallow signals of active-seismic lines acquired in a superhot geothermal field (Barison et al., submitted to NSG 2019)
- Processing of Los Humeros active seismic lines, depth imaging results (OGS, Barison et al., Paper in preparation)

Concerning the next steps within GEMex using those results, it should be mentioned that further investigations for each method is required, not only by consolidating results from each methods, but also by integrating all seismic results together. This will improve the result of each method alone. Then, the integration with other geophysical methods should allow imaging with improved accuracy the structure of Los Humeros.

7 References

Bakulin A. and Calvert R., 2006. The virtual source method: Theory and case study.Geophysics, 71 (4), SI139–SI150.

Bakun WH, Joyner WB, 1984. The ML scale in central California. Bull. Seismol. Soc. Amer. 74:1827–1843

Bard, P.-Y., 1999. Microtremor measurements: a tool for site effect estimation. The effects of surface geology on seismic motion, 3:1251–1279.

Becker, G. & Knapmeyer-Endrun, B., 2018. Crustal thickness across the Trans-European Suture Zone from ambient noise autocorrelations, *Geophys. J. Int.*, **212**, 1237-1254.

Bensen, G., M. Ritzwoller, M. Barmin, A. Levshin, F. Lin, M. Moschetti, N. Shapiro and Y. Yang (2007). Processing seismic ambient noise data to obtain reliable broad-band surface wave dispersion measurements. Geophysical Journal International 169(3): 1239-1260.

Beresnev, I. & Johnson, P., 1994. Elastic-wave stimulation of oil production: A review of methods and results, Geophysics, 59(6), 1000–1017.

Beyreuther M, Barsch R, Krischer L, Megies T, Behr Y, Wassermann J, 2010. ObsPy: A Python Toolbox for Seismology. Seismological Research Letters 81:530–533. doi: 10.1785/gssrl.81.3.530

Böhm G. and Petronio L., 2003. 3D turning ray tomography in a real case. 65th EAGE Conference, Stavanger, Norway, Extended abstract, D-25.

Boullenger, B., Verdel, A., Paap, B., Thorbecke, J. & Draganov, D., 2015. Studying CO2 storage with ambient-noise seismic interferometry: A combined numerical feasibility study and field-data example for Ketzin, Germany, *Geophysics,* **80(1)**, Q1-Q13.

Calcagno P., Evanno G., Trumpy E., Gutiérrez-Negrín L.C., Macías J.L., Carrasco-Núñez G., Liotta D., 2018. Preliminary 3-D geological models of Los Humeros and Acoculco geothermal fields (Mexico) – H2020 GEMex Project. Adv. Geosci. 45:321–333. doi: 10.5194/adgeo-45-321-2018

Calò M. and C. Dorbath, 2013a. Different behaviours of the seismic velocity field at Soultz-sous-Forêts revealed by 4-D seismic tomography: case study of GPK3 and GPK2 injection tests. Geophysical Journal International 194(2): 1119-1137.

Calò M., X. Kinnaert and C. Dorbath, 2013b. Procedure to construct three-dimensional models of geothermal areas using seismic noise cross-correlations: application to the Soultz-sous-Forêts enhanced geothermal site. Geophysical Journal International 194(3): 1893-1899.

Calò M., J. Carrillo, B. Espinosa, I. Chavarria, S. Hernandez, A. Soto, P. Jousset, M. Perton, T. Toledo and E. Gaucher, 2019. Triggered LP seismicity in geothermal fields and its implication on the characterization of the buried structures. General Assembly, EGU2019-12153

Carrasco-Núñez, G., J. Hernández, L. De León, P. Dávila, G. Norini, J. P. Bernal, B. Jicha, M. Navarro and P. López-Quiroz, 2017. Geologic Map of Los Humeros volcanic complex and geothermal field, eastern Trans-Mexican Volcanic Belt/Mapa geológico del complejo volcánico Los Humeros y campo geotérmico, sector oriental del Cinturón Volcánico Trans-Mexicano.

Cerveny, V., 2005. Seismic ray theory. Cambridge University Press, 724 pp.

Compañia Mexicana de Exploraciones S.A., 1998. Informe sismologico final (Vibrosismo) - Area Los Humeros, Prospecto: Los Humeros Sismica2D. 201 pp.

Dangel S., Schaepman M., Stoll E., Carniel R., Barzandji O., Rode E.-D., & Singer J., 2003. Phenomenology of tremor-like signals observed over hydrocarbon reservoirs, Journal of Volcanology and Geothermal Research, 128(1-3), 135–158.

Draganov, D., Campman, X., Thorbecke, J., Verdel, A. & Wapenaar, K., 2009. Reflection images from ambient seismic noise, *Geophysics*, **74**, 63-67.

Draganov, D., Campman, X., Thorbecke, J., Verdel, A.& Wapenaar, K., 2013. Seismic exploration-scale velocities and structure from ambient seismic noise (>1 Hz), *J. geophys. Res*., **118**, 4345-4360.

Draganov, D., Wapenaar, K., Mulder, W., Singer, J. & Verdel, A., 2007. Retrieval of reflections from seismic background-noise measurements, *Geophys. Res. Lett.,* **34**, L04305, doi:10.1029/2006GL028735.

Dziewonski, A. M. and D. L. Anderson, 1981. Preliminary reference Earth model. Physics of the earth and planetary interiors 25(4): 297-356.

Gilbert P., 1972. Iterative methods for the 3D reconstruction of an object from projections. J. Theor. Biol. 76:105–117.

Golub, G. H., M. Heath and G. Wahba, 1979. Generalized cross-validation as a method for choosing a good ridge parameter. Technometrics 21(2): 215-223.

Gorbatov, A., Saygin, E. & Kennett, B., 2013. Crustal properties from seismic station autocorrelograms, *Geophys. J. Int*., **192**, 861-870.

Graf, R., Schmalholz, S., Podlachikov, Y., & Saenger, E. H., 2007. Passive low frequency spectral analysis: Exploring a new field in geophysics, World Oil, pp. 47–52.

Green, A. G. & Greenhalgh, S., 2010. Comment on 'Low-frequency microtremor anomalies at an oil and gas field in Voitsdorf, Austria' by Marc-André Lambert, Stefan Schmalholz, Erik H. Saenger and Brian Steiner, Geophysical Prospecting 57, 393-411, Geophysical Prospecting, 58(2), 335–339.

Gutiérrez-Negrín LCA, Quijano-León J.L., 2004. Analysis of seismicity in the Los Humeros, Mexico, geothermal field. In: Geothermal Resources Council Transactions, pp 467–472

Heath, B., Hooft, E. & Toomey, D., 2018. Autocorrelation of the seismic wavefield at Newberry Volcano: Reflections from the magmatic and geothermal systems, *Geophys. Res. Lett*., **45**, 2311-2318.

Hunter, J. D., 2007. Matplotlib: A 2d graphics environment. Computing In Science & Engineering, 9(3):90–95.

Hurtado, A., 2001. Mecanismos focales y modelamiento (CMT) del sismo del 1ro de julio de 1999, campo geotérmico de Los Humeros. Informe Interno del Instituto de Ingeniería.

Jones, E., Oliphant, T., Peterson, P., et al., 2001. SciPy: Open source scientific tools for Python. [Online; accessed 2019-02-26].

Jousset, P., Haberland, C., Bauer, K. & Arnason, K., 2011. Hengill geothermal volcanic complex (Iceland) characterized by integrated geophysical observations, *Geothermics* 40, 1–24.

Kazantsev, A., Egermann, P., Ramadhan, I., Huguet, F., Formento, C., Peruzzetto, M., Chauris, H., & Métaxian, J.-P., 2017b. An innovative methodology based on Low Frequency Passive Seismic data analysis to map geothermal reservoir steam saturated areas, in 5th International Indonesia Geothermal Conference and Exhibition (IIGCE), Jakarta, Indonesia.

Kelly, M. C., Riahi, N., Ruiz, M., & Weiwei, 2013. Bayesian DHI for seismic data, US Patent US8358561B2; Assignee: Spectraseis AG.

Kennett, B.L.N., Saygin, E. & Salmon, M., 2015. Stacking autocorrelograms to map Moho depth with high spatial resolution in southeastern Australia, *Geophys. Res. Lett*., **42**, 7490-7497.

Kurlenya, M. V. & Serdyukov, S. V., 1999. Low-frequency resonances of seismic luminescence of rocks in a low-energy vibration-seismic field, Journal of Mining Science, 35(1), 1–5.

Lambert, M.-A., Saenger, E., Quintal, B., & Schmalholz, S., 2013. Numerical simulation of ambient seismic wavefield modification caused by pore-fluid effects in an oil reservoir, Geophysics, 78(1), T41–T52.

Lambert, M.-A., Schmalholz, S. M., Saenger, E. H., & Steiner, B., 2009. Low-frequency microtremor anomalies at an oil and gas field in Voitsdorf, Austria, Geophysical Prospecting, 57(3), 393–411.

Lambert, M.-A., Schmalholz, S. M., Saenger, E. H., & Steiner, B., 2010. Reply to comment on 'Low-frequency microtremor anomalies at an oil and gas field in Voitsdorf, Austria' by Marc-André Lambert, Stefan M. Schmalholz, Erik H. Saenger and Brian Steiner, Geophysical Prospecting 57, 393-411, Geophysical Prospecting, 58(2), 341–346.

Lehujeur, M., J. Vergne, J. Schmittbuhl and A. Maggi., 2015. Characterization of ambient seismic noise near a deep geothermal reservoir and implications for interferometric methods: a case study in northern Alsace, France." Geothermal Energy 3(1): 3.

Lermo, J., Havskov, J, and J. Soto, 2001. Sistema de información sismotelemétrica de México (SISMEX). Veintisiete años de servicio. Memorias Técnicas del XIII Congreso Nacional de Ingeniería Sísmica, Guadalajara, Jal. México, Octubre 31-Noviembre 3.

Lermo J., Antayhua Y, Quintanar L, Lorenzo C., 2007. Estudio sismológico del campo geotérmico de Los Humeros, Puebla, México. Parte I: Sismicidad, mecanismos de fuente y distribución de esfuerzos. In: Congreso Anual 2007.

Lermo, J., Antayhua, Y., Quintanar, L. and Lorenzo, C., 2008. Estudio sismológico del campo geotérmico de Los Humeros, Puebla, México. Parte II. Revista Mexicana de Geoenergía

Lermo J., Lorenzo C., Antayhua Y., Ramos E., Jiménez N., 2016. Sísmica pasiva en el campo geotérmico de Los Humeros, Puebla-México y su relación con los pozos inyectores. In: XVIII Congreso Peruano de Geología

Lermo, J., Havskov, J, and J. Soto, (2001), "Sistema de información sismotelemétrica de México (SISMEX). Veintisiete años de servicio", Memorias Técnicas del XIII Congreso Nacional de Ingeniería Sísmica, Guadalajara, Jal. México, Octubre 31-Noviembre 3.

Levander, A. R., 1988, Fourth-order finite-difference P-SV seismograms. Geophysics, 53 (11), 1425-1436.

Levshin, L. and A. Saletskii., 1989. Luminescence and its Measurement. Izdat. Mosk. Gos. Univ., Moscow: 159-172.

Löer, K., Riahi, N., & Saenger, E.H., 2018. Three-component ambient noise beamforming in the Parkfield area, *Geophys. J. Int.*, 213,1478-1491.

Löer K., N Riahi and E. H. Saenger, 2019. Investigating the deep structures of the Los Humeros geothermal field, Mexico, with three-component beamforming of ambient seismic noise. General Assembly EGU2019-16615.

Lomax A, Virieux J, Volant P, Berge-Thierry C., 2000. Probabilistic Earthquake Location in 3D and Layered Models. In: Thurber C, Rabinowitz N (eds) Advances in Seismic Event Location, vol 18. Springer Netherlands, pp 101–134

Lomax A.,2018. The NonLinLoc home page. http://alomax.free.fr/nlloc/. Accessed 15 May 2018

Lowrie, W., 2007. *Fundamentals of Geophysics*, p. 136, Cambridge University Press, Cambridge, UK.

Martins, J., E. Ruigrok, D. Draganov, A. Hooper, R. Hanssen, R. White and H. Soosalu, 2019a. Torfajökull's magmatic plumbing system with seismic interferometry and phase-velocity surface-wave tomography." Journal of Geophysical Research: Solid Earth.

Martins, J.E., C. Weemstra, E. Ruigrok, A. Verdel, P. Jousset, Hersir G.P., 2019b under review. Imaging Reykjanes Peninsula high-enthalpy geothermal field with 3D S-wave velocity from ambient-noise tomography: a study on resolution, J. Volcanol. Geotherm. Res.

Megies T., 2016. Obspyck 0.4.1. [https://github.com/megies/obspyck/wiki. Accessed 17 September 2018](https://github.com/megies/obspyck/wiki)

Mordret, A., M. Landès, N. Shapiro, S. Singh and P. Roux, 2014. Ambient noise surface wave tomography to determine the shallow shear velocity structure at Valhall: depth inversion with a Neighbourhood Algorithm. Geophysical Journal International 198(3): 1514-1525.

Mordret, A., D. Rivet, M. Landès and N. M. Shapiro, 2015. Three-dimensional shear velocity anisotropic model of Piton de la Fournaise Volcano (La Réunion Island) from ambient seismic noise." Journal of Geophysical Research: Solid Earth 120(1): 406-427.

Nikolaevskiy, V. N., Lopukhov, G. P., Yizhu, L., & Economides, M. J., 1996. Residual Oil Reservoir Recovery With Seismic Vibrations, SPE Production & Facilities, 11(02), 89–94.

Obermann, A., T. Kraft, E. Larose and S. Wiemer, 2015. Potential of ambient seismic noise techniques to monitor the St. Gallen geothermal site (Switzerland). Journal of Geophysical Research: Solid Earth 120(6): 4301-4316.

Oren, C. & Nowack, R.L., 2017. Seismic body-wave interferometry using noise autocorrelations for crustal structure, *Geophys. J. Int*., **208**, 321-332.

Park, C. B., R. D. Miller and J. Xia, 1998. Imaging dispersion curves of surface waves on multi-channel record. SEG Technical Program Expanded Abstracts 1998, Society of Exploration Geophysicists: 1377-1380.

Park, C. B., R. D. Miller, J. Xia, J. A. Hunter and J. B. Harris, 1999. Higher mode observation by the MASW method. SEG Technical Program Expanded Abstracts 1999, Society of Exploration Geophysicists: 524-527.

Podladchikov, Y., Lambert, M.-A., Dewarrat, R., & Schmalholz, S., 2010. VH Reservoir Mapping, Patent US7676326B2; Assignee: Spectraseis AG.

Poli, P., Pedersen, H.A., Campillo, M. & POLENET/LAPNET Working Group, 2012. Emergence of body waves from cross-correlations of short period seismic noise, *Geophys. J. Int.*, **188**, 549-558, doi: 10.1111/j.1365- 246X.2011.05271.x.

Quan, Y., and Harris, J. M., 1997. Seismic attenuation tomography using the frequency shift method. Geophysics, 62, 895-905.

Quintal, B., 2012. Frequency-dependent attenuation as a potential indicator of oil saturation, Journal of Applied Geophysics, 82, 119–128.

Riahi, N., Bokelmann, G., Sala, P. & Saenger, E.H., 2013. Time-lapse analysis of ambient surface wave anisotropy: a three-component array study above an underground gas storage, *J. geophys. Res.*, 118(10), 5339–5351.

Ritzwoller, M. H. and A. L. Levshin, 1998. Eurasian surface wave tomography: Group velocities." Journal of Geophysical Research: Solid Earth 103(B3): 4839-4878.

Romero, P. & Schimmel, M., 2018. Mapping the basement of the Ebro Basin in Spain with ambient noise autocorrelations, *J. geophys. Res: Solid Earth*, **123**. https://doi.org/10.1029/2018/JB015498.

Rost, S. & Thomas, C., 2009. Improving seismic resolution through array processing techniques, *Surv. Geophys.*, 30, 271-299.

Ruigrok, E., Campman, X., & Wapenaar, K., 2011. Extraction of P-wave reflections from microseisms, *C. R. Geosci*., **343**(8), 512 - 525.

Saenger, E. H., 2008. Seismic attributes for reservoir localization, Patent US20080288173A1; Assignee: Spectraseis AG.

Saenger, E. H., 2009. Signal integration measure for seismic data, Patent US7590491B2, Assignee: Spectraseis AG.

Saenger, E., Steiner, B., & Schmalholz, S., 2010. Time reverse reservoir localization, Patent US7675815B2; Assignee: Spectraseis AG.

Saenger, E. H., Schmalholz, S. M., Lambert, M.-A., Nguyen, T. T., Torres, A., Metzger, S., Habiger, R. M., Müller, T., Rentsch, S., & Méndez-Hernández, E., 2009. A passive seismic survey over a gas field: Analysis of low-frequency anomalies, Geophysics, 74(2), O29–O40.

Saygin, E., Cummins, P.R. & Lumley, D., 2017. Retrieval of the *P* wave reflectivity response from autocorrelation of seismic noise: Jakarta Basin, Indonesia, *Geophys. Res. Lett*., **44**, 792-799.

Shapiro, N. M. and M. Campillo, 2004. Emergence of broadband Rayleigh waves from correlations of the ambient seismic noise. Geophysical Research Letters 31(7).

Shapiro, N. M., M. Campillo, L. Stehly and M. H. Ritzwoller, 2005. High-resolution surface-wave tomography from ambient seismic noise. Science 307(5715): 1615-1618.

Stefani, J. P., 1995. Turning-ray tomography. Geophysics, 60, 1917-1929.

Steiner, B., Saenger, E. H., & Schmalholz, S. M., 2008. Time reverse modeling of low-frequency microtremors: Application to hydrocarbon reservoir localization, Geophysical Research Letters, 35(3).

Tarantola A, Valette B., 1982. Inverse problems = quest for information. Journal of Geophysics 50:159–170

Tibuleac, I.M. & von Seggern, D., 2012. Crust-mantle boundary reflectors in Nevada from ambient seismic noise autocorrelations, *Geophys. J. Int*., **189**, 493-500.

Tokimatsu, K., 1997. Geotechnical site characterization using surface waves, Earthq. Geotech. Eng., in *Proc. IS-Tokyo'95 First Int. Conf. Earthq. Geotech. Eng.*, pp. 1333–1368. Balkema, Rotterdam.

Toledo, T., Jousset, P., Maurer, H. and Krawczyk, C. 2018. Optimized experimental network design for earthquake location problems: Applications to geothermal and volcanic field seismic network. Journal of Volcanology and Geothermal Research, https://doi.org/10.1016/j.jvolgeores.2018.08.011.

Toledo T., Gaucher E., Metz M., Jousset P., Maurer H., Krawkzyk C., Figueroa A. Calo M., 2019. Seismic earthquake tomography imaging of the Los Humeros geothermal field, Mexico: first results**.** General Assembly EGU2019-15960.

Urban E, Lermo J., 2013. Local seismicity in the exploitation of Los Humeros geothermal field, Mexico. In: 38th Workshop on Geothermal Reservoir Engineering, SGP-TR-19

Verdel, A., Wedemeijer, H., Paap, B., Vandeweijer, V., Weemstra, C., Jousset, P., Franke, S., Blanck, H., Águstsson, K., & Hersir, G. P., 2016. Reykjanes ambient noise reflection interferometry, *Proceedings of the European Geothermal Congress 2016*, Strasbourg, France, 19-24 Sept 2016, ISBN: 978-2-9601946-0-9.

Vesnaver A., Böhm G., 2000. Staggered or adapted grids for seismic tomography? The Leading Edge Journal, Vol 19: 944-950.

Wapenaar K., Draganov D. and Robertsson J. 2008. Seismic interferometry: History and present status. Society of Exploration Geophysics, Geophysics Reprint Series 26, ISBN 978-1-56080-150-4.

Weemstra, C., A. Obermann, A. Verdel, B. Paap, H. Blanck, E. Gunason, G. P. Hersir, P. Jousset and Ó. Sigurdsson, 2016. Time-lapse seismic imaging of the Reykjanes geothermal reservoir. Proc. European Geothermal Congress, Strasbourg, France.

Welch, P., 1967. The use of fast Fourier transform for the estimation of power spectra: a method based on time averaging over short, modified periodograms. IEEE Transactions on audio and electroacoustics, 15(2):70–73.

Werner C. and E. H. Saenger, 2019. Sensitivity maps for time-reverse imaging. General Assembly EGU 2019- 7106.

Yilmaz O., 2001. Seismic Data Analysis: Processing, Inversion, and Interpretation of Seismic Data in Geophysics, vol. 1 & 2, 2065 pp., 2nd edition. Society of Exploration Geophysicists.

Zhan, Z., Ni, S., Helmberger, D. V., & Clayton, R. W., 2010. Retrieval of Moho-reflected shear wave arrivals from ambient seismic noise, *Geophys. J. Int*., **182(1)**, 408-420, doi: 10.1111/j.1365-246X.2010.04625.x.

Zhou, Y., F. Dahlen and G. Nolet, 2004. Three-dimensional sensitivity kernels for surface wave observables. Geophysical Journal International 158(1): 142-168.

Coordination Office, GEMex project

Helmholtz-Zentrum Potsdam
Deutsches GeoForschungsZentrum

Telegrafenberg, 14473 Potsdam

Germany